the Astrophysical Herald

Neutrinos as probes for particle physics and astronomy

Promotores:

prof. dr. K. J. F. Gaemers
prof. dr. R. A. M. J. Wijers

This thesis was reviewed by:

prof. dr. J. W. van Holten
prof. dr. M. de Jong
prof. dr. M. van der Klis
prof. dr. J. Kuijpers
prof. dr. J. Smit

Faculteit der Natuurwetenschappen, Wiskunde en Informatica
Universiteit van Amsterdam

Cover design: Robert van Sluis | www.eyefordetail.nl

the Astrophysical Herald

Neutrinos as probes for particle physics and astronomy

ACADEMISCH PROEFSCHRIFT

ter verkrijging van de graad van doctor
aan de Universiteit van Amsterdam
op gezag van de Rector Magnificus
prof. dr. J. W. Zwemmer
ten overstaan van een door het college van promoties
ingestelde commissie,
in het openbaar te verdedigen in de Agnietenkapel
op vrijdag 21 september 2007, te 10:00 uur

door

Hylke Bernd Jan Koers

geboren te Utrecht

For my parents Albert and Maria,
for continuing inspiration

Preface

This dissertation is based on the following publications:

Koers, H. B. J. 2005, Phys. Lett., B605, 384
Koers, H. B. J. & Wijers, R. A. M. J. 2005, Mon. Not. R. Astron. Soc., 364, 934
Koers, H. B. J. & Wijers, R. A. M. J. 2006, PoS HEP2005, 16
Koers, H. B. J., Pe'er, A., & Wijers, R. A. M. J. 2006, hep-ph/0611219
Koers, H. B. J. & Giannios, D. 2007, A&A, in press (astro-ph/0703719)

Chapters 3–6 contain published results while chapters 2 and 7 are previously unpublished. Modifications to chapters that have been published as papers are as few as possible, and are solely intended to improve the coherence between the chapters. In particular, the method of citation has been made uniform throughout this dissertation and comments on future work and acknowledgments within the chapters have been removed.

Contents

1

Introduction

Neutrinos as probes for particle physics and astronomy

In the last few decades we have witnessed many important discoveries at the interface of particle physics and astronomy. The fruitful interplay between these fields is exemplified by the resolution to the solar neutrino problem, i.e. the discrepancy between predicted and observed fluxes of solar neutrinos: since the 1960s neutrino experiments have measured the flux of solar neutrinos (e.g., Davis et al. 1968) and found fluxes that are typically lower by a factor $\sim$3 compared to the flux predicted by solar models (Bahcall et al. 2001, and references therein). In a truly visionary paper, Gribov and Pontecorvo suggested as early as 1969 that this deficit could be the result of neutrino oscillations (Gribov & Pontecorvo 1969; see also Bahcall & Frautschi 1969 and Pontecorvo 1958; 1968): because the early neutrino experiments are exclusively sensitive to neutrinos of the electron-type, and because solar neutrinos are predominantly of this type, any neutrino oscillations from one type to another will reduce the number of interactions in these detectors. Nearly thirty years later, the Super-Kamiokande collaboration announced evidence for flavor oscillations in atmospheric neutrinos (Fukuda et al. 1998), a result that is widely regarded as the first compelling evidence for neutrino oscillations. Now that these oscillations are well established, we may conclude that observations of the sun have been instrumental in a better understanding of the nature of the neutrino and its place among the other fundamental particles.

Before the 1998 Super-Kamiokande results the existence of neutrino oscillations was supported by the solar neutrino problem, by observations of atmospheric neutrinos, and by accelerator-based experiments (although there was also experimental evidence against neutrino oscillations; see Fisher et al. 1999 for a review). The importance of the results obtained in 1998 is that they demonstrate, for the first time, that the fraction of neutrinos that remains undetected depends on the neutrino path length. This excludes uncertainties in the flux normalization and very strongly supports the oscillation hypothesis. A wealth of experimental data from atmospheric, solar, reactor and accelerator experiments has become available since (see Maltoni et al. 2004 for a recent review). These data corrob-

orate the neutrino oscillation hypothesis and put increasingly stronger bounds on neutrino masses and mixing angles. In particular, the SNO experiment (which is sensitive to neutrinos of all flavors) has found that the total neutrino flux is consistent with the solar model while the electron-neutrino flux is in keeping with earlier findings (Ahmad et al. 2002).

The first neutrinos from sources further away than the sun were observed in 1987, when the blue supergiant Sanduleak - 69202 exploded and became known as supernova SN1987A (see Arnett et al. 1989, Bethe 1990 for reviews). Eighteen hours before the first optical observation, a neutrino signal was detected by the Kamiokande-II (Hirata et al. 1987) and IMB (Bionta et al. 1987) experiments (there are also claims of detection by the Baksan and Mont Blanc laboratories but these are controversial; see Bethe (1990) and references therein). The neutrinos give important information on the physics of the supernova, such as the energies and timescales involved (see Bethe 1990 for a review). Furthermore, properties of the neutrino itself have been inferred from the observations. Bahcall & Glashow (1987) and Gaemers et al. (1989) have derived upper limits on neutrino masses from these observations, and Barbieri & Mohapatra (1988) and Lattimer & Cooperstein (1988) have found an upper limit on the neutrino magnetic moment. More recently, it has been argued that neutrino observations from SN1987A can be used to constrain the size of large extra dimensions (Cullen & Perelstein 1999).

Apart from the discovery of neutrino oscillations and the detection of cosmic neutrinos, there have been many other important discoveries at the interface of particle physics and astronomy in recent years. Measurements of the cosmic microwave background by COBE (Bennett et al. 1996) and WMAP (Hinshaw et al. 2006, Page et al. 2006, Spergel et al. 2006) have provided important information on the physics of the early universe. In combination with other measurements of the large-scale structure in the universe (Cole et al. 2005, Adelman-McCarthy et al. 2006) these results constrain many cosmological parameters of the present universe and point toward what is known as the concordance model — a universe that is spatially flat and whose energy content is dominated by ‘dark energy’ and ‘dark matter’ (see Spergel et al. 2006, Yao et al. 2006 for reviews). Results from supernova surveys (Perlmutter et al. 1999, Riess et al. 2004, Astier et al. 2006) are compatible with the existence of dark energy, while recent observations based on weak gravitational lensing (Clowe et al. 2006) lend support to the existence of dark matter. It should however be stressed that the microphysical origin of these components is still unclear, posing an important challenge for the future.

We have also learned a great deal about the once enigmatic gamma-ray bursts (GRBs) since the first X-ray (Costa et al. 1997) and optical (Van Paradijs et al. 1997) afterglows were observed a decade ago. There is now increasing evidence that long GRBs are related to the death of massive stars (e.g., Woosley & Bloom 2006). Note however that the situation for short GRBs is presently not so clear (e.g., Lee & Ramirez-Ruiz 2007). GRBs are of particular interest for astro-particle physics as they are believed to be astrophysical proton accelerators. Vietri (1995) and Waxman (1995) have found that

GRBs are able to accelerate protons up to $\sim 10^{20}$ eV, which suggests that GRBs can be the long-sought origin of ultra-high-energy cosmic rays. Whereas GRBs may provide the answer as to the origin of cosmic rays, high-energy emission from GRBs may also contribute to a better understanding of the bursts themselves. In particular, high-energy neutrinos would demonstrate that the relativistic outflow associated with GRBs has a hadronic component and could provide further indications regarding the nature of this outflow. The observation of this emission is a very challenging goal for the future.

Given these recent developments, it may be expected that the intersection of particle physics and astronomy will be a very interesting and productive field of research for the coming years. With current and future neutrino experiments such as AMANDA (Andres et al. 2000), ANTARES (Aslanides et al. 1999), KM3NeT (Katz 2006) and IceCube (Ahrens et al. 2003) reaching unprecedented sensitivities, it may also be expected that neutrinos will continue to play an important role in this field. Without doubt, these experimental efforts will be matched with theoretical work to understand the meaning of neutrino observations and of non-observations, to provide continuous motivation for new and improved experiments, and — if we are fortunate — to inspire people with visionary ideas like Gribov and Pontecorvo did nearly four decades ago.

This dissertation concerns two subjects in which cosmic neutrinos may be useful probes of (astro)physical processes. The first subject is pair creation of neutrinos by an external source, a mechanism very similar to electron-positron pair creation in an electric field as studied by Schwinger (1951). We study theoretical aspects of this process, in particular the connection between perturbative and non-perturbative formalisms. Furthermore we investigate whether neutrino emission from neutron stars by this mechanism may be observable. Whereas this study is concerned with properties of the neutrino, and its interaction with other particles, the second subject is based on the potential use of neutrinos as probes for astrophysical systems: we consider the creation and emission of neutrinos in various stages of a developing GRB. We investigate whether these neutrinos could be detected and how such observations can be used to constrain GRB models. These subjects are discussed in more detail below.

Neutrino pair creation by an external source

The equivalence of mass and energy raises the possibility that massive particles can be created, in vacuum, by a gauge field of sufficient strength. One way to view this process is that, in the presence of a strong field, the vacuum can decay to a state containing particles. To preserve quantum numbers, such as the electric charge, the particles are created in pairs. This process is usually referred to as spontaneous pair creation, pair creation by an external source, or pair creation by vacuum decay to discriminate it from pair creation in particle scatterings.

Building on earlier work of some of the pioneers of modern quantum field theory (Klein 1929, Sauter 1931, Heisenberg & Euler 1936), Schwinger (1951) computed the

pair creation rate w of electron-positron pairs in a constant electric field E and found that

$$w = \frac{\alpha\epsilon_0 E^2}{\pi^2\hbar}\sum_{n=1}^{\infty}\frac{1}{n^2}\exp\left(-\frac{n\pi m^2 c^3}{|eE|\hbar}\right) = 10^{51}\ \mathrm{cm}^{-3}\ \mathrm{s}^{-1}\left(\frac{E}{E_*}\right)^2\sum_{n=1}^{\infty}\frac{1}{n^2}\exp\left(-\frac{nE_*}{|E|}\right), \quad (1.1)$$

where m and e denote the electron mass and charge, respectively; α is the fine-structure constant; ϵ_0 denotes the vacuum permittivity; and $E_* = \pi m^2 c^3/(e\hbar) = 4\times 10^{16}$ V cm^{-1} is the electric field strength scale defined by the electron mass and other constants of nature. As the creation of an electron-positron pair by this mechanism requires a very large electric field strength, it is difficult to realize in a laboratory. To date the mechanism has not been directly observed, but experiments with high-intensity optical lasers (e.g., Blaschke et al. 2006) or X-ray free electron lasers (e.g., Alkofer et al. 2001) may be able to do so in the near future.

Even in the absence of observations, pair creation by an external source is very interesting from a theoretical point of view. It is closely related to Hawking radiation (Hawking 1974; 1975) and Unruh radiation (Unruh 1976) and provides a few explicit examples to study the connection between non-perturbative quantum field theory and perturbative expansions (see, e.g., Dunne & Hall 1999). Furthermore spontaneous pair creation plays an important role in the physics of the early universe, e.g. in reheating of the universe after inflation (Turner 1983) and in the generation of perturbations during inflation (Martin 2007).

Electric fields strong enough to create electron-positron pairs through vacuum decay may exist in astrophysical systems such as magnetars (Usov 1992) or black holes (Damour & Ruffini 1975; 1976). In general it is however difficult to identify pair creation by vacuum decay in astrophysical systems due to the competing effects of pair creation by photon – photon interactions and by photon decay in the presence of a magnetic field (see Treves et al. 2000 for a discussion). Preparata et al. (1998) have suggested that charged black holes may be accompanied by a so-called dyadosphere, i.e. a macroscopic region in space where the electric field is stronger than the critical value for vacuum decay. The authors suggest that the energy that can be extracted from the black hole by this mechanism may be sufficient to power a GRB (see also Damour & Ruffini 1975). It is however questionable whether these strong electric fields can develop over astrophysical distances (Page 2006).

Because neutrinos carry weak nuclear charge, a macroscopic configuration of neutrons may create pairs of neutrinos in a very similar manner. The production of neutrinos by this mechanism in a neutron star was considered earlier by Loeb (1990), Kachelriess (1998), and Kusenko & Postma (2002), who treated the problem with a non-perturbative formalism. In this dissertation we study this mechanism using perturbative quantum field theory. An advantage of this method is that it is not limited to a specific source but allows us to draw conclusions with a broad applicability. Furthermore, we gain further insight into the mechanism by comparing our findings to the non-perturbative results

derived earlier (Kusenko & Postma 2002) and by comparing neutrino pair creation to electron-positron pair creation.

Creation and emission of neutrinos in gamma-ray bursts

Whereas the interest in spontaneous pair creation is largely driven by theory, research on GRBs is mostly driven by observations. In fact, theorists have for decades struggled to explain the observed properties of GRBs, which were by many regarded as the biggest mystery in astrophysics.

Since the cosmological origin of GRBs was firmly established by the first afterglow observation in 1997 (Costa et al. 1997, Frail et al. 1997, Van Paradijs et al. 1997), there has been a lot of progress in our understanding of this phenomenon. Observations have shown that at least some GRBs are connected with supernovae, indicating that these are ultimately caused by the core-collapse of massive stars (Van Paradijs et al. 2000, Woosley & Bloom 2006). According to the leading 'fireball / blast wave' paradigm (see, e.g., Mészáros 2006 for a review), the energy that is liberated by such a catastrophic event is initially contained in a very hot and dense plasma (the fireball) which develops into a highly relativistic collimated outflow. In this process, the available energy is transferred to kinetic energy of the baryons that are contained in the outflow. Far away from the GRB central engine, the kinetic energy in this blast wave is partly dissipated by shock acceleration and emitted in the form of gamma rays. The remaining energy is dissipated in the subsequent interaction with the external environment, which results in the afterglow.

The blast wave model correctly describes the general features of both the prompt gamma-ray emission and the afterglow emission, but important questions remain. For example, how is the initial fireball formed and how is it collimated? Is the relativistic outflow dominated by thermal energy or can electromagnetic fields be energetically important? What is the nature of the central engine that powers the outflow? Recent observations by the SWIFT satellite (e.g., Mészáros 2006) have both provided new clues to existing questions (e.g. evidence for extended central engine activity) and raised intriguing new ones (e.g. the possibility of a new population of low-luminosity bursts).

GRBs are well-known candidate sources of cosmic neutrinos: reasonably large neutrino fluxes are expected in the tens-of-MeV range from the initial fireballs (Kumar 1999); in the ∼10-GeV range from neutron – proton collision in the accelerating outflows (Derishev et al. 1999b, Bahcall & Mészáros 2000, Mészáros & Rees 2000); in the ∼100-TeV range from the interaction of shock-accelerated protons with GRB photons (Waxman & Bahcall 1997); and in the ∼1-EeV range from the interaction of the fireball with the external medium (Waxman & Bahcall 2000).

In this dissertation we address the issue of how neutrinos can be used to gain a better understanding of GRBs. We consider the creation and emission of neutrinos by three different mechanisms that take place in different phases of a developing GRB: by leptonic

processes in the initial GRB fireballs, by inelastic neutron – proton scattering in the accelerating outflow and by proton – proton interactions when the outflow is traversing the preburst stellar environment. Neutrinos originating from each of these mechanisms may provide useful information on the physics of GRBs. This is discussed in more detail in the following.

Neutrino emission by the initial fireballs in GRBs — The observed high luminosity and rapid variability of GRBs imply that the initial fireballs should contain a huge amount of energy in a relatively small volume. In such an environment one expects a prolific creation of neutrinos. We study the creation and emission in these early GRB fireballs to establish whether there are regions in the parameter space of the fireball where cooling by neutrino emission is so efficient that it would terminate the developing GRB in the first phase of development. This may then put constraints on the parameter space of the initial fireballs in successful GRBs.

Neutrinos from neutron – proton collisions in the accelerating outflow — One of the important open questions regarding GRBs is as to the nature of the relativistic outflow. In the standard fireball scenario, the energy that is liberated by the central engine is initially stored as thermal energy of the fireball. Alternatively, the initial GRB energy may predominantly be in the form of Poynting flux. The dynamics of the outflow is very different in both cases: for the fireball model, radiation pressure accelerates the flow in such a way that the bulk Lorentz factor Γ is proportional to the distance from the central engine r during the accelerating phase (Paczyński 1986). For the 'AC' model (Spruit et al. 2001 and references therein) — a concrete realization of Poynting-flux dominated GRB outflows — the acceleration is much more gradual and the bulk Lorentz factor Γ is proportional to $r^{1/3}$ during acceleration (Drenkhahn 2002) . We investigate how the difference in dynamics affects neutrino production in inelastic neutron – proton interactions in the outflow and whether this neutrino emission can be used to differentiate between the fireball model and the AC model.

Neutrinos from proton – proton collisions in choked GRBs — In the light of the observed connection between GRBs and supernovae it is an interesting possibility that the formation of a fireball is quite a common phenomenon in supernovae but that only very energetic fireballs have sufficient power to traverse the pre-burst stellar environment and give rise to an actual GRB. In such a scenario it is assumed that fireballs with less energy are stopped below the stellar surface so that any electromagnetic emission is absorbed by the stellar material. However, if shocks form in the fireball at a substellar radius, protons (either cosmic-ray protons or protons contained in the fireball) can be accelerated and collide with target protons in the flow or with the pre-burst environment. This gives rise to high-energy neutrinos, which are likely the only observable signal that can indicate the existence of such a class of choked GRBs. We investigate what these neutrinos, if observed, can tell us about the physics of choked GRBs. For this purpose we derive a parameterization for the energy and angle distribution of pions and kaons created in energetic proton – proton collisions. This parameterization is presented as a

separate result because it can be applied to many other astrophysical scenarios.

Outline of this dissertation

This dissertation is divided into parts following the two subjects discussed above. Spontaneous pair creation is discussed in chapters 2 and 3, while the creation and emission of neutrinos in GRBs is the subject of chapters 4–7.

The present introduction constitutes chapter 1. In chapter 2 we discuss both perturbative and non-perturbative formalisms to compute the number of particles created by an external source. This provides a theoretical background for chapter 3, in which we study neutrino pair creation by an external source using a perturbative method and compare our findings to earlier results that are based on a non-perturbative method. In chapter 4 we consider the creation and emission of neutrinos in the very first stage of a GRB fireball. Chapter 5 concerns the dynamics of neutron-rich GRB flows and particle creation by inelastic neutron – proton collisions in these flows. Here we compare particle emission for the fireball model with particle emission for the 'AC' model, which is based on magnetic reconnection in Poynting-flux dominated GRB flows. In chapter 6 we present a parameterization of the energy and angular distributions of secondary pions and kaons created in energetic proton – proton collisions. This parameterization is used in chapter 7 to investigate possible neutrino signatures of choked GRBs. We present our conclusions in chapter 8.

Neutrino pair creation by an external source

2

Perturbative and non-perturbative methods in spontaneous pair creation

based on work with M. Postma
(unpublished)

2.1 Introduction

Quantum field theory (QFT) predicts that a sufficiently strong classical field can produce pairs of particles through breakdown, or decay, of the vacuum. For electromagnetic fields this effect has been investigated since the early days of quantum electrodynamics (Klein 1929, Sauter 1931, Heisenberg & Euler 1936, Schwinger 1951) and has received considerable interest since (see, e.g., Brezin & Itzykson 1970, Cornwall & Tiktopoulos 1989, Kluger et al. 1992). The creation of an electron-positron pair by this mechanism requires a very large electric field strength $\sim 10^{16}$ V cm^{-1} which is difficult to realize in a laboratory. To date the mechanism has not been directly observed, but experiments with high-intensity optical lasers (e.g., Blaschke et al. 2006) or X-ray free electron lasers (e.g., Alkofer et al. 2001) may be able to do so in the future.

Pair creation by an external source is of great theoretical interest. It is closely connected to phenomena that arise in quantum field theory on a non-trivial background such as Hawking radiation (Hawking 1974; 1975) and the related phenomenon of Unruh radiation (Unruh 1976). Furthermore, a number of pair-creation problems can be solved exactly and thus give insight into the relation between non-perturbative quantum field theory and perturbative expansions. A well-known pair-creation problem that has been solved exactly is due to Schwinger (1951), who considered the creation of electron-positron pairs by a constant electric field and found that the probability w for creating a

pair per unit time and volume is given by the following formula:[1]

$$w = \frac{\alpha\epsilon_0 E^2}{\pi^2} \sum_{n=1}^{\infty} \frac{1}{n^2} \exp\left(-\frac{n\pi m^2}{|eE|}\right), \tag{2.1}$$

where $\alpha \simeq 1/137$ is the fine-structure constant; ϵ_0 is the vacuum permittivity; E is the strength of the electric field; m is the electron mass; and e is the electric charge. This result is non-perturbative because the exponential term cannot be expanded in a Taylor series around $e = 0$. It may however be reproduced from a divergent perturbative series through a Borel dispersion relation (Dunne & Hall 1999).

In this chapter we discuss both the non-perturbative formalism of Bogoliubov transformations (section 2.2) and the perturbative QFT formalism (section 2.3) that can be used to compute the number of particles created by an external source. This provides the theoretical basis for the study on neutrino creation by an external source that is presented in chapter 3. We then present in section 2.4 a toy-model example, that we refer to as the 'time-dependent kink', which can be solved exactly. We show explicitly that the method of Bogoliubov transformation and the perturbative computation agree up to second non-trivial order in the coupling constant for this particular source. For simplicity we restrict ourselves to scalar quantum fields coupled to a scalar source in this chapter. The methodology for fermion pair creation is very similar.

2.2 The Bogoliubov method

In this section we present a brief but self-contained introduction to Bogoliubov coefficients and their use in pair-creation problems. For a more complete treatment the reader is referred to DeWitt (1975), Birrell & Davies (1982) and Bogoliubov & Shirkov (1983).

2.2.1 Quantum fields in a background

In free quantum field theory the dynamical behavior of scalar fields is determined by the Klein-Gordon equation. This equation is solved by the standard plane-wave mode solutions $u_k(x)$ and $v_k(x)$:

$$u_k(x) = v_k(x)^* = \frac{1}{\sqrt{2\omega_k}} e^{-i\omega_k t} e^{i\vec{k}\vec{x}}, \tag{2.2}$$

where ω_k and $\vec{k}$ denote the energy and the momentum, respectively. As these constitute a complete set of wave functions associated with particles (u_k) and antiparticles (v_k), any complex[2] scalar field $\phi(x)$ can be expanded in terms of these solutions with the

[1] In this and the following chapter we use natural units, in which $\hbar = c = 1$.

[2] We consider a complex scalar field throughout this section. For a real scalar field one should identify $a_k \equiv b_k$.

appropriate coefficients a_k and b_k:

$$\phi(x) = \int \frac{d^3k}{(2\pi)^3} \left(a_k u_k(x) + b_k^\dagger v_k(x) \right) . \tag{2.3}$$

The classical field theory is lifted to a quantum field theory by promoting the coefficients a_k and b_k to operators and imposing the appropriate commutation relations (e.g., Itzykson & Zuber 1980). With these operators one can then construct a Fock space with a well-defined number of particles.

The situation is more intricate when the theory is defined on a non-trivial background (e.g., near a black hole or in de Sitter space) or when the scalar fields are coupled to an external source. We consider here the case that the fields are coupled to a spatially homogeneous, time-dependent source that manifests itself as a time-dependent effective scalar mass $m(t)$. The wave equation for $\phi(x)$ can be expressed as follows:

$$\left(\frac{\partial^2}{\partial t^2} - \nabla^2 + m(t)^2 \right) \phi(x) = 0 . \tag{2.4}$$

We now consider a complete set of momentum eigenstates that solve the wave equation and that are grouped into two sets $U_k(x)$ and $V_k(x)$ which are conjugate in the sense that $U_k(x) = V_k(x)^*$. As the source depends only on time, we factorize the time-dependence and express these solutions as

$$U_k(x) = f_k(t) e^{i\vec{k}\vec{x}} , \tag{2.5}$$

where the function $f_k(t)$ should obey:

$$\left(\frac{\partial^2}{\partial t^2} + k^2 + m(t)^2 \right) f_k(t) = 0 . \tag{2.6}$$

Note that this is a second-order differential equation which admits two independent solutions for every k. We insist that the mode functions satisfy the Wronskian condition

$$\mathcal{W}\left[f_k, f_k^* \right] \equiv f_k(t) f_k'(t)^* - f_k'(t) f_k(t)^* = i , \tag{2.7}$$

where the prime indicates a derivative with respect to the time t. Note that eq. (2.7) is time-independent if $f_k(t)$ and $f_k^*(t)$ obey eq. (2.6). The Wronskian condition expressed in eq. (2.7) guarantees orthogonality of the conjugate solutions with respect to the inner product

$$\langle \phi_1, \phi_2 \rangle = -i \int_t d^3x \left(\phi_1 \frac{\partial \phi_2^*}{\partial t} - \frac{\partial \phi_1}{\partial t} \phi_2^* \right) , \tag{2.8}$$

where the integral is over an equal-time hypersurface. Here and in the following we normalize $f_k(t)$ such that:

$$\langle U_k, V_p \rangle = 0 ; \tag{2.9a}$$

$$\langle U_k, U_p \rangle = -\langle V_k, V_p \rangle = (2\pi)^3 \delta(\vec{k} - \vec{p}) . \tag{2.9b}$$

Such a set of conjugate mode solutions is a natural generalization of the plane-wave solutions $u_k(x)$ and $v_k(x)$ for scalar fields in a non-trivial background.

2.2.2 Bogoliubov coefficients

Because the set of conjugate solutions $\{U_k, V_k\}$ is not unique[3], we may express any particular field configuration $\phi(x)$ in terms of different bases. Here we consider two different bases, that we denote as barred and unbarred:

$$\phi(x) = \int \frac{d^3k}{(2\pi)^3} \left(a_k U_k(x) + b_k^\dagger V_k(x) \right) = \int \frac{d^3k}{(2\pi)^3} \left(\bar{a}_k \bar{U}_k(x) + \bar{b}_k^\dagger \bar{V}_k(x) \right) . \tag{2.10}$$

By virtue of completeness we can expand the elements of the barred basis in terms of the unbarred basis elements (and vice versa):

$$\bar{U}_k(x) = \int \frac{d^3p}{(2\pi)^3} \left(\alpha_{k,p} U_p(x) + \beta_{k,p} V_p(x) \right) ; \tag{2.11a}$$

$$\bar{V}_k(x) = \int \frac{d^3p}{(2\pi)^3} \left(\beta^*_{k,p} U_p(x) + \alpha^*_{k,p} V_p(x) \right) , \tag{2.11b}$$

which defines the, time-independent, Bogoliubov coefficients $\alpha_{k,p}$ and $\beta_{k,p}$. Note that there are two independent Bogoliubov coefficients (instead of four) because of the conjugation relationship $\bar{V}_k(x) = \bar{U}_k(x)^*$.

If the external source is homogeneous, as we assume here, the Bogoliubov coefficients are diagonal in momenta and we can write:

$$\alpha_{k,p} = \langle \bar{U}_k, U_p \rangle = -\langle V_p, \bar{V}_k \rangle = (2\pi)^3 \delta(\vec{k} - \vec{p})\, \alpha_k ; \tag{2.12a}$$

$$\beta_{k,p} = -\langle \bar{U}_k, V_p \rangle = \langle U_p, \bar{V}_k \rangle = (2\pi)^3 \delta(\vec{k} - \vec{p}) \beta_k , \tag{2.12b}$$

where α_k and β_k obey the useful relation $|\alpha_k|^2 - |\beta_k|^2 = 1$. Factorizing the time-dependence of the conjugate solutions as in eq. (2.5), we find that

$$\alpha_k = -i \left(\bar{f}_k(t) f_k'^*(t) - \bar{f}_k'(t) f_k^*(t) \right) ; \tag{2.13a}$$

$$\beta_k = i \left(\bar{f}_k(t) f_k'(t) - \bar{f}_k'(t) f_k(t) \right) , \tag{2.13b}$$

which expresses the Bogoliubov coefficients directly in terms of solutions to equation (2.6). The time-independence of α_k and β_k follows from the fact that the right hand sides of eqs. (2.13) can be expressed as Wronskians.

[3] In free field theory in Minkowski space the set of mode solutions is unique up to Lorentz transformations, making it a special case (e.g., DeWitt 1975).

2.2.3 Choice of vacuum density of states

For quantum fields in a non-trivial background, there is no unique expansion into mode solutions and hence no unique definition of creation and annihilation operators. The annihilation operators corresponding to the unbarred mode functions define a vacuum state $|0\rangle$:[4]

$$a_k|0\rangle = 0\,; \quad b_k|0\rangle = 0\,. \tag{2.14}$$

Similarly, the barred annihilation operators define a vacuum state $|\bar{0}\rangle$:

$$\bar{a}_k|\bar{0}\rangle = 0\,; \quad \bar{b}_k|\bar{0}\rangle = 0\,. \tag{2.15}$$

The two vacua are different states, and the state $|0\rangle$ will contain particles from the 'barred' point of view. The operators $\{a_k, b_k\}$ and $\{\bar{a}_k, \bar{b}_k\}$ are related through the Bogoliubov coefficients so that the density of states with momentum $\vec{k}$ in the state $|0\rangle$, as measured in 'barred' quanta, is equal to:

$$\bar{\mathcal{N}}_k = \langle 0|\bar{a}_k^\dagger \bar{a}_k|0\rangle = \int \frac{d^3p}{(2\pi)^3}\frac{d^3q}{(2\pi)^3}\beta^*_{k,p}\beta_{k,q}\langle 0|b_q b_p^\dagger|0\rangle = \int \frac{d^3p}{(2\pi)^3}\left|\beta_{k,p}\right|^2\,. \tag{2.16}$$

Using box normalization to extract a volume factor, this further simplifies to

$$\frac{\bar{\mathcal{N}}_k}{V} = |\beta_k|^2 = \frac{1}{2}\left(|\alpha_k|^2 + |\beta_k|^2 - 1\right)\,, \tag{2.17}$$

which gives the density of states per unit volume. The number of created antiparticles is equal to the number of particles, as can be demonstrated explicitly by evaluating $\langle 0|\bar{b}_k^\dagger \bar{b}_k|0\rangle$.

2.2.4 Adiabatic number operator

Equation (2.17) formally expresses the number of particles in the vacuum state associated with a given set of mode solutions, as measured in quanta of another set. There are infinitely many choices of mode solutions and it there is no a priori reason why any particular choice would be most suited to describe particle creation by an external source. From a physical point of view, a natural choice for the mode solutions is such that the Hamiltonian is diagonal in the corresponding creation and annihilation operators. This requirement defines the adiabatic mode functions f_k^{ad} and $f_k^{\mathrm{ad},*}$, together with the adiabatic creation and annihilation operators $a_k^{\mathrm{ad}(\dagger)}$ and $b_k^{\mathrm{ad}(\dagger)}$.

[4] The term 'vacuum state' may be confusing here because there is no clear physical interpretation of these states. Following the literature however, we will use 'vacuum state' to denote a state that is annihilated by a given choice of annihilation operators.

The Hamiltonian of the system of quantum fields ϕ with a time-dependent mass can be expressed as follows:

$$H(t) = \frac{1}{2}\int d^3x \left(\Pi^2 + (\nabla\phi)^2 + m(t)^2\phi^2\right), \tag{2.18}$$

where $\Pi = \phi'$ is the canonical momentum. We now demand that the Hamiltonian is instantaneously diagonalized at a specific time $t = t_0$:

$$H(t_0) = \int \frac{d^3k}{(2\pi)^3}\frac{\omega_k(t_0)}{2}\left(a_k^{\mathrm{ad},\dagger}a_k^{\mathrm{ad}} + b_k^{\mathrm{ad},\dagger}b_k^{\mathrm{ad}} + 1\right), \tag{2.19}$$

which requires that the adiabatic mode function obeys:

$$\left.\frac{\partial f_k^{\mathrm{ad}}}{\partial t}\right|_{t=t_0} = -i\omega_k(t_0)f_k^{\mathrm{ad}}(t_0)\,. \tag{2.20}$$

The adiabatic number operator is now defined as follows:

$$\mathcal{N}_k^{\mathrm{ad}} := a_k^{\mathrm{ad},\dagger}a_k^{\mathrm{ad}}\,. \tag{2.21}$$

It can be shown that the vacuum state associated with these annihilation operators corresponds to the physical ground state, i.e. the state with lowest energy, at $t = t_0$.

We now consider an external source that becomes constant at $t \to \pm\infty$. Suppose that $f_k^{\mathrm{in}}(t)$ is an exact solution of equation (2.6) for this particular source that reduces to the usual plane-wave solution in the limit $t \to -\infty$. This implies that the vacuum state $|0\rangle_{\mathrm{in}}$ associated with this solution reduces to the usual Minkowski vacuum for $t \to -\infty$. From eq. (2.17), we find that the particle density as measured with the adiabatic number operator at time t_0 is equal to

$$\frac{\mathcal{N}_k^{\mathrm{ad}}(t_0)}{V} = \frac{1}{2}\left(|\alpha_k|^2 + |\beta_k|^2 - 1\right), \tag{2.22}$$

where the Bogoliubov coefficients α_k and β_k are given in eqs. (2.13) with $f_k = f_k^{\mathrm{in}}$, $\bar{f}_k = f_k^{\mathrm{ad}}$, and evaluated at $t = t_0$. Using equation (2.20) this further simplifies to

$$\frac{\mathcal{N}_k^{\mathrm{ad}}(t_0)}{V} = \frac{\omega(t_0)}{2}\left|f_k^{\mathrm{in}}(t_0)\right|^2 + \frac{1}{2\omega(t_0)}\left|f_k^{\mathrm{in}'}(t_0)\right|^2 - \frac{1}{2}\,. \tag{2.23}$$

This equation gives the number density of particles created by an external time-dependent source, measured with the adiabatic number operator.

2.3 Vacuum decay in perturbative quantum field theory

2.3.1 Vacuum decay and generating functionals

Spontaneous particle creation in vacuum can be viewed as the decay of the asymptotic 'in' vacuum state to a different 'out' state. This suggests to express the probability of

vacuum decay in terms of the quantum-mechanical overlap of the 'in' and 'out' states as follows:

$$e^{-W} = |{}_{\text{out}}\langle 0|0\rangle_{\text{in}}|^2 \; ; \qquad W = \int d^4x\, w(x)\,, \tag{2.24}$$

where $w(x)$ is the probability per unit time and volume that two or more particles are created at spacetime position x.

In quantum field theory, the asymptotic 'in' and 'out' vacua are related through the scattering operator S:

$${}_{\text{out}}\langle 0|0\rangle_{\text{in}} = \langle 0|S|0\rangle = \langle 0|\mathcal{T}\exp\left[i\int d^4x\,\mathcal{L}_I\right]|0\rangle\,, \tag{2.25}$$

where $\mathcal{L}_i$ denotes the interaction Lagrangian that we take to be of the following form:[5]

$$\mathcal{L}_i(x) = -\frac{1}{2}j(x)\phi(x)^2\,. \tag{2.26}$$

Here $j(x)$ is a prescribed, external source that creates quanta of the scalar field ϕ. We define the generating functional of Green's functions $Z[j]$ in the usual way:

$$\begin{aligned} Z[j] &= \langle 0|S|0\rangle \\ &= \sum_{n=0}^{\infty}\frac{(-i)^n}{2^n n!}\int d^4x_1\ldots d^4x_n\, j(x_1)\ldots j(x_n)\,G_n(x_1,\ldots,x_n)\,, \end{aligned} \tag{2.27}$$

where the Green's functions G_n are given by:

$$G_n(x_1,\ldots,x_n) = \langle 0|\mathcal{T}\phi(x_1)\phi(x_1)\ldots\phi(x_n)\phi(x_n)|0\rangle\,. \tag{2.28}$$

Note that all ϕ terms appear here in pairs of two due to the quadratic coupling of the fields to the source j as expressed in eq. (2.26).

The generating functional $W[j]$ of connected Green's function is related to $Z[j]$ according to $Z[j] = \exp(iW[j])$, where

$$iW[j] = \sum_{n=1}^{\infty}\frac{(-i)^n}{2^n n!}\int d^4x_1\ldots d^4x_n\, j(x_1)\ldots j(x_n)\,G_n^c(x_1,\ldots,x_n)\,. \tag{2.29}$$

The leading factor i is a convention to ensure that G_n^c is the subclass of G_n that is represented with connected Feynman diagrams. For the interaction Lagrangian given in eq. (2.26), it is easily verified that exponentiation of the connected Green's function indeed leads to the full set of Green's functions with the proper prefactors.

[5]Note that the coupling of the quantum fields to the external source differs from the usual construction to derive correlation functions in perturbative quantum field theory. In that case the source is coupled to the quantum fields through a $j\phi$ term and the limit $j \to 0$ is taken at the end of the computation. Because of the different setup we construct the Green's functions from the interaction Lagrangian explicitly.

The decay parameter W that is defined in equation (2.24) is related to $W[j]$ through $W = 2\,\mathrm{Im}\,W[j]$. Separating W into contributions at different orders of j, we express

$$W = \sum_n W_n\,, \tag{2.30}$$

where

$$W_n := 2\,\mathrm{Im}\left[\frac{(-i)^{n+1}}{2^n n!}\int d^4x_1\ldots d^4x_n\, j(x_1)\ldots j(x_n)\, G_n^c(x_1,\ldots,x_n)\right] \tag{2.31}$$

is the n-source contribution to the vacuum decay probability W.

2.3.2 Connected Green's functions and loop diagrams

We now consider the connected Green's functions (2.28). Using Wick's theorem we evaluate the time-ordered product by summing over all possible contractions of the fields ϕ. The only way to contract all fields in a connected way is by constructing a loop. Hence we express

$$G_n^c(x_1,\ldots,x_n) = S_n S_F(x_1-x_2)S_F(x_2-x_3)\ldots S_F(x_n-x_1)\,, \tag{2.32}$$

where

$$S_F(x_1-x_2) = \langle 0|\mathcal{T}\phi(x_1)\phi(x_2)|0\rangle = i\int\frac{d^4p}{(2\pi)^4}\frac{e^{-ip(x_1-x_2)}}{p^2-m^2+i\epsilon} \tag{2.33}$$

denotes the Feynman propagator, and

$$S_n = 2^{n-1}(n-1)! \tag{2.34}$$

is a combinatorial prefactor that gives the number of ways in which the fields can be contracted to a loop. If there are more topologically distinct ways to combine the propagators to a loop, we should average over these possibilities.

After inserting expression (2.32) in eq. (2.31) we perform the integrals over x_i to transform the equation to momentum space. We then shift the momenta to isolate a single loop momentum q and find that W_n can be expressed as follows:

$$W_n = \mathrm{Im}\left[\frac{-i}{n}\prod_{i=1}^{n}\int\frac{d^4p_i}{(2\pi)^4}\,j(p_i)(2\pi)^4\delta\left(\sum_{j=1}^{n}p_j\right)L_n(p_1,\ldots,p_n)\right], \tag{2.35}$$

where L_n denotes the scalar n-point function:

$$L_n(p_1,\ldots,p_n) := \int\frac{d^4q}{(2\pi)^4}S_F(q)\,S_F(q+p_1)\ldots S_F(q+p_1+\ldots+p_{n-1})\,. \tag{2.36}$$

In this expression S_F denotes the momentum-space Feynman propagator:

$$S_F(q) = \left(\frac{1}{q^2 - m^2 + i\epsilon} \right) . \tag{2.37}$$

Equation (2.35) gives the rate of vacuum decay due to particle production for an arbitrary source j to any order n in perturbation theory in terms of the scalar n-point function L_n.

2.4 Example: scalar pair creation by a time-dependent kink

2.4.1 Setup

In this section we consider particle creation by a spatially homogeneous, time-dependent field configuration ϕ_D:

$$\phi_D(t) = B \tanh(\rho t) , \tag{2.38}$$

which can be thought of as a domain-wall in the time domain with height $2B$ and transition speed ρ.

When this field is coupled to a quantum field ϕ through the usual quartic coupling between scalar fields, the Lagrangian for the field ϕ can be written as

$$\begin{aligned} \mathcal{L}(x) &= \frac{1}{2}\partial_\mu\phi(x)\partial^\mu\phi(x) - \frac{1}{2}(m_0^2 + \phi_D(t)^2)\phi(x)^2 \\ &= \frac{1}{2}\partial_\mu\phi(x)\partial^\mu\phi(x) - \frac{m^2}{2}\phi(x)^2 - \frac{j(t)}{2}\phi(x)^2 . \end{aligned} \tag{2.39}$$

In the last line we shifted the mass and the source so that the latter goes to zero at infinite times:

$$m^2 = m_0^2 + B^2 ; \tag{2.40}$$

$$j(t) = B^2 \left(\tanh^2(\rho t) - 1 \right) . \tag{2.41}$$

The source $j(t)$ will be referred to as the 'time-dependent kink' source in the following. Note that B^2 acts as a coupling constant.

The Fourier transform of the time-dependent kink is given by $j(p) = j(p^0)\left[(2\pi)^3\delta(\vec{p})\right]$, where

$$j(p^0) = -\frac{\pi B^2 p^0 \mathcal{S}(p^0)}{\rho^2} . \tag{2.42}$$

In this expression we introduced the convenient shorthand notation

$$\mathcal{S}(p^0) := \sinh^{-1}\left(\frac{\pi p^0}{2\rho} \right) , \tag{2.43}$$

which will be used frequently hereafter.

In the following we compute the number of particles created by this source using both the method of Bogoliubov transformations and a perturbative calculation based on loop integrals. We note here that the problem of fermion pair creation, which is mathematically closely related to scalar pair creation, by this source was solved by Narozhnyi & Nikishov (1970); see also Rubakov (1984) and Cornwall & Tiktopoulos (1989). A similar problem was discussed by Birrell & Davies (1982) in the context of cosmological pair creation in an expanding universe.

2.4.2 The Bogoliubov method

Because the source that we consider here is homogeneous it is convenient to express, as before, $\phi_k(x) = \exp(i\vec{k}\vec{x}) f_k(t)$. From the interaction Lagrangian (2.39), it follows that $f_k(t)$ should obey:

$$\left(\frac{\partial^2}{\partial t^2} + k^2 + m(t)^2\right) f_k(t) = 0\,, \tag{2.44}$$

where the time-dependent mass is given by:

$$m(t) = \sqrt{m^2 + j(t)}\,. \tag{2.45}$$

In the infinite past or infinite future, eq. (2.44) reduces to the free-field case with frequency $\omega = \omega_\infty := \sqrt{k^2 + m^2}$.

To apply the method of Bogoliubov transformations described in section 2.2, we first have to solve the differential equation (2.44) that describes the dynamics of the quantum scalar field $\phi(x)$ in the presence of the external source. Factorizing the time-dependence as $f_k(t) = \exp(-i\omega_\infty t) g_k(t)$, we find after some algebra that eq. (2.44) can be rewritten in the following form:

$$z(1-z)\frac{\partial^2 g_k(z)}{\partial z^2} + (c - (a+b+1)z)\frac{\partial g_k(z)}{\partial z} - ab g_k(z) = 0\,, \tag{2.46}$$

where

$$z = \frac{1 + \tanh(\rho t)}{2}; \tag{2.47a}$$

$$a = \frac{1}{2} + \frac{1}{2}\sqrt{1 - \frac{4B^2}{\rho^2}}\,; \tag{2.47b}$$

$$b = \frac{1}{2} - \frac{1}{2}\sqrt{1 - \frac{4B^2}{\rho^2}}\,; \tag{2.47c}$$

$$c = 1 - \frac{i\omega_\infty}{\rho}\,. \tag{2.47d}$$

This allows us to express solutions of eq. (2.44) in terms of the hypergeometric function ${}_2F_1$. We choose two independent mode solutions that reduce to the plane-wave mode solutions at infinite times:

$$f_k^{\rm in}(t) = \frac{1}{\sqrt{2\omega_\infty}} \exp\left(-i\omega_\infty t\right) {}_2F_1(a,b,c,z)\,; \tag{2.48}$$

$$f_k^{\rm out}(t) = \frac{1}{\sqrt{2\omega_\infty}} \exp\left(-i\omega_\infty t\right) {}_2F_1(a,b,2-c,1-z)\,, \tag{2.49}$$

whose asymptotic behavior is:

$$f_k^{\rm in}(t\to-\infty) = f_k^{\rm out}(t\to\infty) = \frac{1}{\sqrt{2\omega_\infty}} \exp\left(-i\omega_\infty t\right). \tag{2.50}$$

This means that the solution $\phi_k^{\rm in}$ ($\phi_k^{\rm out}$) reduces to the free-field plane-wave mode solution at $t\to-\infty$ ($t\to\infty$). We note here that the case of an asymmetric domain wall, i.e. $\phi_D(t) = A + B\tanh(\rho t)$, is also solvable in terms of hypergeometric functions but we restrict ourselves to the case $A = 0$.

Using the properties of hypergeometric functions (e.g., Abramowitz & Stegun 1972), we find that the two sets of solutions can be related through the expansion

$$f_k^{\rm in} = \alpha_k^{\rm io} f_k^{\rm out} + \beta_k^{\rm io} f_k^{\rm out,*}\,, \tag{2.51}$$

where

$$\alpha_k^{\rm io} = \frac{\Gamma(c)\Gamma(c-a-b)}{\Gamma(c-a)\Gamma(c-b)}\,; \tag{2.52a}$$

$$\beta_k^{\rm io} = \frac{\Gamma(c)\Gamma(a+b-c)}{\Gamma(a)\Gamma(b)}\,. \tag{2.52b}$$

Hence the asymptotic behavior of $f_k^{\rm in}$ at very late times is:

$$f_k^{\rm in}(t\to\infty) = \frac{\alpha_k^{\rm io}}{\sqrt{2\omega_\infty}} \exp\left(-i\omega_\infty t\right) + \frac{\beta_k^{\rm io}}{\sqrt{2\omega_\infty}} \exp\left(i\omega_\infty t\right). \tag{2.53}$$

We now apply eq. (2.23) to obtain the number of particles as measured with the adiabatic particle number operator. From the asymptotic behavior of $f_k^{\rm in}$ in the infinite past, it follows directly that

$$\left.\frac{\mathcal{N}_k^{\rm ad}}{V}\right|_{t\to-\infty} = \frac{\omega_\infty}{2}\left(\frac{1}{2\omega_\infty}\right) + \frac{1}{2\omega_\infty}\left(\frac{\omega_\infty}{2}\right) - \frac{1}{2} = 0\,. \tag{2.54}$$

In the infinite future, we use eq. (2.53) to find that

$$\begin{aligned}\left.\frac{\mathcal{N}_k^{\rm ad}}{V}\right|_{t\to\infty} &= \frac{1}{4}\left|\alpha_k^{\rm io} e^{-i\omega_\infty t} + \beta_k^{\rm io} e^{i\omega_\infty t}\right|^2 + \frac{1}{4}\left|-i\alpha_k^{\rm io} e^{-i\omega_\infty t} + i\beta_k^{\rm io} e^{i\omega_\infty t}\right|^2 - \frac{1}{2} \\ &= \frac{1}{2}\left(|\alpha_k^{\rm io}|^2 + |\beta_k^{\rm io}|^2\right) = \frac{\cos\left(\pi\sqrt{1-4B^2/\rho^2}\right)+1}{2\sinh^2(\pi\omega_\infty/\rho)}\,,\end{aligned} \tag{2.55}$$

where B may in general be larger than 2ρ (in which case the cosine becomes a hyperbolic cosine). This equation gives the number density of particles with momentum $\vec{k}$ per unit volume created by the time-dependent kink from the infinite past to the infinite future. Since $\omega_\infty^2 = k^2 + m^2$ it is immediately clear from this result that the spectrum peaks at $k = 0$. The number of particles per unit volume equals

$$\frac{N}{V} = \int \frac{d^3k}{(2\pi)^3} \mathcal{N}_k^{\mathrm{ad}} = \frac{2\rho^3}{\pi^5} \left(\cos\left(\pi \sqrt{1 - 4B^2/\rho^2} \right) + 1 \right) \mathcal{G}\left(\frac{\pi m}{2\rho} \right), \tag{2.56}$$

where the function $\mathcal{G}$ is defined as follows:

$$\mathcal{G}(x) := x^3 \int_1^\infty du\, u \sqrt{u^2 - 1}\, \sinh^{-2}(2ux). \tag{2.57}$$

This result indicates that particles will be created by the domain-wall even though the asymptotic 'in' and 'out' vacua are identical (up to a phase) so that particle production by the time-dependent kink should be regarded as a dynamical effect. For further analysis it is useful to express the result (2.56) in terms of the dimensionless parameters $a := \rho/m$ and $b := B/\rho$ (reinserting $\hbar$ and c):

$$\frac{N}{V} = 8.5 \times 10^{11}\ \mathrm{cm}^{-3} \left(\frac{m}{1\ \mathrm{eV}} \right)^3 \left(\cos\left(\pi \sqrt{1 - 4b^2} \right) + 1 \right) a^3 \mathcal{G}\left(\frac{\pi}{2a} \right). \tag{2.58}$$

Pair creation is most effective for large values of a and b, where eq. (2.58) is well approximated with:

$$\frac{N}{V} \simeq 8.8 \times 10^{10}\ \mathrm{cm}^{-3} \left(\frac{m}{1\ \mathrm{eV}} \right)^3 a^3 e^{2\pi b} \qquad (a \gg 1,\ b \gg 1). \tag{2.59}$$

For small values of a the particle density is exponentially suppressed while for small values of b the number of particles scales with b^4:

$$a^3 \mathcal{G}\left(\frac{\pi}{2a} \right) \simeq \sqrt{a} \exp\left(-\frac{2\pi}{a} \right) \qquad (a \ll 1); \tag{2.60a}$$

$$\cos\left(\pi \sqrt{1 - 4b^2} \right) + 1 \simeq 2\pi^2 b^4 \qquad (b \ll 1). \tag{2.60b}$$

In both cases the low particle density is a result of the fact that the source evolves nearly adiabatically. It can be shown that $\omega_k'/\omega_k^2 \leq 2a^3b^2/(3\sqrt{3})$, where $\omega(t) = \sqrt{k^2 + m(t)^2}$. Hence low values of a and b imply that $\omega_k' \ll \omega_k^2$, indicating adiabatic evolution.

2.4.3 Perturbation theory

The non-perturbative result given in eq. (2.56) is an analytic function around $B^2 = 0$ (recall that B^2 acts as the coupling constant). This implies the existence of a unique

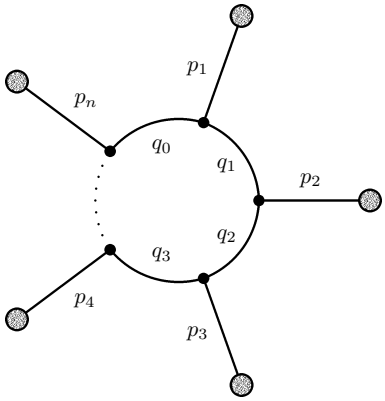

Figure 2.1: Scalar n-point diagram. The figure shows the labeling of the external (p_i) and loop (q_i) momenta.

perturbative expansion around $B^2 = 0$. Up to the first two non-trivial terms, we find the following expansion:

$$\frac{N}{V} = \left(\frac{4B^4}{\rho\pi^3} + \frac{8B^6}{\rho^3\pi^3}\right)\mathcal{G}\left(\frac{\pi m}{2\rho}\right) + O(B^8)\,. \tag{2.61}$$

Note that, in deriving this expression, we treat the mass at infinite times m (rather than the bare mass m_0) as an independent parameter.

In this section we consider the problem of pair creation by the time-dependent kink from a perturbative point of view in order to reproduce the first terms in the series expansion (2.61). In section 2.3 we expressed the rate of particle production by an external source j in terms of n-point contributions W_n. Equation (2.35) gives the contribution W_n as a function of the scalar n-point function L_n and source insertions. The n-point function can be represented by the Feynman diagram shown in fig. 2.1:

$$i\mathcal{M}_{n-\mathrm{pt}} = \int \frac{d^4q}{(2\pi)^4} \prod_{i=0}^{n-1} \mathcal{P}(q_i) = L_n\,, \tag{2.62}$$

where $\mathcal{P}$ denotes a propagator, i.e.

$$\mathcal{P}(q_i) = \left(\frac{1}{q_i^2 - m^2 + i\epsilon}\right). \tag{2.63}$$

Here m is the mass of the particle in the loop. If the source only has a non-zero time component, as is the case for the time-dependent kink source, the integral (2.62) can be solved for any n (see appendix 2.A).

Due to momentum conservation the first contribution is from two sources. From eq. (2.35),

$$W_2 = \mathrm{Im}\left[\frac{-i}{2}\int \frac{d^4p}{(2\pi)^4} j(p)j(-p)L_2(p)\right]. \tag{2.64}$$

Because the time-dependent kink source only has a non-zero time component we can use box normalization to replace $\left[(2\pi)^3\delta(\vec{p})\right]^2 \to V(2\pi)^3\delta(\vec{p})$ and find that

$$\frac{W_2}{V} = \frac{1}{2}\int \frac{dp^0}{(2\pi)}|j(p^0)|^2\,\mathrm{Im}\left[\mathcal{M}_{2-\mathrm{pt}}\right]. \tag{2.65}$$

Inserting eq. (2.81) from appendix 2.A for the imaginary part of the amplitude $\mathcal{M}_{2-\mathrm{pt}}$, we find

$$\frac{W_2}{V} = \frac{1}{32\pi^2}\int_{2m}^{\infty} dp^0|j(p^0)|^2\sqrt{1-\frac{4m^2}{(p^0)^2}} = \frac{2B^4}{\pi^3\rho}\mathcal{G}\left(\frac{\pi m}{2\rho}\right), \tag{2.66}$$

where the function $\mathcal{G}$ was defined in eq. (2.57). The next contribution is from the three-point function:

$$W_3 = \mathrm{Im}\left[\frac{-i}{3}\int \frac{d^4p_1}{(2\pi)^4}\frac{d^4p_2}{(2\pi)^4} j(p_1)j(p_2)j(-p_1-p_2))L_3(p_1,p_2)\right]. \tag{2.67}$$

Similar to the two-point contribution we use box normalization to write

$$\frac{W_3}{V} = \frac{1}{3}\int \frac{dp_1^0}{(2\pi)}\frac{dp_2^0}{(2\pi)} j(p_1^0)j(p_2^0)j(-p_1^0-p_2^0)\,\mathrm{Im}\left[\mathcal{M}_{3-\mathrm{pt}}\right]. \tag{2.68}$$

Inserting eq. (2.82) from appendix 2.A for the three-point function and inserting the time-dependent kink source we find that

$$\frac{W_3}{V} = \frac{B^6}{192\rho^6}\int_{-\infty}^{\infty} dp_1^0\int_{-\infty}^{\infty} dp_2^0\, p_1^0p_2^0(p_1^0+p_2^0)\mathcal{S}(p_1^0)\mathcal{S}(p_2^0)\mathcal{S}(p_1^0+p_2^0) \times \frac{f(p_1^0+p_2^0)-f(p_1^0)-f(p_2^0)}{|p_1^0+p_2^0||p_1^0||p_2^0|}, \tag{2.69}$$

where $\mathcal{S}$ was defined in eq. (2.43) and the function f is defined as:

$$f(x) := \theta\left(x^2-4m^2\right)\sqrt{x^2-4m^2}. \tag{2.70}$$

After some algebra we arrive at the following result for the three-point contribution to the probability of vacuum decay:

$$\frac{W_3}{V} = \frac{4B^6}{\pi^3\rho^3}\mathcal{G}\left(\frac{\pi m}{2\rho}\right). \tag{2.71}$$

In deriving this relation, we used the following formula to reduce the product of three $\mathcal{S}$ functions to a product of two $\mathcal{S}$ functions:

$$\int_0^\infty dv\, \mathcal{S}\left(\frac{u+v}{2}\right)\mathcal{S}\left(\frac{u-v}{2}\right) = 2u\mathcal{S}(u)\,. \tag{2.72}$$

Up to order j^3 only two particles can be created simultaneously so that, to this order, the number of particles created per unit volume is twice the probability of vacuum decay. Adding eqs. (2.66) and (2.71) we find that

$$\left.\frac{N}{V}\right|_{O(j^3)} = 2\left(\frac{W_2}{V} + \frac{W_3}{V}\right) = \left(\frac{4B^4}{\rho\pi^3} + \frac{8B^6}{\rho^3\pi^3}\right)\mathcal{G}\left(\frac{\pi m}{2\rho}\right), \tag{2.73}$$

which is in keeping with eq. (2.61). We find, therefore, that up to the second non-trivial order the perturbative computation with loop integrals presented here reproduces the non-perturbative result of eq. (2.56).

2.5 Discussion

In this chapter we discussed the creation of particles by an external source through vacuum decay in scalar field theory. We presented a brief but self-contained treatment on how Bogoliubov transformations can be used to compute the number of particles created by an external source in a non-perturbative manner. We also discussed vacuum decay in perturbative quantum field theory. This chapter provides a theoretical background for the next chapter, where we consider the creation of neutrinos by an external source. There we present an estimate of the neutrino pair creation rate that is based on perturbative quantum field theory and we compare this to non-perturbative results derived earlier by Kusenko & Postma (2002).

As an example of the presented formalism we considered pair creation by a specific source called the time-dependent kink source (see eq. (2.41)). We presented the exact, non-perturbative, result for the number density of particles created by this source in eq. (2.56). In contrast to the well-known result for electron-positron pair creation in a strong electric field (see eq. (2.1)), the resulting formula is analytic in $B^2 = 0$ (where B^2 is the coupling constant) which implies the existence of a unique, convergent perturbative expansion. Using perturbative quantum field theory we recover the first two non-trivial terms of this expansion in eq. (2.73). The results obtained here can be generalized to fermion pair creation problems to further investigate the relationship between non-perturbative results and perturbative expansions. In this light the result presented in appendix 2.A, where we show how the imaginary part of the scalar n-point function for sources with only time components can be constructed for any n, should be very useful.

Apart from providing an exactly solvable pair-creation problem, the time-dependent kink source is also interesting from a cosmological point of view through the possibility

of false vacuum decay. A universe that finds itself in a metastable, false vacuum may decay to the true vacuum through a tunneling process. A closed universe may undergo a homogeneous phase transition (see Rubakov 1984 and references therein); alternatively a bubble of true vacuum may emerge within the false-vacuum universe (Voloshin et al. 1975, Coleman 1977, Callan & Coleman 1977, Linde 1983). When the difference in energy density between the two vacua is small, the domain-wall between the true and the false vacuum is essentially (up to scaling and Lorentz transformations) given by the time-dependent kink source adopted in this chapter. Building on earlier work (Sawyer 1981, Aoyama 1983, Rubakov 1984, Maziashvili 2004), the results presented in this chapter can be used to further study particle creation by such domain walls.

2.A The n-point scalar loop diagram with only time components

2.A.1 The general case

We consider a loop diagram with n insertions of an external source with only a time component (see fig. 2.1). We denote the external momenta with p_i ($1 < i < n$) and we label the momenta in the loop as follows:

$$q_0 := q\,; \qquad q_{i>0} := q + \sum_{j=1}^{i} p_i\,. \tag{2.74}$$

The diagram shown in fig. 2.1 is transcribed to the following expression:

$$i\mathcal{M}_{n-\mathrm{pt}} = \int \frac{d^4q}{(2\pi)^4} \prod_{i=0}^{n-1} \mathcal{P}(q_i)\,, \tag{2.75}$$

where $\mathcal{P}$ denotes the propagator, cf. eq. (2.63).

When pair creation of particles is possible the matrix element $\mathcal{M}$ develops an imaginary part. Written as a function of s, where $\sqrt{s}$ is the center-of-mass energy, a branch cut develops along the real s-axis when $\mathcal{M}$ develops an imaginary part. It can be shown that the imaginary part and the discontinuity along the branch cut are related as follows (see, e.g., Peskin & Schroeder 1995):

$$\mathrm{Disc}\,[\mathcal{M}] = 2i\,\mathrm{Im}\,[\mathcal{M}]\,, \tag{2.76}$$

which is a manifestation of the optical theorem. The discontinuity can be computed for an arbitrary number of source insertions using the Cutkosky cutting rules (Cutkosky 1960; see also Peskin & Schroeder 1995). We present this construction for time-like sources in the following.

The cutting rules prescribe that we should cut any combination of two propagators appearing in eq. (2.75) and sum the discontinuities of the resulting expression over all combinations. Here cutting a propagator labeled with q_i means replacing

$$\mathcal{P}(q_i) \to \mathcal{P}_c(q_i) := -2\pi i\, \delta(q_i^2 - m^2)\,. \tag{2.77}$$

The two delta functions that arise from these cuts, together with the spatial homogeneity of the external sources, allow us to explicitly perform the integral over d^4q. After some algebra it can be shown that cutting two propagators labeled a and b leads to the following discontinuity along the branch cut:

$$\text{Disc}\,[\mathcal{M}]_{a,b} = \frac{i}{8\pi}\frac{f(x_a - x_b)}{|x_a - x_b|}\prod_{i\neq a,b}\frac{1}{(x_i - x_a)(x_i - x_b)}\,, \tag{2.78}$$

where

$$f(x) = \theta\left(x^2 - 4m^2\right)\sqrt{x^2 - 4m^2} \tag{2.79}$$

was defined in eq. (2.70), and

$$x_0 := 0\,; \qquad x_{i>0} := \sum_{j=1}^{i} p_j^0\,. \tag{2.80}$$

For the two-point function, the product in eq. (2.78), which corresponds to uncutted propagators, should be replaced with unity. The branch-cut discontinuity of a given diagram follows by summing eq. (2.78) over all different combinations of a and b, where both a and b take integer values between 0 and $n-1$.

2.A.2 Two- and three-point scalar loop diagrams

The imaginary part of the n-point diagram for sources with only time components can be constructed from equation (2.78) in a straightforward manner. Here we explicitly compute the imaginary parts of the two- and three-point function because these are used in the main text and because they can be easily verified against the literature.

For the two-point scalar diagram, the routing of momenta is such that $x_0 = 0$ and $x_1 = p_1^0$ and there is only one way to cut both propagators. We find that

$$\text{Im}\left[\mathcal{M}_{2-\text{pt}}\right] = \frac{1}{16\pi}\frac{f(p_1^0)}{|p_1^0|} = \frac{1}{16\pi}\sqrt{1 - \frac{4m^2}{(p_1^0)^2}}\,\theta\left((p_1^0)^2 - 4m^2\right)\,, \tag{2.81}$$

where the function f was defined in eq. (2.70). In the three-point diagram there are three different ways to cut two different propagators, resulting in the following three-term expression:

$$\text{Im}\left[\mathcal{M}_{3-\text{pt}}\right] = \frac{1}{16\pi}\frac{f(p_1^0) + f(p_2^0) - f(p_1^0 + p_2^0)}{|p_1^0||p_2^0||p_1^0 + p_2^0|}\,. \tag{2.82}$$

To verify these results we have computed the imaginary part of the two- and three-point scalar loop diagrams with time like sources following the prescription of 't Hooft & Veltman (1979). We find that the results agree with equations (2.81) and (2.82).

3

Perturbative neutrino pair creation by an external source

Koers, H. B. J. 2005, Phys. Lett., B605, 384

3.1 Introduction

Starting with Schwinger's classical account (Schwinger 1951) of electron-positron pair creation by an external electric field, fermion pair creation has been the subject of continued interest. A variety of pair creation rates for specific external fields in quantum electrodynamics can be found in the literature, such as Brezin & Itzykson (1970), Cornwall & Tiktopoulos (1989), Fried & Woodard (2002), Grifols et al. (2002), Hounkonnou & Naciri (2000), Kim & Page (2002), Kluger et al. (1992), Lin (1999), Neville (1984) and further references therein. The process exemplifies a true quantum field theory phenomenon: the creation of particles from the vacuum.

Because neutrinos carry weak charge, one expects that an external Z-boson field can produce neutrino-antineutrino pairs in a similar manner. The concept of an external Z-boson field can be seen as arising from a distribution of nuclear matter (in the sense of Kusenko & Postma (2002)). Neutron stars are a prime example of such a matter distribution and their neutrino emission by this mechanism was studied using non-perturbative methods (Kachelriess 1998, Kusenko & Postma 2002, Loeb 1990). Pair creation of neutrinos is also studied in relation to the stability of neutron stars, see Kiers & Tytgat (1998) and references therein. Although Kachelriess (1998), Kusenko & Postma (2002) and Loeb (1990) find typical neutrino fluxes that are too small to be observable, we believe it is worthwhile to study such a relatively unexplored neutrino source from a different point of view. In particular, we want to develop a method that is not limited to a specific source but allows us to draw conclusions with a broad applicability. This can then be applied to study e.g. neutrino pair creation by non-standard model weakly interacting particles or domain walls.

In the present letter, we study the creation of neutrino pairs in a perturbative way. We present a first order computation of the pair creation rate per volume, with a dynamical nuclear configuration acting as a source. The reasons for using perturbation theory are twofold. First, the axial coupling to the Z-boson prevents an easy generalization of non-perturbative QED methods. Second, non-perturbative methods generally consider a very specific source, or class of sources, from the start. The perturbative method is more flexible in the sense that a specific source is folded in at the end. This allows us to keep separate the physics of the pair creation process and that of a specific source.

In part, our computation was triggered by the results presented in Kusenko & Postma (2002), in which the creation of neutrinos by a time-dependent nuclear distribution is studied. One of the results in Kusenko & Postma (2002) is that the overall rate is proportional to the square of the neutrino mass. This implies that there can be no pair creation of massless neutrinos. The question arises whether this is a manifestation of a general chiral suppression mechanism or a consequence of the specific source considered. We shall see that the perturbative viewpoint contributes to a more complete understanding of this effect.

This chapter is organized as follows. In section 3.2 we discuss the theoretical background of pair creation processes for fermions and introduce the relevant quantities. In section 3.3, we discuss the perturbative computation. The result is then applied to neutrinos in section 3.4 and we present our conclusions in section 3.5.

3.2 Pair creation physics

We study fermions that are coupled to an external source j. The interaction Lagrangian reads

$$\mathcal{L}_{\text{int}} = j_\mu(x)\,\bar{\psi}(x)\Gamma^\mu\psi(x)\,. \tag{3.1}$$

The source is fully prescribed and has no further dynamics. We choose the coupling of the general form

$$\Gamma^\mu = \gamma^\mu(c_V - c_A\gamma^5)\,, \tag{3.2}$$

where c_V (c_A) is the vector (axial vector) coefficient; the coupling constant is absorbed in j.

Following Itzykson & Zuber (1980), we introduce the overlap of asymptotic 'in' and 'out' vacua to describe the pair creation process:

$$S_0(j) = \langle 0,\infty|0,-\infty\rangle_j = \langle 0,\infty|S|0,\infty\rangle_j\,, \tag{3.3}$$

where S is the scattering operator and the subscript is a reminder that a source is switched on and off adiabatically somewhere between $t=-\infty$ and $t=\infty$. The probability that a

system that started in the vacuum state will remain in the vacuum state is then expressed (Itzykson & Zuber 1980) as:

$$|\langle 0,\infty|0,-\infty\rangle_j|^2 = \exp(-W) = \exp\left(-\int d^4x\, w(x)\right). \tag{3.4}$$

For a positive W, this probability is between zero and one which signals a non-zero probability for the creation of a fermion pair. Now suppose that $w(x) = \bar{w}$ is constant. We can embed the system in a box of size $V \times T$, write $W = \bar{w}VT$ and choose the box small enough such that $W < 1$:

$$|\langle 0,\infty|0,-\infty\rangle_j|^2 \simeq 1 - \bar{w}VT\,, \tag{3.5}$$

which supports the interpretation of the function $w(x)$ as the probability per unit time and volume to create a pair at space-time location x. Such a rate density is the physical quantity of interest. For QED, the Schwinger formula (Schwinger 1951) states that for a photon field of the form $A^\mu(x) = j^\mu(x) = (0,0,0,-eEt)$,

$$\bar{w} = \frac{\alpha\epsilon_0 E^2}{\pi^2}\sum_{n=1}^{\infty}\frac{1}{n^2}\exp\left(-\frac{n\pi m^2}{|eE|}\right), \tag{3.6}$$

where α is the fine-structure constant, ϵ_0 is the vacuum permittivity, and m is the electron mass. We mention that Kachelriess (1998) and Loeb (1990) conclude that this result extends to the case of neutrino pair creation by a source of the same form.

To compute the rate density, we use perturbative quantum field theory:

$$\langle 0,\infty|0,-\infty\rangle_j = Z[j] = \exp(iW[j])\,, \tag{3.7}$$

where $W[j]$ is the generating functional of connected n-point functions.[1] In this context, $W[j]$ is also the effective action for the external field j (Itzykson & Zuber 1980, Neville 1984).

The interaction Lagrangian (3.1) only contains a vertex that couples to the external field. Therefore $W[j]$ represents an infinite sum of fermion loop diagrams, labeled by the number of vertices which are all connected to the external field. In terms of W that was introduced in eq. (3.4),

$$W = 2\,\mathrm{Im}\,W[j]\,. \tag{3.8}$$

The fermion loop diagram with one external field vertex is zero by momentum conservation, so the first non-zero contribution is from the loop with two external field vertices, i.e. the two-point function. This is the object that we will compute in section 3.3. Its

[1] The use of W and $W[j]$ may be confusing, but both symbols are standard in the literature. The generating functional will always be denoted with its argument j.

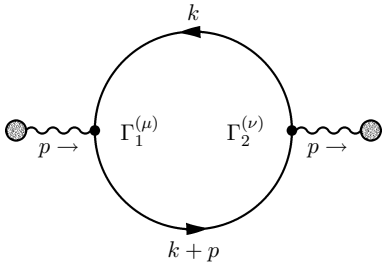

Figure 3.1: Fermion loop diagram with two external sources attached. The external field couples directly (i.e. without propagators) to the loop.

contribution to the pair creation rate W_2 is found by folding in the sources according to the formula[2]

$$W_2 = -\int \frac{d^4p}{(2\pi)^4} j_\mu(p) j_\nu(-p)\, \mathrm{Im}\,\Sigma^{\mu\nu}(p)\,, \tag{3.9}$$

where $\Sigma^{\mu\nu}$ represents the two-point function, with prefactors as chosen in eq. (3.10). For time-like currents, $j_\mu(p) j_\nu(-p)\, \mathrm{Im}\,\Sigma^{\mu\nu}(p) < 0$ since a probability cannot exceed one. For a given W, the pair creation density follows by extracting the function $w(x)$.

There has to be enough energy in the source to put two virtual particles on-shell. For the perturbative mechanism that we describe, this implies a threshold energy for the source insertions. This is in contrast to the non-perturbative effect, which can be thought of as an infinite sum of loop diagrams with an increasing number of source insertions. This infinite number of sources conspire to create a pair and the amount of energy per source insertion can be arbitrarily small.

For QED it is known that the real part of the sum of loop diagrams has a divergent structure, which can be used to extract non-perturbative results by performing a Borel transformation (Dunne & Hall 1999). We do not know whether or not a similar procedure can be applied in this more general situation.

3.3 The two-point function

The two-point function without external sources is transcribed from figure 3.1. We find that, in dimensional regularization with $n = 4 - \epsilon$,

$$\Sigma^{\mu\nu}(p) = -i\mu^{(4-n)} \int \frac{d^nk}{(2\pi)^n} \frac{\mathrm{tr}\left[(\not{k} + m)\,\Gamma^\mu \left(\not{k} + \not{p} + m\right)\Gamma^\nu\right]}{(k^2 - m^2 + i\epsilon)((k+p)^2 - m^2 + i\epsilon)}\,, \tag{3.10}$$

where m is the fermion mass. From eq. (3.9), we are interested in the imaginary part of this expression, which is finite. Note that we integrate over the fermion momentum; in

[2] We use a metric tensor $g^{\mu\nu} = \mathrm{diag}\,(1, -1, -1, -1)$ throughout this dissertation.

the source's rest frame (where the particles are created back to back), the fermion and the antifermion each carry half of the energy.

Expression (3.10) is reduced to a linear combination of scalar integrals in the fashion of Passarino-Veltman (Passarino & Veltman 1979). A series expansion in ϵ reveals the divergent structure, and after some algebra the problem depends only on the one- and two-point scalar integrals. The one-point scalar integral is real, the two-point integral develops an imaginary part if $p^2 > 4m^2$, which means there should be enough energy in the source to create two fermions. If this is not satisfied, $\Sigma^{\mu\nu}$ is purely real and there is no pair creation. The final result is the following expression:

$$\operatorname{Im}\Sigma^{\mu\nu}(p) = \frac{1}{16\pi^2}\left[\left(c_V^2 - c_A^2\right)\Sigma_I^{\mu\nu}(p) + \left(c_V^2 + c_A^2\right)\Sigma_{II}^{\mu\nu}(p)\right]\theta(p^2 - 4m^2)\,; \quad (3.11a)$$

$$\Sigma_I^{\mu\nu}(p) = 4\pi m^2\sqrt{1 - \frac{4m^2}{p^2}}\,g^{\mu\nu}\,; \quad (3.11b)$$

$$\Sigma_{II}^{\mu\nu}(p) = \frac{4}{3}\pi\left(p^2 g^{\mu\nu} - p^\mu p^\nu - \frac{2m^2}{p^2}p^\mu p^\nu - m^2 g^{\mu\nu}\right)\sqrt{1 - \frac{4m^2}{p^2}}\,. \quad (3.11c)$$

For some typical values of the parameters c_V and c_A, this result can be compared to the literature (Chang et al. 1982, Itzykson & Zuber 1980).

From expressions (3.11) we observe that for massless fermions $\Sigma_I^{\mu\nu} = 0$, so that only the second term contributes. This means that the physics is qualitatively insensitive to different choices of c_V and c_A; only the square sum is quantitatively important. We conclude that the difference between the two-point functions with two different normalized sets of couplings (e.g. purely vector, purely axial vector) is proportional to m^2.

The contribution due to the three-point diagram should be interpreted with care. In QED it vanishes by Furry's theorem, but for axial couplings it contributes to the axial anomaly. This means one should verify that the final result does not depend on the regularization procedure. For the present calculation, this is not an issue.

3.4 Neutrino pair creation to first order

3.4.1 The general case

We specialize to neutrino pair creation by putting $c_V = c_A = 1/2$ in the expression for the two-point function (3.11). Combining eqs. (3.9) and (3.11), we find

$$W_2 = -\frac{1}{24\pi}\int\frac{d^4p}{(2\pi)^4}\,\theta(p^2 - 4m^2)\sqrt{1 - \frac{4m^2}{p^2}}\left[\mathcal{F}_0(p,j) + m^2\mathcal{F}_1(p,j)\right], \quad (3.12a)$$

where

$$\mathcal{F}_0(p,j) = p^2\,[j(p)\cdot j(-p)] - [p\cdot j(p)]\,(p\cdot j(-p))\,; \tag{3.12b}$$

$$m^2\mathcal{F}_1(p,j) = -m^2\,[j(p)\cdot j(-p)] - \frac{2m^2}{p^2}\,[p\cdot j(p)]\,(p\cdot j(-p))\,. \tag{3.12c}$$

Without loss of generality, we consider a source with a density component and a spatial current in the $\hat{z}$ direction:

$$j_\mu(p) = (j_0(p), 0, 0, j_3(p))\,; \qquad p_\mu = (E, \vec{p}_T, p_3)\,. \tag{3.13}$$

Here p_μ labels the energy and momentum of the source. Though the current is directed in the $\hat{z}$ direction, we allow for a dependence on the transverse direction by leaving $\vec{p}_T$ unspecified. The two terms in (3.12) can be written as

$$\mathcal{F}_0(p,j) = -\vec{p}_T^{\,2}\left(|j_0|^2 - |j_3|^2\right) - |E\,j_3 - p_3\,j_0|^2\,; \tag{3.14a}$$

$$m^2\mathcal{F}_1(p,j) = -\frac{2m^2}{E^2 - \vec{p}_T^{\,2} - {p_3}^2}\left(E^2|j_0|^2 + {p_3}^2|j_3|^2 - E\,p_3\left(j_0 j_3^* + j_0^* j_3\right)\right) \tag{3.14b}$$

$$-m^2\left(|j_0|^2 - |j_3|^2\right)\,.$$

We do not simplify these equations further, as we do not want to constrain the properties of the source.

It is instructive to analyze the massless limit in more detail. In this case only $\mathcal{F}_0$ in (3.12) contributes, so that

$$W_2\,(m=0) = -\frac{1}{24\pi}\int\frac{d^4p}{(2\pi)^4}\left[p^2\,(j(p)\cdot j(-p)) - (p\cdot j(p))\,(p\cdot j(-p))\right]\,. \tag{3.15}$$

In analogy with QED, we introduce a field strength $F_{\mu\nu}(p) = ip_\nu j_\mu(p) - ip_\mu j_\nu(p)$ and its 'electric' and 'magnetic' components E_i and B_i and find:

$$W_2\,(m=0) = -\frac{1}{48\pi}\int\frac{d^4p}{(2\pi)^4}\left[F_{\mu\nu}(p)F^{\mu\nu}(-p)\right] \tag{3.16a}$$

$$= \frac{1}{24\pi}\int\frac{d^4p}{(2\pi)^4}\left[E_i(p)E_i(-p) - B_i(p)B_i(-p)\right]\,. \tag{3.16b}$$

This is exactly half of the QED result (Itzykson & Zuber 1980) if we insert a factor e^2 from the coupling constants, which reflects the discussion in the previous section. In electrodynamics, $\vec{E}$ and $\vec{B}$ are the physical electric and magnetic fields and one can go to a frame in which $\vec{B} = 0$. Then eq. (3.16) yields a positive result from which we conclude that the creation of massless particles by the two-point mechanism is in general possible. Eq. (3.16) is consistent with the massless limit of the first-order effective action in an axial background that was computed by Maroto (1999).

It is interesting to compare this result to the creation of neutrinos by an external electromagnetic field as computed by Gies & Shaisultanov (2000). In that case, the pair creation rate is proportional to m^2 and depends on the electromagnetic invariant $\vec{E}\cdot\vec{B}$.

3.4.2 The time-dependent density

We consider a time-dependent distribution of nuclear matter, described by the following source term:[3]

$$j_\mu(t) = \frac{G_F}{\sqrt{2}} \langle \bar{n}\gamma_\mu(1-\gamma^5)n\rangle = (j_0(t), 0, 0, 0) \; ; \tag{3.17a}$$

$$j_0(t) = \frac{G_F}{\sqrt{2}} n_N(t) \, , \tag{3.17b}$$

where n_N is the number density of the nuclear matter distribution and G_F is Fermi's constant. This is the specific background that we refer to as a time-dependent density. Our main motivation for this source is to compare the perturbative results with the non-perturbative results of Kusenko & Postma (2002).

For simplicity (and because any source can be decomposed into a trigonometric sum) we assume a monochromatic source: $j_0(t) = E_0 \cos\omega t$. In Fourier space, this is

$$j_0(p) = \frac{E_0}{2}(2\pi)^4 \delta(\vec{p}) \left[\delta(E-\omega) + \delta(E+\omega)\right] \; ; \tag{3.18a}$$

$$E_0 = \frac{G_F}{\sqrt{2}} n_N(0) \, . \tag{3.18b}$$

Inserting the source (3.18) into eq. (3.9) results in products of delta functions. We employ a box normalization procedure to reduce these to a single delta function and a factor $V \times T$ and find

$$W_2 = -VT \frac{{G_F}^2 (n_N)^2}{8} \left[\mathrm{Im}\, \Sigma^{00}(\omega; \vec{p}=0) + \mathrm{Im}\, \Sigma^{00}(-\omega; \vec{p}=0) \right] . \tag{3.19}$$

Using eq. (3.11), with $c_V = c_A = 1/2$, we see

$$\mathrm{Im}\, \Sigma^{00}(\pm\omega; \vec{p}=0) = -\frac{m^2}{8\pi} \sqrt{1 - \frac{4m^2}{\omega^2}} \, , \tag{3.20}$$

leading to the following pair creation probability per unit time and volume:

$$\bar{w}_2 = \frac{W_2}{VT} = \frac{m^2}{32\pi} \sqrt{1 - \frac{4m^2}{\omega^2}} {G_F}^2 {n_N}^2 \, . \tag{3.21}$$

The rate density scales with the square of the nuclear density, as expected for the two-point mechanism.

We see that the rate is proportional to m^2, which could have been anticipated from eq. (3.14) because the time-dependent density (3.17) is characterized by $j_3 = \vec{p}_T = p_3 = 0$

[3] This source originates from an effective four-fermion description, see Kusenko & Postma (2002). Note that j^μ contains the axial current; since the neutrons are massive, axial symmetry is broken and the current need not be divergence-free.

so that $\mathcal{F}_0(p, j) = 0$. Kusenko & Postma (2002) also find the m^2 proportionality for sources with a time-dependent current in the $\hat{z}$-direction. Equation (3.14) suggests that such sources can contribute to first order for a zero neutrino mass.

To derive an order-of-magnitude estimate for the number of created neutrinos per unit volume per unit time, we take the square root factor in eq. (3.21) of order unity, use a neutrino mass of 0.1 eV and assume a 'reduced density' $G_F n_N/\sqrt{2} \sim 1$ eV, such as in a neutron star (Kusenko & Postma 2002):

$$\bar{w}_2 = \frac{(0.1\,\mathrm{eV})^2}{32\pi}\left(2\,\mathrm{eV}^2\right) \sim 10^{-4}\mathrm{eV}^4 \sim 10^{26}\ \mathrm{s}^{-1}\ \mathrm{cm}^{-3}\,. \tag{3.22}$$

At the pair creation threshold, this creation rate corresponds to an energy output of the order 10^{13} erg cm^{-3} s^{-1}. Kusenko & Postma (2002) estimate the energy output of neutrinos that are created non-perturbatively by an oscillating neutron star to be of the order 10^3 erg cm^{-3} s^{-1}. However, these numbers should not be compared because the (realistic) driving frequency that is considered by Kusenko & Postma (2002) is so low that the perturbative mechanism is not operational.

As follows from eq. (3.11), there can only be pair creation by the two-point mechanism if $\omega^2 > 4m^2$. With a neutrino mass of 0.1 eV, the creation of a neutrino-antineutrino pair requires a driving frequency of at least $3 \cdot 10^{14}$ Hz. The coherence length of such a system is roughly 10^{-4} cm, so it is not very feasible to look for an oscillating astrophysical object that would produce an appreciable number of neutrinos with this mechanism. However, the value of our computation lies in its general applicability. We are not limited to this particular type of source, and we believe it may be interesting to study sources of a more transient nature such as a forming neutron star. Alternatively, one could consider weakly interacting particles beyond the standard model or domain walls as a source.

3.5 Conclusions

We have described pair creation of fermions by an external field to first order in perturbation theory and found the contribution by the two-point mechanism for a general coupling. Our main result is eq. (3.11), which should be interpreted in the context of eq. (3.9). We observe that at this order in perturbation theory, the difference in pair creation rates between two sets of normalized coupling coefficients $\{c_V, c_A\}$ is proportional to the square of the fermion mass.

For the case of neutrino pair creation by a distribution of nuclear matter, we have derived expressions (3.12) and (3.14). From this result we observe that, to first order, neutrino pair creation is possible with a suitable source if neutrinos would have been massless particles. We then considered pair creation of neutrinos by the time-dependent density of eq. (3.17). For this specific source, we conclude that the production rate due to the two-point contribution (3.21) is proportional to the square of the neutrino mass.

This conclusion is in qualitative agreement with the non-perturbative result derived by Kusenko & Postma (2002).

Creation and emission of neutrinos in gamma-ray bursts

4

The effect of neutrinos on the initial fireballs in gamma-ray bursts

Koers, H. B. J. & Wijers, R. A. M. J.
2005, Mon. Not. R. Astron. Soc., 364, 934

4.1 Introduction

Due to their tremendous energy, and in view of the connections discovered in recent years between gamma-ray bursts and massive stars (e.g., Van Paradijs et al. (2000), and references therein), it is now generally assumed that a gamma-ray burst (GRB) is initiated when a few solar masses of material collapse to near their Schwarzschild radius. In the simplest possible models of what happens next, a fair fraction of the gravitational energy released in the collapse is deposited into a volume somewhat larger than that of the horizon of the collapsed mass. The subsequent evolution of such a volume of highly concentrated energy – termed 'fireball' – was explored by Cavallo and Rees (1978). These authors introduced a compactness parameter for the volume, which expresses how easily a plasma consisting of baryons, photons, electrons and positrons can emit energy within a dynamical time. For small compactness, the emission is easy and the fireball cools by radiation. For large compactness, photons are trapped and cooling occurs by adiabatic expansion: an explosion results in which a significant fraction of the initial fireball energy is converted to bulk kinetic energy of a relativistic outflow, a condition now thought necessary for producing a gamma-ray burst.

At the time, Cavallo and Rees considered still relatively nearby origins of GRBs, for which the required fireball energies imply conditions that justified their assumption for the fireball composition. However, with cosmological distances to GRBs the required fireball energies are now so large that conditions of copious neutrino production become quite plausible. Motivated by the concern that these neutrinos easily leave their creation site due to their weak interaction with matter, and thereby carry away enough energy to

weaken or prevent an explosion, we investigate the evolution of neutrino-rich fireballs. Neutrino emission was previously considered as a sink of fireball energy, e.g. by Kumar (1999), who included emission of neutrinos in the optically thin limit. Neutrino emissivity has been more widely studied in a slightly different context, namely the evolution post-collapse of the accretion disk or torus around the newborn black hole, which may tap the accretion energy of the torus to power a GRB (Woosley 1993). The effect of neutrino opacity in this process has been the subject of a few recent studies, e.g., by Lee et al. (2004) and by Janiuk et al. (2004).

Here we study the evolution of a spherical fireball with given initial radius, energy, and baryon content. We aim to be general in the physical processes we consider, but accept a few a priori constraints on the initial parameters of the fireball: its initial energy must suffice to power a GRB, hence it should be within a few decades of 10^{52} erg; its initial size cannot be much larger than the Schwarzschild radius of a few solar masses, say $10^{6.5}$ cm, because the mass must collapse to such small radii in order to liberate such a large energy.[1] Lastly, the initial ratio of fireball energy to rest mass, M_0, of the entrained baryons, $\eta \equiv \mathcal{E}/M_0c^2$, must be several hundred (corresponding to almost 1 TeV/baryon) in order that eventually the baryons may be accelerated to a Lorentz factor high enough to produce a GRB. This combination of constraints implies that the fireballs we study here are always very compact in the Cavallo and Rees (or electromagnetic) sense. It also implies, as we show here, that the baryons are relatively unimportant in the neutrino processes.

This chapter is organized as follows: in section 4.2, we discuss some general properties of the fireball environment. Using these, we investigate the most important neutrino interactions in this environment in section 4.3. We introduce the emissivity parameter χ and the optical depth τ to describe the neutrino physics, and we draw a phase diagram for the neutrino fireball. The dynamical evolution of the neutrino fireball is discussed in section 4.4. The neutrino emission is discussed in section 4.5 and we present our conclusions in section 4.6.

4.2 General properties

4.2.1 Composition and temperature

The term 'fireball' refers to a plasma consisting of photons, electrons and positrons, possibly with a small baryonic load (Cavallo & Rees 1978). In this work, we extend this to fireballs that contain neutrinos[2]. We consider a fireball that is initially opaque to neutrinos of all flavors. At some point during the fireball's expansion (to be discussed in section 4.4.2), it becomes transparent to muon- and tau-neutrinos, that subsequently decouple from the plasma. The electron-neutrinos decouple a bit later, which divides the

[1] In this and the following chapters we use cgs units.

[2] Unless the difference is important, we will use the word 'neutrinos' if we mean 'neutrinos and antineutrinos'.

plasma parameter space in three regions: region I where the fireball contains neutrinos of all flavors; region II where it contains only electron-neutrinos; and region III where all the neutrinos are decoupled.

In thermodynamic equilibrium, the energy density and temperature are related by

$$\frac{\mathcal{E}}{V} = gaT^4 \,, \tag{4.1}$$

where a is the radiation constant, and g is a prefactor that depends on the composition of the system. For the three regions introduced above:

$$g_{\rm I} = \frac{43}{8} \,; \qquad g_{\rm II} = \frac{29}{8} \,; \qquad g_{\rm III} = \frac{22}{8} \,. \tag{4.2}$$

Assuming a spherical configuration, the temperature of the plasma can be expressed in terms of the energy and radius as

$$(T_{11})^4 = \frac{100}{g} \, (\mathcal{E}_{52}) \, (R_{6.5})^{-3} \,, \tag{4.3}$$

where $T = T_{11} \times 10^{11}$ K, $\mathcal{E} = \mathcal{E}_{52} \times 10^{52}$ erg and $R = R_{6.5} \times 10^{6.5}$ cm.

We use the following values for the initial fireball energy and radius as a reference (denoted with an asterisk):

$$\mathcal{E}_* = 10^{52} \text{ erg} \,; \tag{4.4a}$$

$$R_* = 10^{6.5} \text{ cm} \,. \tag{4.4b}$$

The reference temperature is

$$T_* = 2.1 \times 10^{11} \text{ K} = 17.9/k_B \text{ MeV} \,. \tag{4.4c}$$

4.2.2 Baryons

As the temperature is higher than typical binding energies, nuclei are dissociated into nucleons. Hence ‘baryons’ means ‘nucleons’ in what follows (‘baryon’ is however the standard terminology). The requirement that there should be 1 TeV of energy available for the baryons leads to a maximum number density of

$$n_{B,*} = 4.7 \times 10^{31} \text{ cm}^{-3} \,, \tag{4.5}$$

which will be used as the reference value in this study. It implies a baryonic mass density of $\rho_{B,*} = 9.4 \times 10^7$ gr cm^{-3}, which corresponds to a total baryonic mass of 6.2×10^{-6} solar masses contained in the volume V_*. Note that the nucleons are non-degenerate.

Because of overall charge neutrality, the ratio of protons to neutrons can be expressed in terms of the electron fraction Y_e:

$$n_B = n_n + n_p \,; \tag{4.6a}$$

$$n_p = Y_e n_B = \Delta n_e \,, \tag{4.6b}$$

where $\Delta n_e = n_{e^-} - n_{e^+}$ is the net electron density. The exact value of Y_e in a physical situation is determined by beta-equilibrium conditions; see e.g. Bethe et al. (1980) and Beloborodov (2003b). As we will see in the next section, the exact value of Y_e is not very important for our purposes.

4.2.3 Electron and positron number densities

Since $T_* \gg m_e c^2$, the electrons and positrons are extremely relativistic. Using $E = pc$, the net electron density and the combined electron-positron density $n_e = n_{e^-} + n_{e^+}$ can be expressed as

$$\Delta n_e = \frac{1}{3\hbar^3 c^3}\left((k_B T)^2 \mu_e + \frac{{\mu_e}^3}{\pi^2}\right); \tag{4.7a}$$

$$n_e = 0.37\frac{(k_B T)^3}{\hbar^3 c^3} + O(\mu_e)^2 , \tag{4.7b}$$

where μ_e is the electron chemical potential.

By definition, $Y_e < 1$, so that $\Delta n_e \leq n_B$. This places an upper bound on the net electron density and, through eq. (4.7a), on the electron chemical potential. With the reference baryon number density of eq. (4.5), we find that the electron chemical potential is very small: $\mu_e/(k_B T_*) \sim 2\times 10^{-4} \ll 1$. From (4.7b), neglecting the chemical potential, we find that at the reference temperature T_*:

$$n_{e^-,*} = n_{e^+,*} = 1.4 \times 10^{35}\ \mathrm{cm}^{-3} . \tag{4.8}$$

Concluding, the fireball under consideration here is nucleon-poor ($n_B \ll n_e$) and has a very small electron chemical potential ($\Delta n_e \ll n_e$). This implies that the electrons and positrons are non-degenerate.

4.3 Fireball neutrino physics

4.3.1 The dominant neutrino processes

The relative importance of interactions between neutrinos and the other components of the plasma depends on the temperature, the electron chemical potential and the baryon density. The most important neutrino production processes are discussed in appendix 4.A.1. Scattering and absorption processes are discussed in appendix 4.B. We use the fact that nucleons, electrons and positrons are non-degenerate.

For the present baryon densities, we observe from figures 4.2 and 4.3 that for temperatures $T > 5 \times 10^{10}$ K, the neutrino physics is dominated by leptonic processes. The dominant neutrino production process is electron-positron pair annihilation:

$$e^- + e^+ \rightarrow \nu + \overline{\nu}, \tag{4.9}$$

and the neutrino mean free path length (mfp) is set by scattering off electrons and positrons:

$$\nu + e^{\pm} \rightarrow \nu + e^{\pm}\,, \tag{4.10}$$

and similar for antineutrinos. Because the initial temperature of the fireball is very high ($T_0 \sim 2 \times 10^{11}$ K), we will only consider these processes in the following.

4.3.2 Neutrino creation rate

We express the neutrino creation rate in terms of the useful parameter $\chi = t_c/t_e$, where $t_c = \mathcal{E}/(VQ)$ is the cooling timescale and $t_e = R/c_s$ is the expansion timescale (c_s is the sound speed in the fireball). This parameter bears no reference to the neutrino transparency of the plasma, which has to be taken into account if one considers cooling by neutrino emission. The emissivity of electron-positron pair annihilation is (see appendix 4.A.1):

$$Q_{\rm pair} = 3.6 \times 10^{33}\ (T_{11})^9\ \ {\rm erg\ s^{-1}\ cm^{-3}}\,. \tag{4.11}$$

Because Q is a function of temperature, it depends on the size, energy and composition of the fireball through equation (4.3). It follows that

$$\chi = 3.7 \times 10^{-3}\, g^{9/4}\, (\mathcal{E}_{52})^{-5/4}\, (R_{6.5})^{11/4}\ , \tag{4.12}$$

where we used $c_s = c/\sqrt{3}$. For the reference values $\mathcal{E}_0 = 10^{52}$ erg and $R_0 = 10^{6.5}$ cm, we find that $\chi_{\rm I} = 0.16$, which means that neutrinos are created reasonably rapidly as compared to the expansion timescale. Neutrinos and antineutrinos are created in pairs by electron-positron annihilation, so they will be present in equal amounts.[3]

A different source of neutrinos is the decay of charged pions due to photopion production (see appendix 4.A.2) by high-energy photons ($E_\gamma > 140$ MeV). The energy stored in the high-energy tail of the photon distribution is relatively small ($\sim 5\%$). The process manifests itself as a high-energy leak, resulting in an increased production of electron- and muon-neutrinos with energies below $m_\mu c^2/2 \simeq 53$ MeV. We will not consider this non-thermal process in the rest of this chapter.

4.3.3 Optical depth

The fireball's opacity to neutrinos is described in terms of the optical depth $\tau = R/\lambda$, where R is the length scale and λ is the mean free path (mfp). The mfp due to electron and positron scattering is (see appendix 4.B.1):

$$\lambda^{(e)} = 3.7 \times 10^6\ (T_{11})^{-5}\ {\rm cm}\,; \tag{4.13a}$$

$$\lambda^{(\mu,\tau)} = 1.6 \times 10^7\ (T_{11})^{-5}\ {\rm cm}\,, \tag{4.13b}$$

[3] This conclusion changes if there is an initial asymmetry between neutrinos and antineutrinos. We do not consider this here.

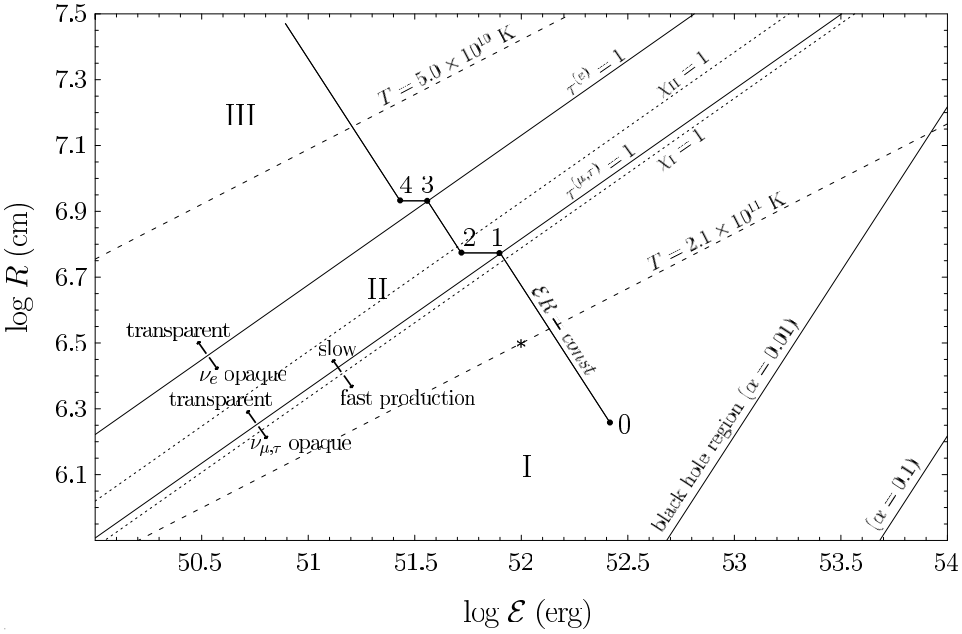

Figure 4.1: A parameter space plot that shows the three phases of the plasma. The solid lines show the $\chi_{\rm I} = 1$, $\chi_{\rm II} = 1$, $\tau^{(\mu,\tau)} = 1$ and $\tau^{(e)} = 1$ contours; the dotted lines are isotemperature curves. The $*$ denotes the reference point with values given in eqs. (4.4). The plotted trajectory and the points '0' to '4' are discussed in section 4.4.2. The black hole lines indicate the Schwarzschild radius as a function of the fireball energy, assuming an initial conversion efficiency $\alpha = E^{(0)}/M_{\rm BH}c^2$.

where the difference originates from the fact that only electron-neutrinos participate in charged current-interactions. Because the mfp for neutrinos and antineutrinos is equal (assuming an equal amount of electrons and positrons), neutrinos and antineutrinos will leave the fireball at the same time.

We consider a generic plasma that moves from region I to II to III, Therefore, we use the value $g = g_{\rm I}$ to find the optical depth for the muon- and tau-neutrinos and $g = g_{\rm II}$ for the electron-neutrinos:

$$\tau^{(e)} = 54 \times (\mathcal{E}_{52})^{5/4} (R_{6.5})^{-11/4} \; ; \tag{4.14a}$$

$$\tau^{(\mu,\tau)} = 7.4 \times (\mathcal{E}_{52})^{5/4} (R_{6.5})^{-11/4} \; . \tag{4.14b}$$

We observe that for reference initial conditions, $\tau^{(e,\mu,\tau)} > 1$ so that the fireball is opaque to neutrinos of all flavors.

4.3.4 Phases of the neutrino fireball

We will assume that neutrinos of some flavor decouple from the plasma instantaneously if the optical depth is one (these transitions will be smoother in reality). Based on equations (4.14), figure 4.1 shows how the parameter space is divided in the regions I, II and III by the $\tau^{(\mu,\tau)} = 1$ and $\tau^{(e)} = 1$ contours. The dynamical evolution of a fireball through these regions will be discussed in section 4.4.2.

We observe that the region of interest has a temperature $T > 5 \times 10^{10}$ K, which justifies the fact that we only consider electron-positron pair annihilation and neutrino scattering off electrons and positrons (see figures 4.2 and 4.3).[4]

The figure also indicates the neutrino creation rate from equation (4.12). In region I this process is fast compared to the expansion time-scale. Together with the reverse process, it aims toward thermodynamic equilibrium between the neutrinos and the other components of the plasma. The neutrinos also interact with the electrons and positrons through scattering. The interaction length of this process is smaller than the size of the fireball. We conclude that thermodynamic equilibrium is established rapidly, and the system will remain in equilibrium throughout its evolution.

4.4 Fireball evolution

4.4.1 Hydrodynamics

As long as the components of the plasma are strongly coupled (i.e. the interaction length is much smaller than the size of the system), the plasma can be described as a homogeneous sphere, in thermodynamic equilibrium with a single temperature. The evolution will be very similar to that of a neutrinoless fireball as described by e.g. Shemi & Piran (1990). The plasma expands by radiation pressure, converting radiative energy to kinetic energy of the baryons. We assume that the expansion is adiabatic. We will denote the radiative energy contained in the fireball (without the decoupled components) as $\mathcal{E}$. The energy and entropy within a sphere of radius R are

$$\mathcal{E} = \frac{4\pi}{3} g a R^3 T^4 ; \tag{4.15a}$$

$$S = \frac{16\pi}{9} g a (RT)^3 . \tag{4.15b}$$

Assuming that the fireball's evolution is reversible (i.e. that entropy is conserved), the temperature-radius relationship reads

$$g(RT)^3 = g_0(R_0 T_0)^3 = const . \tag{4.16}$$

[4] Nuclear processes become competitive with the leptonic processes at these temperatures if the nucleon density is approximately two orders of magnitude higher. In that case, the optical depth- and emissivity-lines in figure 4.1 feature a bend at a cross-over temperature.

As long as there is no change in the plasma composition, the following very useful scaling laws can be used to describe the evolution (Shemi & Piran 1990):

$$\mathcal{E}R = \mathcal{E}_0 R_0 = const\,; \tag{4.17a}$$

$$\frac{\mathcal{E}}{T} = \frac{\mathcal{E}_0}{T_0} = const\,. \tag{4.17b}$$

If a plasma component annihilates, the temperature-radius relationship (4.16) still holds by conservation of entropy. In the early universe, this leads to an increase in the photon temperature after electron-positron annihilation (see e.g. Weinberg 1972), and a similar effect happens in the last stage of the neutrinoless fireball (Shemi & Piran 1990). By contrast, entropy is carried away if a component decouples:

$$S = S_0 - S_{\rm dec}\,, \tag{4.18}$$

where $S_{\rm dec}$ is the entropy in the decoupled components. Since $g = g_0 - g_{\rm dec}$, it follows from eq. (4.15) that the temperature-radius relationship does not change at decoupling:

$$RT = R_0 T_0\,. \tag{4.19}$$

4.4.2 Neutrino decoupling bursts

We will discuss the hydrodynamical evolution of a fireball that starts in region I with a generic initial energy $\mathcal{E}_0$ and size R_0. The trajectory is sketched in figure 4.1. As the fireball expands and cools, it will develop from neutrino-opaque to -transparent. When this happens, neutrinos decouple from the plasma.

Apart from these bursts, neutrinos are emitted continuously in regions where the creation rate is sufficiently high and the plasma is transparent to neutrinos. We will consider this in more detail in section 4.4.3, and restrict our discussion to an expanding fireball with events of instantaneous energy loss here.

Starting from the point denoted as '0' in figure 4.1, the plasma expands along a $\mathcal{E}R = \mathcal{E}_0 R_0$ line until it reaches the $\tau^{(\mu,\tau)} = 1$ contour, where the muon- and tau-neutrinos decouple from the plasma. From eq. (4.14b), we find that the radiative energy and temperature of the plasma just before decoupling are

$$\mathcal{E}_{52}^{(1)} = 0.61 \left(\mathcal{E}_{52}^{(0)}\, R_{6.5}^{(0)}\right)^{11/16}\,; \tag{4.20a}$$

$$T_{11}^{(1)} = 1.26 \left(\mathcal{E}_{52}^{(0)}\, R_{6.5}^{(0)}\right)^{-1/16}\,. \tag{4.20b}$$

The temperature of the plasma at that point depends on the initial conditions only very mildly, but it is interesting that the temperature of the plasma at decoupling is lower if the initial energy is higher. This can be seen from figure 4.1: for a higher $\mathcal{E}_0$, the $\mathcal{E}R = const$ line crosses the $\tau^{(\mu,\tau)} = 1$ contour at a lower temperature. The muon- and tau-neutrinos

carry away $14/43 \simeq 33\%$ of the available radiative energy. This moves the fireball from point 1 to point 2.

Since the size and temperature of the plasma are constant at decoupling, what remains of the fireball continues adiabatic expansion along a new trajectory. The electron-neutrinos remain in thermal equilibrium with the plasma, which enters region II. The expansion continues along a $\mathcal{E}R = \mathcal{E}_2 R_2$ curve until the plasma becomes transparent to electron-neutrinos at $\tau^{(e)} = 1$ (point 3):

$$\mathcal{E}_{52}^{(3)} = 0.28 \left(\mathcal{E}_{52}^{(0)} R_{6.5}^{(0)}\right)^{11/16} ; \tag{4.21a}$$

$$T_{11}^{(3)} = 0.87 \left(\mathcal{E}_{52}^{(0)} R_{6.5}^{(0)}\right)^{-1/16} . \tag{4.21b}$$

At this point, the electron-neutrinos leave the plasma and carry away $7/29 \simeq 24\%$ of the energy (point 4). When all the neutrinos are decoupled, the fireball will develop according to the standard scenario (Shemi & Piran 1990).

The energy that is emitted in neutrinos in the two bursts is:

$$E_{52}^{(\nu \text{ bursts})} = \frac{14}{43}\mathcal{E}_{52}^{(1)} + \frac{7}{29}\mathcal{E}_{52}^{(3)} = 0.27 \left(\mathcal{E}_{52}^{(0)} R_{6.5}^{(0)}\right)^{11/16} , \tag{4.22}$$

which is a significant fraction of the initial radiative energy.

4.4.3 Continuous neutrino cooling

In regions in the parameter space where the neutrino creation rate is high ($\chi \lesssim 1$) and (some of) the neutrinos can escape from the plasma ($\tau \lesssim 1$), we should take neutrino cooling into account in the hydrodynamical evolution.

A plasma expanding adiabatically along a $\mathcal{E}R = const$ contour, converts radiative energy to kinetic energy according to

$$\left.\frac{d\mathcal{E}}{dR}\right|_{\text{exp}} = -\frac{\mathcal{E}}{R} . \tag{4.23}$$

To this we add the energy loss by neutrino cooling $\Delta\mathcal{E} = -fQV\Delta t$, where Q is the emissivity and f is the fraction of the created neutrinos that can leave the plasma. Assuming $\Delta R \simeq c_s \Delta t$, we find that

$$\left.\frac{d\mathcal{E}}{dR}\right|_{\nu \text{ cooling}} \simeq -\frac{fQV}{c_s} = -\frac{f}{\chi}\frac{\mathcal{E}}{R} , \tag{4.24}$$

where $\chi = \chi(\mathcal{E}, R)$ is the creation rate as defined in section 4.3.2. The plasma evolution, including neutrino cooling, can then be determined from the differential equation

$$\frac{d\mathcal{E}}{dR} = -\left(1 + \frac{f}{\chi}\right)\frac{\mathcal{E}}{R} , \tag{4.25}$$

so that, locally, the plasma moves along a $\mathcal{E}R^{1+f/\chi} = const$ trajectory. From eq. (4.12), we find that just after electron- and muon-neutrino decoupling the creation rate parameter is

$$\chi_{\rm II} = 0.81\,, \tag{4.26}$$

independent of initial conditions. Hence the creation rate is reasonably high in this region, where only muon- and tau-neutrinos can escape. Using the emissivity formulae from Munakata et al. (1985), we find that 31% of the neutrinos created by electron-positron pair creation are muon- or tau-neutrinos, so that $f = 0.31$. Combining this with eqs. (4.12) and (4.25), we find that the plasma expands until it reaches the $\tau^{(e)} = 1$ contour at

$$\mathcal{E}_{52}^{(3)} = 0.27\left(\mathcal{E}_{52}^{(0)}\,R_{6.5}^{(0)}\right)^{11/16}\,; \tag{4.27a}$$

$$T_{11}^{(3)} = 0.89\left(\mathcal{E}_{52}^{(0)}\,R_{6.5}^{(0)}\right)^{-1/16}\,, \tag{4.27b}$$

which is almost identical to eqs. (4.21).

After electron-neutrino decoupling, neutrinos of all flavors can leave the plasma. The energy loss due to continuous neutrino cooling in regions II and III is

$$E_{52}^{(\nu,{\rm II})} = 0.027\left(\mathcal{E}_{52}^{(0)}\,R_{6.5}^{(0)}\right)^{11/16}\,; \tag{4.28a}$$

$$E_{52}^{(\nu,{\rm III})} = 0.015\left(\mathcal{E}_{52}^{(0)}\,R_{6.5}^{(0)}\right)^{11/16}\,. \tag{4.28b}$$

The continuous energy loss component is relatively small and hardly affects the fireball evolution. In particular, neutrino cooling is never efficient enough to prevent a hot fireball from exploding.

4.5 Neutrino emission

4.5.1 Observed temperature

For the neutrinoless fireball, it is well known that the temperature of the observed photon spectrum is roughly equal to the initial temperature of the plasma T_0 (Shemi & Piran 1990, Goodman 1986). Let us recall the thermodynamic treatment of this phenomenon (Goodman 1986). The number of photons in a sphere of radius R depends on the temperature T as

$$N_\gamma = \frac{2\zeta(3)}{\pi^2}\left(\frac{k_B T}{\hbar c}\right)^3\left(\frac{4}{3}\pi R^3\right) \sim 1.0\left(\frac{k_B}{\hbar c}\right)^3 (RT)^3\,. \tag{4.29}$$

As long as none of the plasma components annihilates, the number of photons is constant during the evolution. The average available energy per photon for a neutrinoless fireball

is initially

$$\langle E_\gamma \rangle^{(0)} = \frac{4}{11} \frac{E_{\rm tot}}{N_\gamma^{(0)}} \,. \tag{4.30}$$

Since the total energy is conserved, the available energy per photon does not change during the fireball's evolution.

This conclusion is unaffected by the annihilation of electrons and positrons that occurs in the last stage of the fireball: entropy conservation requires that the number of photons increases by a factor of 11/4. However, the total energy is now exclusively available for the photons, so the available energy increases by the same factor. The mean photon energy does not change during the evolution of the neutrinoless fireball and the observed photon spectrum is roughly equal to the initial blackbody (Goodman 1986), with temperature (Shemi & Piran 1990, Piran et al. 1993)

$$T_{\rm obs} = \gamma T \simeq T^{(0)} \,. \tag{4.31}$$

As for photons, the mean available energy for muon- and tau-neutrinos remains constant during the expansion from point 0 to 1, so the observed temperature will roughly equal the initial temperature.

For the electron-neutrinos, the situation is more subtle because energy leaves the plasma when the muon- and tau-neutrinos decouple. Initially, the mean available energy is

$$\langle E_{\nu_e} \rangle^{(0)} = \frac{7}{43} \frac{E_{\rm tot}}{N_{\nu_e}^{(0)}} \,, \tag{4.32}$$

which remains constant throughout the evolution to point 1. At point 2, the available energy is reduced by a factor 29/43, but the electron-neutrinos get a larger share:

$$\langle E_{\nu_e} \rangle^{(2)} = \frac{7}{29} \frac{\frac{29}{43} E_{\rm tot}}{N_{\nu_e}^{(2)}} = \langle E_{\nu_e} \rangle^{(0)} \frac{N_{\nu_e}^{(0)}}{N_{\nu_e}^{(2)}} \,. \tag{4.33}$$

The number of neutrinos[5] in a sphere of radius R is proportional to $(RT)^3$. Because $R_2 T_2 = R_1 T_1 = R_0 T_0$, the mean available energy does not change when some plasma components decouple. We thus conclude that the observed temperature of the electron-neutrino spectrum is also approximately equal to $T^{(0)}$.

4.5.2 Energy

The evolution of a fireball with neutrinos is described in section 4.4. Using the results obtained in eqs. (4.22) and (4.28), we summarize the neutrino emission in table 4.1.

[5] This is similar to eq. (4.29), but for neutrinos (one flavor) the prefactor is 0.38 rather than 1.0.

	$E_{52}^{(\nu\,\mathrm{tot})}$	ν_e :	ν_μ :	ν_τ
$\nu_{\mu,\tau}$ dec.	$0.20 \times \xi_0$	0	0.5	0.5
ν_e dec.	$0.070 \times \xi_0$	1	0	0
cont., II	$0.024 \times \xi_0$	0	0.5	0.5
cont., III	$0.013 \times \xi_0$	0.69	0.15	0.15
total	$0.31 \times \xi_0$	0.26	0.37	0.37

Table 4.1: The total energy that is emitted in neutrinos in various stages. Here 'dec.' stands for decoupling bursts, 'cont.' for continuous emission. The symbol ν means 'neutrino and antineutrino' in the above, and $\xi_0 := (E_{52}^{(0)}\, R_{6.5}^{(0)})^{11/16}$.

Neutrinos and antineutrinos are emitted in equal amounts and share the energy quoted in the table. The total energy that is emitted in neutrinos equals

$$E^{(\nu,\,\mathrm{tot})} = 3.1 \times 10^{51}\ \mathrm{erg} \times \left(E_{52}^{(0)} R_{6.5}^{(0)}\right)^{11/16} . \tag{4.34}$$

The mean neutrino energy follows directly from the initial temperature:

$$\langle E_\nu \rangle = 3.15 k_B T^{(0)} = 56\ \mathrm{MeV} \times \left(E_{52}^{(0)}\right)^{1/4} \left(R_{6.5}^{(0)}\right)^{-3/4} . \tag{4.35}$$

4.5.3 Time spread

The neutrinos are emitted in two decoupling bursts as well as continuously. As is clear from figure 4.1, the fireball has not expanded much in between the two decoupling events: $R^{(1)} - R^{(3)} \sim R^{(1)}$, implying that the various components of neutrino emission overlap in time. The intrinsic time spread is determined by the size of the fireball at the second burst:

$$\Delta t = \frac{R^{(3)}}{c} \sim 0.4\,\mathrm{ms} \times R_{6.5}^{(0)} , \tag{4.36}$$

which is much smaller than the typical time spread for supernova neutrinos that originate from relatively slow deleptonization processes.

Dispersion effects on the way to earth introduce an additional smearing:

$$\begin{aligned} \Delta t_{\mathrm{disp}} &= \frac{D}{c}\left(\frac{1}{\beta} - 1\right) \\ &= 0.6\,\mathrm{ms} \times \left(\frac{m_\nu}{0.1\,\mathrm{eV}}\right)^2 \left(\frac{E_\nu}{56\,\mathrm{MeV}}\right)^{-2} \left(\frac{D}{4\,\mathrm{Mpc}}\right)^2 . \end{aligned} \tag{4.37}$$

For a robust analysis, this time spread should be averaged over a thermal distribution.

4.5.4 Applications

The detectability of a neutrino source as described here was studied by Halzen & Hooper (2002) (see also Halzen et al. (1996), Halzen & Jaczko (1996)). The detection is based on the charged current interaction $\overline{\nu}_e + p \rightarrow n + e^+$ and the subsequent Čerenkov radiation that is emitted by the positron. An analysis based on Halzen & Jaczko (1996) shows that detection could be feasible for sources within a few Mpc for a low-background neutrino telescope.[6] This limits potential sources to our local cluster.

In the context of supernova dynamics, it has been proposed that delayed neutrino emission could revive a stalled supernova shock (Bethe & Wilson 1985). Matter that is surrounding some central, heavy object can escape if the internal energy exceeds the gravitational energy:

$$E_{\rm int} > E_{\rm grav} = \frac{GM}{D}\,, \tag{4.38}$$

where M is the mass of the central object and D the distance of the matter to the central object.

This material can be heated by neutrinos. We assume that the matter consists of nucleons, but for heavier nuclei similar processes can occur. Neglecting loss terms, the total energy that can be deposited by neutrinos from the central object equals

$$\Delta E = N_A \sigma \frac{E^{(\nu,\,\rm tot)}}{4\pi D^2}\,, \tag{4.39}$$

where the cross section for neutrino capture on nucleons reads (the relevant processes and cross sections can be found in appendix 4.B):

$$\sigma \sim 10^{-43}\ {\rm cm}^2 \times \left\langle \frac{E_\nu^2}{1\ {\rm MeV}^2} \right\rangle . \tag{4.40}$$

Following Bethe & Wilson (1985), we adopt here the reference values $D = 150$ km and $M = 1.6 M_\odot = 3 \times 10^{54}/c^2$ erg. With the expressions (4.34) and (4.35) for the neutrino flux found in this work, we find that

$$E_{\rm grav} \sim 2 \times 10^{19}\ {\rm erg\ g^{-1}}\,, \tag{4.41a}$$

$$\Delta E \sim 2 \times 10^{20}\ {\rm erg\ g^{-1}}\,. \tag{4.41b}$$

We conclude that the energy released in neutrinos by the hot fireball considered here is sufficient to release material at a typical distance $D \sim 150$ km from the gravitational pull of a $1.6 M_\odot$ object.

[6] This is a rough signal-over-noise estimate. In particular, it assumes that there is no directional information available for triggering or reconstruction. The observational time window is 0.3 ms.

4.6 Conclusions

In this chapter, we have described the physics of neutrinos in a hot fireball environment. We find that the dominant neutrino processes are leptonic: neutrino creation by electron-positron annihilation and neutrino scattering off electrons and positrons.

For general initial conditions[7], the fireball plasma is initially neutrino-opaque and the rate of neutrino creation is reasonably high. The neutrinos are in thermal equilibrium with the other components of the plasma and follow the hydrodynamical evolution of the fireball. In this evolution, the muon- and tau-neutrino decouple first, followed by the electron-neutrinos. Besides these bursts, the fireball emits neutrinos continuously in regions where it is neutrino-opaque and the creation rate is high. The effect on the evolution of the fireball and on the neutrino emission is small.

The energy spectrum of the emitted neutrinos will be approximately thermal with a temperature equal to the initial temperature of the fireball, i.e. $\langle E_\nu \rangle \sim 60$ MeV. The total energy that is emitted in (anti)neutrinos is

$$E^{(\nu,\,\mathrm{tot})} = 3.1 \times 10^{51}\ \mathrm{erg} \times \left(E_{52}^{(0)}\, R_{6.5}^{(0)}\right)^{11/16} . \tag{4.43}$$

A sizable fraction of the total fireball's energy is converted into neutrinos, and this fraction is not very sensitive to initial conditions. The rather limited detection possibility is mainly due to the isotropic outflow of the neutrinos, as opposed to the observed high-energy gamma rays that originate in ultra-relativistic beamed jets in a later stage of the GRB. If the neutrinos were focused by some mechanism, detection of sources much further away could be possible. On the other hand, fewer sources will be detected since the outflow needs to be directed toward the earth.

We have found that our initial concern that neutrino emission might prevent the production of powerful explosions from fireballs is not justified. The physical reason for this is that for most of the parameter space where neutrino production is fast enough to cool the fireball, the fireball shields itself from cooling by being opaque to those same neutrinos. However, there may well be another snag when one considers the formation of the fireball: this requires a heating mechanism, and at the start of the heating one necessarily approaches the safe zone in the lower right half of figure 1 from the left. Therefore, unless the heating occurs on a timescale close to the dynamical time the evolution track toward high energy may well get stuck in the cooling zone, causing loss of all heating energy into neutrinos. Given that the dynamical timescale is probably the fastest thinkable heating time, it is quite possible that neutrino cooling can prevent high-energy fireballs from forming.

[7] These conclusions apply to fireballs that starts in the neutrino-opaque region that we denoted as region I. This is the case if

$$(E_{0,52})^{-5/4}\,(R_{0,6.5})^{11/4} \lesssim 5 . \tag{4.42}$$

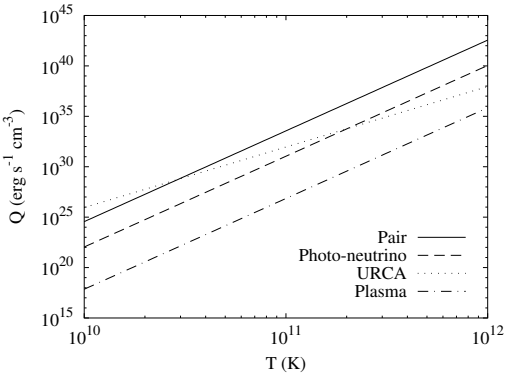

Figure 4.2: Neutrino emissivity of the plasma as a function of temperature due to the pair annihilation (solid line), photo-neutrino (dashed), non-degenerate URCA (dotted), and plasma (dash-dotted) processes. We used a baryon density $\rho = 10^8$ gr cm^{-3}.

4.A Neutrino emitting processes

4.A.1 Direct neutrino production

There is extensive literature on neutrino emitting processes in an electroweak plasma or in a nuclear environment. We refer the reader to Dicus (1972), Braaten & Segel (1993), Bruenn (1985), Dutta et al. (2004), Itoh et al. (1989), Munakata et al. (1985), Ratkovic et al. (2003), Baiko & Yakovlev (1999), Friman & Maxwell (1979), Lattimer et al. (1991), Qian & Woosley (1996) and further references therein for a broader overview on the subject. In the hot fireball environment, the most important processes are:

- photo-neutrino process: $e^{\pm} + \gamma \rightarrow e^{\pm} + \nu_i + \overline{\nu}_i$;
- plasma process: $\gamma \rightarrow \nu_i + \overline{\nu}_i$;
- pair annihilation: $e^- + e^+ \rightarrow \nu_i + \overline{\nu}_i$;
- electron capture: $e^- + p \rightarrow n + \nu_e$;
- positron capture: $e^+ + n \rightarrow p + \overline{\nu}_e$.

The last two processes constitute the non-degenerate URCA process, which is the dominant nuclear neutrino emitting process for low nucleon densities. Neutron decay is too slow to play a role of importance if the neutrons are non-degenerate.

We use the following total (i.e. adding all neutrino flavors) emissivities for the photo-neutrino (Dutta et al. 2004), plasma (Ratkovic et al. 2003), pair annihilation (Itoh et al.

1989) and non-degenerate URCA (Qian & Woosley 1996) processes:

$$Q_{\rm photo} = 1.1\times10^{31}\ (T_{11})^9\ {\rm erg\ s^{-1}\ cm^{-3}}; \quad (4.44a)$$
$$Q_{\rm plasma} = 7.1\times10^{26}\ (T_{11})^9\ {\rm erg\ s^{-1}\ cm^{-3}}; \quad (4.44b)$$
$$Q_{\rm pair} = 3.6\times10^{33}\ (T_{11})^9\ {\rm erg\ s^{-1}\ cm^{-3}}; \quad (4.44c)$$
$$Q_{\rm URCA} = 9.0\times10^{31}\ (T_{11})^6\,(\rho_{B,8})\ {\rm erg\ s^{-1}\ cm^{-3}}, \quad (4.44d)$$

where $\rho_B = \rho_{B,8}\times10^8$ gr cm^{-3}. These emissivities are plotted as a function of temperature in figure 4.2. The emissivity of both the photo-neutrino and the plasma process is several orders of magnitude lower than that of e^-e^+ pair annihilation, which is in keeping with similar comparisons in the literature (Itoh et al. 1989, Prakash et al. 2004, Raffelt 1996).

Electron-positron pair annihilation and non-degenerate URCA have a different scaling behavior with temperature, and the URCA process depends on baryon density. For the environment considered in this study, we conclude that pair annihilation is the dominant process.

4.A.2 Neutrinos from pion decay

Another source of neutrinos is the decay of charged pions:

- pion decay: $\pi^- \rightarrow \mu^- + \overline{\nu}_\mu$
  $\rightarrow e^- + \overline{\nu}_e + \nu_\mu + \overline{\nu}_\mu$,

and the charge-conjugate process for π^+ decay. The pions originate from photopion production or nucleon – nucleon collisions:

- photopion production: $\gamma + n \rightarrow p + \pi^-$;
  $\gamma + p \rightarrow n + \pi^+$;
- N – N collisions: $n + p \rightarrow p + p + \pi^-$;
  $p + p \rightarrow n + p + \pi^+$.

The cross section of pion production in nucleon – nucleon collisions ($\sigma \sim 3\times10^{-26}$ cm^2, see e.g. Bahcall & Mészáros (2000)) is more than an order of magnitude larger than that of the photopion process ($\sigma \sim 10^{-28}$ cm^2, see e.g. Mucke et al. (1999)), but the photon density in the plasma is almost four orders of magnitude higher. This means that photopion production is the dominant pion creating process.

Pion production can only occur at energies higher than the pion mass threshold $E_t \sim 140$ MeV. This implies that only photons in the high-energy tail of the distribution (constituting less than 5% of the total energy in photons) can create pions. Most of the pions are created at threshold, and decay into muon- and electron- (anti)neutrinos with energies below $m_\mu c^2/2 \simeq 53$ MeV. The energy spectrum of the various neutrino types is different, but the mean energies are in the range of 31 to 37 MeV.

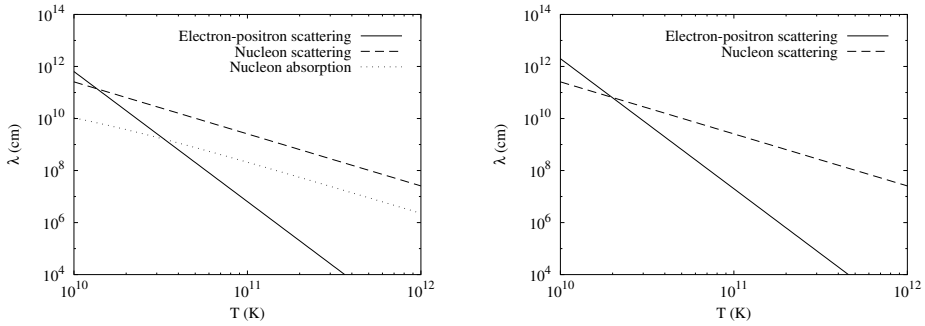

Figure 4.3: Neutrino mean free path lengths as a function of temperature for scattering off electrons and positrons (solid line), nucleon scattering (dashed) and nucleon absorption (dotted). We used the value $Y_e = 0.5$ for nucleon scattering. The left panel applies to electron neutrinos, the right panel to muon- and tau-neutrinos. The graphs for the corresponding antineutrinos are virtually identical.

4.B Neutrino absorption and scattering processes

We summarize the cross section formulae for the following processes:

- $e^{\pm}$ – neutrino scattering: $\nu_i + e^{\pm} \rightarrow \nu_i + e^{\pm}$;
- nucleon – neutrino scattering: $\nu_i + N \rightarrow \nu_i + N$;
- electron-neutrino capture: $\nu_e + n \rightarrow p + e^{-}$;
- electron-antineutrino capture: $\overline{\nu}_e + p \rightarrow n + e^{+}$,

where we assume that all the particles are non-degenerate. The result, in terms of the mean free path length (mfp), is plotted in figure 4.3. We use number densities $n_{e^-} = n_{e^+} = 1.4 \times 10^{35}$ cm^{-3} and $n_B = 5 \times 10^{31}$ cm^{-3}.

From figure 4.3, we conclude that the neutrino mfp in the fireball is determined by scattering off electrons and positrons.

4.B.1 Electron and positron scattering

The cross section[8] for neutrino scattering off electrons in a plasma is (Tubbs & Schramm 1975):

$$\sigma = \frac{3G_F^2\hbar^2c^2}{2\pi}\left((c_V + c_A)^2 + \frac{(c_V - c_A)^2}{3}\right)(k_BT)\,E_\nu\,, \tag{4.45}$$

where $G_F^2\hbar^2c^2 = 5.3 \times 10^{-44}$ cm^2 MeV^{-2} and

$$c_V = 1/2 + 2\sin^2\theta_w\,; \quad c_A = 1/2\,; \quad \sin^2\theta_W = 0.22\,. \tag{4.46}$$

[8]The vacuum cross section scales as T via the neutrino energy ('t Hooft 1971, Sehgal 1974), but it is important to realize that we consider plasma cross sections. The role of the electron mass in the vacuum cross section is taken by the thermal energy, which leads to an increase by a factor $3.15k_BT/m_e$. For a temperature T_*, this is two orders of magnitude.

We average over a thermal neutrino distribution by replacing $E_\nu \to \langle E_\nu \rangle = 3.15\, k_B T$. The formula as it stands applies to electron-neutrinos, which interact with electrons through both the charged and neutral current. For other neutrinos, one should make the following substitutions (Tubbs & Schramm 1975):

$$\begin{array}{rlllll} \nu_\mu, \nu_\tau: & c_A & \to & c_A - 1\,, & c_V \to & c_V - 1\,; \\ \overline{\nu}_e: & c_A & \to & -c_A\,, & c_V \to & c_V\,; \\ \overline{\nu}_\mu, \overline{\nu}_\tau: & c_A & \to & 1 - c_A\,, & c_V \to & c_V - 1\,. \end{array} \tag{4.47}$$

For muon- and tau-neutrinos, this accounts for the fact that these only have a neutral interaction with electrons. The cross section for neutrino – positron scattering is equal to the cross section for the scattering of the corresponding antineutrino off an electron. If the electron and positron densities are equal, these processes can be combined as follows:

$$\begin{aligned} \sigma\left(\nu_i, e^\pm\right) &= \sigma\left(\nu_i, e^-\right) + \sigma\left(\nu_i, e^+\right) \\ &= \sigma\left(\nu_i, e^-\right) + \sigma\left(\overline{\nu_i}, e^-\right)\,, \end{aligned} \tag{4.48}$$

and the mean free path length due to combined electron-positron scattering follows from

$$\lambda^{-1}\left(\nu_i, e^\pm\right) = \sigma\left(\nu_i, e^\pm\right) n_{e^-}\,. \tag{4.49}$$

Because the electron and positron density scales as T^3, the mean free path length is proportional to T^{-5}.

4.B.2 Nucleon scattering

Neutrino – nucleon scattering is independent of neutrino flavor because the interaction is neutral. From Raffelt (1996):

$$\sigma = \frac{G_F^2 \hbar^2 c^2}{\pi} \left(C_V^2 + 3\, C_A^2\right) {E_\nu}^2\,, \tag{4.50}$$

where we understand that $E_\nu^2 \to \langle E_\nu^2 \rangle = 12.9\,(k_B T)^2$. Neutrino – proton and neutrino – neutron scattering have slightly different cross sections because of different strong interaction form factors[9] C_V and C_A. We average the cross section by assuming an equal amount of neutrons and protons ($Y_e = 0.5$):

$$\sigma\left(\nu_i, N\right) = \sigma\left(\nu_i, p\right) + \sigma\left(\nu_i, n\right)\,, \tag{4.51}$$

and compute the mean free path from

$$\lambda^{-1}\left(\nu_i, N\right) = \sigma\left(\nu_i, N\right)\left(0.5 n_B\right)\,. \tag{4.52}$$

The baryon density is independent of temperature[10] so that the mean free path length is proportional to T^{-2}.

[9] We use the values $C_V^2 = 0.0012$ (0.25) and $C_A^2 = 0.47$ (0.33) for protons (neutrons) (Raffelt 1996).

[10] The baryon density does not scale with temperature in a dynamical way. Indirectly, the quantities are related by the requirement that there should be 1 TeV per baryon: a higher temperature permits a higher baryon density.

4.B.3 Nucleon absorption

Electron-neutrinos and -antineutrinos can be absorbed by neutrons and protons through the charged interaction. The cross section is (Tubbs & Schramm 1975)

$$\sigma = \frac{G_F^2 \hbar^2 c^2}{\pi} \left(3\alpha^2 + 1\right) {E_\nu}^2 g(E_\nu)\,; \tag{4.53a}$$

$$g(E_\nu) = \left(1 \pm \frac{Q}{E_\nu}\right)\left(1 \pm 2\frac{Q}{E_\nu} + \frac{Q^2 - (\pm m_e^2)}{E_\nu^2}\right)^{1/2}, \tag{4.53b}$$

where $\alpha = -1.26$ is the nuclear axial coupling coefficient and $Q = 1.3\,\mathrm{MeV}$ is the neutron-proton mass difference. The positive sign applies to neutrino capture on neutrons, the negative sign to antineutrino capture on protons. We do not average cross sections here, because each process is specific to either electron-neutrinos or electron-antineutrinos. Averaging over a thermal neutrino distribution is understood as in the nucleon scattering cross section, and (up to small corrections due to the energy dependence of the function g) the mean free path length is proportional to T^{-2}.

5

Neutron-rich gamma-ray burst flows: dynamics and particle creation in neutron – proton collisions

Koers, H. B. J. & Giannios, D.
2007, A&A, in press (astro-ph/0703719)

5.1 Introduction

In recent years there has been significant progress in our understanding of gamma-ray bursts (GRBs). The observational connection between supernovae and GRBs and studies of GRB host galaxies provide compelling evidence for a connection between long GRBs and the death of massive stars (Van Paradijs et al. 2000, Woosley & Bloom 2006). The general scenario for long GRBs (for recent reviews, see Piran (2004); Mészáros (2006)) starts with core collapse of the massive star leading to the formation of a black hole surrounded by an accretion disk. The black hole – accretion disk system powers a developing outflow along the rotational axis, which accelerates to a bulk Lorentz factor of a few hundred, transferring its energy to the baryons contained in the flow. Dissipation of energy in the outflow leads to the prompt gamma-ray emission while the interaction of the outflow with the external medium results in the afterglow.

The nature of the relativistic outflow is currently one of the most important open questions regarding GRBs. The high Lorentz factor, required to match the inferred energy density of the source and the observed non-thermal character of the emission (the compactness problem; see e.g. Piran (2004)), implies that the ratio of energy to rest mass of the flow must be very high. In the widely used fireball model (Cavallo & Rees 1978, Goodman 1986, Paczyński 1986) the outflow is a photon-electron-positron plasma that is dominated by thermal energy and has a small baryonic load. Alternatively, the energy of the outflow may initially be dominated by Poynting flux (Usov 1992). Such outflows

occur naturally when a magnetized accretion disk surrounds a black hole (Thompson 1994, Mészáros & Rees 1997, Spruit et al. 2001, Van Putten & Ostriker 2001, Vlahakis & Königl 2001, Drenkhahn & Spruit 2002, Lyutikov & Blandford 2003, Lyutikov 2006, Uzdensky & MacFadyen 2006).

Neutrinos and gamma rays may be useful probes to differentiate between fireballs and Poynting-flux dominated (PFD) outflows. The internal shocks that are believed to accelerate electrons in the fireball model will also accelerate protons to very high energies, giving rise to neutrinos with energy $\gtrsim$100 TeV through photopion production (Waxman & Bahcall 1997). In the absence of a mechanism to accelerate protons to very high energies these neutrinos are not expected in PFD outflows. In this chapter we consider neutron – proton (np) collisions in neutron-rich flows and address the question whether neutrinos and gamma rays created in these hadronic interactions can also be used to probe the nature of GRB outflows.

GRB outflows are expected to be neutron-rich. In GRB central engines, the competition of positron capture on neutrons and electron capture on protons favors a neutron-rich environment (Beloborodov 2003b, Pruet et al. 2003, Chen & Beloborodov 2007). Nucleosynthesizing interactions reduce the number of free neutrons in the outflow, but a significant amount of neutrons remains in the flow until neutron decay becomes important (Beloborodov 2003b, Inoue et al. 2003). Deep in the outflow protons and neutrons are strongly coupled through nuclear scattering and behave as a single fluid that accelerates to high Lorentz factors. With increasing distance from the central engine the densities decrease until neutrons decouple and enter the coasting phase. Protons, being electromagnetically coupled to the flow, may be accelerated further. When the relative velocity between neutrons and protons is sufficiently high, inelastic np collisions are possible and lead to pion creation. The pions decay into gamma rays and neutrinos with observer energies in the $\sim 10 - 100$ GeV range. This mechanism has been investigated for fireballs (Derishev et al. 1999b, Bahcall & Mészáros 2000, Mészáros & Rees 2000, Belyanin et al. 2003, Razzaque & Mészáros 2006) but, to the best of our knowledge, not for PFD flows.

The creation of secondary particles in inelastic np collisions can potentially be used to identify a substantial neutron component in GRB flows. Other ways to identify such a component that have been suggested in the literature are through signatures in the early afterglow of GRBs (Derishev et al. 1999a, Beloborodov 2003a, Fan et al. 2005) ultraviolet flashes generated in internal shocks in neutron-rich flows (Fan & Wei 2004) and observational signatures of a two-component jet that may be associated with neutron-rich MHD flows (Vlahakis et al. 2003, Peng et al. 2005).

In this work we consider the 'AC' model as a specific model for PFD outflows. In this model the magnetic field configuration is similar to that produced by an inclined rotator (Coroniti 1990, Lyubarsky & Kirk 2001) with field lines changing polarity on a scale $\lambda \simeq 2\pi c/\Omega$, where Ω denotes the angular frequency of the rotator. This model was recently discussed in connection to GRBs in a series of papers (Spruit et al. 2001,

Drenkhahn 2002, Drenkhahn & Spruit 2002, Giannios & Spruit 2005, Giannios 2006), where it was found that dissipation of the electromagnetic energy by magnetic reconnection can account for both the bulk acceleration of the flow and for the prompt emission.

The dynamics of fireballs and of outflows in the AC model are distinctively different. Fireballs are driven by radiation pressure and exhibit a period of rapid acceleration in which the Lorentz factor $\Gamma \propto r$, where r denotes the distance from the central engine (Paczyński 1986). The flow saturates either when there is no more energy available to further accelerate the baryons or when radiation and matter decouple at the Thomson photosphere. An analysis of the dynamics of neutron-rich fireballs was recently presented by Rossi et al. (2006). The dynamics of neutrons in MHD flows was considered previously by Vlahakis et al. (2003) in the context of a different model for the outflow (Vlahakis & Königl 2003) than the AC model considered here. In the AC model, the acceleration of the flow is quite gradual and can be approximated with $\Gamma \propto r^{1/3}$ (Drenkhahn 2002). Since acceleration of the flow is driven by magnetic forces, the flow can saturate far beyond the photosphere. It is expected that the difference in dynamics affects the number and the energy of secondary particles created in np collisions. Furthermore, the presence of a strong magnetic field can affect the interaction of secondary particles with the flow.

Motivated by the fact that neutrinos and gamma rays from inelastic np collisions could provide an indication about the nature of GRB outflows, we consider in this chapter both fireballs and AC flows with a substantial neutron component. We investigate the dynamics of these flows and the creation of gamma rays and neutrinos in inelastic np collisions. In order to give an accurate comparison between the fireball model and the AC model, we consider both models here. Furthermore we use accurate fitting formulae for both the total and inelastic np cross sections, which has an important effect on the calculated fluences of secondary particles.

This chapter is organized as follows. In section 5.2 we discuss the dynamical behavior of fireballs and of GRB outflows described by the AC model. In section 5.3 we consider particle creation in inelastic np collisions. We discuss here the parameter space in which the mechanism is operational and we compute the fluences and energies of secondary neutrinos and gamma rays. Detection prospects are discussed in section 5.4 and conclusions are presented in section 5.5.

5.2 Dynamics of neutron-rich GRB flows

Deep in the flow neutrons are strongly coupled to protons through elastic collisions, so that the two fluids behave as a single one. This np fluid is accelerated by conversion of thermal energy into kinetic energy in the fireball model and of magnetic energy into kinetic energy in the reconnection model. When the dynamical time of the flow becomes shorter than the np collision time, the two fluids decouple and the neutrons enter the coasting phase. Provided that the flow has not already reached its terminal bulk Lorentz

factor, the protons keep accelerating above the *np* decoupling radius, which results in relative motion of the two fluids.

The analysis of the effect of a neutron component on the dynamics is made separately for the fireball and the reconnection model for the various stages of their evolution. Since the treatment of the mass flux is identical in both models, it is presented first.

5.2.1 Mass flux: protons and neutrons

For an ultrarelativistic, steady, radial flow, assumed by both models under consideration, conservation of mass implies that the baryon outflow rate obeys

$$\dot{M} = \dot{M}_{\rm p} + \dot{M}_{\rm n} = 4\pi r^2 mc \left(\Gamma_{\rm p} n'_{\rm p} + \Gamma_{\rm n} n'_{\rm n}\right) = 4\pi r^2 mc \Gamma_{\rm p} n'_{\rm p} \left(1 + \xi\right) , \tag{5.1}$$

where $\Gamma_{\rm p}$ and $\Gamma_{\rm n}$ stand for the bulk Lorentz factor of the protons and the neutrons, respectively, and $n'_{\rm p}$ and $n'_{\rm n}$ for their proper number densities. The masses of protons and neutrons are assumed equal $m_{\rm p} \simeq m_{\rm n} = m$ and ξ stands for the neutron-to-proton mass flux ratio:

$$\xi \equiv \frac{\dot{M}_{\rm n}}{\dot{M}_{\rm p}} = \frac{\Gamma_{\rm n} n'_{\rm n}}{\Gamma_{\rm p} n'_{\rm p}} . \tag{5.2}$$

The ratio ξ depends on the radius r since free neutrons decay into protons on a comoving timescale $\tau_\beta \sim 900$ sec resulting in

$$\frac{{\rm d}\dot{M}_{\rm n}}{{\rm d}r} = \frac{{\rm d}\dot{M}_{\rm n}}{\Gamma_{\rm n} c {\rm d}t'} = -\frac{\dot{M}_{\rm n}}{\Gamma_{\rm n} c \tau_\beta} , \tag{5.3}$$

where t' stands for the comoving time. Taking into account that a proton is produced for every neutron that decays (i.e. ${\rm d}\dot{M}_{\rm n}/{\rm d}r = -{\rm d}\dot{M}_{\rm p}/{\rm d}r$), eqs. (5.2) and (5.3) yield an expression for ξ as a function of radius:

$$\frac{{\rm d}\xi}{{\rm d}r} = -\frac{\xi(1+\xi)}{\Gamma_{\rm n} c \tau_\beta} . \tag{5.4}$$

From eq. (5.1) one can solve for the number density of protons and neutrons as a function of radius to find that

$$n'_{\rm p} = \frac{1}{1+\xi} \frac{\dot{M}}{4\pi r^2 mc \Gamma_{\rm p}} , \tag{5.5}$$

and

$$n'_{\rm n} = \frac{\xi}{1+\xi} \frac{\dot{M}}{4\pi r^2 mc \Gamma_{\rm n}} . \tag{5.6}$$

The number density of the protons and neutrons is determined once their bulk Lorentz factor as a function of radius is derived. This is the topic of the next sections.

5.2.2 The fireball

In the fireball model most of the energy is initially stored in the form of thermal energy e, which is dominated by the energy density of radiation. The luminosity L of the flow is the sum of kinetic and radiation flux (e.g., Rossi et al. 2006):

$$L = 4\pi r^2 c \left(\Gamma_{\rm p}^2 \left(4e/3 + n'_{\rm p} mc^2\right) + \Gamma_{\rm n}^2 n'_{\rm n} mc^2\right) . \tag{5.7}$$

This expression can be rewritten as

$$L = 4\pi r^2 \Gamma_{\rm p}^2 c n'_{\rm p} mc^2 \left(1 + \xi \frac{\Gamma_{\rm n}}{\Gamma_{\rm p}} + x\right) , \tag{5.8}$$

where we have defined $x \equiv 4e/(3n'_{\rm p} mc^2)$.

An important quantity for the evolution of the flow is the baryon loading parameter $\eta \equiv L/\dot{M}c^2 \gg 1$ where $\dot{M}$ (defined in eq. (5.1)) includes both the contribution of the proton and the neutron fluid. Using expressions (5.1) and (5.8) one derives the expression

$$(1 + \xi)\,\eta = \Gamma_{\rm p}(1 + x) + \xi\Gamma_{\rm n} . \tag{5.9}$$

Assuming that the flow starts from rest (i.e., $\Gamma_{\rm p,0} = \Gamma_{\rm n,0} = 1$) at an initial radius r_0 and initial neutron-to-proton ratio ξ_0, the initial value for x is $x_0 = 4e_0/(3n'_{\rm p,0} mc^2) = (1 + \xi_0)(\eta - 1)$.

As long as the flow is Thomson thick, radiation and particles remain coupled and the evolution of the fireball is fully determined by the adiabatic law[1]

$$e = e_0 \left(\frac{n'_{\rm p}}{n'_{\rm p,0}}\right)^{4/3} . \tag{5.10}$$

From eqs. (5.5), (5.9) and (5.10) one finds for the internal energy-to-proton rest mass ratio in the flow

$$x = x_0 \left(\frac{n'_{\rm p}}{n'_{\rm p,0}}\right)^{1/3} = (1 + \xi_0)\,(\eta - 1) \left(\frac{r_0^2}{r^2 \Gamma_{\rm p}}\right)^{1/3} . \tag{5.11}$$

Differentiating eq. (5.9) with respect to radius r and using eq. (5.11), one has an expression relating the bulk Lorentz factor of the proton and the neutron fluids in the optically thick part of the flow (see also Rossi et al. 2006)

$$\frac{{\rm d}\Gamma_{\rm p}}{{\rm d}r} = \frac{\Gamma_{\rm p}}{r} \frac{2x}{2x + 3} - \frac{3\xi_0}{2x + 3} \frac{{\rm d}\Gamma_{\rm n}}{{\rm d}r} . \tag{5.12}$$

[1] This expression does not take into account the increase of the proton density due to neutron decay. The use of this expression is justified because, for the parameter space relevant for GRB flows, there is only a negligible fraction of neutrons that decays below the photosphere of fireballs. Hereafter, in the Thomson thick part of the flow, we set $\xi = \xi_0$.

For the dynamics of the neutron-rich fireball to be fully determined, one needs to look closer at the momentum exchange between the neutron and the proton fluids because of *np* collisions. This has been studied by Derishev et al. (1999b) and Rossi et al. (2006) who showed that when the two fluids have a relative velocity $\beta_{\rm rel}$, there is a drag force that accelerates the neutrons

$$\frac{{\rm d}\Gamma_{\rm n}}{{\rm d}r} = \frac{n'_{\rm p}\sigma_{\rm tot}}{2}\Gamma_{\rm rel}^2\beta_{\rm rel}^2\,, \tag{5.13}$$

where $\Gamma_{\rm rel} \simeq (\Gamma_{\rm n}/\Gamma_{\rm p} + \Gamma_{\rm p}/\Gamma_{\rm n})/2$ for ultrarelativistic flows and the total *np* scattering cross section $\sigma_{\rm tot}$ is a function of $\beta_{\rm rel}$. This expression accounts for the *np* interaction and does not depend on the acceleration mechanism (thermal or magnetic) of the flow. It can, thus, be applied to both fireballs and MHD flows.

The *np* scattering cross section depends on the relative velocity of the two fluids. For *np* scatterings that take place with energies below the pion creation threshold, the scattering cross section can with good accuracy be taken to scale as $\propto 1/(c_1\beta_{\rm rel} + c_2\beta_{\rm rel}^3)$, while it remains almost constant for higher energies. The constants c_1 and c_2 are found by fitting to experimental data from Yao et al. (2006; see appendix A)

$$\sigma_{\rm tot} \simeq \max\left(\frac{\bar{\sigma}}{0.19\beta_{\rm rel} + 5.2\beta_{\rm rel}^3}, \bar{\sigma}\right), \tag{5.14}$$

where $\bar{\sigma} \equiv 4 \times 10^{-26}$ cm^2. Our fitting formulae for $\sigma_{\rm tot}$ are more accurate than the expressions used by Rossi et al. (2006), where the total *np* scattering cross section is substantially underestimated for $\beta_{\rm rel}\Gamma_{\rm rel} \lesssim 1$ (i.e. before *np* decoupling). This results in some differences in the dynamics close to the decoupling radius. We find that the two fluids decouple over a narrower radial range (i.e. sharper decoupling). Furthermore, the fitting formula (5.14) results in terminal neutron Lorentz factors that are ∼10% higher than those found when we use the Rossi et al. (2006) expressions for the *np* scattering cross section.

With eqs. (5.11), (5.12) and (5.13) one has the complete description of the dynamics of the fireball in the Thomson thick part of the flow (i.e. below the photosphere). In the optically thin part radiation and matter decouple and expression (5.10) is no longer applicable.

Since radiation pressure is the driving mechanism of acceleration in the fireball, one would expect no further acceleration of the flow to take place above the photosphere. On the other hand, although most of the photons do not scatter with electrons above the photosphere, the electrons (outnumbered by the photons by a factor $\sim 10^5$) are still repeatedly scattered resulting in a residual acceleration of the flow in the optically thin region. This residual acceleration is given by the expression (Beloborodov 2002; Rossi et al. 2006, appropriately modified to include the neutron fluid):

$$\frac{{\rm d}\Gamma_{\rm p}}{{\rm d}r} + \xi\frac{{\rm d}\Gamma_{\rm n}}{{\rm d}r} = \frac{\sigma_{\rm T}L_{\rm r}}{16\pi\Gamma_{\rm p}^2 r^2 mc^3}\left(1 - \left(\frac{\Gamma_{\rm p}r_{\rm ph}}{\Gamma_{\rm p}(r_{\rm ph})r}\right)^4\right) + \frac{\Gamma_{\rm p} - \Gamma_{\rm n}}{1+\xi}\frac{{\rm d}\xi}{{\rm d}r}\,, \tag{5.15}$$

where σ_T is the Thomson cross section and $L_r = 16\pi r^2 c\Gamma_p^2 e/3$ stands for the radiative luminosity of the flow. The first term in the right hand side of the last expression accounts for the residual acceleration from radiation and the second for the effect of neutron decay on the dynamics. Using eqs. (5.7) and (5.9), we have for the radiative luminosity of the flow:

$$L_r = L\left(1 - \frac{\Gamma_p + \xi\Gamma_n}{\eta(1+\xi)}\right). \tag{5.16}$$

The expressions (5.4), (5.13), (5.15) and (5.16) describe the dynamics of the flow in the Thomson thin regime.

5.2.3 The reconnection model

In the magnetic reconnection model the flow is considered starting from the Alfvén point r_A and is dominated by Poynting flux. The luminosity of the flow is the sum of the kinetic and Poynting flux:

$$L = 4\pi r^2 c\left(\Gamma_p^2(4e/3 + n_p' mc^2) + \Gamma_n^2 n_n' mc^2\right) + c(rB)^2, \tag{5.17}$$

where B is the magnetic field strength in the central engine frame, which is dominated by its toroidal component.

A detailed investigation of the properties of a neutron-free flow under the assumption of a cold flow (i.e. a flow where the term $4e/3$ is neglected with respect the other terms in eq. (5.17)) is presented in Drenkhahn (2002). A full numerical investigation showed that the dynamical description under the cold flow assumption is rather accurate (Drenkhahn & Spruit 2002). Hereafter, we assume that the flow is cold. One should keep in mind, however, that though of moderate dynamical significance, the internal energy of the flow – dominated by the energy density of radiation – plays a crucial role for its photospheric emission (Giannios 2006, Giannios & Spruit 2007). Furthermore, the cold flow assumption can overestimate the acceleration of the flow in the Thomson thin region by up to 50% in the limit that the internally dissipated energy does not stay in the flow but is efficiently radiated away (Drenkhahn & Spruit 2002). More realistically only a fraction of the dissipated energy is radiated away and the error we make in the Thomson thin region is smaller.

Setting $e = 0$ and using eqs. (5.1) and (5.17) we have

$$L = \frac{\Gamma_p + \xi\Gamma_n}{1+\xi}\dot{M}c^2 + c(rB)^2 = \frac{\Gamma_p + \xi\Gamma_n}{1+\xi}\dot{M}c^2(1+\sigma), \tag{5.18}$$

where $\sigma \equiv (1+\xi)(rB)^2/((\Gamma_p + \xi\Gamma_n)\dot{M}c)$ is the magnetization parameter of the flow and stands for the Poynting-to-kinetic flux ratio. Using the last expression, the baryon loading of the flow is

$$\eta \equiv \frac{L}{\dot{M}c^2} = \frac{\Gamma_p + \xi\Gamma_n}{1+\xi}(1+\sigma). \tag{5.19}$$

In the reconnection model, the flow is considered starting from the Alfvén radius with magnetization σ_0. In the inner part of the flow the very frequent np collisions lead to $\Gamma_{p,0} \simeq \Gamma_{n,0} = \sqrt{\sigma_0}$. In view of eq. (5.19), one has that $\eta = \sqrt{\sigma_0}(1+\sigma_0) \simeq \sigma_0^{3/2}$. The initial magnetization σ_0 is, thus, an alternative means in parameterizing the baryon loading of a PFD flow.

The radial dependence of the magnetic field strength is given by the induction equation that is appropriately modified to take into account the magnetic field dissipation through reconnection (Drenkhahn & Spruit 2002):

$$\frac{\mathrm{d}(rB)}{\mathrm{d}r} = -\frac{rB}{c\tau_\mathrm{d}} \,. \tag{5.20}$$

Here,

$$\tau_\mathrm{d} = \frac{2\pi\Gamma_\mathrm{p}^2}{\epsilon\Omega}\sqrt{\frac{\sigma+1}{\sigma}} \tag{5.21}$$

is the dissipation timescale of the magnetic field (in the central engine frame), Ω stands for the angular frequency of the rotator, and ϵ parameterizes the magnetic reconnection speed v_rec. As in most models of magnetic reconnection, v_rec scales with the Alfvén speed v_A, i.e. $v_\mathrm{rec} = \epsilon v_\mathrm{A}$ (see, for example, Lyubarsky 2005). A nominal value used for ϵ is 0.1.

By combining eqs. (5.4), (5.17), (5.18) and (5.20) one can eliminate the magnetic field B and derive an equation for the bulk Lorentz factor of the protons and the neutrons:

$$\frac{\mathrm{d}\Gamma_\mathrm{p}}{\mathrm{d}r} + \xi\frac{\mathrm{d}\Gamma_\mathrm{n}}{\mathrm{d}r} = \frac{2}{c\tau_\mathrm{d}}\left((1+\xi)\sigma_0^{3/2} - \Gamma_\mathrm{p} - \xi\Gamma_\mathrm{n}\right) + \frac{\Gamma_\mathrm{p}-\Gamma_\mathrm{n}}{1+\xi}\frac{\mathrm{d}\xi}{\mathrm{d}r} \,. \tag{5.22}$$

The last expression, in combination with eqs. (5.4) and (5.13), describes the the dynamics of neutron-rich flows in the reconnection model.

5.2.4 Results

Having derived a closed system of equations that describe the dynamics of neutron-rich flows, we proceed with the investigation of the dependence of their properties on the parameters of the flow for both fireballs and strongly magnetized flows.

The fireball

By numerically solving eqs. (5.11), (5.12) and (5.13) in the Thomson thick part of the flow and eqs. (5.4), (5.13), (5.15) and (5.16) above the photosphere, one can follow the various stages of the neutron-rich fireball (see also Rossi et al. 2006).

In Figs. (5.1) and (5.2), the bulk Lorentz factors of the proton and the neutron fluids are plotted as function of radius for different values of the parameters of the fireball

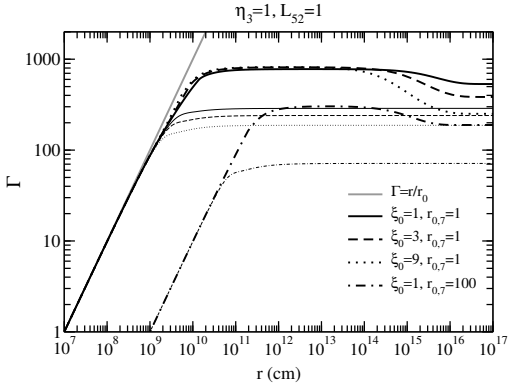

Figure 5.1: Bulk Lorentz factor of the protons (thick lines) and neutrons (thin lines) for different values of the initial neutron-to-proton ratio ξ_0 and radius r_0 of the fireball. At small radii, both protons and neutrons are in the linear acceleration regime (gray line). After np decoupling the neutrons saturate while protons can be further accelerated by radiation pressure. At $r \sim 10^{15}$ cm the neutrons decay into protons that interact and decelerate the preexisting protons.

model. The latter are the luminosity of the flow L, the baryon loading η, the initial neutron-to-proton ratio ξ_0 and initial radius r_0 of the flow. All the models studied have $\eta \gtrsim 100$ relevant for GRB flows.

These low-baryon flows pass through an initial phase of rapid acceleration. During this phase, the neutron and proton fluids are strongly coupled and move practically with the same bulk Lorentz factor. Setting $\Gamma_p \simeq \Gamma_n$ in eq. (5.12) we have

$$\frac{d\Gamma_p}{dr} = \frac{\Gamma_p}{r}\frac{2x}{2x + 3(1+\xi_0)} \,. \tag{5.23}$$

In the limit of $x \gg 3(1+\xi_0)/2$, radiation pressure leads to the well known linear acceleration of the flow as function of radius (cf. Goodman 1986, Paczyński 1986, Piran et al. 1993):

$$\Gamma_p \simeq \Gamma_n = \frac{r}{r_0} \,, \tag{5.24}$$

If no np decoupling were to take place, the bulk Lorentz factor of the flow would saturate at $\Gamma_\infty = \eta$ at the saturation radius $r_s = \eta r_0$.

Note that although at small radii the numerical results follow the linear scaling (5.24) closely, there are deviations from this scaling appearing for $\Gamma_p \gtrsim 100$ for the models presented in Figs. 1 and 2. Since eq. (5.24) is exact for a fireball with a negligible number of baryons, finite-η flows have bulk Lorentz factors $\Gamma(r) < r/r_0$.

At larger radii the density of the flow drops and np scatterings become less frequent. When the comoving dynamical timescale becomes shorter than the np scattering

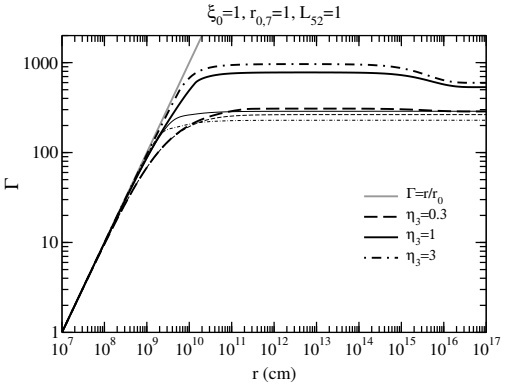

Figure 5.2: Bulk Lorentz factor of the protons (thick lines) and neutrons (thin lines) for different values of the baryon loading η of the fireball. For low baryon loading (high η), the protons are accelerated to much higher bulk Lorentz factors than the neutrons. For high η, the saturation of the protons takes place close to the Thomson photosphere while the photospheric emission is very powerful.

timescale, the two fluids decouple and the neutrons are not accelerated any more. The relative velocity increases rapidly at decoupling. One can define the decoupling condition as $\Gamma_{\rm rel}\beta_{\rm rel} = 1$. Setting this condition in (5.13) and using also (5.24) one finds for the decoupling radius

$$r_{\rm np} = 2.6\times 10^9 \text{ cm} \times L_{52}^{1/3} r_{0,7}^{2/3} \eta_3^{-1/3} \left(\frac{1+\xi_0}{2}\right)^{-1/3} , \tag{5.25}$$

and for the Lorentz factor at decoupling

$$\Gamma_{\rm np} = 2.6\times 10^2 \times L_{52}^{1/3} \eta_3^{-1/3} r_{0,7}^{-1/3} \left(\frac{1+\xi_0}{2}\right)^{-1/3} . \tag{5.26}$$

If the flow reaches its terminal Lorentz factor before np decoupling has taken place, both the neutron and proton flows coast with the same speed.

For a flow with a sufficiently high η, i.e.

$$\eta > \eta_{\rm cr} \equiv 3.6\times 10^2 \times L_{52}^{1/4} r_{0,7}^{-1/4} \left(\frac{1+\xi_0}{2}\right)^{-1/4} , \tag{5.27}$$

the protons keep being accelerated after np decoupling has taken place while the neutrons coast with $\Gamma_{\rm n} \sim \Gamma_{\rm np}$. The bulk Lorentz factor at np decoupling $\Gamma_{\rm np}$ provides a good estimate of the saturation Lorentz factor of the neutrons $\Gamma_{\rm n,s}$. To quantify this statement, we have compared the analytical estimate for $\Gamma_{\rm np}$ with the numerical values of $\Gamma_{\rm n}$ at a large radius (here taken at $r = 10^{17}$ cm) and found that the two quantities

agree with each other within ~25% for the (rather large) parameter space $\eta_{\rm cr} < \eta < 3000$, $0.01 < L_{52} < 10$, $0 < \xi_0 < 10$ and $1 < r_{0,7} < 100$.

When condition (5.27) is satisfied, the protons are further accelerated by radiation pressure after np decoupling until either all internal energy has been used or the flow crosses the photosphere, where the flow becomes transparent with respect to Thomson scattering so that radiation and matter decouple.

An estimate of the maximum Lorentz factor of the protons is given by assuming a neutron-free flow after np decoupling with luminosity $\hat{L}$ that does not include the kinetic energy of neutrons (i.e. $\hat{L} = L - \Gamma_{\rm np}\xi_0\dot{M}c^2/(1+\xi_0)$) and mass flux $\hat{\dot{M}} = \dot{M}/(1+\xi_0)$. The baryon loading of the decoupled proton flow is

$$\hat{\eta} = \frac{\hat{L}}{\hat{\dot{M}}c^2} = \eta(1+\xi_0) - \xi_0\Gamma_{\rm np} \,. \tag{5.28}$$

The acceleration of the proton fluid will saturate at

$$\Gamma_{\rm p,s} = \min\left(\hat{\eta}, \hat{\eta}_{\rm rad}\right) \,, \tag{5.29}$$

where $\hat{\eta}_{\rm rad} = (\hat{L}\sigma_{\rm T}/(4\pi r_0 mc^3))^{1/4}$ gives the terminal Lorentz factor of the protons when the acceleration of the flow is limited by photospheric crossing (Beloborodov 2002). This estimate takes into account the residual acceleration in the optically thin region discussed in section 5.2.2.

At still larger radii of the order of $r_\beta = \Gamma_{\rm np} c\tau_\beta \sim 10^{15} - 10^{16}$ cm, neutron decay has an appreciable effect on the dynamics of the flow. The neutrons decay into protons and interact with the faster moving proton flow, thereby slowing it down. Note that at distances 10^{17} cm, practically all the neutrons have decayed. The terminal Lorentz factor of the protons there is $\Gamma_{\rm p,\infty} \leq \eta$. For flows with $\hat{\eta} > \hat{\eta}_{\rm rad}$, most of the energy is *not* used to accelerate the baryons (resulting in $\Gamma_{\rm p,\infty} \ll \eta$) but instead appears as photospheric emission of the flow.

Further out, the flow enters the afterglow phase where it decelerates because of interaction with the circumburst medium. This last phase is not considered in this study.

The reconnection model

We now present the various phases of the development of the flow in the context of the reconnection model. The neutron-free flow has been studied by Drenkhahn (2002) and Drenkhahn & Spruit (2002). Here we focus on the dynamical effect of the neutrons. In Figs. 5.3 and 5.4, the bulk Lorentz factors of the proton and the neutron fluids are plotted as function of radius for different values of the parameters of the reconnection model. These parameters are the luminosity of the flow L, the initial magnetization σ_0 of the flow (that also parameterizes the baryon loading since $\eta \simeq \sigma_0^{3/2}$), the initial neutron-to-proton ratio ξ_0 and the combination $\epsilon\Omega$ that parameterizes the reconnection speed.

The flow passes through an initial phase of acceleration where the neutron and proton fluids are strongly coupled and move practically with the same bulk Lorentz factor. Setting $\Gamma_p \simeq \Gamma_n$ in eq. (5.22) we have

$$\frac{d\Gamma_p}{dr} = \frac{\epsilon\Omega\sqrt{1-\Gamma_p/\sigma_0^{3/2}}}{\pi c\Gamma_p^2}\left(\sigma_0^{3/2}-\Gamma_p\right). \tag{5.30}$$

In the limit of $\Gamma_p \ll \sigma_0^{3/2}$ (i.e. the flow is still dominated by Poynting flux), the last equation can be integrated analytically to find (Drenkhahn 2002):

$$\Gamma = \left(\frac{3\epsilon\Omega\sigma_0^{3/2}}{\pi c}(r-r_0)+\sigma_0^{3/2}\right)^{1/3}, \tag{5.31}$$

The reconnection model predicts a gradual acceleration of the flow $\Gamma \sim r^{1/3}$ in the regime $\sqrt{\sigma_0} \ll \Gamma_p \ll \sigma_0^{3/2}$ with the bulk Lorentz factor of the flow given by

$$\Gamma_p \simeq \Gamma_n = \left(\frac{3\epsilon\Omega\sigma_0^{3/2}r}{\pi c}\right)^{1/3}. \tag{5.32}$$

This expression is valid as long as the neutrons have not decoupled from the protons and the flow has not reached its terminal Lorentz factor $\Gamma_\infty = \sigma_0^{3/2}$ at the saturation radius

$$r_s = \frac{\pi c}{3\epsilon\Omega}\sigma_0^3. \tag{5.33}$$

At larger radii the density of the flow drops and nuclear scatterings become less frequent. When the comoving dynamical timescale becomes shorter than the *np* scattering timescale, the two fluids decouple and the neutrons are not accelerated any more. Their relative velocity β_{rel} increases rapidly around decoupling. As for fireballs, one can define the decoupling condition as $\Gamma_{rel}\beta_{rel} = 1$. Setting this condition in eq. (5.13) and using also eq. (5.32) one finds for the decoupling radius

$$r_{np} = 4.1\times10^{10}\ \mathrm{cm}\times L_{52}^{3/5}(\epsilon\Omega)_3^{-2/5}\sigma_{0,2}^{-3/2}\left(\frac{1+\xi_0}{2}\right)^{-3/5}. \tag{5.34}$$

The bulk Lorentz factor of the flow at the decoupling is

$$\Gamma_{np} = 1.1\times10^2\times L_{52}^{1/5}(\epsilon\Omega)_3^{1/5}\left(\frac{1+\xi_0}{2}\right)^{-1/5}. \tag{5.35}$$

If the flow reaches its terminal Lorentz factor at r_s before *np* decoupling has taken place, both the neutron and proton flow coast with the same speed. For a flow with a sufficiently high σ_0, such that

$$\sigma_0 > \sigma_{cr} \equiv 23\times L_{52}^{2/15}(\epsilon\Omega)_3^{2/15}\left(\frac{1+\xi_0}{2}\right)^{-2/15}, \tag{5.36}$$

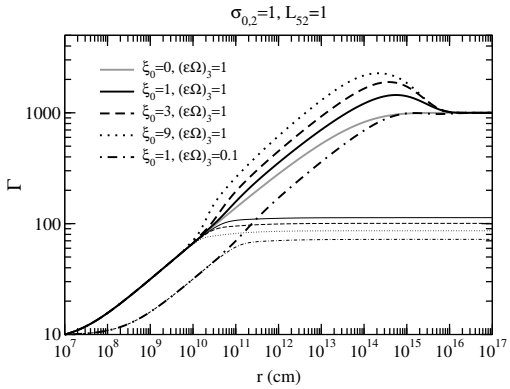

Figure 5.3: Bulk Lorentz factors of the protons (thick lines) and neutrons (thin lines) for different values of the initial neutron-to-proton ratios ξ_0 and reconnection speed parameterized by $\epsilon\Omega$ in the reconnection model. At np decoupling radius the acceleration rate of the protons is enhanced. This effect is particularly pronounced for $\xi_0 \gg 1$ flows. At $r \sim 10^{14} - 10^{15}$ cm, the neutrons decay causing deceleration of the protons.

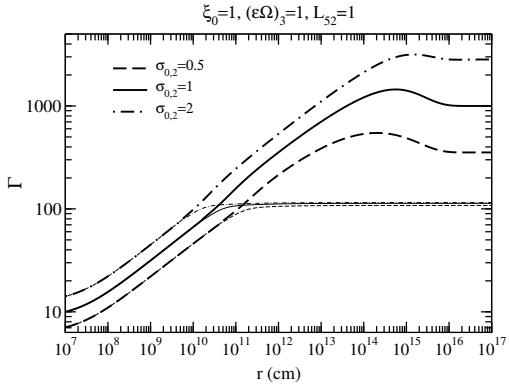

Figure 5.4: Bulk Lorentz factors of the protons (thick lines) and neutrons (thin lines) for different baryon loadings parameterized by the magnetization parameter σ_0 in the reconnection model. The bulk Lorentz factor of the neutrons at np decoupling is essentially independent of σ_0, in agreement with the analytical estimate (5.35).

the protons are further accelerated after *np* decoupling has taken place while the neutrons coast with $\Gamma_n \sim \Gamma_{np}$. The bulk Lorentz factor at *np* decoupling Γ_{np} provides a good estimate of the saturation Lorentz factor of the neutrons $\Gamma_{n,s}$. Comparing the analytical estimate for Γ_{np} with the numerical values of Γ_n at large radii (taken here at $r = 10^{17}$ cm), we have found that the two quantities agree with each other within ∼10% for the parameter space $\sigma_{cr} < \sigma_0 < 300$, $0.01 < L_{52} < 10$, $0 < \xi_0 < 10$ and $0.01 < (\epsilon\Omega)_3 < 10$.

The critical value σ_{cr} corresponds to baryon loading $\eta_{cr} \simeq \sigma_{0,cr}^{3/2} \sim 100$. For baryon loadings $\eta \gtrsim 100$ relevant for GRB flows, *np* decoupling takes place before the saturation radius has been crossed. In this case a substantial amount of magnetic energy is dissipated at radii $r > r_{np}$, which is used to accelerate the protons.

At the *np* decoupling radius the flow becomes effectively less baryon loaded and the protons increase their Lorentz factor more rapidly than the $\Gamma_p \sim r^{1/3}$ scaling. This enhanced acceleration is particularly pronounced in neutron dominated flows (where $\xi_0 \gg 1$; see Fig. 5.3). A similar enhancement in the acceleration has been found by Vlahakis et al. (2003) in the context of a different MHD model for GRBs.

Note that soon after *np* decoupling has taken place the flow crosses the Thomson photosphere. The protons keep accelerating after the photospheric crossing in the magnetized flow since the acceleration is magnetic and not driven by radiation pressure as in the fireball model. At larger radii, the protons can reach bulk Lorentz factors in excess of the limit $\sigma_0^{3/2}$ that characterizes a pure proton flow (shown with dotted line in Fig. 3).

At larger radii the neutrons undergo beta decay. For high-ξ_0 flows, at a typical radius $r \sim \Gamma_{np} c\tau_\beta/\xi_0$ the number of neutrons that have decayed is comparable with the initial number of protons in the flow and the effect of neutron decay on the bulk motion of the protons becomes appreciable.

After magnetic dissipation has ceased and most of the neutrons have decayed, all the available energy has been transferred to the protons. The bulk Lorentz factor of the protons at large radii saturates to the value $\Gamma_{p,\infty} = \sigma_0^{3/2}$. This takes place at $r \sim 10^{16}$ cm. At these radii the flow is expected to enter the afterglow phase which is not considered here.

5.3 Particle creation in inelastic neutron – proton collisions

In the previous section we demonstrated that for low enough baryon loading, the neutrons decouple before the acceleration of the flow is completed in both fireballs and PFD flows. This leads to neutrons and protons developing relative motions and to energetic *np* collisions. Here, we study the production of pions through inelastic *np* collisions in the relativistic outflow and the subsequent decay of pions into gamma rays and neutrinos. We present analytical estimates for the secondary particle fluences and energies, and compare these estimates with numerical results based on the model discussed in

section 5.2.

For the analytical estimates, we approximate the proton and neutron Lorentz factors as follows:

$$\Gamma_{\rm p} \simeq \left(\frac{r}{r_0}\right)^p \; ; \qquad \Gamma_{\rm n} \simeq \min\left(\Gamma_{\rm p}, \Gamma_{\rm np}\right) , \tag{5.37}$$

where $\Gamma_{\rm np}$ is the Lorentz factor of the flow at decoupling, p is a model parameter that allows us to consider the fireball model and the reconnection model together ($p = 1$ for fireballs and $p = 1/3$ for the reconnection model), and r_0 is a suitable length scale. For the fireball model r_0 is the initial radius where the fireball in injected, which is a free parameter of the model. In the reconnection model $r_0 \equiv \pi c/(3\epsilon\Omega\sigma_0^{3/2})$ is a length scale defined by the specific combination of the parameters – it has no deeper physical meaning but merely serves in rewriting the expression (5.32) in a more compact form.

Using the unifying notation (5.37) for the bulk Lorentz factor of the protons and the neutrons, we express the np decoupling radius and the Lorentz factor at decoupling as:

$$r_{\rm np} = \left(\frac{\bar{\sigma} L r_0^{2p}}{8\pi p m c^3 (1+\xi)\eta}\right)^{\frac{1}{2p+1}} \; ; \tag{5.38}$$

$$\Gamma_{\rm np} = \left(\frac{\bar{\sigma} L}{8\pi r_0 p m c^3 (1+\xi)\eta}\right)^{\frac{p}{2p+1}} , \tag{5.39}$$

which combines eqs. (5.25), (5.26), (5.34) and (5.35).

5.3.1 The pion production radius

For sufficiently low baryon loading in the flow, pion creation in inelastic np collisions is possible after np decoupling and the subsequent acceleration of the protons with respect to the neutrons. We define the pion creation radius r_π as the minimum radius where the relative velocity between decoupled neutrons and protons is large enough to create pions through inelastic np collisions.

The production of a secondary particle with mass μ requires center-of-mass energy $\sqrt{s} > 2mc^2 + \mu c^2$. Assuming that $\Gamma_{\rm p}(r) \gg 1$ and $\Gamma_{\rm n}(r) \gg 1$ at radii $r > r_{np}$, and taking the np collision angle equal to zero (tail-on collisions), we express the center-of-mass energy $\sqrt{s}$ as

$$\sqrt{s} = mc^2 \left(\chi^{1/2} + \chi^{-1/2}\right) , \tag{5.40}$$

where we introduce the useful quantity

$$\chi(r) \equiv \frac{\Gamma_{\rm p}(r)}{\Gamma_{\rm n}(r)} . \tag{5.41}$$

From eq. (5.40), we find that pions (which are the lightest mesons) can only be created if $\chi(r) > \chi_\pi$, where $\chi_{\pi^0} = 2.13$ corresponds to neutral pion production and $\chi_{\pi^\pm} = 2.16$ to

charged pion production. We will use the average value $\chi_\pi = 2.15$ in this work. Using the approximate proton and neutron Lorentz factors expressed in eqs. (5.37), we find that

$$r_\pi \simeq \chi_\pi^{1/p} r_{np}\,, \tag{5.42}$$

where the decoupling radius $r_{\rm np}$ is given in eq. (5.38). The radius from which pions can be created is thus substantially larger than the decoupling radius. Since the density of the flow and hence the number of np scatterings decrease rather steeply with radius, it is important to discriminate between $r_{\rm np}$ and r_π when considering particle creation in inelastic np scatterings.

Pion creation by np interactions occurs only when the pion creation radius r_π is reached before the flow saturates. For the fireball model, saturation of the bulk Lorentz factor of the flow occurs either when there is no more energy available to further accelerate the baryons or when the flow crosses the photosphere (cf. eq. (5.29)). It can be shown that saturation occurs beyond the pion creation radius only if the baryon loading of the flow is sufficiently small. We express this condition as $\eta > \eta_\pi$, where η_π is the critical value for inelastic np collisions to occur in the flow. Approximating the proton and neutron Lorentz factors with eqs. (5.37), we estimate that

$$\eta_\pi \simeq 5.1 \times 10^2 L_{52}^{1/4} r_{0,7}^{-1/4} \psi(\xi_0)\,, \tag{5.43}$$

where

$$\psi(\xi_0) \equiv 0.85\,(\chi_\pi + \xi_0)^{3/4}(1+\xi_0)^{-1} \tag{5.44}$$

is a slowly-varying function normalized so that $\psi(1) = 1$. In deriving eq. (5.43) we take neutron decoupling into account by using the neutron-free luminosity $\hat{L}$ and mass flux $\hat{\dot{M}}$ as defined in section 5.2.4. The numerical investigation of the fireball dynamics (see section 5.2.4) shows that the proton Lorentz factors are substantially below the $\Gamma_{\rm p} \propto r$ scaling solution around np decoupling. As a result, the proton – neutron relative velocity is smaller and the pion production radius is pushed outward with respect to the analytical estimate (5.42). This effect makes it more difficult to create pions in the flow and requires η to be higher than the estimate (5.43). Using the numerical model discussed in section 5.2 we find that inelastic np collisions in fireballs occur generally when $\eta/\eta_\pi \gtrsim 2$, where η_π is expressed in eq. (5.43). For neutron-rich flows ($\xi_0 \gtrsim 3$), neutron decoupling results in a relatively pure flow so that the protons follow the scaling approximation (5.43) more closely and inelastic np collisions occur already when $\eta/\eta_\pi \gtrsim 1.5$. Nevertheless, these results place quite stringent conditions on the fireball model parameters so that only a small fraction of GRB fireballs is expected to exhibit inelastic np collisions between bulk protons and neutrons.

For the AC model we find that, similar to the fireball case, inelastic np collisions only occur for a sufficiently low baryon loading. We express this as $\sigma_0 > \sigma_{0,\pi}$, where we

use eqs. (5.37) to estimate that

$$\sigma_{0,\pi} \simeq 38 \times L_{52}^{2/15} \, (\epsilon\Omega)_3^{2/15} \left(\frac{2}{1+\xi_0} \right)^{2/15} . \tag{5.45}$$

We find that eq. (5.45) is consistent with the critical value for σ_0 obtained from numerical results on the proton and neutron dynamics (using the numerical model described in section 5.2). This value of $\sigma_{0,\pi}$ corresponds to a critical baryon loading for inelastic np collisions $\eta_\pi = \sigma_{0,\pi}^{3/2} \sim 230$ which is much lower than the critical value required in fireballs. Inelastic np collisions thus take place for a larger range of the parameter space in the reconnection model with respect to the fireball.

The strength of any neutrino and gamma-ray emission that is a result of the decay of the products (mainly pions) of these collisions depends critically on the optical depth to inelastic np scattering. The calculation of this optical depth is the topic of the next section.

5.3.2 Optical depth

The optical depth $\mathrm{d}\tau$ for a neutron with velocity $c\beta_\mathrm{n}$ to scatter inelastically with a population of protons with velocity $c\beta_\mathrm{p}$ and proper density n'_p within $r \ldots r + \mathrm{d}r$ is given by (see, e.g., Landau & Lifshitz 1971)

$$\mathrm{d}\tau = \sigma_\mathrm{inel} \Gamma_\mathrm{p} n'_\mathrm{p} \left(\frac{\beta_\mathrm{p} - \beta_\mathrm{n}}{\beta_\mathrm{n}} \right) \mathrm{d}r \simeq \frac{\sigma_\mathrm{inel} n'_\mathrm{p}}{2\Gamma_\mathrm{n}} \left(\chi - \frac{1}{\chi} \right) \mathrm{d}r \, , \tag{5.46}$$

where we assume in the last approximation that $\Gamma_\mathrm{p} \gg 1$ and $\Gamma_\mathrm{n} \gg 1$ and that the collisions are tail-on.

At low center-of-mass energies the elastic and inelastic np cross sections are energy dependent. We find that for $\chi_\pi \leq \chi \lesssim 10$ (which is the range of interest here) the elastic cross section is well described with $\sigma_\mathrm{el}(\chi) = 0.75\bar{\sigma}/\ln\chi$, where $\bar{\sigma} \equiv 4 \times 10^{-26}$ cm^2. A comparison between this approximation and experimental data on the elastic cross section taken from Yao et al. (2006) is presented in appendix 5.A. In the following, we express the inelastic np cross section as

$$\sigma_\mathrm{inel}(\chi > \chi_\pi) = \bar{\sigma} \left(1 - \frac{0.75}{\ln\chi} \right) . \tag{5.47}$$

We note here that the energy dependence of the np inelastic cross section has an important effect on the optical depth. If one assumes a constant inelastic cross section $\sigma_\mathrm{inel} = 3 \times 10^{-26}$ cm^2 (as is often done in the literature) the optical depths are larger by a factor $\sim$4 for both the fireball model and the reconnection model. Hence, the more realistic cross section adopted in this work leads to substantially lower estimates for the number of created particles.

We consider, in general, the situation that neutrons coast with a constant Lorentz factor Γ_n while protons are accelerated up to infinity with a Lorentz factor $\Gamma_p \propto r^p$. Keeping p as a free parameter, we integrate eq. (5.46) through the flow to find that

$$\tau(p) = \int_{\chi_\pi}^{\infty} d\chi \left(1 - \frac{0.75}{\ln\chi}\right)\left(\chi^{-1} - \chi^{-3}\right)\chi^{-1/p}, \tag{5.48}$$

where eq. (5.38) was used to eliminate all parameters but p. We thus find that the optical depth for inelastic np scattering is independent of any model parameters but the dynamical power-law index p. This result is valid for all outflows that are characterized by $\Gamma_p \propto r^p$ and Γ_n = const, provided that $r_s \gg r_\pi$. When $r_s \gtrsim r_\pi$, such as in the fireball model, it represents an upper limit.

For fireballs ($p = 1$) we find from eq. (5.48) that $\tau^{FB} < 0.2$, which is an upper limit because the flow saturates close to the decoupling radius. The situation is complicated by the fact that saturation of the fireball can be due to energy requirements or due to crossing of the photosphere. The numerical results presented in section 5.2.4 indicate that both effects cause the flow to accelerate considerably more slowly than the scaling approximation $\Gamma_p \propto r$ near the pion creation radius r_π. This pushes the pion creation radius outward and decreases the optical depth for inelastic np scattering. We compute the optical depth numerically by a straightforward numerical integration of eq. (5.46) using the values of $\Gamma_p(r)$ and $\Gamma_n(r)$ obtained with the numerical model[2] discussed in section 5.2. We find that for the parameter space $3.5\eta_\pi < \eta < 5000$, $0.01 < L_{52} < 10$, $0.3 < \xi < 10$, and $1 < r_{0,7} < 100$ the optical depth is approximated to within ~25% by

$$\tau^{FB} \simeq 0.11\left(1 - \frac{2\eta_\pi}{\eta}\right). \tag{5.49}$$

In the (rather favorable for frequent inelastic scatterings) case where $\eta = 5000$ and $\xi = 5$, the optical depth is $\tau^{FB} \simeq 0.1$. For lower values of the baryon-loading parameter ($\eta/\eta_\pi < 3.5$) the optical depth is smaller than the value given in eq. (5.49). A representative value for a fireball with η a few times the critical value η_π is $\tau^{FB} \simeq 0.05$.

For the reconnection model the saturation radius r_s is typically much larger than r_π. We can therefore estimate the optical depth τ^{AC} for an inelastic np interaction assuming that the protons are accelerated to infinity. (In principle this overestimates the interaction probability, but the difference is very small because the interaction probability decreases rapidly with r.) Inserting $p = 1/3$ in eq. (5.48), we find that $\tau^{AC} \simeq 8 \times 10^{-3}$. This value is consistent with numerical results for flows with $\xi_0 \sim 1$. For reference values of the parameters $L_{52} = \xi_0 = \sigma_{0,2} = (\epsilon\Omega)_3 = 1$, we find also numerically that $\tau^{AC} = 8 \times 10^{-3}$. For high values of ξ_0 (neutron-rich flows), the extra acceleration of the flow after neutron

[2] In the numerical analysis, we use a more accurate but also more elaborate approximation (see appendix 5.A) for the cross section than the one given in eq. (5.47), which results in lower optical depths. Because dynamical effects, discussed in the text, have a larger influence on the optical depth we use expression (5.47) for simplicity to derive an analytical estimate.

decoupling (discussed in section 5.2.4) increases the optical depth by a factor few. We find that for the parameter space $1.5 < \sigma_0/\sigma_{0,\pi} < 10$, $0.01 < L_{52} < 100$, $0.3 < \xi_0 < 10$, and $0.01 < (\epsilon\Omega)_3 < 10$ the optical depth is approximated to within ∼25% by

$$\tau^{\rm AC} \simeq 0.01\,\xi_0^{1/2}\,. \tag{5.50}$$

In particular, the optical depth increases to $\tau^{\rm AC} \simeq 0.03$ for very neutron-rich flows ($\xi_0 \simeq 10$). For $1 < \sigma_0/\sigma_{0,\pi} < 1.5$ pion creation is marginally possible and the optical depth is smaller than the value obtained by eq. (5.50). For very pure flows ($\sigma_0/\sigma_{0,\pi} \gtrsim 10$) neutrons decouple very early (before power-law acceleration $\Gamma \propto r^p$ is reached), which results in an optical depth smaller by a factor ∼2 than the estimate given in eq. (5.50).

The obtained optical depth for inelastic np collisions is the first step in calculating the fluences of secondary pions and their decay products. The calculation of the fluences and energies of stable decay products requires a model for the average number and average energy of neutrinos and gamma rays created by np interactions. In the following sections we consider in detail the production of pions and the subsequent decay into neutrinos and gamma rays.

5.3.3 Pion production

For the collisions studied in this work, the typical incident energy of the proton measured in the rest frame of the neutron is $p'_{\rm p} \sim 1$ GeV/c. In this regime experimental data on pion creation in np collisions is scarce and there is no unambiguous theoretical framework. The available data (in particular, Prokoshin & Tiapkin 1957, Kleinschmidt et al. 1980, Daum et al. 2002; see also electronic data files available at the PPDS website `http://wwwppds.ihep.su:8001/`) show a rapid rise in the single-pion cross sections just above threshold, and indicate that two-pion exclusive production cross sections are comparable to one-pion exclusive cross sections for incident proton energies (as observed in the neutron rest frame K') $p'_{\rm p} \sim 2$ GeV/c. Furthermore, the ratio of $\pi^0 : \pi^\pm$ depends on energy; the ratio $\pi^- : \pi^+$ is 1 : 1 under the assumption of nuclear isospin symmetry.

Based on the available data for incident proton energies $p'_{\rm p} \sim 1$ GeV/c we model the energy distribution and average number of pions resulting from a np collisions as follows. We estimate the ratio of created pions as $\pi^0 : \pi^+ : \pi^- = 2 : 1 : 1$. Hence the average number of neutrinos[3] and gamma rays resulting from a single inelastic np collision is:

$$\mathcal{N}_\gamma = 1.0\,; \quad \mathcal{N}_{\nu_\mu} = 1.0\,; \quad \mathcal{N}_{\nu_e} = 0.5\,. \tag{5.51}$$

Experimental data indicate that, for incident proton energies $p'_{\rm p} = 1.14$ GeV/c, the distribution of kinetic energy $T \equiv E - m_\pi c^2$ for π^+ mesons peaks around 0.6 $T_{\rm max}$, where

[3]Here and in the following ν_μ denotes both muon-neutrinos and -antineutrinos (and similar for electron-neutrinos).

$T_{\rm max}$ is the maximum kinetic energy that can be carried by the pion (Kleinschmidt et al. 1980). For π^0 mesons in the center-of-mass (COM) frame this ratio is almost unity below $p'_{\rm p} < 1.06$ GeV/c and decreases to $T_{\rm peak} = 0.5\,T_{\rm max}$ at $p'_{\rm p} = 1.29$ GeV/c (Prokoshin & Tiapkin 1957). Here we assume a constant fraction of 0.6 for all pion species and take the average pion energy for a single np collision in the COM frame K'' equal to the peak energy:

$$\langle \epsilon''_\pi \rangle = \epsilon''_{\pi,\rm peak} = 0.6\epsilon''_{\pi,\rm max} + 0.4 m_\pi c^2\,, \tag{5.52}$$

where the maximum pion energy is equal to

$$\epsilon''_{\pi,\rm max} = \frac{s - 4m^2c^4 + m_\pi^2 c^4}{2\sqrt{s}}\,, \tag{5.53}$$

and eq. (5.40) relates the center-of-mass energy $\sqrt{s}$ to χ. In these equations, the parameter χ provides the only reference to where the collision has occurred in the developing flow.

When the angular distribution of pions in the COM frame is known, one can derive the full particle distribution of the decay products and transform this to the observer frame in order to find the secondary energy as observed on earth. However, there is to our knowledge no accurate parameterization of the angular distribution of secondary pions created in np collisions. In the absence of such a parameterization we estimate the average observed energy of neutrinos by boosting to the observer frame from an intermediate frame in which the secondary particles are assumed to be isotropic.[4]

Pions are created approximately isotropically in the COM frame of the np collision. When neither pions nor their decay products are affected by the flow, as is the case for neutrino production in the fireball model, the distribution of the daughter particles can be taken to be isotropic in the COM frame. In the AC model however, the strong magnetic field deflects the charged pions significantly since the pion gyration period is much shorter than the pion decay time. We assume that in this case the pions will be distributed isotropically in the frame comoving with the proton fluid. (Any randomized component of the magnetic field will further contribute to isotropization in this frame). Furthermore, in both the fireball model and the AC model gamma rays from neutral pion decay will interact with the soft photon field of the flow, resulting in the emission of lower-energy photons. In the following sections these issues are discussed and estimates are presented for typical neutrino and gamma-ray energies.

The decay of a charged pion also yields one ~35 MeV electron or positron. These contribute to the gamma-ray emission which is discussed in section 5.3.5.

[4] We note that, in the literature, there are various choices regarding the frame (e.g. the neutron rest frame or the proton rest frame) in which the energy distribution of gamma rays and neutrinos is computed before applying the final boost to the observer frame. Any intermediate frame leads to the same results in the observer frame provided that the angular structure of the particle distributions is taken into account. If an isotropic distribution is assumed, the choice of intermediate frame is important and depends on the physics.

5.3.4 Observed neutrino energy

In the fireball model pions do not interact significantly with the flow so that neutrinos from charged pion decay can be taken to be distributed isotropically in the COM frame K'' of the np collision. For a given value of χ, the average energy of the produced neutrinos in this frame is then

$$\langle \epsilon_\nu'' \rangle = \frac{\langle \epsilon_\pi'' \rangle \, \epsilon_\nu^0}{m_\pi c^2} \,, \tag{5.54}$$

where $\epsilon_\nu^0 \simeq 35$ MeV denotes the average neutrino energy in the rest frame of the decaying pion. The average observed energy $\langle \epsilon_\nu \rangle$ is obtained by boosting to the observer frame with Lorentz boost factor $\Gamma_{\rm COM} = \sqrt{\Gamma_{\rm p}\Gamma_{\rm n}}$ (appendix 5.B contains a summary of frames and Lorentz factors used in this work):

$$\left\langle \epsilon_\nu^{\rm FB} \right\rangle = \frac{\Gamma_{\rm COM}}{1+z} \frac{\langle \epsilon_\pi'' \rangle \, \epsilon_\nu^0}{m_\pi c^2} \simeq \frac{\Gamma_{\rm np} \chi^{1/2}}{1+z} \frac{\langle \epsilon_\pi'' \rangle \, \epsilon_\nu^0}{m_\pi c^2} \,, \tag{5.55}$$

where z is the redshift of the source. In the last equality, we approximate the proton and neutron dynamics by eqs. (5.37).

For fireballs the flow saturates close to the pion creation radius and the bulk of the collisions occur when χ is equal to the saturation value $\chi_{\rm s}$. For flows with large $\eta \gtrsim 700$, where saturation is reached due to crossing of the photosphere, the terminal Lorentz factor of the flow equals $\Gamma_{\rm p,s} = \hat{\eta}_{\rm rad}$ (see eq. (5.29)). In this case, the critical value $\chi_{\rm s}$ can be estimated using the scaling law expressed in eqs. (5.37):

$$\chi_{\rm s} \simeq 4.0 \times L_{52}^{-1/12} r_{0,7}^{-1/12} \eta_3^{1/3} \left(\frac{1+\xi}{2} \right)^{1/3} \,. \tag{5.56}$$

For lower values of η, the saturation value $\chi_{\rm s}$ is smaller and reduces to the threshold values $\chi_{\rm s} = \chi_\pi \equiv 2.15$ when $\eta = \eta_\pi$. Adopting the value $\chi = \chi_{\rm s} \simeq 4$ we find from eqs. (5.37), (5.52) and (5.55) that the neutrino energy in the observer frame can be expressed as

$$\langle \epsilon_\nu \rangle = \frac{\alpha \, \Gamma_{\rm np} \epsilon_\nu^0}{1+z} \,, \tag{5.57}$$

where $\alpha^{\rm FB} \simeq 4.5$ accounts for the non-zero kinetic energy of pions when they are created and for the fact that the particle distribution is not isotropic in the neutron rest frame. Using the same parameter range as in section 5.3.2 we find from a numerical analysis that $\alpha^{\rm FB}$ should be slightly higher than this estimate and we will adopt $\alpha^{\rm FB} \simeq 6$ in the following.

In the AC model the situation is more complex because charged pions interact with the flow before decay and because pions are created at various radii in the flow. Since the pion gyration time is much shorter than both the synchrotron cooling time and their lifetime, pions will isotropize in the frame K' comoving with the proton fluid without significant energy loss. In this frame, the secondary pions are injected with energy

$\langle \epsilon'_\pi \rangle = \Gamma''_{\rm p} \langle \epsilon''_\pi \rangle$, where $\Gamma''_{\rm p} = \sqrt{s}/(2mc^2)$ is the Lorentz factor of the incident proton as observed in the COM frame. The observed neutrino energy is then given by the following expression:

$$\left\langle \epsilon_\nu^{\rm AC} \right\rangle = \frac{\Gamma_{\rm p}\Gamma''_{\rm p}}{1+z} \frac{\langle \epsilon''_\pi \rangle \, \epsilon^0_\nu}{m_\pi c^2} \simeq \frac{\Gamma_{\rm np} \left(\chi^{1/2} + \chi^{3/2} \right)}{2(1+z)} \frac{\langle \epsilon''_\pi \rangle \, \epsilon^0_\nu}{m_\pi c^2} \, , \tag{5.58}$$

where we approximate the proton and neutron dynamics by eqs. (5.37) in the last equality. Note that the interaction with the flow results in a substantial increase in the observed energy of the secondary particles.

For flows described by the AC model *np* collisions occur at various radii with different collision energies and different values for the Lorentz boost factor Γ. Therefore, we should average the observed energy given in eq. (5.58) over the developing outflow. We express the probability for an interaction to occur while χ is in the range $\chi \ldots \chi + {\rm d}\chi$ as $\tau(\chi){\rm d}\chi$. Since the scaling approximations (5.37) describe the flow around decoupling quite well in the AC model, we use equation (5.48) to estimate that

$$\tau(\chi) \equiv \frac{{\rm d}\tau}{{\rm d}\chi} = \left(1 - \frac{0.75}{\ln \chi} \right) \left(\chi^{-4} - \chi^{-6} \right) . \tag{5.59}$$

Averaging eq. (5.58) over this distribution we find that the observed neutrino energy can be expressed as in eq. (5.57) with $\alpha^{\rm AC} \simeq 20$. This is in good agreement with numerical results in the same parameter range as in section 5.3.2.

5.3.5 Reprocessing of gamma rays: pair cascades versus synchrotron cooling

While the flow is optically thin with respect to the emitted neutrinos resulting from charged pion decay, this is not the case for the gamma-ray photons that are produced by neutral pion decay. In the proton rest frame, the gamma rays are injected with average energy (for a given value of χ)

$$\langle \epsilon'_\gamma \rangle = \frac{\Gamma''_{\rm p} \langle \epsilon''_\pi \rangle \, \epsilon^0_\gamma}{m_\pi c^2} \, , \tag{5.60}$$

where $\epsilon^0_\gamma = 70$ MeV. Integrating over the developing flow as in the previous section, we express $\langle \epsilon'_\gamma \rangle \simeq \beta \epsilon^0_\gamma$ and estimate analytically that $\beta \simeq 3$ for both the fireball and the AC model. This is consistent with numerical results. Hence gamma rays have a typical energy $\simeq 70\beta \sim 200$ MeV in the proton rest frame and are ejected at radii $r \gtrsim r_\pi$; not far from the Thomson photosphere of the flow.

At these radii both fireballs and reconnection flows carry a soft photon field with characteristic comoving energy in the ~1 keV range (see Derishev et al. 1999b and Giannios 2006 for the fireball and reconnection model, respectively). Because of this intense soft photon field the flow is very optically thick with respect to these ~200 MeV photons,

which are scattered and create pairs. In addition to the pairs that come from neutral pion decay, one energetic electron (or positron) is injected in the flow for every charged pion decay. We have included this contribution in the calculations that follow.

In the fireball model the dominant cooling mechanism of the electron-positron pair is inverse Compton scattering. The upscattered soft photons create more pairs resulting in pair cascades. In the reconnection model the flow is dominated by Poynting flux and the energy density of the magnetic field is much higher than the radiation energy density (see also eq. (10) in Giannios 2006). As a result, the first generation of produced pairs cool down mainly through synchrotron emission. We discuss the outcome of the gamma ray injection separately for the two models.

Pair cascades in fireball

Photons in the fireball are upscattered by pairs and absorbed by soft photons during the pair cascade. In the case of a saturated cascade, where all upscattered photons are absorbed, about ∼10% of the energy of the gamma rays can be converted into rest mass of the pairs (Svensson 1987). More realistically the cascade is expected to be unsaturated, converting a few times less energy into rest mass of pairs (Derishev et al. 1999b, Belyanin et al. 2003).

The result of these pair cascades is twofold. Each injected gamma-ray photon is reprocessed to multiple softer photons and the flow is loaded with pairs that contribute to its opacity. Although the saturation point of the cascade depends on the shape of the soft photon spectrum, we roughly estimate that photons with energies $\epsilon' \sim 3$ MeV in the proton rest frame are able to escape (Belyanin et al. 2003). The overall emitted spectrum will be broad and most energy is emitted with observer energies in the range $\epsilon \sim \Gamma_{\rm p,s}(\epsilon'...10\epsilon')/(1+z) \sim (2...20)/(1+z)$ GeV. The strength of this component and its detection prospects are discussed in the next section.

To estimate the importance of pair loading in the flow, one should compare the number of produced pairs with the number of electrons (or, equivalently, protons) pre-existing in the flow. The flow has ξ_0 neutrons per proton out of which a fraction τ scatters inelastically. This results in $\xi_0\tau$ inelastic scatterings per proton. Every scattering results on average in ∼1 gamma-ray photon (see eq. (5.51)) with a typical energy 70β MeV in the proton rest frame. A fraction $f \sim 3\%$ of this energy is used in rest mass of pairs which results in $\sim 70\beta f$ pairs per gamma ray.

By setting $\xi_0 = 1$ and using the values of β and τ relevant for the reference values of the parameters for a fireball (see section 5.3.2 and the beginning of this section), one finds that the pair cascades result in ∼0.15 pairs per proton. For the neutron-dominated case where $\xi_0 = 5$ we find significantly more pair loading, viz. ∼2 pairs per proton. Note that we find significantly less pair loading of the flow because of pion decay compared to previous works. The main source for this discrepancy comes from the fact that, as we have shown in section 5.3.2, the optical depth for inelastic np scattering is about one

order of magnitude smaller than the value ∼1 that is typically assumed in these studies.

Most of these pairs are produced at large radii – and low densities – so that they do not annihilate but stay in the flow. For $\xi_0 \lesssim 1$, the contribution to the opacity from pair loading is at most moderate. On the other hand, for $\xi_0 \gg 1$ the number of produced pairs exceeds that of the pre-existing electrons. A fraction of those are produced below the Thomson photosphere and its location is pushed to larger radii. This can have some backreaction on the dynamics of fireballs that can be accelerated to slightly higher bulk Lorentz factors than those calculated in section 5.2.4, where this effect is neglected.

Synchrotron cooling in the magnetized flow

We now turn our attention to the reconnection model. The typical energy of the electron-positron pair produced by scattering of a gamma ray (resulting from neutral pion decay) with a soft photon is ∼120 MeV which corresponds to a random electron Lorentz factor $\gamma_e \simeq 200 - 300$. The produced pair finds itself in a strongly magnetized flow with comoving $B' \simeq \sqrt{L/(cr^2\Gamma_p^2)} \sim 10^6$ G for typical values of the parameters and for the radii where most of the pion creation takes place.

Under these conditions, the synchrotron cooling timescale of the pair $t'_s \sim 10^{-6}$ sec is much shorter than the Compton cooling timescale. The lack of pair cascades leads to negligible pair loading of the flow. The peak of the synchrotron emission is located at $\epsilon'_s = e\hbar B'\gamma_e^2/(m_e c)$ ∼0.2...2 keV in the proton rest frame. At the radii where most of the pion production takes place, the bulk proton Lorentz factor is $\Gamma_p \sim 400 - 500$ which results in observer synchrotron peak in the sub-MeV energy range. Keeping the rest of the parameters fixed to their reference values, we find that the synchrotron emission peaks at observer energy $\epsilon_s \simeq 120$ keV for $\xi_0 = 1$ and at $\epsilon_s \simeq 600$ keV for $\xi_0 = 5$. The spectrum is characteristic of fast (synchrotron) cooling particles with an exponential cutoff above the peak and a low-energy spectral slope of $-1/2$. The strength of this component and its detection prospects are given in the next section.

5.4 Detection prospects

Using the results obtained in the previous section on the number and energy of secondary neutrinos and gamma rays created in inelastic np interactions, we discuss the detection prospects here.

5.4.1 Neutrinos

We express the neutrino fluence as observed on earth as

$$\Phi_\nu = \frac{N_n \mathcal{N}_\nu \mathcal{P}_{np}}{4\pi D_p^2}\,, \tag{5.61}$$

where $\mathcal{N}_\nu$ is the average number of neutrinos created per inelastic np interaction (we add the contribution of muon- and electron-(anti)neutrinos given in eq. (5.51) here), $\mathcal{P}_{\rm np}$ is the inelastic np interaction probability, D_p is the proper distance, and

$$N_{\rm n} = \frac{\xi_0}{1+\xi_0}\frac{E}{\eta mc^2} = 3.3\times 10^{52}\left(\frac{2\xi_0}{1+\xi_0}\right)E_{53}\eta_3^{-1} \tag{5.62}$$

denotes the number of neutrons contained in the outflow. In the last equation, E denotes the total isotropic equivalent energy of the burst. Since $\mathcal{P}_{\rm np} \ll 1$ we express $\mathcal{P}_{\rm np} \simeq \tau$, where τ denotes the optical depth for inelastic np collisions.

We consider the optimistic case of a nearby energetic burst at redshift $z = 0.1$. Assuming a universe that consists of matter and a cosmological constant, the proper distance D_p is given by the following expression:

$$D_p = \frac{c}{H_0}\int_0^z \frac{dz'}{\sqrt{\Omega_{\Lambda,0}+\Omega_{m,0}(1+z')^3}}\,, \tag{5.63}$$

where $\Omega_{\Lambda,0}$ and $\Omega_{m,0}$ denotes the current density parameters of the cosmological constant and matter, respectively, and H_0 is the Hubble parameter. Using the currently favored values $\Omega_{\Lambda,0} = 0.76$, $\Omega_{m,0} = 0.24$, and $H_0 = 73$ km s^{-1} Mpc^{-1} (Yao et al. 2006) we find a proper distance $D_p = 1.2\times 10^{27}$ cm. Inserting this in eq. (5.61) we find the following neutrino particle fluences for the two models:

$$\Phi_\nu^{\rm FB} \simeq 10^{-4}\left(\frac{\tau}{0.05}\right)\left(\frac{2\xi_0}{1+\xi_0}\right)E_{53}\eta_3^{-1}\ {\rm cm}^{-2}\,; \tag{5.64}$$

$$\Phi_\nu^{\rm AC} \simeq 2\times 10^{-5}\left(\frac{\tau}{0.01}\right)\left(\frac{2\xi_0}{1+\xi_0}\right)E_{53}\sigma_{0,2}^{-3/2}\ {\rm cm}^{-2}\,. \tag{5.65}$$

As discussed in section 5.3.2, a typical value for the inelastic np optical depth in the fireball model is $\tau^{\rm FB} = 0.05$ and for the reconnection model $\tau^{\rm AC} = 0.01$. The dependence on the model parameters, as obtained from a numerical analysis, is expressed in eqs. (5.49) and (5.50).

From eq. (5.57), the average neutrino energy as observed on earth is equal to

$$\langle\epsilon_\nu\rangle = \frac{\alpha\,\Gamma_{\rm np}\epsilon_\nu^0}{1+z}\,, \tag{5.66}$$

where α is a numerical factor that accounts for the non-zero kinetic energy of pions when they are created and for the fact that the particle distribution is not isotropic in the neutron rest frame while we boost with $\Gamma_{\rm np}$ to the observer frame. Based on the results found in section 5.3.4, we take $\alpha^{\rm FB} = 6$ and $\alpha^{\rm AC} = 20$ for the fireball model and the AC model, respectively. Using eqs. (5.26) and (5.35) for the Lorentz factors at decoupling we find that $\langle\epsilon_\nu^{\rm FB}\rangle \simeq 50$ GeV and $\langle\epsilon_\nu^{\rm AC}\rangle \simeq 70$ GeV for reference values of the parameters and a

burst at redshift $z = 0.1$. These values depend only mildly on the parameters through the Lorentz factor at decoupling $\Gamma_{\rm np}$ but the value of α may change by a factor $\sim$2 depending on the burst parameters.

Following Bahcall & Mészáros (2000) we estimate the number of interactions R_ν in a large-volume neutrino detector due to the diffuse background as $R_\nu = \Phi_\nu \mathcal{R}_b \sigma_\nu N_t$, where $\mathcal{R}_b = 10^3 \mathcal{R}_{b,3}$ denotes the burst rate per year, $\sigma_\nu = 5 \times 10^{-39} \, (\epsilon_\nu / 1\,\mathrm{GeV})\ \mathrm{cm}^2$ is the neutrino interaction cross section and $N_t = 10^{39} N_{t,39}$ is the number of target protons in the detector. For reference values of the parameters and an average redshift $z = 1$ we find that $R_\nu^{\rm FB} \simeq 0.3\ \mathrm{year}^{-1}$ and $R_\nu^{\rm AC} \simeq 0.07\ \mathrm{year}^{-1}$ for the fireball model and the AC model, respectively. Note that, for comparison with the literature, this estimate relies on the rather optimistic reference value of 1000 bursts per year leading to neutrinos through inelastic np collisions.

The predicted diffuse neutrino detection rate for the fireball model is a factor $\sim$5 smaller than the results found by Bahcall & Mészáros (2000). This is primarily due to the more accurate cross sections used in this work and the distinction between np decoupling radius and pion creation radius. This distinction also implies that the condition for inelastic np collisions to occur (as expressed in eq. (5.43)) is more stringent than the condition presented by Bahcall & Mészáros (2000). Therefore, the fraction of GRBs for which np decoupling occurs is expected to be much smaller and the reference value $\mathcal{R}_b = 10^3$ is not very realistic. For the reconnection model, we find that the expected neutrino fluence is typically lower than those for the fireball model by a factor $\sim$5. This results from the fact that the pion production radius is much larger than the np decoupling radius, which is a very robust feature of this model. The condition for inelastic np collisions as expressed in eq. (5.45), on the other hand, is fulfilled in a large range of the parameters of the model. It is therefore expected that np decoupling occurs in a large fraction of GRBs for the reconnection model.

5.4.2 Gamma rays

Secondary gamma rays resulting from np collisions are reprocessed by the flow due to interactions with the soft photon field (see section 5.3.5). This results in pair cascades for fireballs and in electron synchrotron emission for AC outflows. The total energy (in the frame of the progenitor) that is injected in the flow in the form of gamma rays is equal to

$$E_\gamma = \frac{\Gamma_{\rm p} \Gamma''_{\rm p} N_{\rm n} \tau \langle \epsilon''_\pi \rangle \epsilon^0_\gamma}{m_\pi c^2} = \gamma \Gamma_{\rm np} N_{\rm n} \epsilon^0_\gamma \,, \tag{5.67}$$

which defines the factor γ. We find that $\gamma \simeq 0.5$ for both the fireball model (for $\eta \sim$ few η_π) and the AC model (for $\sigma_0 \sim$ few $\sigma_{0,\pi}$). For reference values of the parameters this implies that the fraction of the burst energy that is converted to gamma rays is roughly 5×10^{-3} for fireballs and roughly 2×10^{-3} for the AC model. We assume that the bulk

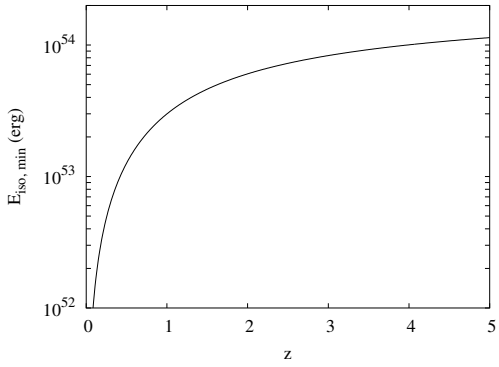

Figure 5.5: Minimum value for the total isotropic burst energy $E_{\rm iso}$ for which the reprocessed gamma-ray emission (in the fireball model) is above the GLAST threshold, as a function of redshift. In this figure we have taken $\xi_0 = r_{0,7} = \eta_3 = 1$, and we have taken the burst duration equal to 10 s.

of the energy given in eq. (5.67) leaves the source after reprocessing, albeit in photons of lower energies.

In section 5.3.5 we estimated that the gamma-ray emission from pair cascades in the fireball model is in the range 2 – 20 GeV in the frame of the progenitor. From this we estimate the gamma-ray number fluence Φ_γ from a source at proper distance D_p as

$$\Phi_\gamma = \frac{E_\gamma}{4\pi D_p^2 \epsilon_\gamma^{\rm casc}} \,, \tag{5.68}$$

where $\epsilon_\gamma^{\rm casc} \simeq 10$ GeV is the average gamma-ray energy emitted by the pair cascades. For an energetic burst at $z = 0.1$ the number fluence is $\Phi_\gamma \simeq 10^{-3}$ cm^{-2} which can be detected with the upcoming GLAST satellite that has an effective area $\sim 10^4$ cm^2 at these energies (Gehrels & Michelson 1999). In fact, we find that this emission is detectable for a fairly large range of parameters. In figure 5.5 we indicate, as a function of redshift, the minimum total isotropic burst energy for which the gamma-ray emission by this mechanism is detectable with GLAST. In producing this figure we have chosen reference values for the relevant model parameters and assumed a burst duration of 10 s.

The isotropic equivalent energy carried by the prompt emission at ∼MeV energies of a typical GRB is in the range $10^{52} - 10^{54}$ erg. This is only a lower limit for the isotropic equivalent energy of the ultrarelativistic flow which may well be a factor ∼10 larger than the energy carried by the prompt emission, depending on the unknown efficiency of the mechanism that generates the prompt emission. Therefore the minimum energy shown in figure 5.5 is not very restrictive and we expect that this emission is detectable for a fairly large fraction of GRBs in which protons and neutrons decouple. This conclusion also holds for high redshifts where the volume for GRBs to occur is largest.

Apart from the collisions between bulk protons and neutrons considered in this work, pions can also be created by nuclear collisions as a result of internal shocks in the sub-photospheric region of the flow (Mészáros & Rees 2000). This mechanism can inject gamma rays in the flow in a different region of the GRB parameter space.

In the AC model the energy is radiated as synchrotron emission with energy of a few hundred keV in the observer frame (see section 5.3.5). The corresponding energy fluence $\sim 10^{-5}$ erg cm^{-2} is lower than the expected prompt emission for a burst at $z = 0.1$ with the reference values adopted here and for a typical prompt emission radiative efficiency $\gtrsim 0.1$. This makes it very hard to disentangle this gamma-ray signal from the prompt emission. Of course this conclusion holds as long as the energy of the reprocessed gamma rays is much less than the energy of the prompt emission and the radiative efficiency for the prompt emission is larger than the energy fraction $\sim 2 \times 10^{-3}$ transferred to gamma rays by np collisions in the AC model. On the other hand, even though this synchrotron component is in general weak, it may have a substantial contribution to the prompt X-ray emission since its flux increases with decreasing energy as $f_\nu \sim \nu^{-1/2}$ (i.e., following the characteristic slope of fast-cooling synchrotron emission).

5.5 Conclusions

In this work we have found that gamma-ray emission resulting from inelastic collisions between differentially streaming neutrons and protons and reprocessed by the flow may be a useful diagnostic of the nature of GRB outflows. Provided that the baryon loading of the flow is sufficiently small, a few per mille of the burst energy is reinjected in the flow through np collisions in both the fireball model and in the AC model, which was used in this work as a specific model for GRB flows that are powered by magnetic reconnection. In the fireball model, the injection of these gamma rays in the outflow leads to pair cascades and subsequently to the emission of gamma rays with observer energy in the range of 2 - 20 GeV $/(1 + z)$. In figure 5.5, we show the minimum total isotropic burst energy, as a function of redshift, for which this emission can be detected by GLAST. The constraint on the energy is not very restrictive and hence this gamma-ray emission should be detectable for a fairly large fraction of the GRBs in which np decoupling occurs. In the AC model, synchrotron energy loss prevents pair cascading and the energy is radiated away at much lower observer energies of a few hundred keV. This component is expected to be dominated by the prompt gamma-ray emission.

The neutrino particle fluence from $\pi^\pm$ decay created in inelastic np collisions in the fireball model is found to be an order of magnitude smaller than previous estimates. This is due to the more accurate cross sections for elastic and inelastic np scattering used in this work and the distinction between np decoupling radius and the pion production radius. The neutrino fluence in the AC model is smaller by another factor ~ 5 due to the very gradual acceleration of the flow, which is a very robust feature of the model. The energy of neutrinos from np interactions in GRB outflows as observed on earth is in the

range 50-70 GeV for reference values of the parameters, which is somewhat higher than previous estimates. We find that the observed neutrino energy in the AC model is higher than in the fireball model because the strong magnetic field causes the charged pions to isotropize in the proton rest frame rather than in the collision COM frame. Unfortunately the neutrino emission in both models is so low that it is very difficult to use its properties to constrain the physics of GRB outflows.

In both the fireball model and the AC model we find that inelastic np collisions occur only if the baryon loading is sufficiently low (see section 5.3.1). For the fireball model, this condition is quite restrictive and we expect that inelastic np collisions are only possible for exceptional bursts. On the other hand, inelastic collisions occur for a large range of the parameters in the reconnection model.

The above results rely on a proper understanding of the dynamics of the flow. We have discussed the effect of neutrons on the dynamics of the flow in section 5.2 (some numerical results are presented in Figs. 5.1-5.4). We present a numerical model which includes the acceleration of the protons due to energy conversion in the flow, coupling of neutrons to protons by nuclear scattering (and the dynamical decoupling of neutrons and protons) and neutron decay. To a first approximation the dynamics of protons and neutrons can be described by the analytical model given in eqs. (5.37). This model provides a useful estimate for the np inelastic optical depth (section 5.3.2) and the energies of neutrinos (section 5.3.4) and gamma rays (section 5.3.5). These estimates are generally in good agreement with results obtained from the numerical model described in section 5.2 (some differences are discussed in the main text). The analytical estimates can be extended in a straightforward manner to any flow with $\Gamma_{\rm p} \propto r^p$ and $\Gamma_{\rm n} = \text{const}$.

From an observational point of view, the most promising conclusion of this work is that gamma-ray emission resulting from np interactions may provide a signature of the nature of the flow (section 5.3.5). The difference in energy of the reprocessed gamma-ray emission between the fireball model and the AC model results essentially from the difference in the ratio of magnetic energy density to radiation energy density. Therefore the energy of this emission appears to be a robust probe for the physics of GRB outflows. In this work we have estimated the gamma-ray energy and fluence for reference values of the burst parameters. A more detailed analysis is necessary to study the spectral properties of the emission and compare it with other emission mechanisms over a broad range of parameters.

It was pointed out recently that a substantial neutron component in GRB flows may affect the properties of GRB afterglows (Beloborodov 2003a). This provides a way of constraining the physics of GRB outflows from afterglow observations. The numerical model discussed in this work can be used to study this possibility in more detail. Another interesting question is whether inhomogeneities in the flow can cause significant particle production through np collision in the AC model (for fireballs, this was discussed by Mészáros & Rees (2000)). These issues are left for future work.

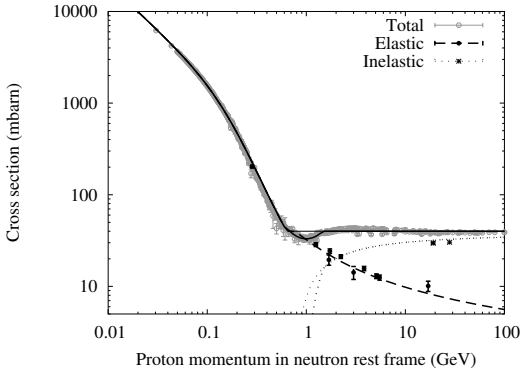

Figure 5.6: Experimental data and approximations of the total, elastic and inelastic *np* cross sections. The thin lines show the approximations used for the analytical model; the thick lines show those used in the numerical computation.

5.A Cross section approximations

In this work we use the following approximations for the total and elastic *np* cross sections:

$$\sigma_{\rm tot} = \max\left[\frac{\bar{\sigma}}{0.19\beta_{\rm rel} + 5.2\beta_{\rm rel}^3}, \bar{\sigma}\right]; \tag{5.69}$$

$$\sigma_{\rm el}(\chi \geq \chi_\pi) = \frac{0.75\bar{\sigma}}{\ln\chi}, \tag{5.70}$$

where $\bar{\sigma} \equiv 4{\times}10^{-26}$ cm^2 and $\chi \equiv \Gamma_{\rm p}/\Gamma_{\rm n}$. At energies below the pion production threshold ($\chi < \chi_\pi$) the elastic cross section $\sigma_{\rm el} = \sigma_{\rm tot}$. Hence the inelastic cross section above the pion production threshold can be approximated with:

$$\sigma_{\rm inel}(\chi \geq \chi_\pi) = \sigma_{\rm tot} - \sigma_{\rm el} = \bar{\sigma}\left(1 - \frac{0.75}{\ln\chi}\right). \tag{5.71}$$

In these equations, $\beta_{\rm rel}$ and χ are related to the incident proton momentum in the neutron rest frame $p'_{\rm p}$ as follows:

$$\beta_{\rm rel} \equiv \frac{p'_{\rm p}}{\sqrt{{p'_{\rm p}}^2 + m^2c^2}}; \tag{5.72}$$

$$\chi \equiv \frac{\Gamma_{\rm p}}{\Gamma_{\rm n}} = \frac{p'_{\rm p}}{mc} + \sqrt{\frac{{p'_{\rm p}}^2}{m^2c^2} + 1}. \tag{5.73}$$

The approximations given in eqs. (5.69), (5.70) and (5.71) are shown in figure 5.6, together with experimental data (Yao et al. 2006) and the approximation that was used to describe the inelastic cross section in the numerical analysis.

5.B Frames and Lorentz factors

The Lorentz factor of protons and neutrons in the observer frame K are denoted with Γ_p and Γ_n, respectively, and we assume that both $\Gamma_\mathrm{p} \gg 1$ and $\Gamma_\mathrm{n} \gg 1$. In the observer frame, the COM frame K'' of the np collision is moving with Lorentz factor

$$\Gamma_\mathrm{COM} = \sqrt{\Gamma_\mathrm{p}\Gamma_\mathrm{n}}\,. \tag{5.74}$$

In the COM frame, protons and neutrons are moving in opposite directions with Lorentz factors

$$\Gamma''_\mathrm{p} = \Gamma''_\mathrm{n} = \frac{\sqrt{s}}{2mc^2} = \frac{1}{2}\left(\frac{\Gamma_\mathrm{p}}{\Gamma_\mathrm{n}}\right)^{1/2} + \frac{1}{2}\left(\frac{\Gamma_\mathrm{n}}{\Gamma_\mathrm{p}}\right)^{1/2}\,, \tag{5.75}$$

where we take the proton and neutron masses equal to m. In the main text we use K' to denote the rest frame of either the proton or the neutron. If K' denotes the proton rest frame, $\Gamma'_\mathrm{p} = 1$ by definition and

$$\Gamma'_\mathrm{n} = \frac{1}{2}\left(\frac{\Gamma_\mathrm{p}}{\Gamma_\mathrm{n}} + \frac{\Gamma_\mathrm{n}}{\Gamma_\mathrm{p}}\right) = 2\,(\Gamma''_\mathrm{n})^2 - 1\,. \tag{5.76}$$

6

Parameterization of the energy and angular distributions of secondary pions and kaons produced in energetic proton – proton collisions

Koers, H. B. J., Pe'er, A., & Wijers, R. A. M. J.
2006, hep-ph/0611219

6.1 Introduction

The possibility of proton acceleration to very high energies in astrophysical sources may provide unique observational opportunities. The interaction of energetic protons with photons or nucleons results in copious production of secondary mesons decaying into high-energy gamma rays and neutrinos that can be observed with current and future detectors. The recently observed TeV gamma-ray emission from supernova remnant RX J1713.7-3946 (Aharonian et al. 2006) has been attributed to this mechanism (Butt et al. 2001), although such an origin is still under debate (Reimer et al. 2002). TeV gamma rays have been reported in coincidence with gamma-ray burst (GRB) 970417a (Atkins et al. 2000; 2003) but also in this case it is not established whether the origin is hadronic (Pe'er & Waxman 2005; Erratum-ibid. 638:1187, 2006).

The existence of astrophysical proton accelerators is indicated by observations of high-energy cosmic rays (CRs). There is evidence for a substantial proton component above the 'knee' at $\sim 4 \times 10^6$ GeV in the cosmic-ray spectrum (see e.g. Bhattacharjee & Sigl (2000) for a review). Observations of extensive air showers due to CRs with energies up to $\sim 10^{11}$ GeV are consistent with nucleon primaries, although other primaries are also possible (e.g., Halzen et al. (1995)).

Various astrophysical systems have been suggested as CR sources. Galactic supernova remnants are the leading candidate for the generation of CRs with energies up to $\sim 10^8$ GeV (e.g., Biermann et al. 1995). Several extragalactic sources have been consid-

ered as possible sources of higher energy CRs, such as active galactic nuclei (Berezinsky et al. 2002; see however Norman et al. 1995), hot spots of Fanaroff-Riley class II radio galaxies (Rachen & Biermann 1993, Norman et al. 1995), pulsars (Venkatesan et al. 1997) and GRBs (Vietri 1995, Waxman 1995).

A population of high-energy protons in these sources would carry a rich phenomenology. In GRBs for example, the interaction of accelerated protons with GRB photons leads to $\sim 10^5$ GeV neutrinos (Waxman & Bahcall 1997) and to $\sim 10^2 - 10^3$ GeV gamma rays (Bottcher & Dermer 1998, Pe'er & Waxman 2005; Erratum-ibid. 638:1187, 2006). High-energy proton interactions may play an important role in the interaction of a developing GRB with its environment, e.g. when the fireball has not yet emerged from the stellar surface (Mészáros & Waxman 2001, Razzaque et al. 2003b) or when energetic GRB protons collide with cold protons in the GRB surroundings (Granot & Guetta 2003, Razzaque et al. 2003a; 2004a).

Detailed parameterizations of the distributions of secondary particles created in proton – proton (pp) collisions are essential in the study of particle production in astrophysical proton accelerators. Parameterizations of the energy spectra were recently presented by Kamae et al. (2006) and by Kelner et al. (2006). However, the parameterizations presented by these authors do not include the angular distributions of the secondary particles. These angular distributions may have an important influence on observational quantities in a non-isotropic environment. Furthermore, in the absence of these distributions, the parameterizations can only be applied to the scattering geometry for which they were derived, viz. with a target proton at rest.

Parameterizations of the complete particle distributions represent an important generalization because they contain all the correlations between the energy and the angle of outgoing particles. Furthermore they provide, through Lorentz transformations, secondary particle distributions and energy spectra for a collision of two protons with arbitrary energies and an arbitrary collision angle. Such a parameterization can therefore be applied to any scattering geometry. This is of particular interest in astrophysical sources where a significant fraction of the protons may be accelerated.

A prime example of an astrophysical system where the energy and angular distributions of secondary particles created in pp collisions are expected to have an important effect on observational signals is provided by choked GRBs, i.e. developing GRBs where the jet is not energetic enough to traverse the pre-burst stellar environment. Mészáros & Waxman (2001) have suggested that protons can be accelerated in internal shocks at substellar radii in these choked bursts. These high-energy protons interact with the developing outflow and with the stellar environment. In particular, collisions of accelerated protons with stellar protons (nuclei) results in secondary neutrinos. The flux and energy spectrum of the corresponding neutrino signal on earth will in general depend on the angle between the developing outflow and the line of sight. The energy and angular distributions of pions created in the pp interactions play an important role in this viewing effect. Therefore a detailed modeling of secondary particle creation in pp interactions

is required to determine the fraction of choked GRBs that may be observable by neutrino detectors and to establish what may be learned about (choked) GRBs from neutrino observations.

Badhwar et al. (1977), Stephens & Badhwar (1981) and Blattnig et al. (2000) have presented parameterizations of the complete distributions of charged and neutral pions and charged kaons created in pp collisions. However, these parameterizations are valid for incident proton energies $E_p \lesssim 2 \times 10^3$ GeV, which is much lower than the highest proton energies $\sim 10^{11}$ GeV expected in accelerating astrophysical sources.

In this chapter we present parameterizations of the complete distributions of secondary particles produced in pp collisions based on Monte Carlo simulations. We consider a proton with energy 10^3 GeV $< E_p < 10^6$ GeV that collides with a proton at rest, which corresponds to center-of-mass energy 43 GeV $< \sqrt{s} < 1.4 \times 10^3$ GeV. Because of the symmetry of this setup the distributions of secondary particle species are invariant under rotations around the collision axis, which implies that they can be fully parameterized with two independent kinematical variables. Here we present parameterizations of the energy and rapidity distributions of secondary pions and kaons. The parameterizations are based on Monte Carlo data in the simulated energy range, but they are suited for extrapolation to higher energies.

The use of a Monte Carlo event generator is necessitated by the present incomplete understanding of pp collisions. Hadron interactions have a complex phenomenology due to the compositeness of the ingoing and outgoing particles, making it impossible to compute the cross section or the resulting particle distribution from first principles. We use the event generator `PYTHIA` (Sjöstrand et al. 2003) to generate Monte Carlo data. `PYTHIA` is tested against experimental data and is widely used in particle physics. It is capable of simulating various incident and target particles so that it is possible to extend this work to proton – neutron and proton – photon interactions with essentially the same code. We stress that the use of a Monte Carlo event generator introduces a model dependence on the results presented here. Nevertheless these results represent an important step in including the current understanding of proton interactions in astrophysical models because they contain the first parameterizations of both the energy and angular distribution of pions and kaons created in energetic pp collisions that is based on a realistic particle physics model.

We consider only secondary pions and kaons and not their stable decay products, viz. electrons, neutrinos and gamma rays. This approach separates the physics in the pp collision from subsequent decay processes. Energy spectra and particle distributions of the resulting stable daughter particles are readily found from our results (either analytically or as part of a computer code) and the well-known decay spectra of pions and kaons (see e.g. Halzen & Martin (1984) and Kelner et al. (2006)). We do not separately consider short-lived mesons (such as η, ρ or ω) because their lifetime is much shorter than that of charged kaons and pions. The decay products of these mesons, mostly pions and gamma rays, are grouped together with the prompt secondaries. The restriction to the pp inter-

action *per se* gives our results a broad applicability. For example, it has been pointed out recently (Kashti & Waxman 2005, Asano & Nagataki 2006) that energy losses of pions and kaons can leave an imprint on the energy spectra of the daughter particles in GRB jets. A proper treatment of this effect requires knowledge of the pion and kaon distributions.

This chapter is organized as follows: in section 6.2, we present experimental data on the pp cross section and the charged multiplicity, i.e. the number of charged particles created in a single inelastic collision. In section 6.3 we discuss the kinematics of the simulated interaction and introduce the particle distribution with respect to energy and rapidity. Details on the event simulation with `PYTHIA` and the fitting procedure are discussed in section 6.4. In section 6.5, we present a comparison between `PYTHIA` results and experimental data and we present the parameterizations of the energy spectra and particle distributions of secondary pions and kaons. Applications of these parameterizations are considered in section 6.6. We demonstrate through explicit examples how the parameterizations can be used to study particle production in collisions of protons with different energies and an arbitrary incident angle. We also present an example in which we derive the gamma-ray energy spectrum resulting from $\pi^0 \to \gamma\gamma$ decay. In section 6.7, we discuss the application of the parameterizations to incident protons with very high energies. We discuss the results in section 6.8. Conclusions are presented in section 6.9.

6.2 Experimental data on the cross section and secondary multiplicity in proton – proton interactions

In this section, we discuss experimental data on the cross section of pp interactions and on the number of charged particles created in a pp interaction. The data presented in this section are used in section 6.5 to validate our numerical method.

6.2.1 Cross section

Proton – proton interactions are usually separated into elastic scattering, in which no particles are created; diffractive interactions, in which the energy transfer between the protons is small; and inelastic non-diffractive interactions (also called 'minimum-bias' events) which contain both hard QCD processes, in which the energy transfer is large enough for the constituent quarks and gluons to interact, and soft minimum-bias events. The total pp cross section σ_{tot} can be expanded in terms of these processes as

$$\sigma_{\mathrm{tot}} = \sigma_{\mathrm{nd}} + \sigma_{\mathrm{sd}} + \sigma_{\mathrm{dd}} + \sigma_{\mathrm{el}}\,, \tag{6.1}$$

where σ_{nd}, σ_{sd}, σ_{dd} and σ_{el} are the cross sections for non-diffractive processes, single diffraction ($AB \to XB$ or $AB \to AX$), double diffraction ($AB \to XY$), and elastic scattering ($AB \to AB$) respectively. We do not explicitly separate diffractive and non-diffractive

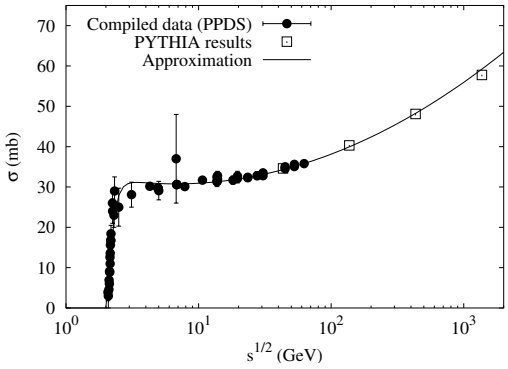

Figure 6.1: Comparison between the inelastic pp cross section calculated with `PYTHIA` (open squares) and experimental data (disks). The solid line represents the fit given in eq. (6.3). Experimental data is taken from the PPDS (see footnote 1).

processes because we are mostly interested in astrophysical applications where it will be impossible to distinguish between these components; see Kamae et al. (2006) for a separate treatment.

We are primarily interested in the inelastic pp cross section $\sigma_{\rm inel} = \sigma_{\rm nd} + \sigma_{\rm sd} + \sigma_{\rm dd}$ because all processes that create secondary particles are contained in this quantity. At energies above the threshold energy $E_{\rm th} = 1.22$ GeV and below $\sqrt{s} = 3 \times 10^4$ GeV, the inelastic cross section for a proton with energy E_p interacting with a target proton at rest can be fitted with (Kelner et al. 2006):

$$\sigma_{\rm inel}^{\rm fit}(E_p) = \left(33.24 - 3.624 \log E_p + 1.325 \left(\log E_p\right)^2\right) \times \left(1 - \left(\frac{E_{\rm th}}{E_p}\right)^4\right)^2 \text{ mb}\,, \tag{6.2}$$

where E_p is measured in GeV. This formula is valid under the assumption that the ratio of the inelastic cross section to the total cross section, which for energies in the range 43 GeV $< \sqrt{s} <$ 63 GeV is given by (Amaldi & Schubert 1980)

$$\sigma_{\rm tot} = 1.21\, \sigma_{\rm inel}\,, \tag{6.3}$$

does not change at higher energies 63 GeV $< \sqrt{s} < 3 \times 10^4$ GeV. The incident proton energy E_p in eq. (6.2) is related to the center-of-mass energy $\sqrt{s}$ as

$$E_p = \frac{s}{2 m_p c^2} - m_p c^2\,, \tag{6.4}$$

where m_p is the proton mass. In figure 6.1, we show the approximation given in eq.

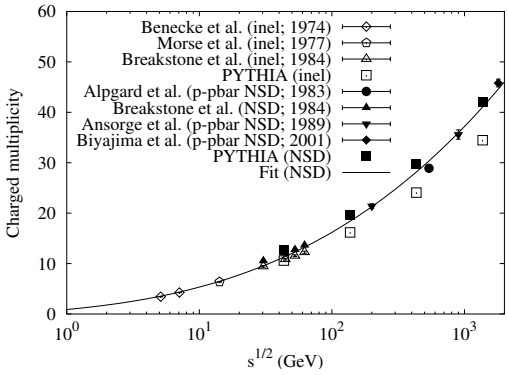

Figure 6.2: Comparison between the charged multiplicity calculated with PYTHIA (squares) and experimental data (other symbols). Open symbols correspond to inelastic processes (inel), solid symbols correspond to non-single-diffractive (NSD) processes. The solid line shows the approximation given in eq. (6.5).

(6.2) together with PYTHIA results (see section 6.5 below) and the available experimental data.[1] This shows the validity of approximation (6.2).

6.2.2 Secondary multiplicity

Bubble chamber and accelerator experiments have shown that the number of charged particles created in proton – (anti)proton collisions, i.e. the charged multiplicity, increases as a function of the incident proton energy.[2] We find that up to the highest energies currently accessible, $\sqrt{s} \leq 1.8\times10^3$ GeV, the charged particle multiplicity in non-diffractive pp interactions is well fitted with

$$\mathcal{M}_{\rm ch}^{\rm fit}(s) = 0.89 + 1.24\log s + 0.34\log^2 s + 0.077\log^3 s\,. \tag{6.5}$$

This functional form is an extension of an approximation due to Matthiae (Matthiae 1983) (see also Collins & Martin (1984)) which is valid only up to $\sqrt{s} \leq 540$ GeV. The last logarithmic term, which does not appear in the approximation by Matthiae, is required in order to fit the multiplicity at both high and low energies. We present in figure 6.2 experimental data[3] together with the approximation given in eq. (6.5) and PYTHIA results (see section 6.5 below).

[1] A compilation of experimental data on the inelastic pp cross section is available at the Particle Physics Data System (PPDS) website `http://wwwppds.ihep.su:8001/`. In producing figure 6.1, we have not considered experimental data that is marked with the warning comment 'W'.

[2] The charged particle multiplicity in pp and $p\bar{p}$ interactions is virtually identical at ISR center-of-mass energies $\sqrt{s} = 53$ GeV (Breakstone et al. (1984b); see also Collins & Martin (1984)).

[3] The experimental data is taken from Ansorge et al. (1989), Alpgard et al. (1983), Benecke et al. (1974), Biyajima et al. (2001), Breakstone et al. (1984a) and Morse et al. (1977). The data at $\sqrt{s} = 1.8\times10^3$ GeV is

A logarithmic dependence $\mathcal{M}_{\rm ch} \propto \log s$ is commonly interpreted as due to an increase in phase space because the range of allowed rapidities scales as $\log(s/m^2c^4)$ (e.g., Collins & Martin (1984)). A stronger increase in secondary multiplicity is then attributed to an additional rise in the level of the observed central rapidity plateau, the origin of which is not understood from first principles.

At high energies, data on the neutral particle multiplicity is scarce because of experimental difficulties. As a result, there is no fit to the neutral particle multiplicity that extends to $\sqrt{s} \gtrsim 50$ GeV which is based on experimental data. A fit to the separate multiplicities of both charged and neutral pions and charged kaons created in pp collisions for center-of-mass energies $\sqrt{s} < 53$ GeV was presented by Antinucci et al. (1973).

The scarcity of experimental data on separate particle multiplicities at high energies motivates the use of event generators such as `PYTHIA`. In section 6.5.1, we show that `PYTHIA` correctly reproduces experimental results on the total charged multiplicity. In section 6.5.2, we present a fit to `PYTHIA` results on charged and neutral pion and kaon multiplicities in the energy range 43 GeV $< \sqrt{s} < 1.4 \times 10^3$ GeV.

6.3 Kinematics and secondary particle distribution

In this and the following sections, we consider an energetic proton that moves along the z-axis and collides with a proton at rest, i.e. a fixed target. This scattering geometry is referred to as the lab frame. We use p_z to denote a longitudinal momentum, along the z-axis, and p_T to denote a transverse momentum.

6.3.1 Kinematics

Assuming that the secondary particle distribution is symmetric around the collision axis, the phase space of the outgoing particles is fully parameterized with two independent kinematical variables. Here, we choose the energy ϵ and the rapidity y, which is defined as

$$y = \frac{1}{2} \ln\left(\frac{\epsilon + p_z c}{\epsilon - p_z c}\right) \quad \Leftrightarrow \quad \tanh y = \frac{p_z c}{\epsilon} \,. \tag{6.6}$$

For given particle energy ϵ, the rapidity cannot take any value. The mass-shell relation implies that $-y_1 < y < y_1$, where

$$y_1 = \operatorname{arccosh}\left(\frac{\epsilon}{mc^2}\right) , \tag{6.7}$$

and m is the secondary (pion or kaon) mass. A second requirement follows from energy conservation in the pp collision. If the energy of the secondary particle $\epsilon > m_p c^2$, the

obtained by the E735 experiment (Lindsey et al. 1992), which does not cover the full particle phase space. We use results from Biyajima et al. (2001), who have determined the charged particle multiplicity through a fit to experimental data on the multiplicity distribution.

rapidity is additionally bounded by $y > y_2$, where

$$y_2 = \operatorname{arctanh}\left(\frac{1}{\beta'_p} - \frac{2m_pc^2}{\beta'_p\epsilon}\right). \tag{6.8}$$

In this equation β'_p is the proton velocity in the center-of-mass frame in units of c, which we take to be equal to one for incident proton energies $E_p \gg m_pc^2$ in the following calculations. Note that eq. (6.7) can be applied in any frame, while eq. (6.8) only holds in the lab frame.

6.3.2 Secondary particle distribution

We are interested in the particle distribution for one-pion and one-kaon inclusive processes,

$$pp \to XY\,, \tag{6.9}$$

where X denotes a single pion or a single kaon and Y may be any combination of particles with the appropriate quantum numbers. We denote by $n(\epsilon, y)d\epsilon dy$ the number of created particles of a given species with energy and rapidity in the range $(\epsilon \ldots \epsilon + d\epsilon) \times (y \ldots y + dy)$:

$$n(\epsilon, y) = \frac{d^2N}{d\epsilon dy} = \frac{1}{\sigma_{\text{inel}}}\frac{d^2\sigma}{d\epsilon dy}\,, \tag{6.10}$$

where $\sigma_{\text{inel}} = \sigma_{\text{nd}} + \sigma_{\text{sd}} + \sigma_{\text{dd}}$ is the inelastic pp cross section and σ is the inclusive cross section to detect a particle of a given kind (assuming an ideal detector). This cross section is equal to the weighted sum of n-particle exclusive cross sections σ_n (i.e., the cross section to create exactly n particles)[4]:

$$\sigma = \sum_n n\sigma_n = \mathcal{M}\sigma_{\text{inel}}\,, \tag{6.11}$$

where $\mathcal{M} = \mathcal{M}(s)$ is the multiplicity of the given particle species. The particle distribution $n(\epsilon, y)$ is related to the Lorentz invariant differential cross section $\epsilon\, d^3\sigma/dp^3$, which is often used to represent experimental data, as follows:

$$n(\epsilon, y) = \frac{2\pi}{c}\left(\frac{m^2 + p_T^2}{\sigma_{\text{inel}}\epsilon}\right)\left(\epsilon\frac{d^3\sigma}{d^2p_T dp_z}\right). \tag{6.12}$$

[4] We do not consider the exclusive cross sections separately because we are interested in particle creation by all processes together. To a first approximation, the relative sizes of the n-particle exclusive cross sections depend on energy only through the total multiplicity (Koba et al. 1972). This 'KNO scaling' is known to be violated at energies $\gtrsim 500$ GeV (Alpgard et al. 1983, Alner et al. 1984).

6.4 Numerical method

6.4.1 Configuration of PYTHIA and initial conditions

The pp interaction is simulated with PYTHIA version 6.324 using default values for most of the control parameters. Elastic and diffractive processes are included by selecting MSEL=2. In comparing PYTHIA results to experimental data on the cross section and charged multiplicity, we allow for pion and kaon decay. In determining the parameterizations of the particle distributions, pion and kaon decay are switched off with the command MDCY(PYCOMP(ID),1)=0, where ID is the corresponding particle identification number. This approach separates the physics in the pp collision from subsequent processes, such as secondary synchrotron emission prior to decay, etc.

The PYTHIA code relies on the Lund string model (Andersson et al. 1983) for the fragmentation process, through which the final-state hadrons are formed. Since this process plays an essential role in the determination of the distribution and multiplicity of secondary particles, we present a brief discussion of the string model in its most elementary form in appendix 6.A. The physics described by PYTHIA is much more sophisticated, including e.g. multiple parton interactions. We note that version 6.3 contains a completely new treatment of multiple parton interactions. Details on this and other models in PYTHIA can be found in the PYTHIA manual (Sjöstrand et al. 2003).

We simulate pp collisions for incident proton energies $E_p = 10^3$ GeV, 10^4 GeV, 10^5 GeV and 10^6 GeV colliding with a proton at rest. For higher values of the incident proton energy, PYTHIA signals a loss of accuracy in kinematical variables in some of the generated events.

6.4.2 Fitting procedure

The secondary particle distributions are discretized, spanning the full range of available energy and kinematically allowed rapidity. In this process, the energy is divided into 200 bins with size $\Delta\epsilon_i$ with a logarithmic division and the rapidity is divided into 100 bins with size Δy_i with a linear division. The logarithmic energy division is chosen because we consider up to seven energy decades; the rapidity division is linear because the range of allowed rapidities scales with the logarithm of energy. The number of bins is limited by computational issues, as data files become increasingly large and fitting becomes increasingly time-consuming with an increasing number of bins. We have verified that this number of bins is sufficient for convergence of the resulting parameterization.

We use MINUIT[5] as a minimization algorithm for the weighted squared difference between the PYTHIA results and the particle distribution fit function $n(\epsilon, y)$.[6] We consider only statistical errors in the PYTHIA results. We simulate $N_{\rm ev} = 10^6$ collisions for

[5] CERN Program Library entry D506; documentation is available on the website http://wwwasdoc.web.cern.ch/wwwasdoc/minuit/

[6] We do not explicitly write the dependence of n on E_p here and in the following sections.

every incident proton energy, which results in a statistical error of a few percent near the maximum values of $\epsilon\, n(\epsilon, y)$. We compare our results with parameterizations based on other event generators to obtain an estimate of the importance of systematic uncertainties within the models underlying PYTHIA in section 6.8.1.

The relative deviation between a PYTHIA data point n_i and the fitted value $n(\epsilon_i, y_i)$ is expressed as

$$\delta_i = \frac{n(\epsilon_i, y_i) - n_i}{n_i}\,, \tag{6.13}$$

where n_i is the number of particles in a bin with average energy ϵ_i and average rapidity y_i divided by the bin size $\Delta\epsilon_i \times \Delta y_i$. We note that the deviations are expected to follow a Gaussian distribution with average value

$$\langle \delta_i \rangle \quad \propto \quad \sqrt{\frac{1}{\epsilon_i n_i}}\,, \tag{6.14}$$

where the dependence on energy is due to the logarithmic energy binning. In particular, the average deviation size is expected to be roughly independent of energy in the case of a $n(\epsilon) \propto \epsilon^{-1}$ energy spectrum.

6.5 Results

6.5.1 Comparison of PYTHIA results with experimental data

We show in figures 6.1 and 6.2 experimental data on the pp cross section and charged multiplicity together with PYTHIA results. In producing these figures, we have not switched off any natural particle decays in the PYTHIA simulations in order to compare PYTHIA results with experimental data (cf. section 6.4.1).

We observe from figure 6.1 that the PYTHIA cross sections are compatible with an extrapolation of the experimental data (see footnote 1 for references) in the energy range $43\ \text{GeV} < \sqrt{s} < 1.4 \times 10^3\ \text{GeV}$. In figure 6.2, we show a comparison between experimental data and PYTHIA results on the charged multiplicity. Here we are interested in particle creation by all inelastic processes. However, experimental data on the charged multiplicity resulting from all inelastic processes is available only up to $\sqrt{s} = 62$ GeV (Benecke et al. 1974, Breakstone et al. 1984a, Morse et al. 1977). Experimental data on the charged multiplicity resulting from the restricted class of non-single-diffractive (NSD) interactions is available up to much higher energies $\sqrt{s} = 1.8 \times 10^3$ GeV (Alner et al. 1986, Ansorge et al. 1989, Biyajima et al. 2001, Breakstone et al. 1984a). To verify our numerical method, we have performed a separate simulation[7] of NSD interactions

[7] For the NSD case, we have switched off single diffraction in the event generation with the commands MSUB(92)=0 and MSUB(93)=0.

	N_p	N_s	γ	π^+	π^-	π^0	K^+	K^-	K^0	$\overline{K^0}$
f	0.56	0.033	0.013	0.13	0.095	0.12	0.016	0.011	0.014	0.011

Table 6.1: Average fraction of the incident proton energy carried by the outgoing particle species.

	π^+	π^-	π^0	K^+	K^-	K^0	$\overline{K^0}$
c_0	4.5	3.8	4.9	0.49	0.32	0.36	0.29
c_1	−1.7	−1.7	−2.1	−0.23	−0.20	−0.17	−0.18
c_2	0.50	0.50	0.58	0.063	0.060	0.054	0.054

Table 6.2: Numerical values for the constants in the multiplicity approximation formula (6.15).

to compare the NSD charged multiplicity with experimental data. We show in figure 6.2 that the PYTHIA results on the charged multiplicity due to both inelastic processes and NSD processes are compatible with experimental data.

6.5.2 Average secondary energy and multiplicity

We find that, within the simulated energy range, the fraction f of the incident proton energy carried by a certain secondary particle species is virtually independent of the incident proton energy.[8] The average fractions for nucleons, photons, pions and kaons are given in table 6.1. In this table, N_p and N_s denote primary and secondary nucleons, respectively (see below). Other possible secondaries (direct electrons, muons, neutrinos) together carry less than 0.1% of the incident proton energy.

We define the primary nucleon as the most energetic outgoing nucleon. The probability that the primary nucleon is a proton is 0.70; if it is a proton, it carries an average fraction 0.63 of the incident proton energy. The probability that the primary nucleon is a neutron is 0.30; if this is the case, the average energy fraction is 0.41. The energy fraction carried by the primary nucleon as shown in table 6.1 represents the weighted average.

We fit PYTHIA results on the secondary particle multiplicities within the energy range $43\ \text{GeV} < \sqrt{s} < 1.4 \times 10^3\ \text{GeV}$. We find that both charged and neutral pion and kaon multiplicities are well approximated with the following function:

$$\mathcal{M}_i = c_0 + c_1 \log s + c_2 \log^2 s\,, \tag{6.15}$$

where c_0, c_1 and c_2 are numerical constants whose values are given in table 6.2 and s is expressed in units of GeV^2. The charged kaon multiplicity deduced from eq. (6.15) is within ∼5% of experimental data at $\sqrt{s} = 45$ GeV (Antinucci et al. 1973). The charged

[8] Feynman scaling (Feynman 1969) relies on these fractions being constant for all proton energies. It is known that Feynman scaling is violated by the observed breakdown of KNO scaling, which is a consequence of Feynman scaling (see footnote 4). Scaling violations are incorporated in PYTHIA; see e.g. the discussion by Kamae et al. (2005).

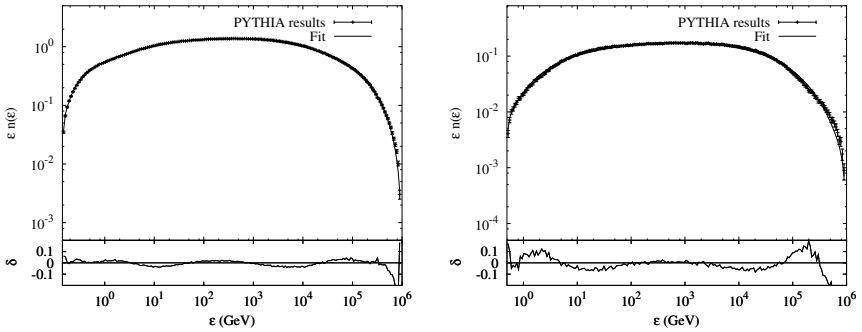

Figure 6.3: Energy spectra of π^+ (left panel) and K^+ (right panel) mesons created in a collision with incident proton energy $E_p = 10^6$ GeV. Note the different scales on the vertical axes. Upper graphs: comparison of `PYTHIA` results and fit to the energy spectrum normalized as $\epsilon\, n(\epsilon)$; lower graphs: deviation $\delta_i = n(\epsilon_i, y_i)/n_i - 1$ between `PYTHIA` results and fitted values.

pion multiplicities determined by this equation are ~10% lower than the experimental values. We have verified that this discrepancy is partly due to the fact that we have considered only prompt pions (i.e., excluding pions from kaon decay). When we include meson decay, the charged pion multiplicities are within 5% of the experimental data.

6.5.3 Pion and kaon energy spectra

We present in figure 6.3 the π^+ and K^+ energy spectra resulting from a collision of a proton with incident energy $E_p = 10^6$ GeV with a proton at rest. We find that the energy spectra for all secondary particles and incident proton energies 10^3 GeV $< E_p < 10^6$ GeV are similar in shape.[9] To a first approximation, the energy spectra follow a ϵ^{-1} power-law, reflecting the absence of an energy scale between the secondary mass and the maximum available energy. This is supplemented with additional functions that we denote with $\alpha(\epsilon)$, $\beta(\epsilon)$, $\gamma_1(\epsilon)$ and $\gamma_2(\epsilon)$ (here and in the following we do not explicitly write the dependence of the model parameters on the incident proton energy E_p to avoid cluttering of the notation). Thus we write the pion and kaon energy spectrum in the following way:

$$n(\epsilon) = n_0 \epsilon^{-1} \alpha(\epsilon)\beta(\epsilon)\gamma_1(\epsilon)\gamma_2(\epsilon)\,, \tag{6.16}$$

where n_0 is a normalization constant, $\alpha(\epsilon)$ accounts for the convex shape on a log-log scale, $\beta(\epsilon)$ incorporates an exponential decline at higher and lower energies, $\gamma_1(\epsilon)$ is a strong cutoff near the mass threshold and $\gamma_2(\epsilon)$ is a strong cutoff near the maximum

[9] Figures of these and others fits are available at `http://www.nikhef.nl/~hkoers/ppfit`.

available energy. These functions are parameterized as follows:

$$n_0 = 1.21 \times 10^{p_0 + p_1 p_2^2}; \tag{6.17a}$$
$$\alpha(\epsilon) = \epsilon^{p_1(\log(\epsilon) - 2p_2)}; \tag{6.17b}$$
$$\beta(\epsilon) = 10^{-(\epsilon/\epsilon_3)^{p30}}\, 10^{-(\epsilon/\epsilon_5)^{p50}}; \tag{6.17c}$$
$$\gamma_1(\epsilon) = \tanh\left(p_{70} \log\left(\epsilon/mc^2\right)\right); \tag{6.17d}$$
$$\gamma_2(\epsilon) = \tanh\left(p_{80} \log\left(E_p/\epsilon\right)\right), \tag{6.17e}$$

where $\epsilon_3 \equiv 10^{p_2+p_4}$, $\epsilon_5 \equiv 10^{p_2+p_6}$ and all energies are expressed in units of GeV. The following parameters vary with incident proton energy:

$$p_0 = p_{00} + p_{01} \log(E_p); \tag{6.18a}$$
$$p_1 = p_{10} + p_{11} \log(E_p); \tag{6.18b}$$
$$p_2 = p_{20} + p_{21} \log(E_p); \tag{6.18c}$$
$$p_4 = p_{40} - p_2; \tag{6.18d}$$
$$p_6 = p_{60} + p_2. \tag{6.18e}$$

Thus, the energy spectrum of secondary pions and kaons is fully described in terms of 12 free parameters p_{ij} for every particle species. These parameters and their numerical values, which are determined by a least-squares fit, are given in table 6.3.

For pions, deviations between fit values $n(\epsilon_i)$ and `PYTHIA` results n_i are less than 5% except for very high energies ($\epsilon \geq E_p/2$) and some occasional points near the mass threshold where the deviation is ~10%. For kaons, statistical fluctuations are larger since the number of kaons to pions is roughly 1:10. At intermediate energies the fit is nevertheless within ~5% of `PYTHIA` results except for some isolated points. Near the mass threshold deviations increase to ~20%; at very high energies, where $\epsilon\, n(\epsilon, y)$ is typically more than an order of magnitude smaller than its maximum value, deviations can increase to ~40%. In this energy range, differences between particle distributions obtained by different Monte Carlo generators are much larger (see section 6.8.1). We have verified that the parameterized spectra integrate to the right multiplicities as given in eq. (6.15) within a few percent, except for the K^0 spectrum for which the deviation is ~10% at the low end of the simulated proton energy range.

6.5.4 Pion and kaon energy and rapidity distributions

We present the pion and kaon rapidity distributions, i.e. $n(\epsilon, y)$ at fixed $\epsilon = \epsilon_0$, for incident proton energy $E_p = 10^6$ GeV and secondary particle energy $\epsilon = 10^3$ GeV in figure 6.4. We find that rapidity distributions for different proton energies and different secondary particle energies are very similar in shape. This shape is different for pions and for kaons, hence we treat pions and kaons separately in the following.

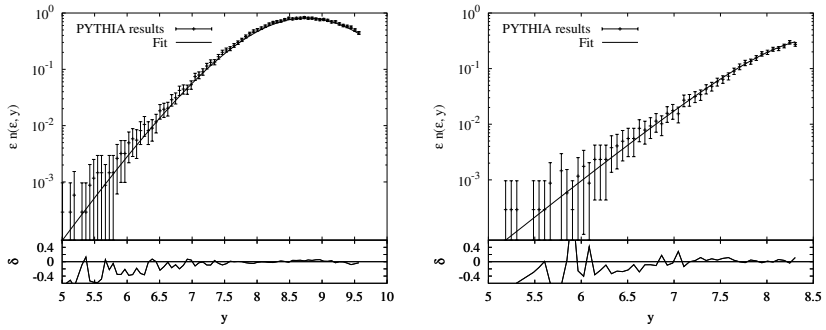

Figure 6.4: Rapidity distributions of π^+ (left panel) and K^+ (right panel) secondaries created in a collision of a proton with energy $E_p = 10^6$ GeV with a proton at rest. The secondary particle energy is taken to be $\epsilon = 10^3$ GeV. Upper graphs: comparison of PYTHIA results and fit to the rapidity distribution $\epsilon\, n(\epsilon, y)$ as a function of y; lower graphs: deviation $\delta_i = n(\epsilon_i, y_i)/n_i - 1$ between PYTHIA results and fitted values.

Pions

The pion rapidity distributions at fixed energy are found to be approximately Gaussian near their maximum values (see fig. 6.4). At intermediate pion energies, $\epsilon \sim \sqrt{E_p}$, the distributions exhibit a low-rapidity tail that falls off exponentially (all energies are expressed in units of GeV). The distributions fall off very steeply at the boundaries of the kinematical domain given in eqs. (6.7) and (6.8).

We factorize the full particle distribution $n(\epsilon, y)$ into a modified energy spectrum $\tilde{n}(\epsilon)$ and a rapidity-dependent function $\phi(\epsilon, y)$ that contains both a Gaussian and an exponential part:

$$n_\pi(\epsilon, y) = \tilde{n}(\epsilon)\phi(\epsilon, y)\,, \tag{6.19}$$

where

$$\tilde{n}(\epsilon) = n_0 \epsilon^{-1} \alpha(\epsilon)\beta(\epsilon)\gamma_2(\epsilon) 10^{q_0+2q_3}\,; \tag{6.20a}$$

$$\phi(\epsilon, y) = 10^{-2\sqrt{q_3 q_1^2 (y-q_2)^2 + q_3^2}}\,, \tag{6.20b}$$

and n_0, $\alpha(\epsilon)$, $\beta(\epsilon)$ and $\gamma_2(\epsilon)$ are defined in eqs. (6.17). Here and in the following we assume that ϵ and y are within the kinematically allowed range (see eqs. (6.7) and (6.8)); outside this range all distributions are identically zero. The parameters q_i depend on the pion energy ϵ and on the incident proton energy E_p in the following way (here and in the following we do not explicitly write the dependence of the parameters q_i on the pion and

proton energies to avoid cluttering of notation):

$$q_0 = q_{00} + q_{01}\xi^2 ; \tag{6.21a}$$

$$q_1 = q_{10} + q_{11}\left(\xi + q_{12}\right)^2 + q_{13}\xi^4 ; \tag{6.21b}$$

$$q_2 = \ln(\epsilon) + q_{20} + q_{21}\left(\log(\epsilon) + 1\right) - 10^{q_{22}\log(E_p)\log\left(\epsilon/E_p\right)} + 10^{q_{23}\log(E_p)\log(m/\epsilon)} ; \tag{6.21c}$$

$$q_3 = q_{30} + 10^{q_{31}+q_{32}\log(\epsilon)} , \tag{6.21d}$$

where we introduced the variable

$$\xi \equiv 2\log(\epsilon)/\log(E_p) - 1 . \tag{6.22}$$

Hence, we have parameterized the pion energy and rapidity distributions in terms of 24 free parameters q_{ij} for every pion species (π^+, π^- and π^0). The fitted values for the coefficients are given in table 6.4.

We realize that the number of free parameters in the parameterization is quite large. However we have not found a parameterization that approximates the PYTHIA results (essentially a three-dimensional dataset) with the same accuracy and fewer parameters. We remark here that the models employed by PYTHIA are based on a large body of experimental results so that the fit parameters are not underconstrained. For example, the parameterization of the total hadronic cross sections used by PYTHIA builds on work by Donnachie & Landshoff (1992) who propose a phenomenological Regge model for these cross sections and support this with experimental data on proton – proton, proton – antiproton, proton – meson and proton – photon interactions. There are also several experimental results on the total charged multiplicity in pp interactions (see section 6.2.2).

Deviations between the parameterizations and PYTHIA results are within 10% in the range in which the rapidity distribution is within one order of magnitude of the maximum value and for pion energies $1\,\mathrm{GeV} < \epsilon < 0.1\,E_p$, except for a few isolated points that are typically within 20%. At high energies, $\epsilon \geq 0.1\,E_p$, deviations increase to ~30% at the borders of the considered rapidity interval, in concordance with eq. (6.14). The magnitude of the deviations is compatible with the statistical errors in the PYTHIA results.

We have verified that integrating the energy and rapidity distributions over rapidity reproduces the energy spectra. The deviations between these spectra and PYTHIA results are similar to the deviations for the direct fit to the energy spectra (see section 6.5.3), except at very low energies $\epsilon \lesssim 2m_\pi$ where deviations increase to ~30%. The multiplicities obtained by integrating the distributions over energy and rapidity are within a few percent of those given by eq. (6.15).

Kaons

The shape of the kaon rapidity distributions is similar to the low-rapidity part of the pion rapidity distributions (see fig. 6.4). We find that the kaon energy and rapidity

distributions are well described with:

$$n_K(\epsilon, y) = \overline{n}(\epsilon)\phi(\epsilon, y)\,, \tag{6.23}$$

where $\phi(\epsilon, y)$ is defined in terms of model parameters q_i in eqs. (6.20) and $\overline{n}(\epsilon)$ is a modified energy spectrum:

$$\overline{n}(\epsilon) = n_0 \epsilon^{-1} \alpha(\epsilon)\beta(\epsilon) 10^{q_0+2q_3}\,. \tag{6.24}$$

The quantities n_0, $\alpha(\epsilon)$ and $\beta(\epsilon)$ are defined in eqs. (6.17). We find that the parameterizations for q_i given in eqs. (6.21) approximate the PYTHIA results well if we fix $q_{23} = 0$. Therefore, the kaon energy and rapidity distributions are fully parameterized in terms of 23 free parameters for every kaon species (K^+, K^-, K^0 and $\overline{K^0}$). The fitted values for these parameters are presented in table 6.4.

Deviations between the approximation (6.23) and PYTHIA results are similar to the deviations for the parameterizations of the pion distributions, except that fluctuations are larger. This results in deviations up to ~30% at isolated points for all energies.

For the K^- and $\overline{K^0}$ mesons, integrating the full distributions over the rapidity reproduces the energy spectra with deviations similar to those for the direct parameterizations of the energy spectra presented in eq. (6.16). For K^+ and K^0 mesons, deviations near the mass threshold are ~30%, while at very high energies ($\epsilon \gtrsim E_p/2$) the deviations can increase to ~50%. These large deviations occur only at energies where $\epsilon\, n(\epsilon, y)$ is more than an order of magnitude smaller than the maximum value. The multiplicities obtained by integrating the parameterized distributions (6.23) over energy and rapidity are within a few percent of the values given by eq. (6.15).

6.6 Applications

In this section, we demonstrate how the parameterizations of the particle distributions presented in eqs. (6.19) and (6.23) can be applied to derive energy spectra and angular distributions of secondary mesons and their decay products. We present examples of the energy spectrum of gamma rays resulting from the decay of π^0 mesons created in pp interactions. We also present examples of the angular distributions of π^0 mesons created in pp collisions. For clarity, we consider only π^0 mesons in this section, but the presented methods are applicable to all pions and kaons. We stress that these examples are only intended to demonstrate how the parameterizations presented in this chapter can be used in a dedicated study. Astrophysical applications of the parameterizations are discussed in section 6.8.2.

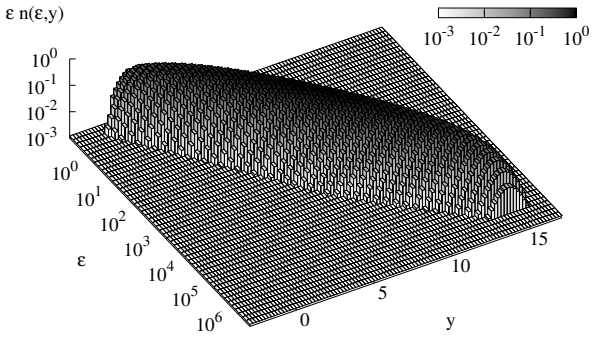

Figure 6.5: The π^0 distribution $\epsilon\, n(\epsilon, y)$ as a function of energy ϵ and rapidity y after a collision of a proton with energy 10^6 GeV with a proton at rest (lab frame). The discretization and the observed 'floor' are for presentational purposes.

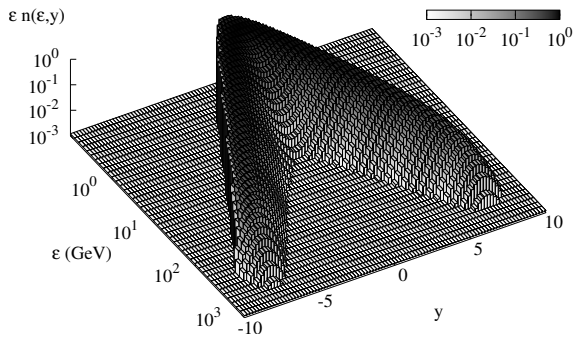

Figure 6.6: The π^0 distribution $\epsilon\, n(\epsilon, y)$ as a function of energy ϵ and rapidity y after a collision of two protons with energy 730 GeV (center-of-mass frame). The discretization and the observed 'floor' are for presentational purposes.

6.6.1 Head-on proton – proton collision

Full secondary particle distribution

First, we consider the energy and rapidity distribution of π^0 mesons created in a collision of an energetic proton p with a fixed-target proton q. This is the scattering geometry for which the parameterizations presented in this chapter are derived. We denote the Lorentz frame corresponding to this scattering geometry with K throughout this section. In figure 6.5, we present the π^0 distribution for incident proton energy $E_p = 10^6$ GeV. We observe that the energy and rapidity of the secondary pions are strongly correlated: pions with higher energies are emitted closer to the direction of the incoming energetic proton (corresponding to higher values of the rapidity y; see eq. (6.6)).

Next, we consider two protons p and q colliding head-on with energies E'_p and E'_q which defines the reference frame K'. Without loss of generality, we take the protons to be moving in the z' direction. The secondary particle distribution in this frame is given by

$$n'(\epsilon', y') = \left(\frac{\epsilon'}{\epsilon}\frac{\cosh^2 y}{\cosh^2 y'}\right) n(\epsilon, y)\,, \tag{6.25}$$

which follows from eq. (6.12) and the invariance of $\epsilon\, n(p_x, p_y, p_z)$ In this equation, $n(\epsilon, y)$ is the particle distribution in the frame K which is parameterized in eq. (6.19). Note that eq. (6.25) is only valid if the frames K and K' are connected with a single Lorentz boost in the z (z') direction, i.e. for protons colliding head-on along the z' axis in the K' frame.

As a concrete example, we consider two protons that collide with equal energies $E'_p = E'_q = 730$ GeV. In this case, K' coincides with the center-of-mass (COM) frame for a collision between a proton with energy $E_p = 10^6$ GeV and a proton at rest. In particular, this means that the center-of-mass energy $\sqrt{s}$ and the secondary multiplicities are identical for the scattering geometries in the frames K and K'.

In figure 6.6, we show the π^0 energy and rapidity distribution after the collision in the COM frame K'. In this frame, the scattering geometry is invariant under the interchange of the two protons so that the secondary particle distribution is symmetric under the transformation $y \to -y$. It is observed from the figure that this is indeed the case for the distribution derived from the parameterization presented in this chapter. This is an *a posteriori* verification of the parameterization, which is derived in the lab frame without considering this symmetry.

Energy spectrum of secondary particles and decay products

In figure 6.7, we show the secondary π^0 energy spectra for the scattering geometries associated with the K and K' frames, together with the gamma-ray energy spectra resulting from the decay $\pi^0 \to \gamma\gamma$. The decay spectrum $n_\gamma(\epsilon_\gamma)$ is related to the pion spectrum $n(\epsilon)$

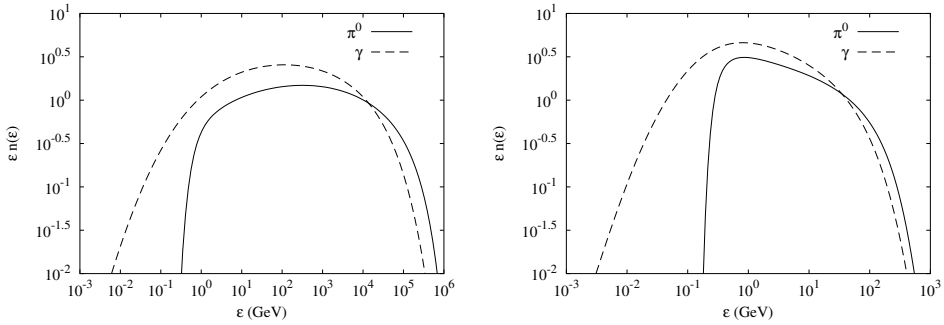

Figure 6.7: Energy spectra of π^0 mesons created in a pp collision and of the resulting gamma rays. Left panel: lab frame, corresponding to a proton with energy $E_p = 10^6$ GeV colliding with a proton at rest; right panel: center-of-mass frame, corresponding to two protons with energy 730 GeV colliding head-on.

as follows (see, e.g., Stecker (1971)):

$$n_\gamma(\epsilon_\gamma) = 2 \int_{\epsilon_\gamma + m_\pi^2 c^4/4\epsilon_\gamma}^{\infty} \frac{n(\epsilon)}{\sqrt{\epsilon^2 - m_\pi^2 c^4}}\, d\epsilon\,, \tag{6.26}$$

where $n(\epsilon)$ is the π^0 energy spectrum. Because this formula is valid in all frames, n and ϵ may be replaced by n' and ϵ' to derive the gamma-ray energy spectrum from the pion energy spectrum in the K' frame.

6.6.2 Proton – proton collision at an arbitrary angle

In this section, we consider two protons with energies E'_p and E'_q that collide at an arbitrary angle. Without loss of generality, we take proton p to be moving along the x' axis in the $+x'$ direction and proton q to be moving in the $x' - y'$ plane at an angle ϕ'_p with respect to the x' axis.

We parameterize the distribution of secondary π^0 mesons created in this interaction with the pion energy ϵ', the zenith angle θ'_π (with respect to the z' axis) and the azimuthal angle ϕ'_π (in the $x' - y'$ plane). The pion momentum is thus expressed as follows:

$$k'_x = |\vec{k}'| \sin\theta'_\pi \cos\phi'_\pi\,; \tag{6.27a}$$

$$k'_y = |\vec{k}'| \sin\theta'_\pi \sin\phi'_\pi\,; \tag{6.27b}$$

$$k'_z = |\vec{k}'| \cos\theta'_\pi\,, \tag{6.27c}$$

where $c|\vec{k}'| = \sqrt{\epsilon'^2 - m_\pi^2 c^4}$. In the following, we derive the secondary π^0 angular distribution in the scattering plane and the π^0 energy spectrum.

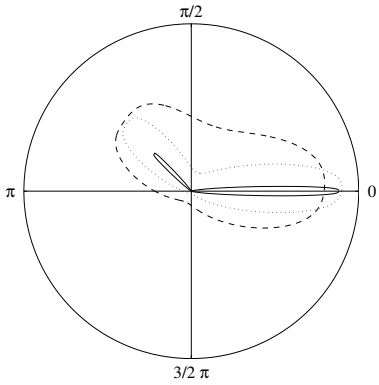

Figure 6.8: Polar plot of the π^0 distribution $n'(\epsilon', \phi'_\pi)$ as a function of the azimuth angle ϕ'_π after a collision of a 10^4 GeV proton with a 10^2 GeV proton at an angle $\phi'_q = (3/4)\pi$. We plotted the distribution for pion energies $\epsilon' = 5$ GeV (solid line), $\epsilon' = 1$ GeV (dotted line) and $\epsilon' = 0.5$ GeV (dashed line).

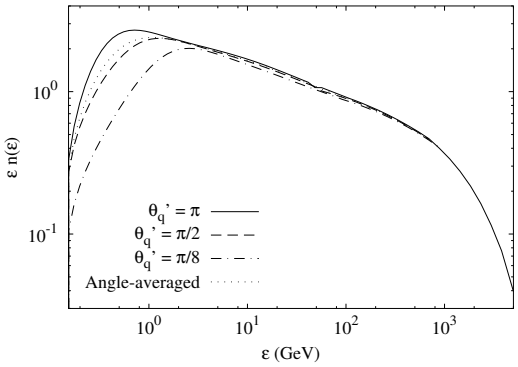

Figure 6.9: Energy spectra of secondary π^0 mesons created in a collision of a 10^4 GeV proton with a 10^2 GeV proton for three different incident angles θ'_q. Also shown is the angle-averaged spectrum (see text). For numerical reasons we only plot the energy spectrum for head-on collisions at energies $\epsilon \gtrsim 10^3$ GeV. We have verified with `PYTHIA` simulations that this part of the spectrum is independent of the incident angle between the protons.

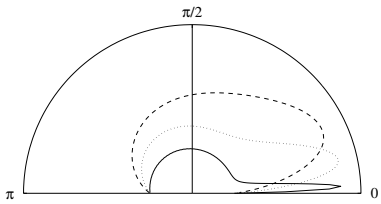

Figure 6.10: Polar plot of the π^0 distribution $n'(\epsilon', \theta'_\pi)$ as a function of the zenith angle θ'_π after a collision of a 10^4 GeV proton with an isotropic distribution of 10^2 GeV protons. The meaning of the lines is the same as in figure 6.8.

Secondary angular distribution in the scattering plane

The pion distribution in the frame K' is derived from the parameterization in the fixed-target frame K by Lorentz transformations. The frames K' and K are connected by a Lorentz boost to the rest-frame of proton p, followed by a rotation to align the incoming proton q with the z axis. The number of secondary pions with energy and angles in the range $(\epsilon' \ldots \epsilon' + d\epsilon') \times (\theta'_\pi \ldots \theta'_\pi + d\theta'_\pi) \times (\phi'_\pi \ldots \phi'_\pi + d\phi'_\pi)$ is equal to $n'(\epsilon', \theta'_\pi, \phi'_\pi) \sin\theta'_\pi d\theta'_\pi d\phi'_\pi d\epsilon'$, where

$$n'(\epsilon', \theta'_\pi, \phi'_\pi) = \left(\frac{\epsilon \sqrt{\epsilon'^2 - m_\pi^2 c^4}}{m_\pi^2 c^4 + \epsilon^2 (1 - \tanh^2 y)} \right) \frac{n(\epsilon, y)}{2\pi} \,. \tag{6.28}$$

In this formula, ϵ and y are the pion energy and rapidity in the K frame, respectively, and $n(\epsilon, y)$ denotes the pion energy and rapidity distribution which is parameterized in eq. (6.19).

In figure 6.8, we present the distribution of secondary π^0 mesons with respect to the azimuthal angle ϕ'_π, i.e.,

$$n'(\epsilon', \phi'_\pi) \equiv \int_0^\pi n'(\epsilon', \theta'_\pi, \phi'_\pi) \sin\theta'_\pi d\theta'_\pi \,, \tag{6.29}$$

for different values of the pion energy ϵ'. In producing this figure, we have chosen incident proton energies $E'_p = 10^4$ GeV and $E'_q = 10^2$ GeV and incident angle $\phi'_q = (3/4)\pi$. As can be seen from the figure, the pions are produced mostly in the direction of the incident protons. The degree of collimation is correlated with the energy: for pion energies ϵ' below a few GeV, where the pion spectrum is highest (see fig. 6.9), the pion direction can be significantly different from the direction of the colliding protons. At energies above a few GeV, the angle of the outgoing pion is typically within a few degrees of the direction of one of the colliding protons. We have verified that this result holds for all secondary pions and kaons.

Secondary energy spectrum

In figure 6.9 we present pion energy spectra (integrated over pion angles) resulting from a collision of two protons with energies $E'_p = 10^4$ GeV and $E'_q = 10^2$ GeV for different values of the proton collision angle ϕ'_q. For comparison, we also show in this figure the pion spectrum averaged over incident proton angles (see below).

While the energy spectrum at high energies is independent of the incident proton angle, there are significant differences at low energies. For small values of the incident proton angle ϕ'_q, i.e. close to a tail-on collision, the low-energy part of the spectrum is suppressed as expected.

6.6.3 Isotropic distribution of target protons

In this section, we consider a single high-energy proton p with energy E'_p that interacts with an isotropic distribution (in three dimensions) of mono-energetic low-energy protons q with energy E'_q. We derive the distribution of secondary pions with respect to the angle between the high-energy proton and the pion, as well as the energy spectrum. For an isotropic distribution of target protons, the resulting pion distribution does not depend on the azimuthal angle around the direction of the high-energy proton. In order to keep the former definition of pion angles (eqs. (6.27)) we consider in this section a high-energy incident proton that moves along the z' axis in the $+z'$ direction. With this choice, the zenith angle between the high-energy proton and the pion is equal to θ'_π.

The momentum of proton q is expressed in terms of angles in the same way as the pion momentum in eqs. (6.27): the angle θ'_q denotes the zenith angle with respect to the z'-axis and ϕ'_q denotes the azimuth angle with respect to the x' axis in the $x' - y'$ plane.

Zenith angle distribution of secondary pions

The secondary pion distribution, averaged over the incoming angles of low-energy protons q, is given by the following expression:

$$\overline{n}'(\epsilon', \theta'_\pi, \phi'_\pi) \equiv \frac{d^3\overline{N}}{d\epsilon' d\cos\theta'_\pi d\phi'_\pi} = \frac{1}{\overline{\sigma}'_{\text{inel}}} \frac{d^3\overline{\sigma}'}{d\epsilon' d\cos\theta'_\pi d\phi'_\pi}\,, \tag{6.30}$$

where N is the total number of created pions, σ'_{inel} is the inelastic pp cross section and σ is the inclusive cross section to detect a particle of a given species assuming an ideal detector (cf. section 6.3.2). In this section, we use a bar to indicate that a quantity is averaged over the incoming angles of low-energy protons q.

For clarity we assume in this section that both protons are very energetic, so that we may take $\beta'_p = \beta'_q = 1$. The averaged inelastic cross section is then equal to

$$\overline{\sigma}'_{\text{inel}} = \frac{1}{2}\int_0^\pi d\theta'_q \sin\theta'_q (1 - \cos\theta'_q)\, \sigma_{\text{inel}}(s(\theta'_q))\,. \tag{6.31}$$

In this equation, $\sigma_{\rm inel}$ depends on the proton angle θ'_q through the center-of-mass energy $\sqrt{s}$, where

$$s(\theta'_q) = 2m_p c^2 + 2E'_p E'_q (1 - \cos\theta'_q)\,. \tag{6.32}$$

The dependence of the inelastic cross section on s is expressed in eqs. (6.2) and (6.4).

For given values of the proton angles θ'_q and ϕ'_q, the differential inclusive cross section and the secondary particle distribution are related as follows:

$$\left.\frac{d^3\sigma'}{d\epsilon' d\cos\theta'_\pi d\phi'_\pi}\right|_{\theta'_q,\phi'_q,} = (1-\cos\theta'_q)\sigma'_{\rm inel}(s(\theta'_q))n'(\epsilon',\theta'_\pi,\phi'_\pi;\theta'_q,\phi'_q)\,, \tag{6.33}$$

where we have explicitly written the dependence of the pion distribution n' on the proton angles θ'_q and ϕ'_q. The total inclusive cross section $\bar{\sigma}'$ is obtained by integrating eq. (6.33) over the outgoing pion angles and averaging over the incident proton angles. The resulting pion distribution is homogeneous in the ϕ'_π variable. We use this rotational invariance to replace the integral over ϕ'_q with a factor 2π and choose the value $\phi'_q = 0$ to find:

$$\begin{aligned}\bar{\sigma}' = \frac{1}{2}\int d\epsilon' d\theta'_\pi d\phi'_\pi \sin\theta'_\pi \int d\theta'_q\ \sin\theta'_q(1-\cos\theta'_q) \\ \times \sigma'_{\rm inel}(s(\theta'_q))\, n'(\epsilon',\theta'_\pi,\phi'_\pi;\theta'_q,\phi'_q=0)\,,\end{aligned} \tag{6.34}$$

where the integrals cover the full phase space. The pion distribution with respect to the pion energy ϵ' and scattering angle θ'_π is defined as:

$$\bar{n}'(\epsilon',\theta'_\pi) = \frac{d^2\bar{N}}{d\epsilon' d\theta'_\pi} = \sin\theta'_\pi \int_0^{2\pi} d\phi'_\pi \frac{d^3\bar{N}}{d\epsilon' d\cos\theta'_\pi d\phi'_\pi}\,. \tag{6.35}$$

Using eqs. (6.30) and (6.34), we find that

$$\begin{aligned}\bar{n}'(\epsilon',\theta'_\pi) = \frac{\sin\theta'_\pi}{2\,\bar{\sigma}'_{\rm inel}} \int_0^\pi d\theta'_q\ \sin\theta'_q(1-\cos\theta'_q)\sigma'_{\rm inel}(s(\theta'_q)) \\ \times \int_0^{2\pi} d\phi'_\pi\, n'(\epsilon',\theta'_\pi,\phi'_\pi;\theta'_q,\phi'_q=0)\,,\end{aligned} \tag{6.36}$$

where $\bar{\sigma}'_{\rm inel}$ is defined in eq. (6.31).

In figure 6.10 we show the distribution $\bar{n}'(\epsilon',\theta'_\pi)$ as a function of θ'_π for three different values of the pion energy ϵ'. In producing this figure, we have considered a collision of an energetic proton with energy $E'_p = 10^4$ GeV with an isotropic distribution of mono-energetic protons with energy $E'_q = 10^2$ GeV. From the figure we observe that pions with higher energy are collimated stronger within the direction of the incoming proton, as expected. We have verified that this holds for all secondary mesons. In the maximally forward direction, i.e., near $\theta'_\pi = 0$, the distribution decreases because the available phase space is proportional to $\sin\theta'_\pi$.

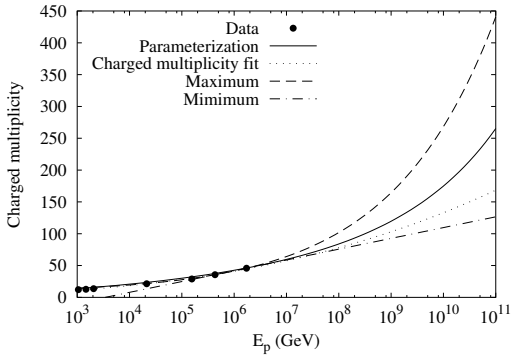

Figure 6.11: Charged multiplicity as a function of incident proton energy. The solid line shows an extrapolation of eq. (6.5); the dotted line shows the multiplicity estimated from the parameterized charged pion distributions presented in this chapter; the dashed and dash-dotted lines show the minimum and maximum multiplicities given in eqs. (6.38). The data is taken from Ansorge et al. (1989), Alpgard et al. (1983), Benecke et al. (1974), Biyajima et al. (2001) and Breakstone et al. (1984a).

Energy spectrum of secondary pions

The secondary π^0 energy spectrum for the interaction of a 10^4 GeV proton with the distribution of 10^2 GeV protons is expressed as

$$\overline{n}'(\epsilon') = \int_0^{\pi} d\theta'_\pi \, \overline{n}'(\epsilon', \theta'_\pi) \,, \tag{6.37}$$

where $\overline{n}'(\epsilon', \theta'_\pi)$ is given in eq. (6.36). We show in figure 6.9 the energy spectrum averaged over the incoming angles of the low-energy protons q. We find that the averaged spectrum is very close to the spectrum resulting from a collision of a 10^4 GeV proton with a 10^2 GeV proton with incident angle $\theta'_q \simeq (5/8)\pi$, i.e. in the forward direction but not head-on. Qualitatively, this is as expected because the cross section $\sigma'_{\text{inel}}(s(\theta'_q))$ and the flux factor $(1 - \cos\theta'_q)$ are largest for head-on collisions while the phase-space volume factor $\sin\theta'_q$ suppresses head-on collisions.

6.7 Extrapolation to the highest cosmic-ray energies

The parameterizations presented in section 6.5 are based on simulated pp collisions for incident proton energies 10^3 GeV $< E_p < 10^6$ GeV, where data is available to verify the experimentally accessible parts of the resulting particle distributions. Cosmic-ray observations suggest that the maximum proton energy that can be generated in astrophysical proton accelerators may be as high as 10^{11} GeV. Thus, in order to account for interactions of the highest-energy protons, the parameterizations presented in this chapter need

to be applied in a region where they cannot be directly tested. This should be done with caution because the extrapolation to high energy is intrinsically model dependent. We refer the reader to Engel (1998) for a discussion on the relationship between experimental data obtained in collider experiments and the modeling of pp interactions at cosmic-ray energies.

In this section, we compare the high-energy behavior of the parameterizations derived here with an extrapolation of existing data and with theoretical models. Extrapolations of experimental data as well as theoretical models for incident proton energies $E_p > 10^6$ GeV are available predominantly for the charged multiplicity, due to the availability of experimental data at lower energies. Therefore, we focus in this section on the charged multiplicity contained in the parameterizations presented in this chapter.

The charged multiplicity is dominated by pions, hence we estimate the charged multiplicity from the parameterized charged pion distributions. We derive the charged pion multiplicity $\mathcal{M}^{\rm par}_{\pi^\pm} = \mathcal{M}^{\rm par}_{\pi^+} + \mathcal{M}^{\rm par}_{\pi^-}$ by integrating eq. (6.19) over energy and rapidity. To account for charged particle creation due to decay processes and for the contribution of other charged particles, we estimate the charged multiplicity with $\mathcal{M}^{\rm par}_{\rm ch} = 2 + 1.47\,\mathcal{M}^{\rm par}_{\pi^\pm}$, where the numerical value 1.47 is found by comparing $\mathcal{M}^{\rm par}_{\pi^\pm}$ and $\mathcal{M}_{\rm ch}$ at the proton energies considered in our simulations. The leading term 2 accounts for the number of outgoing protons for low secondary multiplicities (corresponding to low center-of-mass energies).

Using experimental data at low energies, Engel (1998) has found that the charged multiplicity should increase faster than $\log(s)$ but not as fast as s^p, where $0.1 < p < 0.3$, at high energies. In order to compare our results with these limiting cases, we have re-derived[10] the explicit functional form based on the two data points with highest energy (Ansorge et al. 1989, Biyajima et al. 2001):

$$\mathcal{M}^{\rm min}_{\rm ch} = -65 + 17 \log s\,; \tag{6.38a}$$

$$\mathcal{M}^{\rm max}_{\rm ch} = 7.0 + 1.4\, s^{0.22}\,, \tag{6.38b}$$

where s is expressed in units of GeV^2. In figure 6.11 we show the charged multiplicity estimated from the parameterizations presented in this chapter, together with the minimum and maximum values of the multiplicity given in eqs. (6.38). Also shown is an extrapolation of the approximation $\mathcal{M}^{\rm fit}_{\rm ch}$ given in eq. (6.5). We observe that the charged multiplicity estimated from our parameterizations increases faster than the extrapolation of $\mathcal{M}^{\rm fit}_{\rm ch}$ but is well within the limits derived by Engel (1998). We thus conclude that the high-energy behavior of the parameterizations presented here is consistent with theoretical expectations. We estimate from figure 6.11 that the uncertainty in the normalization at the highest energies, $E_p \simeq 10^{11}$ GeV, is within a factor ~2.

[10] The explicit form of these functions was not given in the original work (Engel 1998). The numerical value of 0.22 is chosen for comparison with fig. 8 of Engel (1998).

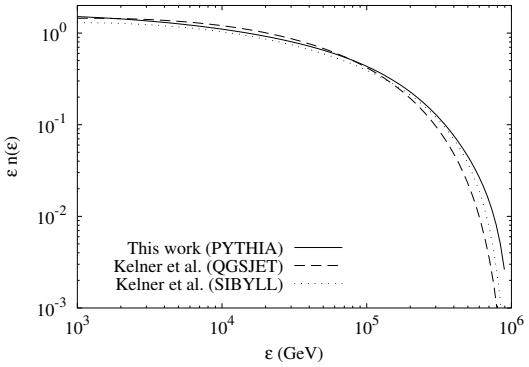

Figure 6.12: Comparison of parameterizations of the π^0 energy spectrum $\epsilon\, n(\epsilon)$ for incident proton energy $E_p = 10^6$ GeV. The energy range is chosen for comparison with fig. 1 of Kelner et al. (2006).

6.8 Discussion

6.8.1 Comparison with previous work

We have verified that the parameterizations of the pion and charged kaon distributions presented in this chapter are similar to those by Badhwar et al. (1977) and Stephens & Badhwar (1981) at the lowest energies considered here, $\sqrt{s} = 45$ GeV. The difference between our parameterization of the neutral pion distribution and that of Blattnig et al. (2000) is larger. These authors provide an accurate fit to the particle distribution at large transverse momentum. However, the number of particles in this region is very small and we find that the parameterization does not reproduce the total multiplicity correctly for center-of-mass energy $\sqrt{s} = 45$ GeV.

In figure 6.12, we present a comparison of the parameterization of the π^0 energy spectrum presented in this chapter with two parameterizations by Kelner et al. (2006). These parameterizations are based on Monte Carlo results generated with `QGSJET` and `SYBILL` instead of `PYTHIA`. We observe from figure 6.12 that, for incident proton energy $E_p = 10^6$ GeV, our parameterization is closer to the `QGSJET` fit at intermediate energies and closer to the `SYBILL` fit at high energies. The differences between the energy spectra described by the three parameterizations are up to ~10% for intermediate pion energies, which is larger than the fit inaccuracy (see section 6.5). We note that Kelner et al. (2006) find ~30% differences between `QGSJET` and `SYBILL` in some regions of the parameter space (see figure 3 of their work). These discrepancies suggest that a more precise description of the energy spectra and particle distributions requires a better theoretical understanding of the pp physics, in particular of the fragmentation process, rather than more accurate fits to Monte Carlo results.

In this chapter we have used PYTHIA 6.324, which was the latest available version of the code when this work was initiated. As of version 6.3, the PYTHIA code uses a new treatment of multiple parton interactions, which is relevant for hadron – hadron interactions (see Sjöstrand et al. 2003). Several tuning models for PYTHIA version 6.2 can be found in the literature, such as CDF tune A (Field[11]; see also Buttar et al. (2005)) or the tuning proposed by Buttar et al. (2004). In the absence of a thoroughly tested tuning for PYTHIA version 6.3 we have used the default parameter values. (Note that a preliminary tuning for PYTHIA 6.3 is presented by Moraes A. (2006)). A systematic study of the influence of PYTHIA parameters on the resulting particle distributions, taking into account constraints from experimental data, is beyond the scope of this work.

6.8.2 Astrophysical applications

There are several astrophysical systems in which a population of high-energy protons is believed to be present, e.g. supernova remnants, active galactic nuclei, radio galaxies, pulsars and gamma-ray bursts (see section 6.1 for a more detailed discussion and references). Proton – proton interactions may contribute significantly to the gamma-ray and neutrino emission of these sources. To extract as much information on the source as possible from (future) observations of gamma rays and neutrinos, it is important to understand the properties of secondary particles created in pp interactions. This requires a realistic model for the particle physics. Such a model is presented here in the form of explicit parameterizations of numerical results generated with PYTHIA. In this section we discuss two examples where a detailed analysis of the signature of neutrinos produced in pp interactions can provide a way to probe the physics of the source.

Within the fireball model for GRBs, the prompt gamma-ray emission is attributed to synchrotron radiation from accelerated electrons. These electrons are believed to be accelerated by internal shocks but the details of the acceleration process are still unclear. The mechanism responsible for the dissipation of the fireball energy may accelerate a substantial fraction of the protons contained in the fireball to high energies. Since the optical depth for pp interactions can be larger than a few, these collisions will occur and give rise to high-energy neutrinos and gamma rays. Because the high-energy secondary mesons are collimated within the direction of the energetic proton, the energy and angular distribution of these secondaries depends on the distribution of the high-energy protons. Therefore, the resulting neutrino and gamma-ray signals may contain information about the details of the acceleration mechanism. We note however that in this scenario both interacting protons are moving toward an observer with ultra-relativistic velocities so that all particle distributions are collimated by relativistic beaming. This implies that also low-energy secondaries will be collimated in the observer frame and it will be difficult to extract information from the resulting signals. Nevertheless, the angle-energy correlations of the emitted secondary particles may make it possible to

[11] See the website http://www.phys.ufl.edu/~rfield/cdf/tunes/py_tuneA.html.

extract information about the acceleration mechanism.

On general grounds one expects that interactions between energetic protons occur less frequently than interactions between energetic and cold protons. Also in the latter case the resulting neutrino signal may carry information on the physics of the source. A very interesting scenario in this respect is that of 'failed GRBs' (Mészáros & Waxman 2001, Razzaque et al. 2003b) (see also Razzaque et al. (2004b) and Razzaque et al. (2005)). This scenario builds on the possibility that the mechanisms associated with the early phases of a developing GRB may be present in a large fraction of supernovae, but only lead to an observed GRB under special circumstances. For example, it may be the case that the formation of a fireball is quite a common phenomenon but that a large fraction of fireballs has insufficient energy to traverse the pre-burst stellar environment. However, if shocks form at a sub-stellar radius, protons can be accelerated and collide with target protons (nuclei), giving rise to neutrinos. It is presently not clear whether or not these failed (dark) GRBs exist in nature; if they do the model uncertainties are large which makes it difficult to predict the resulting neutrino fluxes. Nevertheless, neutrino emission is likely the only signals that could indicate the existence of these phenomena. Therefore, the question what may be learned about failed GRBs from neutrino observations deserves a detailed investigation. Since the energy and flux of the neutrinos that reach the earth depend strongly on the collimation of the secondary neutrinos created in pp collisions, a detailed model of the proton interactions is essential to study the properties of the neutrino emission and to investigate how neutrino observations can be used to constrain these models.

6.9 Conclusions

In this chapter we have presented parameterizations of the energy spectra (eq. (6.16)) and of the energy and rapidity distributions (eqs. (6.19) and (6.23)) of secondary pions and kaons created in energetic pp collisions. These parameterizations are based on numerical results obtained with the event generator `PYTHIA`. We considered an incident proton with energy 10^3 GeV $< E_p < 10^6$ GeV colliding with a target proton at rest. This corresponds to center-of-mass energy 43 GeV $< \sqrt{s} < 1.4 \times 10^3$ GeV.

The results presented here are model dependent because they are based on results obtained with a Monte Carlo event generator. Nevertheless, the parameterizations represent an important step in including the current understanding of proton interactions in astrophysical models because they are the first parameterizations of the full distribution of secondary mesons created in energetic pp collisions that are based on a realistic particle physics model.

In section 6.7, we have argued that the results can be applied with some confidence to pp interactions for protons with energies $E_p > 10^6$ GeV. At the highest CR energies, $E_p \simeq 10^{11}$ GeV, we have estimated the uncertainty in the overall normalization due to the extrapolation to very high energies to be within a factor ~2.

We have parameterized the particle distributions of meta-stable pions and kaons, as opposed to stable decay products, because this captures the essential properties of the pp interaction without making any assumptions about the importance of pion and kaon energy loss prior to decay (for concrete implications of pion decay in an astrophysical context, see e.g. Kashti & Waxman (2005) and Asano & Nagataki (2006)). Energy spectra and full particle distributions of neutrinos and gamma rays are derived from the parameterizations presented in this chapter in a straightforward manner.

The energy and rapidity distributions fully describe the kinematics of the secondary mesons, so that the derived parameterizations contain all correlations between energy and angle of the outgoing particles. This implies that our results can be applied to a general scattering geometry, two protons with different energies colliding under an arbitrary angle, which opens a wealth of astrophysical applications.

In section 6.6, we demonstrated how the parameterizations can be used to derive energy spectra and angular distributions of secondary mesons and their decay products. We derived the gamma-ray spectrum resulting from π^0 decay after a pp collision (see figure 6.7) and we presented angular distributions of π^0 mesons produced in a pp collision (see figure 6.8). The results presented in this chapter can be used for a detailed study of pp interactions in the early prompt emission of GRBs and in the interaction of a developing GRB with its surroundings (see section 6.8.2). A particularly interesting possibility is the existence of a class of developing GRBs for which the fireball has insufficient energy to traverse the pre-burst stellar environment. If shocks are formed at a sub-stellar radius, these will accelerate protons that collide with target protons and create neutrinos. The fluence and energy of neutrinos that reach the earth depend sensitively on the correlations between the energy and outgoing angle of the secondary mesons that are created in these pp interactions. Therefore a detailed modeling of the pp interaction is required to investigate how neutrino observations can constrain these models. The parameterizations presented here can be used to study this scenario in detail. We aim to investigate this in the future.

We emphasize that the parameterizations presented in this chapter are based on the current, incomplete, understanding of pp collisions. With new experimental results on pp interactions (e.g., from the LHC experiments) the parameterizations presented here should be carefully reevaluated.

The parameterizations presented in this chapter can be extended with proton – neutron and proton – photon interactions, all of which can be studied with `PYTHIA`. The same holds for the energy spectrum and angular distribution of primary nucleons (the primary nucleon is the outgoing nucleon with the highest energy). This allows a more precise study of multiple nucleon – nucleon interactions.

	π^+	π^-	π^0	K^+	K^-	K^0	$\overline{K^0}$
p_{00}	−0.497	−0.501	−0.456	−1.23	−1.46	−1.29	−1.50
p_{01}	0.0934	0.0934	0.0950	0.0657	0.101	0.0690	0.101
p_{10}	−0.140	−0.128	−0.142	−0.147	−0.109	−0.142	−0.118
p_{11}	0.0131	0.0118	0.0135	0.0161	0.00865	0.0154	0.0101
p_{20}	−0.455	−0.437	−0.457	−0.00411	−0.0577	−0.00717	−0.0567
p_{21}	0.495	0.494	0.494	0.493	0.491	0.493	0.491
p_{30}	−2.06	−0.945	−1.49	−0.989	−1.22	−1.03	−1.25
p_{40}	−0.896	−1.03	−0.981	−0.345	−0.164	−0.294	−0.169
p_{50}	1.11	0.963	1.01	0.777	1.04	0.839	1.05
p_{60}	0.791	0.598	0.723	−0.235	−0.279	−0.272	−0.272
p_{70}	37.7	15.3	22.1	42.7	18.6	33.8	21.2
p_{80}	7.69	7.23	8.53	12.0	4.23	10.1	4.07

Table 6.3: Numerical values of the energy spectrum fit parameters p_{ij}.

6.A The Lund string model

The Lund string model (Andersson et al. 1983) is an iterative model used in `PYTHIA` to describe meson formation after a hard QCD process. In the model, quark-antiquark pairs that are created in a hard QCD scattering process form 'strings' that are connected through a color flux-tube with energy per unit length κ. This string breaks into a meson and a remainder string that will undergo the same process (baryons are generated through a generalization of this process). At every step in the iteration, a meson is created with a certain energy and rapidity according to a probability distribution.

The mechanism to break the string is the creation of a new quark-antiquark pair through quantum-mechanical tunneling. The probability to create a $q\bar{q}$ pair with mass m and transverse momentum p_T is given by

$$\mathcal{P} = \exp\left(-\frac{\pi}{\kappa}\left(m^2c^4 + p_T^2c^2\right)\right), \tag{6.39}$$

which derives from the Schwinger formula (Schwinger 1951). This implies that lighter mesons are created more prolifically than heavier mesons and that the probability to create a meson falls off exponentially with increasing p_T. After a meson is created, the probability that it carries a fraction z of the string's $E + p_z$ is determined by the so-called fragmentation function (Andersson et al. 1983, Sjöstrand et al. 2003). Together with eq. (6.39), this fragmentation function determines the secondary particle distributions after the hard QCD process. Free parameters within the model are adjusted to reproduce experimental data. A detailed description can be found in Andersson et al. (1983) and Sjöstrand et al. (2003).

	π^+	π^-	π^0	K^+	K^-	K^0	$\overline{K^0}$
p_{00}	−0.474	−0.461	−0.420	−1.03	−1.20	−1.13	−1.37
p_{01}	0.0846	0.0796	0.0821	−0.00299	0.0377	0.0168	0.0501
p_{10}	−0.115	−0.124	−0.118	−0.0375	−0.0291	−0.0604	−0.0579
p_{11}	0.0102	0.0117	0.0107	0.00396	−0.000110	0.00621	0.00351
p_{20}	−0.560	−0.604	−0.598	−0.835	−0.606	−0.655	−0.467
p_{21}	0.497	0.496	0.497	0.494	0.497	0.497	0.497
p_{30}	−1.15	−0.641	−0.815	−0.742	−0.845	−0.788	−0.917
p_{40}	−1.03	−1.11	−1.17	−0.167	−0.155	−0.237	−0.176
p_{50}	1.12	0.980	0.987	0.716	0.934	0.840	1.01
p_{60}	0.962	0.891	0.954	1.08	0.597	0.789	0.371
p_{70}	-	-	-	-	-	-	-
p_{80}	6.98	6.93	7.45	-	-	-	-
q_{00}	−0.167	−0.149	−0.161	0.539	0.363	0.405	0.382
q_{01}	0.0497	0.108	0.0737	0.222	0.228	0.149	0.195
q_{10}	0.668	0.668	0.637	0.889	1.06	0.997	1.12
q_{11}	0.329	0.328	0.307	0.523	0.673	0.612	0.719
q_{12}	0.116	0.0806	0.107	0.227	0.328	0.216	0.298
q_{13}	−0.162	−0.154	−0.144	−0.304	−0.141	−0.306	−0.155
q_{20}	2.03	2.05	2.16	0.902	0.695	0.676	0.579
q_{21}	−0.0577	−0.0654	−0.0704	−0.0694	−0.0648	−0.0525	−0.0527
q_{22}	0.247	0.233	0.216	0.185	0.226	0.242	0.261
q_{23}	0.665	0.381	0.556	0	0	0	0
q_{30}	1.04	1.24	1.37	0.319	0.198	0.238	0.184
q_{31}	3.94	4.51	4.92	1.16	1.17	0.951	1.08
q_{32}	−1.37	−1.54	−1.65	−0.597	−0.699	−0.559	−0.684

Table 6.4: Numerical values of the energy and rapidity distribution fit parameters p_{ij} (refitted modified energy spectrum) and q_{ij}. A hyphen indicates that the parameter is not used in the parameterization.

7

Neutrino emission from choked gamma-ray bursts

based on work with R. A. M. J. Wijers
(publication in preparation)

7.1 Introduction

Observational evidence for a connection between long-duration gamma-ray burst (GRBs) and the death of massive stars has accumulated since the observation of the first GRB afterglows in 1997 (Costa et al. 1997, Frail et al. 1997, Van Paradijs et al. 1997). Observations have indicated correlations between the rate of long GRBs and the global star formation rate and between burst locations and star forming regions within galaxies, and there is also spectroscopic evidence that typical long GRB host galaxies are actively star forming (see Woosley & Bloom 2006 for a recent review). Definite proof that at least some long GRBs occur together with supernovae (SNe) has come from the observation of SN spectra emerging from the fading afterglow of a GRB. The most compelling cases of these observations are GRB980425 (SN1998bw); GRB 031203 (SN 2003lw); and GRB030329 (SN 2003dh), but more associations of GRBs with SNe have been put forward (see Woosley & Bloom 2006). More recently, however, two nearby long GRBs have been observed without an accompanying SN component, which clearly indicates that not all long GRBs have an associated SN (Fynbo et al. 2006).

Given that there is some connection between GRBs and SNe, it is an intriguing possibility that the mechanisms associated with the early phases of a developing GRB are present in a large fraction of SNe but only lead to an observed GRB under special circumstances. For example, it may be the case that the formation of a fireball is quite a common phenomenon but that only very energetic fireballs have sufficient power to traverse the pre-burst stellar environment. Fireballs with less energy would be stopped below the stellar surface, in which case the stellar material absorbs all electromagnetic

emission. Numerical simulations (e.g., MacFadyen et al. 2001) support the possibility of these 'smothered' or 'choked' jets.

In the absence of electromagnetic radiation, neutrinos (and possibly gravitational waves) may be the only observable signal of choked GRBs. Pruet (2003) studied the creation of neutrinos in collisions between neutrons coasting in the jet with decelerated neutrons in the jet head and found that the typical observer energy of these neutrinos is ∼1 GeV. Neutrinos of higher energy may be produced in interactions of shock-accelerated protons with target protons and photons in the jet or the pre-burst stellar environment. A number of shocks accompany the jet while it is traversing the pre-burst stellar environment (see, e.g., Waxman & Mészáros 2003): a forward shock is driven into the stellar material, a reverse shock decelerates the jet plasma, and internal shocks may occur within the jet if the variability timescale of the central engine is short enough (Mészáros & Waxman 2001). The production of high-energy neutrinos by shock-accelerated protons has been investigated both for ultra-relativistic jets with Lorentz factor ∼100 (Mészáros & Waxman 2001, Razzaque et al. 2003b) and for mildly relativistic jets with Lorentz factor ∼ few (Razzaque et al. 2003a; 2004a;b; 2005, Ando & Beacom 2005).

The creation of high-energy ($\gtrsim 10$ GeV) neutrinos in GRBs occurs almost exclusively through the decay of charged mesons created in interactions of high-energy protons. These protons may interact both with target protons and with target photons. For very high proton energies ($\gtrsim 10$ TeV) photon – proton interactions constitute the dominant production mechanism to create secondary pions and kaons. At lower energies only a small fraction of the photon distribution is above the kinematic threshold to create secondary mesons. As a result, inelastic proton – proton (pp) collisions are the dominant mechanism to create secondary mesons for proton energies $\lesssim 10$ TeV. The contribution to the total neutrino output from protons in this regime may be substantial because the spectrum of accelerated protons is expected to be highest at low energies. Furthermore, synchrotron cooling of secondary mesons strongly suppresses the neutrino flux at high energies (Ando & Beacom 2005; see also Asano & Nagataki 2006).

In this chapter we consider neutrino production through energetic pp collisions in choked GRBs. We use the parameterization presented in the previous chapter to take account of the energy and angular distribution of secondary pions and kaons created in the pp interactions. This allows us to study the energy spectrum and angular distribution of the resulting neutrino signal in more detail than previous studies. We restrict ourselves to pp interactions with the energetic proton moving in the radial direction, i.e. toward the observer. In principle the spectrum of shock-accelerated protons depends on the angle to the shock normal (e.g., Gallant & Achterberg 1999, Achterberg et al. 2001). However, a detailed analysis of the proton energy spectrum and angular distribution is beyond the scope of this work. The study presented in this chapter also applies to the first stages of successful GRBs if the Lorentz factor of the jet is of the order ten.

This chapter is organized as follows. We investigate the environment of the jet and

the jet head in section 7.2. We then consider proton energy loss mechanisms in this environment in section 7.3 and we consider meson energy loss in section 7.4. In section 7.5 we study the resulting neutrino spectrum. Based on this we discuss the detection prospects in section 7.6. We discuss our results in section 7.7 and we present our conclusions in section 7.8.

7.2 The jet and jet head environment

Building on earlier work (see Razzaque et al. 2005 and references therein) we adopt the following physical picture. We consider core-collapse of a massive star with a He core extending to $\sim 3 \times 10^{11}$ cm that may be surrounded by an H envelope extending to $\sim 10^{13}$ cm. It was recently pointed out that large angular momentum may be a requirement for a successful GRB progenitor (Yoon & Langer 2005, Woosley & Heger 2006). The presence of an H envelope would prevent the stellar core from achieving such a large angular momentum and may thus not seem very likely for a GRB progenitor. However, as the nature of GRB progenitors (in particular of choked GRBs) remains unclear, we consider the H envelope as a possibility. As we will show below, the H envelope does not affect the possibility of neutrino creation in internal shocks but it facilitates the emission of neutrinos with energy $\gtrsim$100 GeV resulting from proton acceleration in the reverse shock.

After core-collapse we assume that an energetic, collimated outflow is formed which makes it way through the pre-collapse stellar environment. While this jet is traversing the pre-burst stellar material, a forward (bow) shock is driven into the pre-collapse stellar environment and a reverse shock propagates back into the jet. Between the forward and the reverse shock there is a region of shocked jet and stellar material propagating with Lorentz factor $\Gamma_h < \Gamma_j$, which is referred to as the jet head. In the following we will use the subscripts j and h to refer to quantities in the jet and in the jet head, respectively. We discuss here the jet and jet head environments. In particular, we estimate the comoving magnetic field strength, and the comoving proton and photon densities. These quantities determine the importance of various proton energy-loss mechanisms which are discussed in the next section.

7.2.1 The jet

The essential parameters that determine the physics of the jet are the total available energy $E = 10^{52} E_{52}$ erg (some fraction of the total SN energy), the jet lifetime $t = 10 t_1$ s, the variability timescale $\delta t = 0.1 \delta t_{-1}$ s, the bulk Lorentz factor of the jet $\Gamma_j = 10 \Gamma_{j,1}$, and the jet opening angle $\theta = 0.1 \theta_{-1}$. The isotropic equivalent luminosity of the jet is

$$L_{\rm iso} \simeq \frac{2E}{t\theta^2} \simeq 2 \times 10^{53} \text{ erg s}^{-1} \times \theta_{-1}^{-2} E_{52} t_1^{-1} . \quad (7.1)$$

We consider the coasting phase of the jet, where the energy is dominated by the bulk kinetic energy of the protons. The comoving proton density is given by:

$$n'_{p,j} = \frac{L}{4\pi r^2 \Gamma_j^2 m_p c^3} \simeq 4 \times 10^{20}\ \mathrm{cm}^{-3} \times r_{11}^{-2}\,(\Gamma_j\theta)_0^{-2}\,E_{52}\,t_1^{-1}\,, \tag{7.2}$$

where $r = 10^{11} r_{11}$ cm is the radial coordinate, m_p denotes the proton mass, and we use the notational convention $x_a \equiv 10^{-a}x$. We keep the radius r as a free parameter so that our results can be applied to both the reverse shock, where r is a free parameter, and to internal shocks, where the radius $r_{\rm int}$ where internal shocks occur is determined from the variability timescale and the jet Lorentz factor (see below).

We assume in the following that the magnetic field carries a fraction ϵ_B of the total energy in the flow so that the comoving magnetic field strength in the jet is

$$B'_j \simeq 10^9\ \mathrm{G} \times r_{11}^{-1}\,(\Gamma_j\theta)_0^{-1}\,(\epsilon_B E)_{51}^{1/2}\,t_1^{-1/2}\,. \tag{7.3}$$

If the reverse shock is collisionless, as we will assume here, it accelerates both protons and electrons. The accelerated electrons cool very rapidly by synchrotron radiation and these synchrotron photons interact with the protons in the flow through Thomson scattering. The Thomson optical depth $\tau_{\rm T}$ for a photon to scatter off a proton between r and infinity is given by

$$\tau_{\rm T} \simeq \sigma_T n'_{p,j} r \simeq 2 \times 10^7 \times r_{11}^{-1}\,(\Gamma_j\theta)_0^{-2}\,E_{52}\,t_1^{-1} \gg 1\,, \tag{7.4}$$

where σ_T denotes the Thomson cross section. This huge optical depth implies that the synchrotron photons will thermalize at every radius r over a very wide range of parameters. Assuming that a fraction $\epsilon_e \sim 0.1$ of the total energy in the flow is converted to a thermal photon distribution in this way, the comoving photon density $n'_{\gamma,j}$ and temperature T'_j are given by:

$$n'_{\gamma,j} = 3 \times 10^{24}\ \mathrm{cm}^{-3} \times r_{11}^{-3/2}\,(\Gamma_j\theta)_0^{-3/2}\,(\epsilon_e E)_{51}^{3/4}\,t_1^{-3/4}\,; \tag{7.5}$$

$$T_j = (4\ \mathrm{keV}/k_B) \times r_{11}^{-1/2}\,(\Gamma_j\theta)_0^{-1/2}\,(\epsilon_e E)_{51}^{1/4}\,t_1^{-1/4}\,. \tag{7.6}$$

Internal shocks may occur in the outflow when shells with different Lorentz factors collide with each other. The radius $r_{\rm int}$ where this happens is estimated to be:

$$r_{\rm int} \simeq 2c\Gamma_j^2 \delta t \simeq 6 \times 10^{11}\ \mathrm{cm} \times\ \Gamma_{j,1}^2\,\delta t_{-1}\,. \tag{7.7}$$

The internal shocks will also accelerate electrons that subsequently emit photons through synchrotron radiation. Due to the relatively small internal shock radius given in eq. (7.7), the comoving proton density near the internal shocks is very high. Inserting eq. (7.7) into (7.2), we find that the comoving proton density at the internal shock radius equals:

$$n'_{p,\rm int} \simeq 10^{19}\ \mathrm{cm}^{-3} \times \Gamma_{j,1}^{-6}\,\theta_{-1}^{-2}\,E_{52}\,t_1^{-1}\,\delta t_{-1}^{-2}\,. \tag{7.8}$$

As a result of this high density, the Thomson optical depth $\tau \gtrsim 10^6$ so that the synchrotron photons will thermalize. Assuming, as before, that a fraction $\epsilon_e \sim 0.1$ of the total energy in the flow is converted to radiation by in the internal shocks, the comoving photon density $n'_{\gamma,j}$ and temperature T'_j at the internal shock radius are given by:

$$n'_{\gamma,\,\mathrm{int}} = 2\times 10^{23}\ \mathrm{cm}^{-3} \times \Gamma_{j,1}^{-9/2}\,\theta_{-1}^{-3/2}\,(\epsilon_e E)_{51}^{3/4}\,t_1^{-3/4}\,\delta t_{-1}^{-3/2}\,; \tag{7.9}$$

$$T_{\mathrm{int}} = (2\ \mathrm{keV}/k_B) \times \Gamma_{j,1}^{-3/2}\,\theta_{-1}^{-1/2}\,(\epsilon_e E)_{51}^{1/4}\,t_1^{-1/4}\,\delta t_{-1}^{-1/2}\,. \tag{7.10}$$

7.2.2 The jet head

While traversing the pre-burst environment, the relativistic outflow drives forward a 'cork' (in the terminology of Waxman & Mészáros 2003) of shocked stellar material and decelerated jet plasma that we call the jet head. The proper density of protons in the jet head is (e.g., Mészáros & Waxman 2001)

$$n'_{p,h} = 4\Gamma_{\mathrm{rel}} n'_{p,j} = 7\times 10^{21}\ \mathrm{cm}^{-3} \times r_{11}^{-2}\,\Gamma_{j,1}^{-1}\,\theta_{-1}^{2} E_{52}\,t_1^{-1}\,\Gamma_h^{-1}\,, \tag{7.11}$$

where $\Gamma_{\mathrm{rel}} \simeq \Gamma_j/(2\Gamma_h)$ is the relative velocity of the jet and the jet head. The Lorentz factor of the jet head $\Gamma_h < \Gamma_j \simeq$ few may be determined by balancing the pressure before and after the jet head. However, the exact value is not very important in this study and we leave it as a free parameter. The comoving width Δ' of the jet head can be estimated with (Mészáros & Waxman 2001):

$$\Delta' = 0.2\theta_j r = 2\times 10^9\ \mathrm{cm} \times r_{11}\,\theta_{-1}\,. \tag{7.12}$$

Also in the jet head the Thomson optical depth is very large, $\tau_T \simeq 10^7$, so that synchrotron photons emitted by shock-accelerated electrons will thermalize. The comoving photon density and temperature in the jet head are given by the following expressions:

$$n'_{\gamma,h} = 9\times 10^{25}\ \mathrm{cm}^{-3} \times r_{11}^{-3/2}\,\theta_{-1}^{-3/2}\,(\epsilon_e E)_{51}^{3/4}\,t_1^{-3/4}\,\Gamma_h^{-3/2}\,; \tag{7.13}$$

$$T_h = (14\ \mathrm{keV}/k_B) \times r_{11}^{-1/2}\,\theta_{-1}^{-1/2}\,(\epsilon_e E)_{51}^{1/4}\,t_1^{-1/4}\,\Gamma_h^{-1/2}\,. \tag{7.14}$$

We assume also in the jet head that the magnetic field carries a fraction ϵ_B of the total energy in the flow so that the comoving magnetic field strength in the jet is

$$B'_h \simeq 10^{10}\ \mathrm{G} \times r_{11}^{-1}\,\theta_{-1}^{-1}\,(\epsilon_B E)_{51}^{1/2}\,t_1^{-1/2}\,\Gamma_h^{-1}\,. \tag{7.15}$$

7.3 Proton acceleration and energy loss

In this section we consider proton acceleration and energy loss in the jet. These results can be applied to proton acceleration in internal shocks. Protons that are accelerated by the reverse shock are subject to interactions in both the jet and the jet head. In this case, the results presented here apply to the downstream region.

7.3.1 Acceleration and energy loss timescales

The comoving acceleration timescale $t'_{\rm a}$ for proton acceleration can be estimated from the comoving Larmor radius as (e.g., Waxman 1995)

$$t'_{\rm a} \simeq \frac{\kappa R'_L}{c} = \frac{\kappa E'_p}{qcB'} = 10^{-9}\ {\rm s} \times E'_{p,3}\, r_{11}\, (\Gamma_j\theta)_0\, (\epsilon_B E)_{51}^{-1/2}\, t_1^{1/2}\, \kappa_1\,, \tag{7.16}$$

where $E'_p = 10^3 E'_{p,3}$ GeV denotes the proton energy in the comoving frame, q denotes the electron charge and $\kappa = 10\kappa_1$ is an ignorance parameter for the acceleration process. The maximum proton energy attainable is in principle limited both by energy losses and by the shock lifetime. The lifetime can be estimated from the dynamical timescale t'_d:

$$t'_d = \frac{r}{c\Gamma_j} = 3 \times 10^{-1}\ {\rm s} \times r_{11}\, \Gamma_{j,1}^{-1}\,. \tag{7.17}$$

Synchrotron radiation is the dominant energy loss mechanism at very high proton energies. For large proton energies, the synchrotron energy loss time is equal to (e.g., Rybicki & Lightman 1979):

$$t'_{\rm s} = \frac{6\pi m_p^4 c^3}{\sigma_{\rm T} m_e^2 B'^2 E'_p} = 3 \times 10^{-3}\ {\rm s} \times E'^{-1}_{p,3}\, r_{11}^2\, (\Gamma_j\theta)_0^2\, (\epsilon_B E)_{51}^{-1}\, t_1^1\,, \tag{7.18}$$

We approximate the cross section for pp collisions with $\sigma_{pp} = 5 \times 10^{-26}$ cm^2 and the fractional energy loss $K_{pp} = 0.5$. The energy-loss timescale is then equal to

$$t'_{pp} = \frac{1}{cK_{pp}\sigma_{pp}(1-\xi_p)n'_p} = 4 \times 10^{-6}\ {\rm s} \times r_{11}^2\, (\Gamma_j\theta)_0^2\, E_{52}^{-1}\, t_1\,, \tag{7.19}$$

where ξ_p denotes the fraction of protons that is accelerated to high energies, which we assume to be small in the second equality, and n'_p denotes the comoving proton density.

The computation of the energy loss timescale due to photopion production is somewhat more involved because the protons interact with a thermal distribution of target photons with an energy-dependent cross section. We express the energy loss time as:

$$\begin{aligned} t'^{-1}_{p\gamma\pi} &= -\frac{1}{E'_p}\frac{dE'_p}{dt'} \\ &= \frac{c}{2}\int_{-1}^{1} d\mu', (1-\beta'_p\mu') \int d\epsilon'_\gamma\, n(\epsilon'_\gamma)\sigma_{p\gamma\pi}(\sqrt{s})K_{p\gamma\pi}(\sqrt{s})\,. \end{aligned} \tag{7.20}$$

Here β'_p is the dimensionless proton velocity, which we will take equal to unity in the following; μ' is the cosine of the proton – photon incident angle; $\sigma_{p\gamma\pi}$ is the cross section; and $K_{p\gamma\pi}$ is the proton's fractional energy loss. Both the cross section and the fractional energy loss depend on the proton and photon energies and the collision angle through the

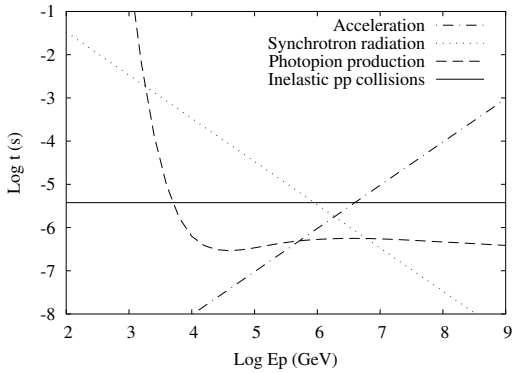

Figure 7.1: Proton acceleration timescale (dash-dotted) together with energy loss timescales due to photopion production (dashed), synchrotron radiation (dotted) and inelastic pp collisions (solid). In producing this figure, we have chosen reference values of the model parameters and chosen the radius $r = 10^{11}$ cm.

center-of-mass energy $\sqrt{s}$. We use here a parameterization of the proton – photon cross section $\sigma_{p\gamma\pi}$ that is presented in appendix 7.A. Furthermore we estimate $K_{p\gamma\pi} = 0.2$.

Energy loss due to Inverse Compton (IC) scattering is at most comparable to synchrotron loss as long as $\epsilon_e \simeq \epsilon_B$. In the Thomson limit, which is applicable when

$$E'_p \ll \frac{m_p^2 c^4}{\langle \epsilon'_\gamma \rangle} \simeq 7 \times 10^4 \text{ GeV} \times r_{11}^{1/2} \, (\Gamma_j \theta)_0^{1/2} \, (\epsilon_e E)_{51}^{-1/4} \, t_1^{1/4} \,, \tag{7.21}$$

the IC energy loss time $t'_{\rm IC} = (\epsilon_B/\epsilon_e) t'_{\rm sync}$, while for higher proton energies the energy loss time is much longer due to Klein-Nishina suppression. We therefore do not consider proton IC energy loss here. Using approximations presented by Chodorowski et al. (1992), we find that, depending on the model parameters, the energy-loss time due to electron-positron pair creation is at most comparable to that of pp interactions. Therefore these collisions will not prevent pp interactions but they may change the energy spectrum of the high-energy incident protons.

7.3.2 Critical energies

In figure 7.1 we show the acceleration timescale together with the energy loss timescales in the jet for reference values of the burst parameters and radius $r = 10^{11}$ cm. We observe from this figure that around $E'_p = 10^6$ GeV the acceleration time t'_a is close to the energy loss times due to synchrotron radiation, photopion production and pp collisions. Therefore, depending on the values of the model parameters, the maximum proton energy may be limited by each of these processes. Below we analyze when each of these process is dominant by defining a number of typical proton energies and estimating how these de-

pend on the model parameters. We denote the proton energy for which the energy loss timescale of processes a and b are equal with $E_p'^{(a,b)}$.

First we estimate the energy loss time due to photopion production at energies well above the threshold energy as:

$$t'_{p\gamma\pi} \simeq \frac{1}{c\bar{\sigma}_{p\gamma}\bar{K}_{p\gamma}n_{\gamma,j}} = 6\times10^{-7}\ \mathrm{s}\times r_{11}^{3/2}\,(\Gamma_j\theta)_0^{3/2}\,(\epsilon_e E)_{51}^{-3/4}\,t_1^{3/4}\,, \tag{7.22}$$

where $\bar{\sigma}_{p\gamma} := 10^{-28}\ \mathrm{cm}^2$ and $\bar{K}_{p\gamma} = 0.2$. Using this estimate together with eqs. (7.16), (7.18), and (7.19), we find that

$$E_p'^{(\mathrm{acc,\,s})} = 2\times10^6\ \mathrm{GeV}\times r_{11}^{1/2}\,(\Gamma_j\theta)_0^{1/2}\,(\epsilon_B E)_{51}^{-1/4}\,t_1^{1/4}\,\kappa_1^{-1/2}\,; \tag{7.23}$$

$$E_p'^{(\mathrm{acc},\,p\gamma\pi)} = 6\times10^5\ \mathrm{GeV}\times r_{11}^{1/2}\,(\Gamma_j\theta)_0^{1/2}\,\epsilon_{B,-1}^{1/2}\,\epsilon_{e,-1}^{-3/4}\,E_{52}^{-1/4}\,t_1^{1/4}\,\kappa_1^{-1}\,; \tag{7.24}$$

$$E_p'^{(\mathrm{acc},\,pp)} = 4\times10^6\ \mathrm{GeV}\times r_{11}\,(\Gamma_j\theta)_0\,\epsilon_{B,-1}^{1/2}E_{52}^{-1/2}\,t_1^{1/2}\,\kappa_1^{-1}\,. \tag{7.25}$$

Hence the maximum proton energy

$$E'_{p,\mathrm{max}} = \min\left[E_p'^{(\mathrm{acc,\,s})}, E_p'^{(\mathrm{acc},\,p\gamma\pi)}, E_p'^{(\mathrm{acc},\,pp)}\right] \tag{7.26}$$

is limited by pp interactions for small radii,

$$r \lesssim r_*^{pp} = 3\times10^9\ \mathrm{cm}\times(\Gamma_j\theta)_0\,\epsilon_{e,-1}^{-3/2}\,E_{52}^{1/2}\,t_1^{-1/2}\,. \tag{7.27}$$

For larger radii the proton energy is limited by photopion production as long as $\epsilon_e \sim \epsilon_B$ and $\kappa >$ few.

We now estimate the proton energy range for which pp collisions are dominant over photopion production. First we note that only photons with sufficient energy can create pions. Photopion production is possible when (averaging over an isotropic photon distribution)

$$E'_p\epsilon'_\gamma \geq \frac{m_\pi^2c^4}{2} + m_\pi m_p c^4 = 1.4\times10^5\ \mathrm{MeV}^2\,. \tag{7.28}$$

To find the photon energy $\epsilon_\gamma'^{(pp,\,p\gamma\pi)}$ for which the energy loss times due to pp and photopion interactions are equal, we require that the fraction $\xi_{p\gamma}$ of photons that participates in photopion production be equal to:

$$\xi_{p\gamma} = \frac{\sigma_{pp}K_{pp}n'_p}{\sigma_{p\gamma}K_{p\gamma}n'_\gamma} \simeq 3\times10^{-2}\times r_{11}^{-1/2}\,(\Gamma_j\theta)_0^{-1/2}\,\epsilon_{e,-1}^{-3/4}\,E_{52}^{1/4}\,t_1^{-1/4}\,. \tag{7.29}$$

Given a photon distribution with temperature T_j, the fraction of photons that has energy greater than ϵ'_γ can be expressed in terms of the dimensionless parameter

$$x_{p\gamma} = \frac{\epsilon'_\gamma}{k_B T_j}\,. \tag{7.30}$$

We find that for $x_{p\gamma} \simeq 7$, this fraction is approximately 0.03 as required by eq. (7.29). (The estimate is quite robust: when $\xi_{p\gamma}$ varies within an order of magnitude, $x_{p\gamma}$ is within a factor 2 of this estimate). Together with eq. (7.28) this defines the critical proton energy where energy loss due to photopion production and pp interactions are equally important:

$$E'^{\,(pp,\,p\gamma\pi)}_p = 5 \times 10^3 \text{ GeV} \times r_{11}^{1/2} \, (\Gamma_j \theta)_0^{-1/2} \, (\epsilon_e E)_{51}^{-1/4} \, t_1^{1/4} \, . \tag{7.31}$$

Razzaque et al. (2005) have found previously that pp interactions in a mildly relativistic jet associated with a choked GRB are dominant at energies $E'_p \lesssim 10^4$ GeV and $E'_p \gtrsim 10^5$ GeV. We find however that the high-energy range is an artifact of the Delta-resonance approximation used by these authors to estimate the photopion cross section. This approximation is accurate for interactions near the pion production threshold but it strongly underestimates the proton energy loss time at high proton energies. Using a more realistic cross section (see appendix 7.A), we find that pp interactions are only dominant at low energies, $E'_p < E'^{\,(pp,\,p\gamma\pi)}_p$, where $E'^{\,(pp,\,p\gamma\pi)}_p$ is given in eq. (7.31).

7.3.3 Proton acceleration by internal shocks

The internal shock radius was estimated in eq. (7.7) to be equal to

$$r_{\rm int} \simeq 2c\Gamma_j^2 \delta t \simeq 6 \times 10^{11} \text{ cm} \times \Gamma_{j,1}^2 \delta t_{-1} \, . \tag{7.32}$$

To address proton acceleration and energy loss in internal shocks, we can use results obtained in the previous section by inserting $r = r_{\rm int}$. Because this alters the dependence on the model parameters we explicitly give the acceleration time, shock lifetime, synchrotron energy loss time, and pp energy loss time in the internal shocks:

$$t'_{\rm a,\,int} \simeq 6 \times 10^{-9} \text{ s} \times E'_{p,3} \, \Gamma_{j,1}^3 \, \theta_{-1} \, (\epsilon_B E)_{51}^{-1/2} \, t_1^{1/2} \, \delta t_{-1} \, \kappa_1 \, ; \tag{7.33}$$

$$t'_{\rm d,\,int} \simeq 2 \text{ s} \times \Gamma_{j,1} \, \delta t_{-1} \, ; \tag{7.34}$$

$$t'_{\rm s,\,int} \simeq 1 \times 10^{-1} \text{ s} \times E'^{-1}_{p,3} \, \Gamma_{j,1}^6 \, \theta_{-1}^2 \, (\epsilon_B E)_{51}^{-1} \, t_1^1 \, \delta t_{-1}^2 \, ; \tag{7.35}$$

$$t'_{pp,\rm int} \simeq 10^{-4} \text{ s} \times E_{52}^{-1} \, \Gamma_{j,1}^6 \, \theta_{-1}^2 \, t_1 \, \delta t_{-1}^2 \, . \tag{7.36}$$

We find that the maximum attainable proton energy in internal shocks is limited by photopion energy loss as long as $\epsilon_e \simeq \epsilon_B$ and $\kappa >$ few, which is in keeping with conclusions drawn by Ando & Beacom (2005). The maximum energy is found by inserting eq. (7.7) into eq. (7.24):

$$E'^{\,(\rm acc,\,p\gamma\pi)}_p = 2 \times 10^6 \text{ GeV} \times \Gamma_{j,1}^{3/2} \, \theta_1^{1/2} \, \epsilon_{e,-1}^{-3/4} \, \epsilon_{B,-1}^{1/2} \, E_{52}^{-1/4} \, t_1^{1/4} \, \delta t_{-1}^{1/2} \, \kappa_1^{-1} \, , \tag{7.37}$$

and the energy where energy-loss due to photopion processes and pp collisions are equally important is

$$E'^{\,(pp,\,p\gamma\pi)}_p = 10^4 \text{ GeV} \times \Gamma_{j,1}^{3/2} \, \theta_{-1}^{1/2} \, (\epsilon_e E)_{51}^{-1/4} \, \delta t_{-1}^{1/2} \, t_1^{1/4} \, . \tag{7.38}$$

Hence for proton energies $E'_p < E'^{(pp,\,p\gamma\pi)}_p$, pp interactions are the dominant source of proton energy loss. These interactions occur very frequently; in fact, the optical depth τ_{pp} for a pp interaction to occur in the outflowing jet from radius r to infinity can be estimated with

$$\tau_{pp} = \frac{\sigma_{pp} n'_{p,j} r}{\Gamma_j} = 3 \times 10^4 \times \Gamma_{j,1}^{-5}\, \theta_{-1}^{-2}\, E_{52}\, t_1^{-1}\, \delta t_{-1}^{-1}\,. \tag{7.39}$$

Therefore protons with energy smaller than $E'^{(pp,\,p\gamma\pi)}_p$ will lose all their energy in pp interactions when internal shocks occur. This is different in the model put forward by Mészáros & Waxman (2001), where $\Gamma_j \simeq 100$. Because of the larger Lorentz factor and the lower isotropic luminosity assumed in that work, the optical depth for pp interactions in the jet is small. In this scenario high-energy protons from internal shocks lose energy predominantly in interactions with the photon gas in the jet head.

7.3.4 Proton acceleration by the reverse shock

Protons that are accelerated by the reverse shock suffer energy loss both in the jet head (upstream of the shock) and in the jet itself (downstream). The estimates presented in sections 7.3.1 and 7.3.2 apply only to the downstream region. From the estimates on the comoving proton and photon densities given in section 7.2, we find that the critical proton energies in the upstream region are similar to those in the downstream region. Therefore we use the results derived in these sections to estimate the maximum proton energy that can be acquired by acceleration in the reverse shock.

At small radii, $r \lesssim r_*^{pp}$, proton acceleration is limited by pp collisions and therefore $E'_{p,\max} = E'^{(\mathrm{acc},\,pp)}_p$. With increasing r the maximum energy increases according to $E'_{p,\max} \propto r$ until r equals r_*^{pp}. Here photopion production becomes important: the maximum proton energy is now limited by photopion production and $E'_{p,\max} = E'^{(\mathrm{acc},\,p\gamma\pi)}_p$ which increases more gradually $\propto r^{1/2}$.

Protons lose energy both by pp collisions and by photopion production. Energy loss by photopion production is dominant over pp collisions for high proton energies, $E'_p > E'^{(pp,\,p\gamma\pi)}_p$. The highest proton energy that is available for pp collisions is just before the critical radius r_*^{pp}, where $E'_{p,\max} \simeq 10^5$ GeV. As soon as photopion interactions become important, the maximum proton energy for pp collisions drops dramatically to $E'_{p,\max} \simeq 10^3$ GeV and thereafter increases with radius according to $\propto r^{1/2}$.

Protons that are accelerated in the reverse shock also lose virtually all their energy in interactions with the flow before impacting on the pre-burst stellar material. The optical depth for pp interactions in the jet head is equal to

$$\tau_{pp} = n'_{p,h} \sigma_{pp} \Delta' = 7 \times 10^5 \times r_{11}^{-1}\, (\Gamma_j \theta)_0^{-1}\, E_{52}\, \Gamma_h^{-1}\, t_1^{-1}\,, \tag{7.40}$$

where the comoving width of the jet head is given in eq. (7.12). We conclude that protons with energy below $E'_p < E'^{(pp,\,p\gamma\pi)}_p$ lose all their energy in pp collisions with target protons in the jet head before they can interact with the pre-burst stellar material.

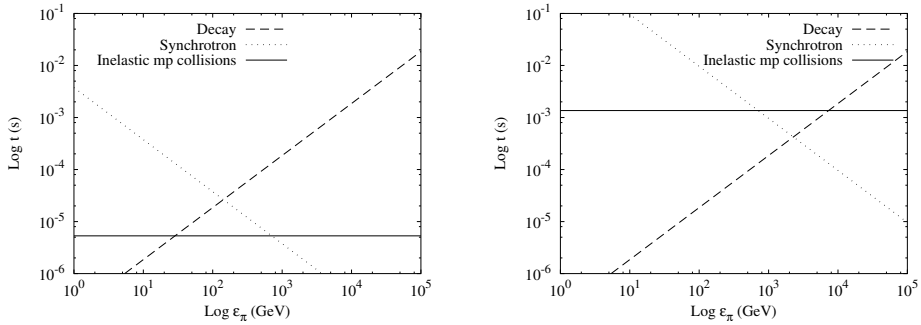

Figure 7.2: Pion decay timescale (dashed) together with energy loss timescales due to synchrotron radiation (dotted) and inelastic mp collisions (solid). Both panels correspond to the internal shock scenario. Left panel: $\Gamma_j = 5$, right panel: $\Gamma_j = 20$. We have chosen reference values for the other model parameters.

7.4 Meson cooling

Charged secondary mesons created in pp interactions can lose a substantial amount of their energy before decay, which suppresses the flux of high-energy neutrinos. Here we compare the energy loss times due to synchrotron radiation and meson – proton interaction with the meson decay time, both for the internal shock and the reverse shock scenario.

7.4.1 Meson energy loss in the jet

The synchrotron cooling timescale is given by equation (7.18) with the replacement $m_p \to m_m$ (we use the subscript m to denote either the π or K meson) and using $r = r_{\rm int}$:

$$t'_{\pi,\rm s} = 6\times10^{-5}\ {\rm s}\times\epsilon'^{-1}_{\pi,3}\,\Gamma^{6}_{j,1}\,\theta^{2}_{-1}\,(\epsilon_B E)^{-1}_{51}\,\delta t^{2}_{-1}\,t^{1}_{1}\,; \tag{7.41}$$

$$t'_{K,\rm s} = 10^{-2}\ {\rm s}\times\epsilon'^{-1}_{\pi,3}\,\Gamma^{6}_{j,1}\,\theta^{2}_{-1}\,(\epsilon_B E)^{-1}_{51}\,\delta t^{2}_{-1}\,t^{1}_{1}\,. \tag{7.42}$$

Using an average meson – proton cross section $\sigma_{mp} = 5\times10^{-26}$ cm^2 and an average meson fractional energy loss $K_{pm} = 0.8$ we find

$$t'_{\pi,\pi p} = t'_{K,Kp} = 8\times10^{-5}\ {\rm s}\times\Gamma^{6}_{j,1}\,\theta^{2}_{-1}E^{-1}_{52}\,\delta t^{2}_{-1}\,t^{1}_{1}\,. \tag{7.43}$$

We do not consider energy loss due to Inverse Compton scattering because it is at most comparable to synchrotron energy loss when $\epsilon_e \simeq \epsilon_B$. The comoving meson decay times are given by the expressions:

$$t'_{\pi,\rm dec} = 2\times10^{-4}\ {\rm s}\times\epsilon_{\pi,3}\,; \tag{7.44}$$

$$t'_{K,\rm dec} = 2\times10^{-5}\ {\rm s}\times\epsilon_{K,3}\,. \tag{7.45}$$

From these decay times and energy loss times we estimate the following critical energies, where we use the notation $\epsilon'_m{}^{(a,b)}$ to denote the meson energy where the timescales associated with processes a and b are equal:

$$\epsilon'_\pi{}^{(\mathrm{dec},\pi p)} = 5\times10^2\ \mathrm{GeV}\times\Gamma_{j,1}^6\,\theta_{-1}^2\,E_{52}^{-1}\,\delta t_{-1}^2\,t_1\,; \tag{7.46}$$

$$\epsilon'_\pi{}^{(\mathrm{dec,s})} = 6\times10^2\ \mathrm{GeV}\times\Gamma_{j,1}^3\,\theta_{-1}\,(\epsilon_B E)_{51}^{-1/2}\,\delta t_{-1}\,t_1^{1/2}\,; \tag{7.47}$$

$$\epsilon'_\pi{}^{(\mathrm{s},\pi p)} = 7\times10^2\ \mathrm{GeV}\times\epsilon_{B,-1}^{-1}\,, \tag{7.48}$$

and

$$\epsilon'_K{}^{(\mathrm{dec},Kp)} = 4\times10^3\ \mathrm{GeV}\times\Gamma_{j,1}^6\,\theta_{-1}^2\,E_{52}^{-1}\,\delta t_{-1}^2\,t_1\,; \tag{7.49}$$

$$\epsilon'_K{}^{(\mathrm{dec,s})} = 2\times10^4\ \mathrm{GeV}\times\Gamma_{j,1}^3\,\theta_{-1}\,(\epsilon_B E)_{51}^{-1/2}\,\delta t_{-1}\,t_1^{1/2}\,; \tag{7.50}$$

$$\epsilon'_K{}^{(\mathrm{s},Kp)} = 10^5\ \mathrm{GeV}\times\epsilon_{B,-1}^{-1}\,. \tag{7.51}$$

In figure 7.2 we have plotted the comoving pion energy loss times due to synchrotron radiation and inelastic mp collisions together with the comoving decay time. We have chosen two values for the Lorentz factor of the jet, $\Gamma_j = 5$ (left panel) and $\Gamma_j = 20$ (right panel), to demonstrate that there may or may not be a meson energy range where mp collisions provide the shortest timescale. This distinction is important because it determines the shape of the neutrino spectrum: if synchrotron is the only important energy loss mechanism, the resulting neutrino spectrum will have a single break energy where the neutrino spectrum is suppressed by $\zeta(\epsilon'_m) = t'_{m,\mathrm{s}}/t'_{m,\mathrm{dec}} \propto \epsilon_m^{'-2}$, where $\zeta(\epsilon'_m)$ denotes the neutrino suppression factor. In case inelastic mp collisions are important, the spectrum will have two break energies. At every break the spectrum is suppressed by a factor $\epsilon_m^{'-1}$.

7.4.2 Meson energy loss in the jet head

Due to the higher proton density and stronger magnetic field in the jet head, cooling of mesons is stronger than in the jet. We summarize here the critical energies for meson cooling in the jet head. For pions we find:

$$\epsilon'_\pi{}^{(\mathrm{dec},\pi p)} = 6\times10^{-1}\ \mathrm{GeV}\times r_{11}^2\,\Gamma_{j,1}\,\theta_{-1}^2\,E_{52}^{-1}\,t_1\,\Gamma_h\,; \tag{7.52}$$

$$\epsilon'_\pi{}^{(\mathrm{dec,s})} = 9\ \mathrm{GeV}\times r_{11}\,\theta_{-1}\,(\epsilon_B E)_{51}^{-1/2}\,t_1^{1/2}\,\Gamma_h\,; \tag{7.53}$$

$$\epsilon'_\pi{}^{(\mathrm{s},\pi p)} = 1\times10^2\ \mathrm{GeV}\times\Gamma_{j,1}^{-1}\,\epsilon_{B,-1}^{-1}\,\Gamma_h\,, \tag{7.54}$$

and for kaons:

$$\epsilon'_K{}^{(\mathrm{dec},Kp)} = 5\ \mathrm{GeV}\times r_{11}^2\,\Gamma_{j,1}\,\theta_{-1}^2\,E_{52}^{-1}\,t_1\,\Gamma_h\,; \tag{7.55}$$

$$\epsilon'_K{}^{(\mathrm{dec,s})} = 3\times10^2\ \mathrm{GeV}\times r_{11}\,\theta_{-1}\,(\epsilon_B E)_{51}^{-1/2}\,t_1^{1/2}\,\Gamma_h\,; \tag{7.56}$$

$$\epsilon'_K{}^{(\mathrm{s},Kp)} = 2\times10^4\ \mathrm{GeV}\times\Gamma_{j,1}^{-1}\,\epsilon_{B,-1}^{-1}\,\Gamma_h\,. \tag{7.57}$$

These break energies are used in the following sections to discuss the neutrino energy spectrum and the detection prospects.

7.5 Neutrino emission

7.5.1 Neutrino flux and proton spectrum

We express the observed differential neutrino flux Φ_ν as follows:

$$\Phi_\nu(\epsilon_\nu) = \frac{1}{4\pi D_p^2 t}\frac{dn_\nu}{d\epsilon_\nu}\,, \tag{7.58}$$

where $D_p = 100\,D_{p,2}$ Mpc denotes the distance to the burst, and we recall that t denotes the burst duration. The neutrino energy spectrum can be computed from the spectrum of high-energy protons through a model for the production of secondary pions and kaons in pp collisions. In section 7.5.3 we describe a numerical approach to this problem that is based on the full parameterization (see chapter 6) of the energy and angular distribution of secondary pions and kaons produced in energetic pp collisions . Here we present estimates of the neutrino flux with some simplifying assumptions regarding the energy and multiplicity of the secondary pions and kaons. We use the same approximations as Ando & Beacom (2005) for comparison.

We consider only the prompt neutrino from kaon and pion decay. Neutrinos from subsequent muon decay are expected to have a very low energy due to the relatively long muon lifetime. Following Ando & Beacom (2005), we take the pion and kaon multiplicities as $\mathcal{M}_\pi = 1$ and $\mathcal{M}_K = 0.1$, respectively, and we assume that both pions and kaons receive 20% of the proton energy. Muon-neutrinos from pion and kaon decay receive approximately 50% and 25% of the parent meson's energy, respectively. As the neutrinos are produced very forward in the jet frame, the neutrino energy is boosted to the observer frame with a Lorentz boost $\Gamma \simeq 2\Gamma_j$. From these considerations we express the observed neutrino energy ϵ_ν in terms of the comoving proton energy E'_p as follows:

$$\epsilon_\nu = \alpha_m \Gamma_j E'_p\,, \tag{7.59}$$

where $\alpha_\pi = 0.1$ and $\alpha_K = 0.2$. It follows that the (observer-frame) neutrino spectrum can be approximated by

$$\frac{dn_\nu}{d\epsilon_\nu} = \frac{\mathcal{M}_m \mathcal{B}_m \zeta(\epsilon_\nu)}{\alpha_m \Gamma_j}\frac{dN_p}{dE'_p}\,, \tag{7.60}$$

where $\zeta(\epsilon_\nu)$ denotes the suppression factor due to meson energy loss (see previous section) and $\mathcal{B}_m$ denotes the branching ratio for the meson-to-neutrino decay ($\mathcal{B}_\pi = 1$ and $\mathcal{B}_K = 0.63$).

We assume in the following that the accelerated protons follow a power-law distribution with index p and that these protons constitute a fraction $\xi_p = 0.01\xi_{p,-2}$ of all nucleons in the flow. Hence the proton spectrum, in the jet frame, reads

$$\frac{dN_p}{dE'_p} = \frac{\xi_p N_{N,\rm iso}(p-1)E_p^{'-p}}{(m_p c^2)^{1-p}}\,, \tag{7.61}$$

where

$$N_{N,\rm iso} = \frac{E_{\rm iso}}{m_p c^2 \Gamma_j} = 10^{56} \times \Gamma_{j,1}^{-1}\,\theta_{-1}^{-2}\,E_{52} \tag{7.62}$$

is the isotropic-equivalent amount of neutrons in the flow.

7.5.2 Spectral breaks and maximum energy

As discussed in section 7.4, meson energy loss prior to decay suppresses the number of high-energy neutrinos. Here we estimate the energy of the corresponding spectral breaks in the (observer-frame) neutrino spectrum using the simplifying assumptions for the particle physics discussed in the previous section.

We restrict ourselves to the case that the neutrino spectrum has two distinct break energies (which may be above the maximum energy or below the detector threshold). For neutrino production in internal shocks this is the case for jet Lorentz factors $\Gamma_j \lesssim 10$, which follows from equating the critical meson energies presented in section 7.4.1. For the reverse shock the neutrino spectrum from pion decay has two distinct spectral breaks for radii $r \lesssim 10^{12}$ cm. The corresponding radius for neutrino from kaon decay is $\sim 7 \times 10^{13}$ cm, which is beyond the radius of the H envelope.

We approximate the break energies for neutrinos from pion decay as follows:

$$\epsilon_{\nu(\pi)}^{\rm br,1} \simeq 5\Gamma_{j,1}\epsilon_\pi'^{\,({\rm dec},\pi p)}\,; \tag{7.63}$$

$$\epsilon_{\nu(\pi)}^{\rm br,2} \simeq 5\Gamma_{j,1}\epsilon_\pi'^{\,({\rm s},\pi p)}\,. \tag{7.64}$$

For neutrino production in internal shocks the critical pion energies are given in eqs. (7.46) and (7.48), respectively. For neutrino production in the reverse shock, the critical energies are given in eqs. (7.52) and (7.54). Similarly, we find that the break energies for neutrinos from kaon decay are

$$\epsilon_{\nu(K)}^{\rm br,1} \simeq 10\Gamma_{j,1}\epsilon_K'^{\,({\rm dec},\pi p)}\,; \tag{7.65}$$

$$\epsilon_{\nu(K)}^{\rm br,2} \simeq 10\,\Gamma_{j,1}\epsilon_K'^{\,({\rm s},\pi p)}\,. \tag{7.66}$$

For internal shock the critical energies are given in eqs. (7.49) and (7.51), for the reverse shock they are expressed in eqs. (7.55) and (7.57).

In section 7.3 we estimated the maximum proton energy $E_p'^{(pp,\,p\gamma\pi)}$ for pp interactions in the jet. From this energy we estimate the maximum neutrino energy from pion and kaon decay as

$$\epsilon_{\nu(\pi)}^{\max} \simeq \Gamma_{j,1} E_p'^{(pp,\,p\gamma\pi)}; \tag{7.67}$$

$$\epsilon_{\nu(K)}^{\max} \simeq 2\Gamma_{j,1} E_p'^{(pp,\,p\gamma\pi)}, \tag{7.68}$$

respectively. Here $E_p'^{(pp,\,p\gamma\pi)}$ denotes the maximum proton energy available for pp interactions. For internal shocks this energy is expressed in eq. (7.38). For the reverse shock, the maximum proton energy available for pp interactions is determined both by the upstream and the downstream region. As discussed in section 7.3.4, the resulting constraints are similar and we can use eq. (7.31) to estimate $E_p'^{(pp,\,p\gamma\pi)}$.

7.5.3 Numerical method

In chapter 6 we have presented a parameterization of the energy and angular distribution of secondary pions and kaons produced in energetic pp collisions. Here we use this parameterization to study in detail the properties of neutrino emission by pp interaction in the choked jet.

In our numerical method, we first discretize the distribution of secondary pions and kaons created in the interaction of a distribution of high-energy protons with a target proton at rest (in the comoving frame). In this process the meson energy is divided into 100 bins with logarithmic division and the rapidity is divided into 100 bins with a linear division. The effect of meson cooling is taken into account by multiplying the number of mesons in every bin with the cooling suppression factor ζ (see section 7.4). The neutrino outgoing angle and energy are discretized, in the observer frame, in 100 bins each with a logarithmic division. Then, for every neutrino and meson bin, we compute the neutrino energy as observed in the rest frame of the decaying meson. The neutrino distribution in the bin under consideration is then computed from the meson decay spectrum using the invariance of $\epsilon_\nu\, d^3n_\nu/d^3p_\nu$. The distribution is weighed with the number of mesons in the meson bin and averaged over the azimuthal angle between neutrino and decaying meson. This process is repeated for all meson and neutrino bins.

The meson decay process is kinematically fully prescribed so that the resulting neutrinos are mono-energetic. For numerical reasons we have introduced a decay width of a few MeV, which does not affect the resulting spectra strongly. We have verified that the number of bins is sufficient for convergence of the results.

7.5.4 Results

In figure 7.3 we show the differential neutrino flux from energetic pp collisions in internal shocks. Shown are the analytical approximations based on the break energies

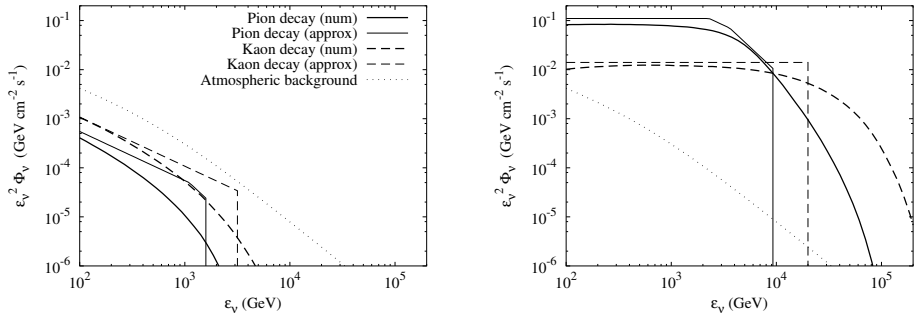

Figure 7.3: Differential neutrino flux due to pion decay (solid lines) and kaon decay (dashed) produced in energetic pp collisions in internal shocks for a choked GRB at 100 Mpc. The thick lines show numerical results, the thin lines show the analytical approximations. The dotted line shows the atmospheric neutrino background (see section 7.6.2). In the left panel we have used $\Gamma_j = 3$, in the right panel $\Gamma_j = 10$. We have chosen reference values for the other model parameters. The meaning of the lines in the right panel is the same as in the left panel.

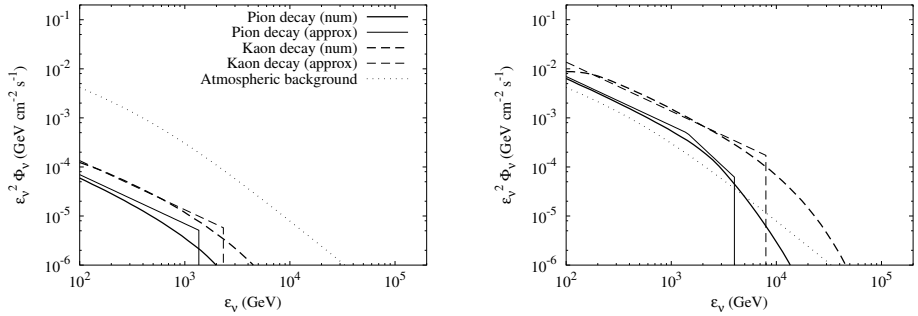

Figure 7.4: Differential neutrino flux due to pion decay (solid lines) and kaon decay (dashed) produced in energetic pp collisions in the reverse shock for a choked GRB at 100 Mpc. The thick lines show numerical results, the thin lines show the analytical approximations. The dotted line shows the atmospheric neutrino background (see section 7.6.2). In the left panel we have used $r = 10^{10}$ cm, in the right panel $r = 10^{11}$ cm. We have chosen reference values for the other model parameters. The meaning of the lines in the right panel is the same as in the left panel.

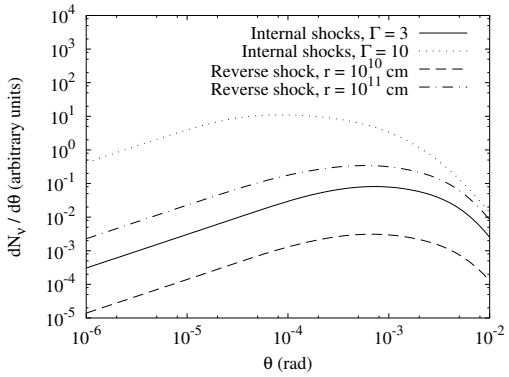

Figure 7.5: Zenith angle distribution of neutrinos with energy > 100 GeV around the incident proton direction. We plotted here the combined distribution of neutrinos from pion and kaon decay, for four different scenarios.

estimated in section 7.5.2 together with results obtained with the numerical method described in section 7.5.3. We have plotted neutrinos with energy larger than 100 GeV because this is roughly the threshold energy for detection with a cubic-kilometer neutrino telescope.

For both pions and kaons the analytical approximations describe the numerical results reasonably well. The locations of the cooling breaks, which are smoothened in the numerical results, are accurate and the neutrino flux around the threshold energy is within ∼30%. The discrepancy between numerical results and analytical estimates is largest at high neutrino energies. For the detection estimates this is not very important because the number of detectable neutrinos is dominated by lower energies for proton index $p \gtrsim 2$. We will come back to this in section 7.6.

We observe from figure 7.3 that the differential neutrino flux depends very sensitively on the Lorentz factor of the jet. This reflects the fact that the location of the first break energy scales with $\epsilon_\nu^{\mathrm{br},1} \propto \Gamma_j^7$ in the case of neutrino production in internal shocks. This is largely due to the fact that the internal shock radius $r_{\mathrm{int}} \propto \Gamma_j^2$.

In figure 7.4 we show the neutrino flux arising from pp interactions after proton acceleration in the reverse shock. The shape of the neutrino spectrum is similar to the examples shown in figure 7.3. Again we find a reasonably good agreement between the analytical estimates and numerical results for energies well below the maximum energy.

7.5.5 Angular dependence

The numerical method employed here yields both the energy spectrum of the secondary neutrinos as well as the angular distribution. In figure 7.5 we show the angular distribution of secondary neutrinos around the direction of an incident high-energy proton.

Indicated are the angular distributions of neutrinos resulting from proton acceleration in internal shocks with $\Gamma_j = 3$ (see the left panel of fig. 7.3), in internal shocks with $\Gamma_j = 10$ (right panel of fig. 7.3), in the reverse shock at radius $r = 10^{10}$ cm (left panel of fig. 7.4), and in the reverse shock at radius $r = 10^{11}$ cm (right panel of fig. 7.4). In all cases the neutrinos are emitted very close to the direction of the high-energy proton.

In the jet model considered here, the high-energy protons are emitted within a cone of angle θ. Since the neutrinos are strongly collimated in the direction of the protons, the neutrino signal falls off very steeply outside the jet opening angle. In this work we have only considered proton interactions where the energetic proton is moving in the radial direction. A full investigation of the prospects of detecting off-axis neutrino emission in choked GRBs requires more detailed modeling of the shock-acceleration process. This is beyond the scope of this work.

7.6 Detection estimates

7.6.1 Neutrino interactions in a cubic-kilometer detector

In this section we estimate the number of neutrino interactions inside a cubic-kilometer neutrino detector due to pp interactions in choked GRBs. We present estimates on the detection possibilities of individual choked GRBs and the diffuse neutrino flux due to unresolved bursts in section 7.6.2.

Using data from Yao et al. (2006), we approximate the neutrino – nucleon cross section with $\sigma_{\nu N}(\epsilon_\nu) = 7 \times 10^{-39}\ \mathrm{cm}^2 \times (\epsilon_\nu / 1\ \mathrm{GeV})$. For $N_t \simeq 10^{39}$ target protons,

$$\begin{aligned} N_{\mathrm{det}} &= tN_t \int d\epsilon_\nu \Phi_\nu(\epsilon_\nu)\sigma_{\nu N}(\epsilon_\nu) \\ &= 8 \times \mathcal{E}_\nu \mathcal{M}_m \mathcal{B}_m (10\alpha_m)^{p-1}(p-1)\,\Gamma_{j,1}^{p-2}\,\theta_{-1}^{-2}\,E_{52}\,\xi_{p,-2}\,d_{p,2}^{-2}\,. \end{aligned} \tag{7.69}$$

In this expression

$$\mathcal{E}_\nu := \mathrm{GeV}^{-1} \int_{\epsilon_\nu^{\mathrm{th}}} d\epsilon_\nu\, \zeta(\epsilon_\nu) \left(\frac{\epsilon_\nu}{\mathrm{GeV}}\right)^{-p+1} \tag{7.70}$$

represents the integral over the neutrino energy distribution weighed with the energy-dependent cross section, and $\epsilon_\nu^{\mathrm{th}}$ represents the detector threshold neutrino energy. Because the cross section scales with energy, $\mathcal{E}_\nu$ is also a measure of the energy in the neutrino distribution.

Internal shocks

We first consider neutrino production in internal shocks. For simplicity we consider a proton distribution with power-law index $p = 2$. Furthermore we neglect the effect of the maximum proton energy on the neutrino spectrum because the largest contribution to the

number of detected neutrinos is from neutrinos with energy within an order of magnitude from the threshold energy (assuming a proton distribution with power-law index $\gtrsim 2$). Therefore the exact location of the maximum energy is not very important as long as $\epsilon_\nu^{\rm max} \gg 10^3$ GeV. We have verified that the optical depth for neutrino – proton scattering in the jet is very small for the neutrino energies considered here.

We consider the case that the neutrino energy spectrum has two spectral breaks. The integral that determines $\mathcal{E}_\nu$, given in eq. (7.70), is then easily solved and yields:

$$\mathcal{E}_\nu = f\left(\frac{\epsilon_\nu^{\rm br,1}}{\epsilon_\nu^{\rm th}}\right) - \frac{\epsilon_\nu^{\rm br,1}}{2\epsilon_\nu^{\rm br,2}}\,, \tag{7.71}$$

where the function f is defined as follows:

$$f(x) := \begin{cases} x & (x \le 1) \\ \log(x) + 1 & (x > 1) \end{cases}\,. \tag{7.72}$$

The second term is much smaller than the first over a large range of model parameters and we neglect this term. Using the estimated values for the neutrino break energies given in section 7.5.2, we find:

$$N_{\rm det\,(\pi)} = 8 \times \theta_{-1}^{-2}\, E_{52}\, d_{p,2}^{-2}\, \xi_{p,-2}\, f\left(23\,\Gamma_{j,1}^{7}\theta_{-1}^{2} E_{52}^{-1}\delta t_{-1}^{2} t_1\right)\,; \tag{7.73}$$

$$N_{\rm det\,(K)} = 1 \times \theta_{-1}^{-2}\, E_{52}\, d_{p,2}^{-2}\, \xi_{p,-2}\, f\left(350\,\Gamma_{j,1}^{7}\theta_{-1}^{2} E_{52}^{-1}\delta t_{-1}^{2} t_1\right)\,. \tag{7.74}$$

Note that the dependence on the jet Lorentz factor Γ_j is very strong. In particular, in the case that the first spectral break is below the detector threshold, $N_{\rm det} \propto \Gamma_j^7$. This strong dependence is due to the fact that $N_{\rm det}$ is very sensitive to the location of the first cooling peak.

In figure 7.6 (left panel) we plot the estimated number of neutrino events as a function of the jet Lorentz factor Γ_j (eqs. (7.73) and (7.74)) together with results obtained from numerical integration of the neutrino spectrum obtained with our numerical method. Note the break at $\Gamma_j \simeq 3$ ($\Gamma_j \simeq 6$) for neutrinos due to kaon (pion) decay, which marks the point where the first cooling break coincides with the detector threshold energy. We observe that the contribution due to kaon decay is dominant at smaller Lorentz factors, where the neutrino spectrum from pion decay is strongly suppressed by cooling. At larger values of Γ_j the first cooling break of the neutrino spectrum for both pion decay and kaon decay is above the detector threshold. In this case, the contribution of neutrinos from pion decay is dominant due to the larger multiplicity. At $\Gamma_j = 3$ we find that most neutrinos are from kaon decay, which is in keeping with results found by Ando & Beacom (2005). Using the reference values adopted by these authors, $\Gamma_j = 3$ and $E = 3 \times 10^{51}$ erg, we find $N_{\rm det} \simeq 3$ for a burst at 10 Mpc. This is an order of magnitude smaller than estimates presented by these authors, which results from a different normalization of the distribution of accelerated protons. For a Lorentz factor $\Gamma_j = 10$ we

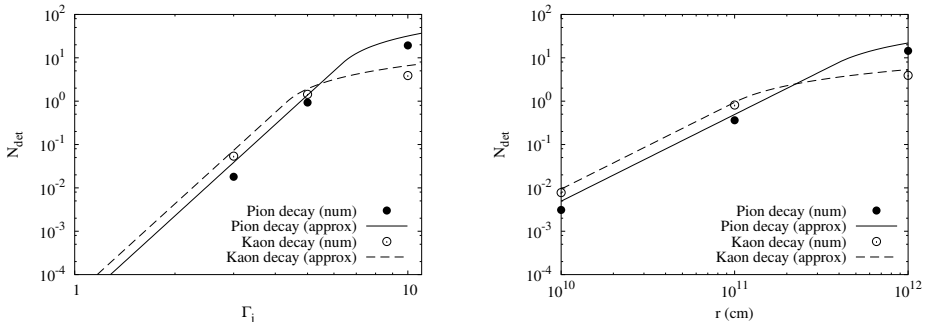

Figure 7.6: Estimated number of neutrino interactions in a cubic-kilometer neutrino detector for a choked GRB at 100 Mpc. The left panel shows the number of neutrino events resulting from internal shocks as a function of the jet Lorentz factor Γ_j; the right panel shows the number of events due to the reverse shock as a function of the shock radius r. In both panels the lines represent analytical approximations (see text), while the dots represent numerical results. In producing this plot we have used reference values for the model parameters and $\Gamma_h = 2$.

find that, for reference values of the other parameters, a burst at 100 Mpc leads to a $\gtrsim$10 neutrino interactions inside a cubic-kilometer neutrino detector.

The number of neutrino events also depends on other model parameters such as the energy E, the variability timescale δt, the burst duration t, and the proton power-law index p. A full parametric exploration of the effect of these parameters on the expected number of neutrino events is beyond the scope of this work.

The reverse shock

Here we consider neutrino production in the reverse shock. In the case that the neutrino spectrum has two spectral breaks, we can use eq. (7.71) directly to estimate the number of detected neutrinos:

$$N_{\det(\pi)} = 8 \times \theta_{-1}^{-2} E_{52} d_{p,2}^{-2} \xi_{p,-2} f\left(0.032 r_{11}^2 \Gamma_{j,1}^2 \theta_{-1}^2 E_{52}^{-1} t_1 \Gamma_h\right); \quad (7.75)$$

$$N_{\det(\mathrm{K})} = 1 \times \theta_{-1}^{-2} E_{52} d_{p,2}^{-2} \xi_{p,-2} f\left(0.49 r_{11}^2 \Gamma_{j,1}^2 \theta_{-1}^2 E_{52}^{-1} t_1 \Gamma_h\right), \quad (7.76)$$

where the function f is defined in eq. (7.72). Adding the contribution of neutrinos due to pion and kaon decay, we find that neutrino emission from the reverse shock may be detectable for radii $r \gtrsim r_*^{\mathrm{rev,\,det}}$, where

$$r_*^{\mathrm{rev,\,det}} = 8 \times 10^{10}\ \mathrm{cm} \times \Gamma_j^{-1} t_1^{-1/2} \xi_{p,-2}^{-1/2} d_{p,2} \Gamma_h^{-1/2}. \quad (7.77)$$

For smaller radii meson cooling is so strong that the resulting neutrino signal is prohibitively small. Neutrino interactions in the jet head or with stellar material are not important at radii larger than 10^{10} cm for the neutrino energies considered here.

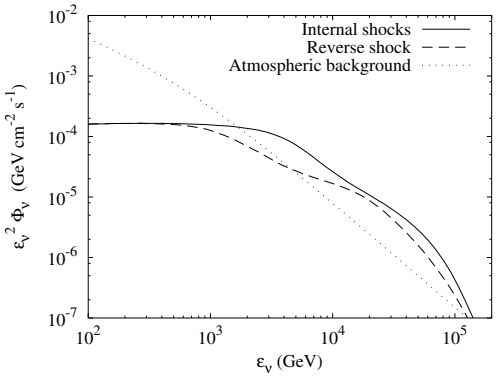

Figure 7.7: Comparison of diffuse neutrino flux due to choked GRBs and the atmospheric neutrino background. Shown are the contributions from internal shocks (solid line) and the reverse shock (dashed line). In producing this figure we have chosen $\Gamma_j = 10$, $r = 10^{12}$ cm for the reverse shock, and reference values for the other model parameters. We have added the contributions from pion and kaon decay here.

In figure 7.6 (right panel) we show the number of detected events due to the reverse shock as a function of the radius r. The plot is qualitatively similar to the corresponding plot for neutrino emission in internal shocks (left panel of figure 7.6). The number of detected neutrinos due to kaon decay shows a break at the radius $\sim 10^{11}$ cm, where the first cooling break coincides with the detector threshold energy. For radii much smaller than this critical radius neutrinos from kaon decay are dominant, while at larger radii most detectable neutrinos are due to pion decay. For radii $\gtrsim 10^{12}$ cm, neutrino emission due to proton acceleration in the reverse shock can be substantial. For reference values of the model parameters, we find $\gtrsim 10$ neutrino interactions for a burst at 100 Mpc.

7.6.2 Point sources and diffuse flux

In the previous section we have found that a choked GRB at 100 Mpc may result in $\gtrsim 10$ neutrino interactions inside a cubic-kilometer neutrino detector (both for proton acceleration in internal shocks and in the reverse shock). Here we compare the neutrino flux of individual bursts to the atmospheric neutrino background and estimate the diffuse flux of unidentified choked GRBs.

We first estimate the rate of choked GRBs within 100 Mpc. Following Porciani & Madau (2001), we adopt the following type-II supernova rate $\dot{n}_{\rm SN}$ as a function of redshift z:

$$\dot{n}_{\rm SN}(z) = \frac{4 \times 10^{-3} \exp(3.4z)}{\exp(3.8z) + 45} \ {\rm yr}^{-1}\,{\rm Mpc}^{-3}\,, \tag{7.78}$$

where we use the currently favored value $H_0 = 73$ km s^{-1} Mpc^{-3} for the Hubble param-

eter (Yao et al. 2006). Within the current ΛCDM cosmological paradigm, the comoving volume element dV within the redshift range $z \ldots z+dz$ can be expressed in the following way:

$$dV = \frac{4\pi c D_p^2 dz}{H_0 \sqrt{\Omega_{\Lambda,0} + \Omega_{m,0}(1+z)^3}}\,, \tag{7.79}$$

where $\Omega_{\Lambda,0} = 0.76$ and $\Omega_{m,0} = 0.24$ represent the current density parameters of the cosmological constant and matter, respectively (Yao et al. 2006). The proper density D_p is expressed as

$$D_p = \frac{c}{H_0} \int_0^z \frac{dz'}{\sqrt{\Omega_{\Lambda,0} + \Omega_{m,0}(1+z)^3}}\,. \tag{7.80}$$

Integrating the redshift-dependent supernova rate given in eq. (7.78) over the comoving volume up to $z = 0.024$ (100 Mpc), we find that the rate of SNe within 100 Mpc is $\sim$400 yr^{-1}. Due to the collimation of the relativistic flow, a fraction $\theta^2/2$ of choked bursts is pointed toward earth. Therefore the rate of choked GRBs emitting neutrinos toward earth within 100 Mpc is estimated as follows:

$$\dot{N}_{\rm CGRB} = 2\ {\rm yr}^{-1} \times \xi_{\rm SN} \theta_{-1}^2\,, \tag{7.81}$$

where $\xi_{\rm SN}$ is the fraction of supernovae that is endowed with the type of relativistic outflows considered in this work. This is a conservative estimate in the sense that the reference opening angle adopted here, $\sim$5 degrees, is relatively small.

Following Razzaque et al. (2005) we adopt the following parameterization for the flux of atmospheric muon-neutrinos in the relevant energy range:

$$\Phi_{\nu,\,\rm atm} = (4\pi)\, 0.012 \left(\frac{\epsilon_\nu}{1\ {\rm GeV}}\right)^{-2.74} \left(1 + 0.002 \left(\frac{\epsilon_\nu}{1\ {\rm GeV}}\right)\right)^{-1}\,, \tag{7.82}$$

where we have included the factor 4π to account for background signals from all directions. If the choked GRB is accompanied by a visible SN the number of background events can be strongly reduced by using directional information (a full analysis of the neutrino reconstruction potential with and without directional and temporal information is beyond the scope of this work).

In figures 7.3 and 7.4 we show the estimated neutrino fluxes from a choked GRB at 100 Mpc together with the atmospheric neutrino background expressed in eq. (7.82). For neutrino production in internal shocks we observe that the neutrino flux is well above the atmospheric background for $\Gamma_j = 10$, but below the background for $\Gamma_j = 3$. For the reverse shock, the resulting neutrino flux is above the atmospheric background for radii $r \gtrsim 10^{11}$. Therefore, provided that protons are accelerated in the reverse shock, or that protons are accelerated in internal shocks and that $\Gamma_j \gtrsim 5$, we expect that a few

individual bursts will be detected per year for reference values of the model parameters and for $\xi_{\rm SN} \simeq 1$.

We now consider the diffuse flux due to unresolved choked GRBs. We neglect the effect of redshift on the observed neutrino break energies for simplicity. In this case averaging over a cosmological distribution of SNe only affects the normalization of the neutrino spectrum through the dependence on D_p (cf. eq. 7.58). We can therefore estimate the diffuse flux from previous results on the neutrino flux from a single burst by using an effective distance $D_{p,*}^{\rm diff}$ defined as follows:

$$D_{p,*}^{\rm diff} = \left(\frac{\theta^2 \xi_{\rm SN} t}{2} \int_0^\infty \frac{\dot{n}_{SN}(z)}{D_p(z)^2} \frac{dV}{dz}\, dz \right)^{-1/2} \simeq 2.4\ {\rm Gpc} \times \theta_{-1}^{-1} \xi_{\rm SN}^{-1/2} t_1^{-1/2}\,, \tag{7.83}$$

which accounts for the fact that a fraction $\theta^2/2$ of choked GRBs are directed toward earth. In figure 7.7 we show the diffuse neutrino flux due to choked GRBs estimated in this way together with the atmospheric neutrino background. We have indicated both neutrinos resulting from proton acceleration in internal shocks (adopting $\Gamma_j = 10$) and in the reverse shock (adopting $r = 10^{12}$ cm). We take reference values for the other parameters and assume that $\xi_{\rm SN} = 1$, so that the fluxes indicated in the figure represent an upper limit. The neutrino flux is based on the numerical model described in section 7.5.3. For these values of the model parameters we find that the diffuse flux is dominated by the atmospheric background for neutrino energies $\lesssim 10^3$ GeV. For neutrino energies $10^3\ {\rm GeV} \lesssim \epsilon_\nu \lesssim 10^5$ GeV the diffuse flux is a factor few larger than the background and is potentially detectable. At higher energies the figure indicates that the neutrino spectrum is suppressed. In this regime pp interactions are dominated by photopion production, which we have not considered here. Including photopion production may increase the diffuse flux significantly in this energy regime. We note that the diffuse neutrino flux due to choked GRBs within ~100 Mpc is expected to reflect the distribution of galaxies within that distance, which may help to discriminate it from the atmospheric background.

Razzaque et al. (2005) have found previously that the diffuse neutrino flux is below the atmospheric background for the reference values of the model parameters adopted in that work, in particular $\Gamma_j = 3$. For this value of the jet Lorentz factor we also find that the resulting neutrino flux is several orders below the atmospheric background.

7.7 Discussion

In the previous section we have found that pp interactions in a choked GRB may lead to observable neutrino fluxes in a cubic-kilometer neutrino detector. This applies both to the case that protons are accelerated by the reverse shock (for sufficiently large radii) and to the case that protons are accelerated by internal shocks (for sufficiently large Lorentz factors). Here we point out some uncertainties in these results.

First we stress that some of the model parameters are uncertain. In particular, the fraction of protons that is shock-accelerated may well be orders of magnitude smaller than the reference value $\xi_p \simeq 0.01$ adopted here. However, for the case of neutrino production in internal shocks, we have found that the number of detectable neutrinos is very sensitive to the Lorentz factor of the jet. Therefore a large increase in the number of detectable neutrinos requires only a small increase in Lorentz factor.

A second caveat of the results presented here is the dependence on collisionless shocks. The existence of internal shocks in choked GRBs is speculative because it is not clear whether they can indeed develop while the jet is traversing the star and has not yet created a low-density funnel[1]. The reverse shock is, on the other hand, a robust feature of the interaction of the relativistic outflow with the cold pre-burst environment. It is however less clear if the reverse shock can accelerate protons. Whether or not it may be treated as collisionless depends on the coherence length of the magnetic field, which is uncertain and difficult to predict theoretically.

7.8 Conclusions

In this chapter we studied neutrino creation through pp interactions in choked GRBs. This builds on previous work by Razzaque et al. (2005, and references therein) and Ando & Beacom (2005). We considered both proton acceleration in internal shocks, which was considered earlier, and in the reverse shock, which has not been studied in detail for choked GRBs. We used a detailed parameterization of the energy spectrum and angular distribution of secondary mesons created in pp collisions that allowed us to treat the proton interactions in more detail than previous studies.

The accelerated protons lose virtually all their energy by interactions in the jet and the jet head. Inelastic pp collisions are the dominant energy-loss mechanism at proton energies $\lesssim 10^4$ GeV, where the proton flux is relatively large, and give rise to secondary pions and kaons that decay into neutrinos. Prior to decay the mesons lose energy both through synchrotron cooling and in inelastic meson – proton collisions, which strongly affects the neutrino spectrum and hence the detection prospects.

We have considered the number of neutrinos that is detectable by a cubic-kilometer neutrino detector with energy threshold 100 GeV. For neutrino creation in internal shocks we find that, for reference values of the model parameters, a choked burst at 100 Mpc may be detectable when $\Gamma_j \gtrsim 5$. The number of neutrino events depends strongly on the jet Lorentz factor because the energy where meson cooling becomes important depends strongly on Γ_j. For neutrino production in the reverse shock, we find that the neutrino emission from a choked GRB at 100 Mpc may be detectable for radii $\gtrsim 10^{11}$ cm. The dependence on Γ_j is milder in this case. These conclusions also apply to the first stages of a successful GRB characterized by the model parameters adopted here. If the Lorentz

[1] We thank Thomas Janka for pointing this out recently (private communication).

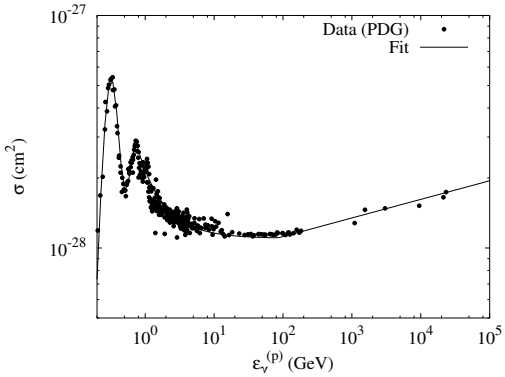

Figure 7.8: Photopion cross section as a function of the photon energy in the proton rest frame. The line indicates the fit (see text), the dots represent data taken from Yao et al. (2006).

factor of the jet is of the order 100, as inferred from observations, the optical depth for pp interactions in the jet becomes less than unity. However accelerated protons still interact with protons in the jet head which also leads to neutrino emission.

The number of choked GRBs pointing toward earth from 100 Mpc may be as large as a few per year. Therefore, provided that a sizable fraction of SNe is endowed with the relativistic outflows studied here, and provided that either the reverse shock ($r \gtrsim 10^{11}$ cm) or internal shocks ($\Gamma_j \gtrsim 5$) accelerate a significant fraction of the protons, we expect up to a few detected individual bursts per year. The diffuse flux due to unresolved choked GRBs may be a factor few above the background of atmospheric neutrinos for optimistic values of the model parameters (see fig. 7.7). Also here the Lorentz factor of the jet is the dominant parameter (for internal shocks). Hence detection of the diffuse flux may also be possible but the detection prospects for individual bursts are more promising. A more detailed exploration of the dependence on the model parameters is required to corroborate these results.

7.A Proton - photon cross section approximation

In figure 7.8 we show experimental data from Yao et al. (2006) on the total proton – photon cross section, together with the following approximation:

$$\sigma_{p\gamma} = \begin{cases} 0.53 g_1(\epsilon_\gamma^{(p)}, 0.32, 7) + 0.28 g_1(\epsilon_\gamma^{(p)}, 0.75, 5) & (\epsilon_\gamma^{(p)} < 0.75 \text{ GeV}) ; \\ 0.11 + 0.17 g_2(\epsilon_\gamma^{(p)}, 0.75, 1.1) & (0.75 \text{ GeV} < \epsilon_\gamma^{(p)} < 80 \text{ GeV}) ; \\ 0.11 (\epsilon_\gamma^{(p)}/80 \text{ GeV})^{0.08} & (\epsilon_\gamma^{(p)} > 80 \text{ GeV}) . \end{cases}$$

Here $\epsilon_\gamma^{(p)}$ denotes the photon energy in the proton rest frame, and the functions g_1 and g_2 are defined as follows:

$$g_1(\epsilon, \epsilon_0, w) = \frac{\exp\left[\left(\frac{\epsilon_0}{\epsilon}\right)^{w \log(\epsilon/\epsilon_0)}\right] - 1}{\exp(1) - 1}\,; \tag{7.84}$$

$$g_2(\epsilon, \epsilon_0, w) = \frac{\exp\left[\left(\frac{\epsilon_0}{\epsilon}\right)^{w}\right] - 1}{\exp(1) - 1}\,. \tag{7.85}$$

8

Conclusions

Although the possibility to use neutrinos as diagnostic tools for (astro)physical processes has been recognized long ago, it remains a challenging task to identify concrete realizations of this potential. In this dissertation we have studied two subjects where neutrinos may be used to increase our understanding of particle physics and astronomy. In chapters 2 and 3 we have studied spontaneous pair creation by an external source and considered the possibility of neutrino pair creation by a configuration of neutrons with a time-dependent density. In chapters 4–7 we have studied how neutrinos may be used to probe the physics of gamma-ray bursts (GRBs). We present our conclusions regarding these two subjects in the following.

Spontaneous pair creation has been studied extensively in the context of QED but is also a potential mechanism to create neutrinos. The creation of neutrinos by an external source was studied earlier by Kusenko & Postma (2002), who considered neutrino pair creation by collective motion of neutrons in oscillating neutron stars. Using the non-perturbative method of Bogoliubov transformations, they found that the rate of pair creation is proportional to the neutrino mass. This result indicates that the mechanism is only operational for massive neutrinos and hints at chiral suppression of pair creation mediated by the weak nuclear force. We have studied the same problem using perturbative quantum field theory in chapter 3. For the source considered by Kusenko & Postma, we also find that the number of created neutrinos is proportional to the neutrino mass (cf. eq. (3.21)). We demonstrate however that for other background fields neutrino pair creation remains possible in the limit of vanishing neutrino mass (cf. eqs. (3.16)). Therefore we conclude that the scaling with neutrino mass is not a general feature of pair creation by the weak nuclear force. We have also presented estimates of the neutrino flux from neutron stars up to first order in perturbation theory. At the perturbative level, neutrino pair creation by an oscillating neutron star requires a very large driving frequency. Because this limits the size of the region in which neutrinos can be created, and hence the resulting neutrino flux, the prospects of detecting neutrinos created by this mechanism are poor. It is therefore unlikely that experimental verification of spontaneous pair

creation will come from astrophysical neutrinos.

Both perturbative and non-perturbative methods to study pair-creation problems have been discussed in chapter 2. In this chapter we have introduced an example of an exactly solvable pair-creation problem, i.e. an external source for which the number of created pairs can be represented by an explicit analytic function of the coupling constant. This external source, that we call the 'time-dependent kink' (see section 2.4), corresponds to a homogeneous, time-dependent scalar field that represents a domain wall in the time domain. It is coupled to the quantum scalar fields through a quartic coupling in the Lagrangian which results in an effective, time-dependent mass for the quantum scalar fields. We compute the number of particles created by the source using Bogoliubov transformations and derive an analytic function in the coupling constant. This result can be expanded around zero coupling constant to find a convergent perturbative expansion. The first few terms of this expansion are reproduced using Feynman diagram calculus, which explicitly demonstrates the equivalence of both methods. For future work it may be interesting to generalize the setup to fermion pair creation by a time-varying mass and to fermion pair creation by an external electric field. In the last case, the analogy with the Schwinger formula suggests that the number of created pairs is a non-analytic function of the coupling constant, so that a perturbative computation will lead to a divergent series. The transition from convergent to divergent perturbative expansions can be studied further using the results obtained in chapter 2, in particular the expression that was derived for the imaginary part of scalar n-point integrals for a source with only time components (see appendix 2.A).

In chapters 4–7 of this dissertation we have considered the creation and emission of neutrinos in GRBs. In recent years there has been much progress in our understanding of these phenomena. Although the currently favored 'fireball / blast wave' model of GRBs can account for many observational features, some important questions remain. In particular, the nature of the central engine that powers the burst, the formation of the relativistic outflow associated with GRBs, and the physics of the early phases of this outflow remain elusive. The properties of the prompt gamma-ray emission as well as those of the afterglow are mostly determined by the physical conditions in the blast wave, when the bulk of the GRB energy is carried by baryons. Neutrino emission may however be a useful diagnostic of the earlier phases of a developing GRB and thus shed light on some important open questions.

Chapter 4 is concerned with the effect of neutrinos on the dynamics of early GRB outflows in the fireball model. We found that the fireball plasma is opaque to neutrinos in the part of the parameter space where neutrinos are created rapidly enough to provide a potentially important cooling mechanism (see the phase diagram in fig. 4.1). In this regime neutrinos are in thermal equilibrium with the other plasma components and energetically important. As the expanding and cooling neutrino-opaque fireball becomes transparent to neutrinos, a sub-millisecond burst of neutrinos is emitted. Largely independent of the initial conditions, these neutrinos carry away approximately 30 percent of

the initial GRB energy. This implies that neutrino cooling is not dramatic and neutrino cooling cannot terminate a developing GRB. Therefore neutrino cooling considerations do not put strong constraints on the parameter space of early GRB fireballs. Due to the relatively low energy of ~60 MeV, detection of these neutrinos is possible for nearby galaxies only.

In chapter 4 we found that neutrino-opaque conditions in a GRB fireball can be realized when the central engine releases energy to fuel the fireball on very short timescales. A way to develop neutrino-opaque conditions in a fireball in a gradual way was suggested by Woosley (1993). In this scenario, neutrinos that are emitted by the central-engine accretion disk transfer energy to the fireball through electron – neutrino scattering. This increases the plasma temperature and hence the opacity to neutrino scattering. This leads to run-away behavior which, in principle, may result in neutrino-opaque conditions. However, the timescale to develop this instability is an order of magnitude larger than the dynamical timescale so that it may be difficult to realize in nature (see also Asano & Iwamoto 2002).

In the fireball model, that is adopted in chapter 4, the relativistic outflow is initially dominated by thermal energy. The energy of the flow may also be predominantly in the form of Poynting flux, which, for example, is expected if the central engine contains a magnetized accretion disk. High-energy neutrinos may be used to discriminate between these models. The fireball model requires a separate dissipation mechanism to explain the prompt gamma-ray emission, which is usually assumed to be electron acceleration in internal shocks. Protons are also accelerated in these shocks and give rise to high-energy neutrino emission. As these shocks are not expected in Poynting-flux dominated outflows, the observation of high-energy neutrino emission together with the prompt emission would favor the fireball model.

Neutrinos may also be produced in neutron – proton (np) collisions in the accelerating phase of the outflow. Because the acceleration profile in the fireball model and in Poynting-flux models is generally different, the signature of these neutrinos may also give information on the nature of the flow. This possibility is investigated in detail in chapter 5. We restrict ourselves to the 'AC' model, a concrete model of Poynting-flux dominated GRB outflows put forward by Spruit et al. (2001). An attractive feature of this model is that it can account for both the bulk acceleration of the flow and the prompt gamma-ray emission through magnetic reconnection.

We find that inelastic np collisions can occur only when the flow is sufficiently pure, i.e. when the ratio of energy to rest mass is sufficiently high. For fireballs this implies that the terminal Lorentz factor of the flow should be ~700 while for the AC model the Lorentz factor should be ~200. Given that the canonical value of GRB Lorentz factors is believed to be a few hundred, np decoupling is expected be relatively rare in fireballs but common in AC flows.

The neutrino emission due to collisions between differentially streaming neutrons and protons is so weak that detection is prohibitive for both the fireball model and the

AC model. For the fireball model we find that the resulting neutrino particle fluence is roughly an order of magnitude smaller than previous estimates in the literature. This difference is mostly due to the more accurate cross sections used in this work and the distinction between the np decoupling radius and the pion production radius. Both these considerations primarily affect the regime close to the pion production threshold. This regime gives the dominant contribution to the total optical depth for inelastic np scattering due to the relatively large nucleon densities. In the AC model, the neutrino fluence is lower by another factor $\sim$5 due to the more gradual acceleration of the flow, which is a robust feature of the model.

Inelastic np collisions also create neutral pions which decay into gamma rays. These gamma rays are subject to multiple interactions with soft X-ray photons carried with the flow. In the fireball model this results, via electron-positron pair cascades, to the emission of a few per mille of the energy of the flow in 2 - 20 GeV gamma rays. This gamma-ray signal is observable by the upcoming GLAST satellite up to large redshifts (see fig. 5.5). In the AC model, this energy is radiated away at a few hundred keV due to synchrotron radiation. Therefore this gamma-ray emission is a promising probe of the nature of the relativistic flow in the early phases of a GRB. However a more detailed analysis of the spectral properties is required to compare it with other emission mechanisms.

Whereas neutrino observations may provide information that is complementary to the gamma-ray emission for the type of GRBs that have been observed so far, they could be the only observable signal from a hypothetical class of 'choked' GRBs. The existence of such a class of failed GRBs has been hypothesized in the literature recently (see Razzaque et al. 2005 and references therein). Based on the observational connection between GRBs and supernovae, it is an interesting possibility that the early phases of a developing GRB occur in a relatively large fraction of all supernovae, but that only under special circumstances this leads to an actual GRB. For example, it may the case that the formation of a relativistic outflow is a frequent phenomenon, but that only very energetic outflows give rise to an actual GRB.

We consider in chapter 7 the energy spectrum and angular distribution of neutrinos that are produced by a choked GRB. In this scenario neutrinos are predominantly produced in the decay of charged pions and kaons created in the interactions of shock-accelerated protons with nucleons and photons in the flow. Because the number density of shock-accelerated protons decreases with increasing energy, and because meson energy loss prior to decay strongly suppresses the flux of high-energy neutrinos, most observable neutrinos are within an order of magnitude of the threshold energy for cubic-kilometer neutrino detectors ($\sim$100 GeV). In this regime proton energy loss is dominated by proton – proton (pp) interactions.

Protons can be accelerated both by the reverse shock that arises in the interaction of the relativistic outflow with the stellar material, and in internal shocks that may arise due to variability of the flow. We find that in both cases, depending on the parameters, neutrino emission from choked GRBs can be strong. For reference values of the parame-

ters we find that a choked GRB at 100 Mpc is detectable above the atmospheric neutrino background with a cubic-kilometer neutrino detector. Because the rate of choked GRBs pointing toward earth within 100 Mpc may be as large as a few per year, neutrino emission from a few choked GRBs per year could be detected. This result depends on some model parameters that are poorly known. However, in the case of proton acceleration by internal shocks, we find that the most important parameter in determining the number of neutrino events in a cubic-kilometer neutrino detector is the jet Lorentz factor Γ_j. Provided that a substantial amount of protons is accelerated in internal shocks, the detection prospects for a single choked GRB with $\Gamma_j \gtrsim 5$ are excellent (e.g., see the right panel of fig. 7.3). For optimistic values of the model parameters, the diffuse flux due to pp interactions in unresolved choked GRBs may be a factor few above the atmospheric background (see fig. 7.7). For neutrino energies $\gtrsim 10^5$ GeV photopion production, which we have not considered, is expected to contribute significantly to the diffuse flux, further enhancing the detection prospects.

The production of secondary pions and kaons in pp interactions is modeled with parameterizations of the energy and angular distribution of these mesons that are presented in chapter 6. These parameterizations are included in this dissertation as a separate chapter because they can be applied to many other astrophysical systems where high-energy pp interactions are important.

Acknowledgments

First of all I would like to thank Karel Gaemers and Jan-Willem van Holten for giving me the opportunity to do PhD research at Nikhef, the Dutch national institute for subatomic physics. I have good memories of our time behind the blackboard in the beginning of my PhD research. Also many thanks to all the people in the Nikhef theory group for creating a very stimulating and enjoyable atmosphere. In particular, I greatly enjoyed working together with Marieke Postma and Tim Dijkstra. I am grateful to Chris White for his help with some of the subtleties of the English language.

Nikhef has been a very pleasant place to work, with many helpful colleagues. I appreciated the frequent interaction with members of the ANTARES group and I wish them well with the last steps of deploying the detector. I would also like to thank Jeff Templon and Ronald Starink for their help in using the GRID computer cluster.

In my second year as a graduate student I started collaborating with Ralph Wijers on the physics of neutrinos in gamma-ray bursts. I am very grateful for the guidance that he provided in this subject. During our collaboration I have developed a very high regard for Ralph's physical insight, his stimulating enthusiasm, and his abilities as a group leader. I would also like to thank the other members of the gamma-ray burst group at the Sterrenkundig Instituut 'Anton Pannekoek' for many pleasant discussions. In particular I am grateful to Asaf Pe'er for the lessons that I have learned from his critical questions.

During my PhD research I have had the opportunity to visit many scientific institutes and to discuss my research with outstanding researchers as Francis Halzen, Thomas Janka, Peter Mészáros and Jack Steinberger. I thank them for their time and interest. I would like to acknowledge the hospitality of the Université Libre de Bruxelles, where part of the introduction of this dissertation was written, and the Max-Planck-Institut für Astrophysik in Garching, where part of the research described in chapter 5 was done. I thank Dimitrios Giannios for the very pleasant collaboration and for the excellent time in Garching and Munich. I have also enjoyed the many discussions with Joachim Moortgat on the physics described in this dissertation. Furthermore I would like to thank the members of the reading committee for their time. In particular, I am grateful to Jan Smit for comments that have helped to improve chapter 2.

There are many people that have helped in one way or the other with the completion of this dissertation and the road toward completion. I thank all my friends for their

continuous support and interest. In particular, I would like to thank Guiot Duermeijer and Paul van der Nat for stimulating my creativity and for being critical when necessary. I believe that both creativity and criticism are essential in science, and therefore I am very happy to have you both as *paranimf*. Special thanks go to Paul for a critical reading of the Dutch summary.

I thank my parents Albert and Maria Koers for their stimulation to pursue what I love most and for their support in my choices. Finally I would like to express to Sandra Duenk how much I value her unlimited support, her fresh perspective, and the courage that lets us follow our hearts.

Samenvatting

‘Beste radioactieve dames en heren’,

Met deze aanhef opende Wolfgang Pauli een brief die hij op 4 december 1930 naar een groep experimentele kernfysici stuurde aan de vooravond van een wetenschappelijk congres. In deze brief refereert Pauli aan een belangrijk natuurkundig probleem in die tijd: er was aantal waarnemingen bekend waarin energie verloren lijkt te gaan tijdens het verval van atoomkernen. De wet van behoud van energie is één van de fundamentele natuurwetten en een schending van deze wet zou de natuurkunde op haar grondvesten doen trillen. Het belang van deze behoudswet maakte dat Pauli, die bekend stond als wars van speculatieve ideeën, een gedurfde hypothese aandroeg: het bestaan van een tot dan toe onontdekt gebleven deeltje dat de ‘verloren’ energie met zich mee zou dragen. Dit deeltje kennen wij tegenwoordig als het neutrino.[1]

Het neutrino als boodschapper

Het is geen toeval dat het neutrino voorspeld werd op grond van theoretische beschouwingen voordat het werd waargenomen in een experiment: het neutrino is erg moeilijk te detecteren omdat het nauwelijks wisselwerkt met de materie om ons heen. Op de allerkleinste lengteschalen kent de hedendaagse natuurkunde vier verschillende krachten die verantwoordelijk zijn voor alle interacties tussen deeltjes, namelijk de zwaartekracht, de elektromagnetische kracht, de sterke kernkracht en de zwakke kernkracht. De laatste twee krachten zijn alleen indirect merkbaar in het dagelijkse leven; de sterke kernkracht houdt atoomkernen bij elkaar terwijl de zwakke kernkracht verantwoordelijk is voor radioactief verval van deze kernen. Van deze vier fundamentele krachten hebben slechts de zwaartekracht en de zwakke kernkracht vat op het neutrino. Het effect van de zwaartekracht is op microscopische schaal verwaarloosbaar klein en de zwakke kernkracht zorgt slechts sporadisch voor interacties tussen deeltjes. Het duurde dan ook tot 1956 voordat

[1] Pauli doopte het deeltje in zijn brief ‘neutron’. Toen James Chadwick in 1932 een deeltje ontdekte dat de door Pauli voorgestelde eigenschappen leek te bezitten, identificeerde hij het nieuwe deeltje met Pauli’s neutron. Later werd duidelijk dat Chadwick een ander, veel zwaarder, deeltje had ontdekt. Dit zware deeltje staat tegenwoordig bekend als het neutron terwijl Pauli’s deeltje, door toedoen van de Italiaanse natuurkundige Enrico Fermi, bekend is geworden als het ‘neutrino’ — Italiaans voor het ‘kleine neutron’.

Frederick Reines en zijn collega's het bestaan van neutrino's experimenteel konden bewijzen (Cowan et al. 1956; zie ook Reines & Cowan 1953). Inmiddels zijn neutrino's afkomstig uit diverse bronnen op aarde en daarbuiten waargenomen, zoals de zon (zie bv. Davis et al. 1968), de aardatmosfeer (zie bijv. Fukuda et al. 1998), en SN1987A. Dit is een supernova die in 1987 werd waargenomen en tot op heden de enige gedetecteerde bron van neutrino's buiten ons zonnestelsel is (zie bijv. Bethe 1990).

Het feit dat neutrino's nauwelijks wisselwerken heeft ook een uiterst belangrijk voordeel. Neutrino's die afkomstig zijn uit een bron in het heelal kunnen de aarde bereiken zonder noemenswaardige verstoringen onderweg, zelfs als de bron op vele lichtjaren afstand staat. Hierin onderscheidt het neutrino zich van andere deeltjes die uit het heelal komen, zoals fotonen en protonen. Fotonen uit een astrofysische bron bereiken vaak de aarde niet omdat ze worden geabsorbeerd door interstellair stof of door de kosmische achtergrondstraling. De baan van protonen wordt beïvloedt door verstrooiing en door magneetvelden in het heelal, waardoor het moeilijk is om uit waarnemingen de bron van kosmische protonen te herleiden.

Er is op dit moment veel interesse in de rol van neutrino's als 'boodschappers' van astrofysische processen. Omdat de interactiewaarschijnlijkheid van een enkel neutrino gering is, vereist waarneming van neutrino's uit het heelal een grote detector. Op grond van theoretische beschouwingen wordt verwacht dat een detector met een volume van een kubieke kilometer ruwweg één interessante detectie per jaar op kan leveren. Zulke detectoren worden op dit moment ontworpen en gebouwd in de Middellandse Zee (KM3NeT; zie Katz 2006) en op de Zuidpool (IceCube; zie Ahrens et al. 2003).

Dit proefschrift gaat over de vraag wat we kunnen leren van waarnemingen met de toekomstige generatie neutrinodetectoren zoals KM3NeT en IceCube. Nauwkeurig onderzoek naar de signatuur van neutrino-emissie door astrofysische bronnen is noodzakelijk om bronnen experimenteel te kunnen onderscheiden en om op grond van neutrinowaarnemingen onderscheid te kunnen maken tussen verschillende modellen voor de bron. In het bijzonder behandelen we twee onderwerpen op het snijvlak van de fysica van elementaire deeltjes en de sterrenkunde: spontane paarcreatie van neutrino's en de productie en emissie van neutrino's in gammaflitsers (Engels: gamma-ray bursts).[2] Deze onderwerpen worden hieronder besproken.

Spontane paarcreatie van neutrino's

De essentie van $E = mc^2$, misschien wel de meest bekende formule uit de natuurkunde, is samen te vatten in de uitspraak dat massa een vorm van energie is. Dat wil zeggen dat deeltjes met massa kunnen annihileren waarbij een navenante hoeveelheid energie vrijkomt. Aan de andere kant is het ook mogelijk dat deeltjes 'spontaan' ontstaan uit

[2]Het onderzoek dat hieraan ten grondslag ligt is in de afgelopen vier jaar verricht aan het Nikhef, het nationale instituut voor subatomaire fysica. Dit instituut is nauw betrokken bij de ontwikkeling en ingebruikname van huidige (ANTARES) en toekomstige (KM3NeT) neutrinodetectoren. Daarnaast was er een intensieve samenwerking met onderzoekers verbonden aan het sterrenkundig instituut 'Anton Pannekoek'.

een externe bron, een hoeveelheid energie die in een bepaald volume is geconcentreerd. Een bekend voorbeeld van dit proces is het ontstaan van elektron-positronparen in een extreem sterk elektrisch veld.[3] Dit fenomeen werd voorspeld door Julian Schwinger in 1950, maar is nog nooit direct waargenomen. Dit is te verklaren doordat het erg moeilijk is om elektrische velden van de vereiste sterkte (zo'n 10^{16} V/cm) in een laboratorium op te wekken. Spontane deeltjescreatie is theoretisch ook mogelijk voor neutrino's, wat een andere mogelijkheid biedt om het bestaan van dit mechanisme te verifiëren. Spontane creatie van neutrino's is het onderwerp van hoofdstuk 2 en 3 van dit proefschrift.

In tegenstelling tot elektron-positronparen, die gecreëerd kunnen worden door toedoen van de elektromagnetische kracht, worden neutrino's vrijwel uitsluitend gecreëerd door de zwakke kernkracht.[4] Het opwekken van een sterk veld van de zwakke kernkracht over macroscopische afstanden is vrijwel onmogelijk in een laboratorium. Zulke velden kunnen wel bestaan in neutronensterren, compacte sterren met een hoge dichtheid die vrijwel geheel uit neutronen bestaan. Een collectieve oscillatie van de neutronen in een neutronenster wekt een sterk, tijdsafhankelijk veld op dat de zwakke kernkracht overbrengt. De energie die met deze oscillaties gepaard gaat kan in principe worden gebruikt om neutrino's te creëren.

Spontane paarcreatie van neutrino's in een neutronenster is eerder bestudeerd door Kusenko & Postma (2002). Deze auteurs concluderen dat de flux van neutrino's die op deze manier wordt geproduceerd te klein is om waar te kunnen nemen. Verder vinden zij dat, voor de specifieke bron die wordt aangenomen, het aantal neutrino's dat per tijdseenheid wordt gecreëerd recht evenredig is met de neutrinomassa. Deze bevinding is vooral van belang omdat het betekent dat het paarcreatiemechanisme niet werkt als de gecreëerde deeltjes massaloos zouden zijn geweest. Dit is niet het geval voor elektron-positronpaarcreatie en geeft dus aanleiding tot verder onderzoek.

Kusenko & Postma maken gebruik van een wiskundig formalisme waarmee het aantal neutrino's op een niet-perturbatieve manier wordt berekend. Dit formalisme geeft exacte resultaten maar kan alleen worden toegepast op een specifieke klasse van bronnen. In dit proefschrift beschouwen we neutrinopaarcreatie met behulp van een perturbatieve methode, waarin het aantal gecreëerde neutrino's wordt benaderd met behulp van een storingsreeks. Deze methode is toepasbaar op vrijwel alle bronnen, wat de mogelijkheid biedt om te bestuderen of de massa-afhankelijkheid een algemeen resultaat is of dat deze afhankelijkheid een gevolg is van de keuze die Kusenko & Postma voor de bron hebben gemaakt. We beperken ons in deze analyse tot homogene bronnen.

In hoofdstuk 2 van dit proefschrift behandelen we spontane paarcreatie binnen het raamwerk van de quantumveldentheorie. We geven een beknopte inleiding in het gebruik van Bogoliubov-transformaties en van Feynman-lusdiagrammen, respectievelijk

[3] Spontane creatie van elektronen, positronen, en neutrino's gebeurt altijd in paren omdat de lading (net als de totale energie, impuls, en de draai-impuls) een behouden grootheid is.

[4] Neutrino's kunnen ook gecreëerd worden door de elektromagnetische kracht met tussenkomst van virtuele deeltjes die de zwakke kernkracht overbrengen. Dit type proces is echter sterk onderdrukt.

niet-perturbatieve en perturbatieve methodes om het aantal deeltjes dat gecreëerd wordt door een externe bron uit te rekenen.

In hoofdstuk 3 beschouwen we spontane paarcreatie van neutrino's met behulp van de Feynman-lusdiagrammen die in hoofdstuk 2 zijn besproken. Dit leidt tot een algemene formule die, in eerste orde in een storingsreeks, het aantal neutrino's geeft dat gecreëerd wordt door een willekeurige homogene bron. Uit deze formule blijkt dat spontane creatie van neutrino's in het algemeen mogelijk zou zijn als neutrino's geen massa hadden gehad. Onze berekeningen bevestigen dat voor de specifieke bron die door Kusenko & Postma is aangenomen, het aantal neutrino's recht evenredig is met de neutrinomassa. Net als Kusenko & Postma concluderen we dat het aantal neutrino's dat door het mechanisme van spontane creatie in een neutronenster opgewekt kan worden, te klein is om waar te nemen.

Gegeven de bovenstaande conclusie lijkt het onwaarschijnlijk dat het bestaan van spontane paarcreatie geverifieerd kan worden door middel van waarnemingen met neutrinodetectoren. Het bestuderen van deze mogelijkheid heeft wel geleid tot nieuwe inzichten in het paarcreatiemechanisme, met name wat betreft de rol van de neutrinomassa. Verder bieden onze resultaten perspectief om verdere inzichten in het mechanisme te ontwikkelen, in het bijzonder in de verhouding tussen perturbatieve en niet-perturbatieve beschrijvingen.

Productie en emissie van neutrino's in gammaflitsers

Hoofdstukken 4–7 van dit proefschrift gaan over de vraag wat we kunnen leren over de fysica van gammaflitsers door toekomstige waarnemingen met de nieuwe generatie neutrinodetectoren. Waar de nadruk in het voorgaande deel vooral ligt op het neutrino en zijn interacties, ligt de nadruk in dit deel van het proefschrift vooral op de fysica van de bron.

Gammaflitsen zijn korte, zeer intense flitsen van gammastraling afkomstig uit het heelal. In termen van vermogen zijn het, voorzover bekend, de meest krachtige verschijnselen sinds de oerknal. Zo is er een gammaflits waargenomen van een bron op meer dan 10 miljard lichtjaar afstand! De energie in de gammaflits wordt, voor astronomische begrippen, in een korte tijd uitgestraald. Hierbij wordt onderscheid gemaakt tussen korte gammaflitsen, met een typische duur van 0.2 s, en lange gammaflitsen, met een typische duur van 20 s.

Sinds de toevallige ontdekking van gammaflitsen door militaire *Vela* satellieten eind jaren zestig van de vorige eeuw (Klebesadel et al. 1973), zijn er verschillende satellieten gelanceerd om dit fenomeen nader te bestuderen. Het vakgebied kreeg een geweldige impuls door de lancering van de *Compton Gamma Ray Observatory* met daarop de *Burst and Transient Source Explorer (BATSE)* in 1991. *BATSE* registreerde ongeveer één gammaflits per dag. Met behulp van deze waarnemingen werd onder andere aangetoond dat gammaflitsers isotroop over de hemel verdeeld zijn, wat een klasse van bronnen die

beperkt is tot ons Melkwegstelsel vrijwel uitsluit. De kosmologische oorsprong van gammaflitsen werd bevestigd door de *BeppoSAX* satelliet. In 1997 werd met behulp van deze satelliet voor het eerst het nagloeien van gammaflitsers waargenomen, dat wil zeggen straling die na de gammaflits wordt uitgezonden en in sommige gevallen tot jaren na de flits kan worden waargenomen. Met behulp van dit nagloeien was het mogelijk om de roodverschuiving van de bron te bepalen en op die manier de afstand vast te stellen. Een nieuwe mijlpaal in het onderzoek naar gammaflitsers diende zich aan in 1998, toen gelijktijdig met het uitdovende nagloeien van een gammaflitser een supernovaspectrum werd waargenomen. Samen met vergelijkbare waarnemingen daarna leverde dit het bewijs dat sommige gammaflitsers en supernova's een gedeelde oorsprong hebben. Op het moment van schrijven is de *Swift* satelliet, die eind 2004 werd gelanceerd, verantwoordelijk voor de ontdekking van de meeste nieuwe gammaflitsen. Waarnemingen met deze satelliet hebben verschillende interessante ontdekkingen opgeleverd, met name in het tijdsgebied tussen de gammaflits en het nagloeien (zie Mészáros 2006).

De belangrijkste eigenschappen van de waargenomen gammaflitsen kunnen worden verklaard met behulp van het *vuurbal/schokgolfmodel* (Engels: fireball / blast wave model).[5] In dit model ontstaan gammaflitsen als gevolg van de ineenstorting van de kern van een zware ster of als gevolg van de samensmelting van twee neutronensterren, respectievelijk voor lange en korte gammaflitsen. De energie die hierbij vrijkomt wordt gebruikt om een vuurbal te vormen, een zeer energierijk plasma van fotonen, elektron-positronparen en een relatief kleine hoeveelheid nucleonen. Als gevolg van stralingsdruk zet het plasma snel uit, waarbij een zeer hoge, ultrarelativistische snelheid bereikt wordt. Vervolgens, zo zegt het model, ontstaan er botsingen tussen opeenvolgende schillen van nucleonen. Deze botsingen leiden tot het ontstaan van schokken, waarvan bekend is dat zij geladen deeltjes tot zeer hoge energieën kunnen versnellen. Elektronen die versneld worden door deze schokken zenden synchrotronstraling uit en verhogen de energie van deze straling door Inverse-Comptoninteracties. De straling die zo ontstaat wordt verantwoordelijk gehouden voor de waargenomen gammaflits, terwijl de interactie van het plasma met de interstellaire materie tot het nagloeien leidt.

Op grond van het vuurbal/schokgolfmodel wordt verwacht dat een gammaflitser ook grote hoeveelheden neutrino's uitzendt. Deze neutrino's ontstaan in verschillende fase in de ontwikkeling van de gammaflitser, bijv. door elektron-positronannihilatie vlak na de vorming van de vuurbal, door proton-fotonbotsingen of proton-nucleonbotsingen in de vuurbal, en door botsingen van protonen die worden versneld in de schokgolf met nucleonen rondom de bron.

Ondanks het succes van het vuurbal/schokgolfmodel zijn een aantal belangrijke vragen omtrent gammaflitsers tot op heden onbeantwoord. Hoe wordt, bijvoorbeeld, de vuurbal gevormd? Kunnen magnetische velden energetisch belangrijk zijn in de dyna-

[5] Het is in deze beperkte ruimte ondoenlijk om uit te leggen hoe verschillende waarnemingen hebben bijgedragen aan de totstandkoming van het vuurbal/schokgolfmodel. We verwijzen de geïnteresseerde lezer naar de uitgebreide beschouwingen door Piran (2004) en Mészáros (2006).

mica van het plasma? Hoe werkt schokversnelling precies? Waarnemingen met neutrinodetectoren kunnen een essentiële rol spelen in het beantwoorden van deze belangrijke vragen omdat neutrino's de bron verlaten terwijl deze nog niet transparant is voor fotonen. Hierdoor zijn neutrino's (en mogelijk zwaartekrachtgolven, die ook vroegtijdig de bron kunnen verlaten) vrijwel de enige mogelijkheid om informatie te verkrijgen over de eerste fase in de ontwikkeling van een gammaflitser.

In hoofdstuk 4 bestuderen we in detail de rol van neutrino's in de allereerste fase van een vuurbal. In het bijzonder zijn we geïnteresseerd in de vraag of het mogelijk is dat neutrino's zo veel energie van de bron met zich meevoeren dat dit een zich ontwikkelende gammaflitser in de kiem zou smoren. We vinden echter dat dit nooit het geval is omdat efficiënte neutrinoproductie alleen mogelijk is wanneer de vuurbal ondoorzichtig is voor neutrino's. In dat geval kunnen de geproduceerde neutrino's de vuurbal niet verlaten en blijft de energie dus in het plasma. Doordat de vuurbal ondoorzichtig is voor neutrino's ontstaat er thermisch evenwicht tussen neutrino's, fotonen, en elektron-positronparen, waarin de neutrino's ongeveer 30% van de energie van de vuurbal dragen.

De vuurbal expandeert door stralingsdruk, waardoor de energiedichtheid en de temperatuur van het plasma afnemen. Op het moment dat de temperatuur voldoende is gedaald, ontkoppelen de neutrino's van de andere componenten van de vuurbal: de vuurbal wordt doorzichtig voor neutrino's. Deze verlaten hierop de vuurbal en dragen ongeveer 30% van de energie van de vuurbal met zich mee. Dit is een aanzienlijk deel van de totale energie, maar nooit genoeg om de ontwikkeling tot gammaflitser te stoppen. Vanwege de relatief lage energie van de neutrino's op het moment van ontkoppelen, ongeveer 60 MeV, is detectie van deze neutrino's alleen mogelijk voor gammaflitsers in de directe omgeving van ons Melkwegstelsel.

In hoofdstuk 5 bestuderen we neutrinoproductie door middel van botsingen tussen neutronen en protonen. We vergelijken hier voorspellingen van het vuurbalmodel met die van het *AC-model*, een alternatief model voor gammaflitsers waarin elektromagnetische velden de energie in het plasma domineren. In beide modellen zijn de protonen door middel van elektromagnetische interacties krachtig aan het plasma gekoppeld, terwijl neutronen alleen via elastische neutron-protonbotsingen zijn gekoppeld. Hierdoor kunnen neutronen en protonen ontkoppelen wanneer de dichtheid van nucleonen voldoende is afgenomen door de uitzetting van het plasma. Als dit gebeurt ontstaat er een relatieve snelheid tussen neutronen en protonen die groot genoeg kan worden om neutrino's en gammastraling te produceren in inelastische botsingen. We vinden dat de hoeveelheid neutrino's die op deze manier wordt geproduceerd in het AC-model een factor 5 kleiner is dan in het vuurbalmodel. Helaas is de verwachte neutrinoflux in beide modellen zo klein dat, zelfs voor een krachtige en nabije gammaflits, het neutrinosignaal niet waargenomen kan worden met neutrinodetectoren van een kubieke kilometer.

Behalve neutrino's wordt er ook gammastraling geproduceerd in inelastische neutron-protonbotsingen. Deze straling wisselwerkt met het plasma en wordt vervolgens met een andere energie uitgezonden. Uit ons onderzoek blijkt dat de energie waarmee deze

straling wordt uitgezonden anders is in het vuurbalmodel dan in het AC-model. In het AC-model is de typische energie van de straling vergelijkbaar met die van de gammaflits, namelijk een paar honderd keV. Hierdoor is het erg moeilijk om deze twee componenten obervationeel te onderscheiden. In het vuurbalmodel, daarentegen, wordt de straling uitgezonden rond 10 GeV, hetgeen goed te onderscheiden is van de gammaflits. Deze straling kan vanaf grote afstand worden waargenomen met de toekomstige *GLAST* satelliet (die volgens de planning in 2008 gelanceerd zal worden). Dit vereist echter wel dat het plasma aanvankelijk voldoende energie per nucleon bevat, omdat er anders geen inelastische neutron-protonbotsingen optreden. Detectie van deze straling zou het vuurbalmodel ondersteunen.

Hoofdstuk 7 van dit proefschrift is gewijd aan een hypothetische klasse van 'gesmoorde' gammaflitsers, dat wil zeggen objecten die de eerste stadia van de ontwikkeling tot gammaflitser doorlopen maar nooit gammastraling uitzenden. Dit kan bijvoorbeeld het gevolg zijn van het feit dat de vuurbal niet genoeg energie heeft om de helium- of waterstof-mantel van de ontploffende ster te doorkruisen, waardoor de geproduceerde gammastraling wordt geabsorbeerd voordat zij de bron heeft kunnen verlaten. Gegeven het observationele verband tussen gammaflitsers en supernova's is het een interessante mogelijkheid dat een substantiële fractie van alle supernova's gepaard gaat met een, al dan niet gesmoorde, gammaflits. Dit zou mogelijk kunnen bijdragen aan het beantwoorden van de vraag hoe een supernova precies ontstaat.

In tegenstelling tot gammastraling kunnen neutrino's die geproduceerd worden in de ontwikkeling van een gesmoorde gammaflitser de bron vrijwel ongehinderd verlaten. Voor de detectie van deze neutrino's is vooral het energiegebied tussen 100 GeV en 10 TeV interessant; bij lagere energieën is de detectiewaarschijnlijkheid laag en bij hogere energieën is de neutrinoflux laag. Wij vinden dat het merendeel van de neutrino's in dit energiegebied ontstaat in inelastische proton-protonbotsingen in de vuurbal. Hierbij speelt de hoeveelheid energie per nucleon in de vuurbal een essentiële rol. Indien deze energie groter is dan ongeveer vijf maal de massa van de nucleonen (bij standaardwaarden van de overige parameters) kan het neutrinosignaal tot op honderden miljoenen lichtjaren worden waargenomen. Tenzij de fractie van supernova's die gepaard gaat met een (gesmoorde) gammaflitser veel kleiner dan één is, verwachten we dat dit leidt tot een paar detecties per jaar met een neutrinodetector van een kubieke kilometer.

Neutrino's worden vrijwel uitsluitend geproduceerd in proton-protonbotsingen via de creatie en het verval van pionen en kaonen. Om de productie van deze deeltjes in een gammaflitser nauwkeurig te kunnen modelleren, hebben we een parametrisatie afgeleid die beschrijft hoeveel pionen en kaonen er per proton-protonbotsing worden geproduceerd als functie van de energie van het geproduceerde deeltje, de energie van de protonen en de botsingsgeometrie. Omdat deze parametrisatie op een veelheid van astrofysische systemen kan worden toegepast, is ze als een apart hoofdstuk in dit proefschrift opgenomen (hoofdstuk 6).

Concluderend kunnen we zeggen dat het potentieel van neutrino's als boodschappers

van de fysica van gammaflitsers voor de scenario's beschreven in hoofdstukken 4 en 5 moeilijk te realiseren is vanwege de zeer geringe detectiemogelijkheden. Onze conclusies voor de gesmoorde gammaflitsers beschreven in hoofdstuk 7 zijn optimistischer: voor een groot deel van de parameterruimte verwachten we dat waarnemingen met een neutrinodetector van een kubieke kilometer het bestaan van deze hypothetische klasse van gammaflitsers kunnen bevestigen, danwel zinvolle grenzen aan de parameters van het model kunnen stellen.

Bibliography

Abramowitz, M. & Stegun, I. A. 1972, Handbook of mathematical functions (Dover publications)

Achterberg, A., Gallant, Y. A., Kirk, J. G., & Guthmann, A. W. 2001, Mon. Not. R. Astron. Soc., 328, 393

Adelman-McCarthy, J. K. et al. 2006, Astrophys. J. Suppl., 162, 38

Aharonian, F. et al. 2006, Astron. Astrophys., 449, 223

Ahmad, Q. R. et al. 2002, Phys. Rev. Lett., 89, 011301

Ahrens, J. et al. 2003, Nucl. Phys. Proc. Suppl., 118, 388

Alkofer, R., Hecht, M. B., Roberts, C. D., Schmidt, S. M., & Vinnik, D. V. 2001, Phys. Rev. Lett., 87, 193902

Alner, G. J. et al. 1984, Phys. Lett., B138, 304

Alner, G. J. et al. 1986, Phys. Lett., B167, 476

Alpgard, K. et al. 1983, Phys. Lett., B121, 209

Amaldi, U. & Schubert, K. R. 1980, Nucl. Phys., B166, 301

Andersson, B., Gustafson, G., Ingelman, G., & Sjostrand, T. 1983, Phys. Rept., 97, 31

Ando, S. & Beacom, J. F. 2005, Phys. Rev. Lett., 95, 061103

Andres, E. et al. 2000, Astropart. Phys., 13, 1

Ansorge, R. E. et al. 1989, Z. Phys., C43, 357

Antinucci, M. et al. 1973, Lett. Nuovo Cim., 6, 121

Aoyama, H. 1983, Nucl. Phys., B221, 473

Arnett, W. D., Bahcall, J. N., Kirshner, R. P., & Woosley, S. E. 1989, Ann. Rev. Astron. Astrophys., 27, 629

Asano, K. & Iwamoto, S. 2002, Astrophys. J., 581, 381

Asano, K. & Nagataki, S. 2006, Astrophys. J., 640, L9

Aslanides, E. et al. 1999, arXiv preprint astro-ph/9907432

Astier, P. et al. 2006, Astron. Astrophys., 447, 31

Atkins, R. et al. 2000, Astrophys. J., 533, L119

Atkins, R. et al. 2003, Astrophys. J., 583, 824

Badhwar, G. D., Stephens, S. A., & Golden, R. L. 1977, Phys. Rev., D15, 820

Bahcall, J. N. & Frautschi, S. C. 1969, Phys. Lett., B29, 623

Bahcall, J. N. & Glashow, S. L. 1987, Nature, 326, 476

Bahcall, J. N. & Mészáros, P. 2000, Phys. Rev. Lett., 85, 1362

Bahcall, J. N., Pinsonneault, M. H., & Basu, S. 2001, Astrophys. J., 555, 990

Baiko, D. A. & Yakovlev, D. G. 1999, Astron. Astrophys., 342, 192

Barbieri, R. & Mohapatra, R. N. 1988, Phys. Rev. Lett., 61, 27

Beloborodov, A. M. 2002, Astrophys. J., 565, 808

Beloborodov, A. M. 2003a, Astrophys. J., 585, L19

Beloborodov, A. M. 2003b, Astrophys. J., 588, 931

Belyanin, A. A., Derishev, E. V., Kocharovsky, V. V., & Kocharovsky, V. V. 2003, in AIP Conf. Proc. 662: Gamma-Ray Burst and Afterglow Astronomy 2001: A Workshop Celebrating the First Year of the HETE Mission, ed. G. R. Ricker & R. K. Vanderspek, 159

Benecke, J. et al. 1974, Nucl. Phys., B76, 29

Bennett, C. L. et al. 1996, Astrophys. J., 464, L1

Berezinsky, V., Gazizov, A. Z., & Grigorieva, S. I. 2002, arXiv preprint astro-ph/0210095

Bethe, H. A. 1990, Rev. Mod. Phys., 62, 801

Bethe, H. A., Applegate, J. H., & Brown, G. E. 1980, Astrophys. J., 241, 343

Bethe, H. A. & Wilson, J. R. 1985, Astrophys. J., 295, 14

Bhattacharjee, P. & Sigl, G. 2000, Phys. Rept., 327, 109

Biermann, P. L., Gaisser, T. K., & Stanev, T. 1995, Phys. Rev., D51, 3450

Bionta, R. M. et al. 1987, Phys. Rev. Lett., 58, 1494

Birrell, N. D. & Davies, P. C. W. 1982, Quantum fields in curved space (Cambridge Universiy Press)

Biyajima, M., Mizoguchi, T., Nakajima, N., Ohsawa, A., & Suzuki, N. 2001, Phys. Lett., B515, 470

Blaschke, D. B., Prozorkevich, A. V., Roberts, C. D., Schmidt, S. M., & Smolyansky, S. A. 2006, Phys. Rev. Lett., 96, 140402

Blattnig, S. R., Swaminathan, S. R., Kruger, A. T., Ngom, M., & Norbury, J. W. 2000, Phys. Rev., D62, 094030

Bogoliubov, N. N. & Shirkov, D. V. 1983, Quantum fields (Benjamin/Cummings)

Bottcher, M. & Dermer, C. D. 1998, Astrophys. J., 499, L131

Braaten, E. & Segel, D. 1993, Phys. Rev., D48, 1478

Breakstone, A. et al. 1984a, Phys. Rev., D30, 528

Breakstone, A. et al. 1984b, Z. Phys., C23, 9

Brezin, E. & Itzykson, C. 1970, Phys. Rev., D2, 1191

Bruenn, S. W. 1985, Astrophys. J. Suppl., 58, 771

Butt, Y. M., Torres, D. F., Combi, J. A., Dame, T., & Romero, G. E. 2001, Astrophys. J., 562, L167

Buttar, C. M., Clements, D., Dawson, I., & Moraes, A. 2004, Acta Phys. Polon., B35, 433

Buttar, C. M. et al. 2005, in HERA and the LHC - A workshop on the implications of HERA for LHC physics: Proceedings Part A, ed. A. De Roeck & H. Jung

Callan, C. G., J. & Coleman, S. R. 1977, Phys. Rev., D16, 1762

Cavallo, G. & Rees, M. J. 1978, Mon. Not. R. Astron. Soc., 183, 359

Chang, T. H., Gaemers, K. J. F., & van Neerven, W. L. 1982, Nucl. Phys., B202, 407

Chen, W.-X. & Beloborodov, A. M. 2007, Astrophys. J., 657, 383

Chodorowski, M. J., Zdziarski, A. A., & Sikora, M. 1992, Astrophys. J, 400, 181

Clowe, D., Bradač, M., Gonzalez, A. H., et al. 2006, Astrophys. J., 648, L109

Cole, S. et al. 2005, Mon. Not. R. Astron. Soc., 362, 505

Coleman, S. R. 1977, Phys. Rev., D15, 2929

Collins, P. D. B. & Martin, A. D. 1984, Hadron Interactions (Adam Hilger Ltd.)

Cornwall, J. M. & Tiktopoulos, G. 1989, Phys. Rev., D39, 334

Coroniti, F. V. 1990, Astrophys. J, 349, 538

Costa, E. et al. 1997, Nature, 387, 783

Cowan, C. L., Reines, F., Harrison, F. B., Kruse, H. W., & McGuire, A. D. 1956, Science, 124, 103

Cullen, S. & Perelstein, M. 1999, Phys. Rev. Lett., 83, 268

Cutkosky, R. E. 1960, J. Math. Phys., 1, 429

Damour, T. & Ruffini, R. 1975, Phys. Rev. Lett., 35, 463

Damour, T. & Ruffini, R. 1976, Phys. Rev., D14, 332

Daum, M. et al. 2002, Eur. Phys. J., C23, 43

Davis, Jr., R., Harmer, D. S., & Hoffman, K. C. 1968, Phys. Rev. Lett., 20, 1205

Derishev, E. V., Kocharovsky, V. V., & Kocharovsky, V. V. 1999a, Astron. Astrophys., 345, L51

Derishev, E. V., Kocharovsky, V. V., & Kocharovsky, V. V. 1999b, Astrophys. J, 521, 640

DeWitt, B. S. 1975, Phys. Rept., 19, 295

Dicus, D. A. 1972, Phys. Rev., D6, 941

Donnachie, A. & Landshoff, P. V. 1992, Phys. Lett., B296, 227

Drenkhahn, G. 2002, Astron. Astrophys., 387, 714

Drenkhahn, G. & Spruit, H. C. 2002, Astron. Astrophys., 391, 1141

Dunne, G. V. & Hall, T. M. 1999, Phys. Rev., D60, 065002

Dutta, S. I., Ratkovic, S., & Prakash, M. 2004, Phys. Rev., D69, 023005

Engel, R. 1998, Nucl. Phys. B (Proc. Suppl.), 75A, 62

Fan, Y.-H. & Wei, D. M. 2004, Astrophys. J., 615, L69

Fan, Y.-H., Zhang, B., & Wei, D. M. 2005, Astrophys. J., 628, 298

Feynman, R. P. 1969, Phys. Rev. Lett., 23, 1415

Fisher, P., Kayser, B., & McFarland, K. S. 1999, Ann. Rev. Nucl. Part. Sci., 49, 481

Frail, D. A., Kulkarni, S. R., Nicastro, S. R., Feroci, M., & Taylor, G. B. 1997, Nature, 389, 261

Fried, H. M. & Woodard, R. P. 2002, Phys. Lett., B524, 233

Friman, B. L. & Maxwell, O. V. 1979, Astrophys. J., 232, 541

Fukuda, Y. et al. 1998, Phys. Rev. Lett., 81, 1562

Fynbo, J. P. U. et al. 2006, Nature, 444, 1047

Gaemers, K. J. F., Gandhi, R., & Lattimer, J. M. 1989, Phys. Rev., D40, 309

Gallant, Y. A. & Achterberg, A. 1999, Mon. Not. R. Astron. Soc., 305, L6

Gehrels, N. & Michelson, P. 1999, Astropart. Phys., 11, 277

Giannios, D. 2006, Astron. Astrophys., 457, 763

Giannios, D. & Spruit, H. C. 2005, Astron. Astrophys., 430, 1

Giannios, D. & Spruit, H. C. 2007, Astron. Astrophys., 469, 1

Gies, H. & Shaisultanov, R. 2000, Phys. Lett., B480, 129

Goodman, J. 1986, Astrophys. J., 308, L47

Granot, J. & Guetta, D. 2003, Phys. Rev. Lett., 90, 191102

Gribov, V. N. & Pontecorvo, B. 1969, Phys. Lett., B28, 493

Grifols, J. A., Masso, E., Mohanty, S., & Shajesh, K. V. 2002, Phys. Rev., D65, 055004

Halzen, F. & Hooper, D. 2002, Rept. Prog. Phys., 65, 1025

Halzen, F., Jacobsen, J. E., & Zas, E. 1996, Phys. Rev., D53, 7359

Halzen, F. & Jaczko, G. 1996, Phys. Rev., D54, 2779

Halzen, F. & Martin, A. D. 1984, Quarks and Leptons (John Wiley & Sons)

Halzen, F., Vazquez, R. A., Stanev, T., & Vankov, H. P. 1995, Astropart. Phys., 3, 151

Hawking, S. W. 1974, Nature, 248, 30

Hawking, S. W. 1975, Commun. Math. Phys., 43, 199

Heisenberg, W. & Euler, H. 1936, Z. Phys., 98, 714

Hinshaw, G. et al. 2006, arXiv preprint astro-ph/0603451

Hirata, K. et al. 1987, Phys. Rev. Lett., 58, 1490

Hounkonnou, M. N. & Naciri, M. 2000, J. Phys., G26, 1849

Inoue, S., Iwamoto, N., Orito, M., & Terasawa, M. 2003, Astrophys. J., 595, 294

Itoh, N., Adachi, T., Nakagawa, M., Kohyama, Y., & Munakata, H. 1989, Astrophys. J., 339, 354

Itzykson, C. & Zuber, J. B. 1980, Quantum field theory (McGraw-Hill)

Janiuk, A., Perna, R., Di Matteo, T., & Czerny, B. 2004, Mon. Not. R. Astron. Soc., 355, 950

Kachelriess, M. 1998, Phys. Lett., B426, 89

Kamae, T., Abe, T., & Koi, T. 2005, Astrophys. J., 620, 244

Kamae, T., Karlsson, N., Mizuno, T., Abe, T., & Koi, T. 2006, Astrophys. J., 647, 692

Kashti, T. & Waxman, E. 2005, Phys. Rev. Lett., 95, 181101

Katz, U. F. 2006, Nucl. Instrum. Meth., A567, 457

Kelner, S. R., Aharonian, F. A., & Bugayov, V. V. 2006, Phys. Rev., D74, 034018

Kiers, K. & Tytgat, M. H. G. 1998, Phys. Rev., D57, 5970

Kim, S. P. & Page, D. N. 2002, Phys. Rev., D65, 105002

Klebesadel, R. W., Strong, I. B., & Olson, R. A. 1973, Astrophys. J., 182, L85

Klein, O. 1929, Z. Phys., 53, 157

Kleinschmidt, M. et al. 1980, Z. Phys., A298, 253

Kluger, Y., Eisenberg, J. M., Svetitsky, B., Cooper, F., & Mottola, E. 1992, Phys. Rev., D45, 4659

Koba, Z., Nielsen, H. B., & Olesen, P. 1972, Nucl. Phys., B40, 317

Kumar, P. 1999, Astrophys. J., 523, L113

Kusenko, A. & Postma, M. 2002, Phys. Lett., B545, 238

Landau, L. D. & Lifshitz, E. M. 1971, The classical theory of fields (Pergamon Press)

Lattimer, J. M. & Cooperstein, J. 1988, Phys. Rev. Lett., 61, 23

Lattimer, J. M., Prakash, M., Pethick, C. J., & Haensel, P. 1991, Phys. Rev. Lett., 66, 2701

Lee, W. H. & Ramirez-Ruiz, E. 2007, New J. Phys., 9, 17

Lee, W. H., Ramirez-Ruiz, E., & Page, D. 2004, Astrophys. J., 608, L5

Lin, Q.-G. 1999, J. Phys., G25, 17

Linde, A. D. 1983, Nucl. Phys., B216, 421

Lindsey, C. S. et al. 1992, Nucl. Phys., A544, 343

Loeb, A. 1990, Phys. Rev. Lett., 64, 115

Lyubarsky, Y. & Kirk, J. G. 2001, Astrophys. J, 547, 437

Lyubarsky, Y. E. 2005, Mon. Not. R. Astron. Soc., 358, 113

Lyutikov, M. 2006, New J. Phys., 8, 119

Lyutikov, M. & Blandford, R. D. 2003, arXiv preprint astro-ph/0312347

MacFadyen, A. I., Woosley, S. E., & Heger, A. 2001, Astrophys. J., 550, 410

Maltoni, M., Schwetz, T., Tortola, M. A., & Valle, J. W. F. 2004, New J. Phys., 6, 122

Maroto, A. L. 1999, Phys. Rev., D59, 063501

Martin, J. 2007, arXiv preprint 0704.3540

Matthiae, G. 1983, in Proceedings of HEP83, Brighton, ed. J. Guy & C. Costain

Maziashvili, M. 2004, Mod. Phys. Lett., A19, 1391

Mészáros, P. 2006, Rept. Prog. Phys., 69, 2259

Mészáros, P. & Rees, M. J. 1997, Astrophys. J., 482, L29

Mészáros, P. & Rees, M. J. 2000, Astrophys. J., 541, L5

Mészáros, P. & Waxman, E. 2001, Phys. Rev. Lett., 87, 171102

Moraes A., & Buttar, C. M. 2006, in Proceedings of Les Houches Workshop on Physics at TeV Collider, ed. C. Guy, J. & Costain

Morse, W. M. et al. 1977, Phys. Rev., D15, 66

Mucke, A., Rachen, J. P., Engel, R., Protheroe, R. J., & Stanev, T. 1999, Publ. Astron. Soc. Austral., 16, 160

Munakata, H., Kohyama, Y., & Itoh, N. 1985, Astrophys. J., 296, 197

Narozhnyi, N. B. & Nikishov, A. I. 1970, Sov. J. Nucl. Phys., 11, 596

Neville, D. E. 1984, Phys. Rev., D30, 1695

Norman, C. A., Melrose, D. B., & Achterberg, A. 1995, Astrophys. J., 454, 60

Paczyński, B. 1986, Astrophys. J., 308, L43

Page, D. N. 2006, Astrophys. J., 653, 1400

Page, L. et al. 2006, arXiv preprint astro-ph/0603450

Passarino, G. & Veltman, M. J. G. 1979, Nucl. Phys., B160, 151

Pe'er, A. & Waxman, E. 2005; Erratum-ibid. 638:1187, 2006, Astrophys. J., 633, 1018

Peng, F., Königl, A., & Granot, J. 2005, Astrophys. J., 626, 966

Perlmutter, S. et al. 1999, Astrophys. J., 517, 565

Peskin, M. E. & Schroeder, D. V. 1995, An Introduction to quantum field theory (Addison-Wesley)

Piran, T. 2004, Rev. Mod. Phys., 76, 1143

Piran, T., Shemi, A., & Narayan, R. 1993, Mon. Not. R. Astron. Soc, 263, 861

Pontecorvo, B. 1958, Sov. Phys. JETP, 7, 172

Pontecorvo, B. 1968, Sov. Phys. JETP, 26, 984

Porciani, C. & Madau, P. 2001, Astrophys. J., 548, 522

Prakash, M., Ratkovic, S., & Dutta, S. I. 2004, in Compact Stars: The Quest for New States of Dense Matter, ed. D. K. Hong, C.-H. L. H. K. Lee, D.-P. Min, T.-S. Park, & M. Rho, 476

Preparata, G., Ruffini, R., & Xue, S.-S. 1998, Astron. Astrophys., 338, L87

Prokoshin, I. D. & Tiapkin, A. A. 1957, Sov. Phys. JETP, 5, 618

Pruet, J. 2003, Astrophys. J., 591, 1104

Pruet, J., Woosley, S. E., & Hoffman, R. D. 2003, Astrophys. J., 586, 1254

Qian, Y. Z. & Woosley, S. E. 1996, Astrophys. J., 471, 331

Rachen, J. P. & Biermann, P. L. 1993, Astron. Astrophys, 272, 161

Raffelt, G. G. 1996, Stars as laboratories for fundamental physics: The astrophysics of neutrinos, axions, and other weakly interacting particles (Chicago, Univ. Pr.)

Ratkovic, S., Dutta, S. I., & Prakash, M. 2003, Phys. Rev., C67, 123002

Razzaque, S. & Mészáros, P. 2006, Astrophys. J., 650, 998

Razzaque, S., Mészáros, P., & Waxman, E. 2003a, Phys. Rev. Lett., 90, 241103

Razzaque, S., Mészáros, P., & Waxman, E. 2003b, Phys. Rev., D68, 083001

Razzaque, S., Mészáros, P., & Waxman, E. 2004a, Phys. Rev., D69, 023001

Razzaque, S., Mészáros, P., & Waxman, E. 2004b, Phys. Rev. Lett., 93, 181101

Razzaque, S., Mészáros, P., & Waxman, E. 2005, Mod. Phys. Lett., A20, 2351

Reimer, O., Pohl, M., Butt, Y. M., Torres, D. F., & Romero, G. E. 2002, Astron. Astrophys., 390, L43

Reines, F. & Cowan, C. L. 1953, Phys. Rev., 92, 830

Riess, A. G. et al. 2004, Astrophys. J., 607, 665

Rossi, E. M., Beloborodov, A. M., & Rees, M. J. 2006, Mon. Not. R. Astron. Soc., 369, 1797

Rubakov, V. A. 1984, Nucl. Phys., B245, 481

Rybicki, G. B. & Lightman, A. P. 1979, Radiative Processes in Astrophysics (John Wiley & Sons)

Sauter, F. 1931, Z. Phys., 69, 742

Sawyer, R. F. 1981, Phys. Rev., D24, 1581

Schwinger, J. S. 1951, Phys. Rev., 82, 664

Sehgal, L. M. 1974, Nucl. Phys., B70, 61

Shemi, A. & Piran, T. 1990, Astrophys. J,, 365, L55

Sjöstrand, T., Lonnblad, L., Mrenna, S., & Skands, P. 2003, arXiv preprint hep-ph/0308153

Spergel, D. N. et al. 2006, arXiv preprint astro-ph/0603449

Spruit, H. C., Daigne, F., & Drenkhahn, G. 2001, Astron. Astrophys., 369, 694

Stecker, F. W. 1971, Cosmic Gamma Rays (Mono Book Corp.)

Stephens, S. A. & Badhwar, G. D. 1981, Astrophysics and Space Science, 76, 213

Svensson, R. 1987, Mon. Not. R. Astron. Soc., 227, 403

't Hooft, G. 1971, Phys. Lett., B37, 195

't Hooft, G. & Veltman, M. J. G. 1979, Nucl. Phys., B153, 365

Thompson, C. 1994, Mon. Not. R. Astron. Soc., 270, 480

Treves, A., Turolla, R., & Popov, S. B. 2000, Nuovo Cimento B Serie, 115, 863

Tubbs, D. L. & Schramm, D. N. 1975, Astrophys. J., 201, 467

Turner, M. S. 1983, Phys. Rev., D28, 1243

Unruh, W. G. 1976, Phys. Rev., D14, 870

Usov, V. V. 1992, Nature, 357, 472

Uzdensky, D. A. & MacFadyen, A. I. 2006, Astrophys. J., 647, 1192

Van Paradijs, J., Kouveliotou, C., & Wijers, R. A. M. J. 2000, Ann. Rev. Astron. Astrophys., 38, 379

Van Paradijs, J. et al. 1997, Nature, 386, 686

Van Putten, M. H. P. M. & Ostriker, E. C. 2001, Astrophys. J., 552, L31

Venkatesan, A., Miller, M. C., & Olinto, A. V. 1997, Astrophys. J., 484, 323

Vietri, M. 1995, Astrophys. J., 453, 883

Vlahakis, N. & Königl, A. 2001, Astrophys. J., 563, L129

Vlahakis, N. & Königl, A. 2003, Astrophys. J., 596, 1080

Vlahakis, N., Peng, F., & Königl, A. 2003, Astrophys. J., 594, L23

Voloshin, M. B., Kobzarev, I. Y., & Okun, L. B. 1975, Sov. J. Nucl. Phys., 20, 644

Waxman, E. 1995, Phys. Rev. Lett., 75, 386

Waxman, E. & Bahcall, J. 1997, Phys. Rev. Lett., 78, 2292

Waxman, E. & Bahcall, J. N. 2000, Astrophys. J., 541, 707

Waxman, E. & Mészáros, P. 2003, Astrophys. J., 584, 390

Weinberg, S. 1972, Gravitation and cosmology (John Wiley & Sons)

Woosley, S. & Heger, A. 2006, Astrophys. J., 637, 914

Woosley, S. E. 1993, Astrophys. J., 405, 273

Woosley, S. E. & Bloom, J. S. 2006, Ann. Rev. Astron. Astrophys., 44, 507

Yao, W. M. et al. 2006, J. Phys., G33, 1

Yoon, S.-C. & Langer, N. 2005, Astron. Astrophys., 443, 643